

Reciprocal Impacts of Land Settlement and Jakarta Rail Tunnel

Numerical Analysis of MRT Jakarta North-South Line Phase 2



Reciprocal Impacts of Land Settlement and Jakarta Rail Tunnel

Numerical Analysis of MRT Jakarta North-South Line Phase 2

by

Johannes M.S. Simanjuntak
4505743

in partial fulfilment of the requirements for the degree of

Master of Science
in Hydraulic Engineering
at Technische Universiteit Delft

August 10th, 2017

Supervisor:	Prof. Dr. Ir. K.G. Gavin, TU Delft
Thesis committee:	Ir. K.J. Reinders, TU Delft
	Dr. Ir. Y. Yang, TU Delft

[This page is intentionally left blank]

Significant development of Jakarta infrastructure is necessary to keep up with the economic growth. For the new Jakarta underground rail network, imminent extension of the North-South Line Phase 1 (NSL-P1) tunnel heads towards the northern part of city. One of the engineering challenges that exist in the area is the substantial amount of reported surface settlement over the years, which is indicated by the continuous sea wall improvement project and the increase of flooded area. The recent GPS survey reported an average subsidence rate of 5 centimeters per year and could reach a maximum of 15 centimeters per year on several hotspots in North Jakarta.

Being an underground structure, the rail tunnel would be affected by the settling environment and the reciprocity can be expected. Operational interruptions of the tunnel could occur in the future as a product of differential structural displacement. On the other hand, alterations in settlement rate or pattern must also be anticipated. The aforementioned reciprocity underlines the importance of structural and geotechnical assessments in the area. The assessment then can be used as a reference to determine and improve the safety level of the tunnel as well as the surrounding infrastructures.

The study was commenced with the investigation of prevalent driving factors of Jakarta land subsidence from the preceding researches. The initial stage of the study elaborated the concepts used in the analysis, including geotechnical data interpretation, soil consolidation and creep, numerical model formulation, and past studies regarding the loads on bored tunnels.

A segment of proposed North-South Line Phase 2 (NSL-P2) tunnel was selected for this study. The selection was motivated by the the amount of available geotechnical information and the severity of differential land subsidence in the respective area. Longitudinal and cross-sectional two-dimensional numerical model of the selected segment were developed in Plaxis 2D, based on the combination of in-situ soil tests and the outcome of earlier studies about Jakarta geotechnical characteristics. Into the model, four time-dependent groundwater level scenarios were assigned to simulate the surface settlement. As the research emphasizes on the long-term settlement, a 100-year study period was chosen and started in the year 2000.

Given that the NSL-P2 tunnel design has not been confirmed at the time of writing, the numerical study adopted an identical design to the NSL-P1 tunnel. A 6.65-m diameter concrete tunnel was added into the model at an average depth of 15-m. From the longitudinal numerical analysis, total structural displacement in time and additional longitudinal forces were obtained. Subsequently, further analysis was performed on the cross-section, in the transverse direction, which displayed most settlement at the end of the analysis period. At the cross-sectional perspective, the development of forces as well as soil stress around the tunnel ring due to settlement and structural deformation were acquired.

Finally, this study reached a general conclusion which explains that the land subsidence in Jakarta posed non-governing additional loads to the future NSL-P2 tunnel. A majority of the total surface settlement was caused by the consolidation and compression of the upper soil layers. However, special attention must be paid to the station-tunnel interface as substantial differential settlement could take place. To minimize further issues, several design recommendations are provided at the end of the research.

[This page is intentionally left blank]

ACKNOWLEDGEMENT

This thesis serves as a partial fulfillment for the degree of Master of Science in Hydraulic Engineering at TU Delft. The study was carried out for 9 months with supervision from a diverse thesis committee, consists of TU Delft faculty members in geotechnical, hydraulic, and structural engineering.

Behind this achievement is the blessing and guidance of many. First and foremost, I would like to thank my family, especially my parents, Andy Simanjuntak and Mona Sakaria, for their love and endless support from 7000 miles away. Also to my brother, Sergio Simanjuntak, for the periodical conversations which successfully left me homesick on several occasions. Thank you to Patricia Djuhadi, for all her love, encouragements, moral supports, arguments, sesame snaps, and jokes.

On top of everything, my greatest gratitude goes to my mentors at TU Delft, the best I could ever asked for. I would like to specially thank: Ir. Kristina Reinders for the continuous supports, encouragements, and feedbacks; Dr. Yuguang Yang for the constructive insights; and Prof. dr. Ken Gavin for the critical advices to improve my study. The time and energy that they spent in the midst of their busy schedule made it possible for me to graduate.

I would also like to express my gratitude to my colleagues and seniors who helped me acquiring the data for my research: Mr. Rizki Shebubakar, Mr. Rizki Novianto, Ms. Riska Muslimah, Ms. Weni Husin, Mr. Allan Tandiono, Mr. Wilman Sidjabat, and everyone at MRT Jakarta. Furthermore, special thanks to Robin Renardi, who extended my enquiry to his network and successfully obtained the SPT data.

Finally, to my friends at TU Delft and across the globe: thank you for being there when I need you the most. It was indeed not an easy journey, but you guys made it enjoyable.

"You'll never walk alone"

*Johannes M.S. Simanjuntak
Delft, 2017*

[This page is intentionally left blank]

TABLE OF CONTENTS

Abstract	3
Acknowledgement	5
Table of Contents	7
List of Notations	10
1. Introduction	12
1.1 Background	12
1.2 Objective and Scope of Study	13
1.3 Research Methodology	14
1.4 Report Outline	15
2. Literature Review	16
2.1 Basic Soil Mechanics	16
2.1.1 Stress and Strain on Soil	16
2.1.2 Void Ratio and Porosity	16
2.1.3 Pore Water	17
2.2 Soil Consolidation	18
2.2.1 Primary Consolidation	19
2.2.2 Secondary Compression	20
2.2.3 Time Rate Consolidation	21
2.3 Material Properties	23
2.3.1 Soft Soil.....	23
2.3.2 Interpretation of Field Investigation	23
2.3.3 Other Soil Properties	25
2.3.4 Creep in Concrete.....	26
2.4 Soil Constitutive Models	26
2.4.1 Mohr-Coulomb Model.....	27
2.4.2 Soil Hardening Model	27
2.4.3 Soft Soil Creep Model	28
2.5 Bored Tunnels	28
2.5.1 Tunnel Orientation	28
2.5.2 Beam Model	29
2.5.3 Loads on Tunnel Structure	29
2.5.4 Structural Response.....	31
2.5.5 Longitudinal Beam Stiffness	32
2.5.6 Segmental Joint Stiffness.....	34
2.5.7 Internal Bending Moment	36
2.5.8 Water Tightness	37
2.6 Soil Arching	37
3. Case Study: Jakarta	40
3.1 General Information	40
3.1.1 Geographical Features.....	40
3.1.2 Population	40
3.1.3 Topography	40
3.1.4 Subsurface Profile.....	41

3.2	Groundwater Extraction Issue	42
3.2.1	History	42
3.2.2	Present Trend	42
3.2.3	Groundwater Table	43
3.3	Land Subsidence	44
3.3.1	Mechanism of Land Subsidence	44
3.3.2	Rate of Subsidence	45
3.4	Mass Rapid Transit Jakarta	47
3.4.1	General Information	47
3.4.2	Project Sequence	47
3.4.3	NSL-P1 Tunnel Properties	48
4.	Site Characterization	49
4.1	Collected Information	49
4.2	Boundary Conditions	50
4.2.1	Site Selection	50
4.2.2	Estimation of Consolidation in The Shallow Aquifer	53
4.3	Recapitulation of SPT Result	56
4.3.1	Overall Observation	57
4.3.2	N-SPT Corrections	58
4.3.3	Simplified Soil Types	58
4.4	SPT Correlations	59
4.4.1	SPT to Elasticity Moduli	59
4.4.2	SPT to Strength Parameters	60
4.5	Consolidation Coefficients	61
4.6	Unit Weight and Void Ratio	62
4.7	Stress History	63
4.8	Hydraulic Aspects	64
4.8.1	Head Functions	64
4.8.2	Permeability	65
4.9	Interface Coefficient	65
4.10	Structural Aspect	66
4.10.1	Concrete Material and Capacity	66
4.10.2	Tunnel Lining and Segmental Joints	66
4.10.3	Longitudinal Properties	67
4.10.4	Tunnel Boring Machine Thrust Force	67
4.11	Ground Surcharge	67
4.12	Proposed Parameters for Numerical Model	68
5.	Numerical Study Details	69
5.1	Software	69
5.2	Setup and Phasing	69
5.2.1	Constitutive Models	69
5.2.2	Simulation Phases	69
5.2.3	Calculation and Loading Type	70
5.3	Numerical Model	70
5.3.1	Structural Model	70
5.3.2	Longitudinal Model	71
5.3.3	Cross Sectional Model	71
6.	Results and Discussion	73
6.1	Forces in Longitudinal Perspective	73

6.1.1	Vertical Displacement.....	73
6.1.2	Additional Forces.....	74
6.2	Soil and Structural Stresses in the Tunnel Ring	77
6.2.1	Progression of Soil Stress.....	77
6.2.2	Ring Deformation	79
6.2.3	Axial Force at Lining.....	81
6.2.4	Bending Moment.....	82
6.2.5	Normal Stress	82
6.3	Behavior of Surrounding Soil	83
6.3.1	Consolidation in Calibration and Transitional Period	83
6.3.2	Consolidation in Analysis Period	84
6.3.3	Influence of Tunnel on Total Settlement.....	85
7.	Further Analysis	87
7.1	Stiffer Tunnels.....	87
7.1.1	Equivalent Beam Stiffness	87
7.1.2	Deformation and Bending Moment	88
7.2	Presence of Stiffer Structures	89
7.2.1	Reflection from Shanghai Subway Tunnel.....	90
7.2.2	Analysis of Proposed NSL-P2 stations and Design Recommendations.....	91
7.3	Summary and Design Improvements	96
8.	Conclusions	97
8.1	Conclusion.....	97
8.2	Limitations and Further Studies	98
9.	References	100

LIST OF NOTATIONS

σ	Total stress (geotechnical) or stress in general (structural)
σ'	Effective stress
σ_w	Hydrostatic pressure
K_0	Coefficient of lateral earth pressure
φ	Friction angle of soil (geotechnical)
σ_h	Horizontal stress
σ_v	Vertical stress
OCR	Over-consolidation ratio
σ'_{pc}	Effective preconsolidation stress
σ'_{V0}	Effective existing stress
Δl	Change in length parameter
l	Length parameter
ε	Strain
n	Porosity (geotechnical)
e	Void ratio (geotechnical)
V_V	Volume of void
V_S	Volume of solid
V_T	Total volume
K	Hydraulic conductivity (hydraulic) or Rankine coefficient (geotechnical)
k	Intrinsic permeability
μ_w	Viscosity of water
γ_w	Unit weight of water
i	Hydraulic gradient
$h_{a,b}$	Hydraulic head at point a or b
Q	Flow rate
q	Flow rate per unit area
C_C	Compressive coefficient
C_S	Swelling coefficient
C_α	Creep coefficient
m_v	Volume compressibility
S_C	Primary consolidation
S_S	Secondary compression
t	Time
H	Layer thickness (geotechnical)
U_V	Degree of consolidation
T_V	Time factor
u	Excess pore water pressure
d	Drainage length (hydraulic) or segmental thickness (tunnel)
E	Elasticity modulus, subnotation S for soil, T for tunnel, C for concrete
N	SPT blow counts
c_u	Undrained cohesion
p_a	Atmospheric pressure
ϕ	Time dependent creep coefficient
λ^*	Modified compression index
κ^*	Modified swelling index
μ^*	Modified creep index

r	Tunnel radius
$C_{n0,n2,M}$	Soil-structure interaction coefficient
η	Efficiency of bending rigidity
I	Moment of inertia
λ	Joint stiffness ratio
m	Number of joints
l_t	Height of contact area
K_θ	Rotational spring stiffness
b	Half segmental length in longitudinal direction
τ	Shear stress
R_{Inter}	Interface coefficient

1. INTRODUCTION

A sudden population boom could be hardly matched by the improvement of infrastructures in it. This has been the case in national economic centers of multiple developed and developing countries, such as the Philippines, Indonesia, India, and Mexico (UN, 2014). The population boom forms squatters, increases traffic congestions, causes environmental damage, and reduces the life quality, in general, of its inhabitants. Especially in Jakarta, the capital city of Indonesia, these issues are interrelated and thus require strategic plans to tackle most issues with least resources.

This MSc thesis discusses one of the modern issues in Jakarta from the geotechnical engineering perspective. The interaction between upcoming infrastructure and the environment is the main focus of the study. The details of the research are briefly presented in this chapter.

1.1 Background

One of the great challenges faced by Jakarta is the high rate of urbanization. As the economic center of Indonesia, Jakarta remains to be an attractive destination for people all over the archipelago to seek better opportunities. However, the infrastructure has been struggling to accommodate continuous migration as the rate of infrastructural growth tends to be lower than the population influx. Moreover, the interrelated issues that follow population growth pose new challenges in the field of underground infrastructure engineering.

An approach taken by the government to solve mobility issue is by developing the Mass Rapid Transit (MRT) Jakarta, a rail-based urban transport system. As of now, the mega project is divided into 3 phases based on its construction timeline, namely the North-South line Phase 1 (NSL-P1), North-South line Phase 2 (NSL-P2), and the East-West line (EWL). The planned MRT network is presented in Figure 1.1 below.

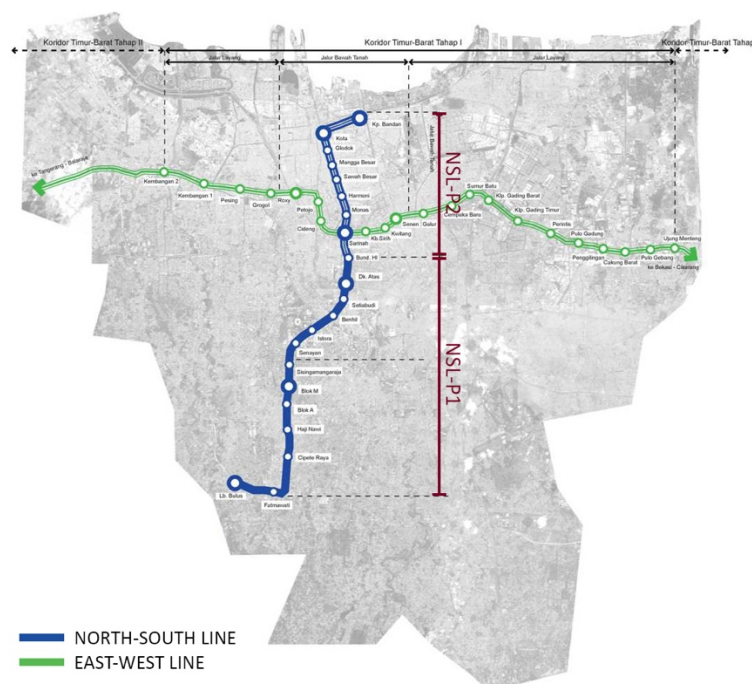


Figure 1.1: Complete MRT Jakarta network (MRT Jakarta, 2014 - with adaptations)

The NSL-P1 project was commenced in 2013 and expected to start the operations in 2019. According to the company's website, the northward extension, NSL-P2, is targeted to operate in the year 2020. Furthermore, the EWL project is expected to complete as early as 2024. The NSL-P1 combines elevated and underground sections, while the NSL-P2, based on the the latest publication, will be fully underground (MRT Jakarta, 2016).

Not only increases the demand of infrastructure, Jakarta's population influx is deemed to have significant influence on the land subsidence as it induces the growth of unregulated groundwater extraction. Being on a deltaic area, Jakarta's subsurface is characterized by the compressible alluvial soil layers. That being said, groundwater has an important role to the overall soil strength and thus contributed greatly to the land subsidence (Abidin et al., 2010). Per report by Deltares (n.d.), Jakarta leads the race among other deltaic cities in Asia in terms of average land subsidence, presented in Figure 1.2, with approximately 2-meter declination since the 1950s.

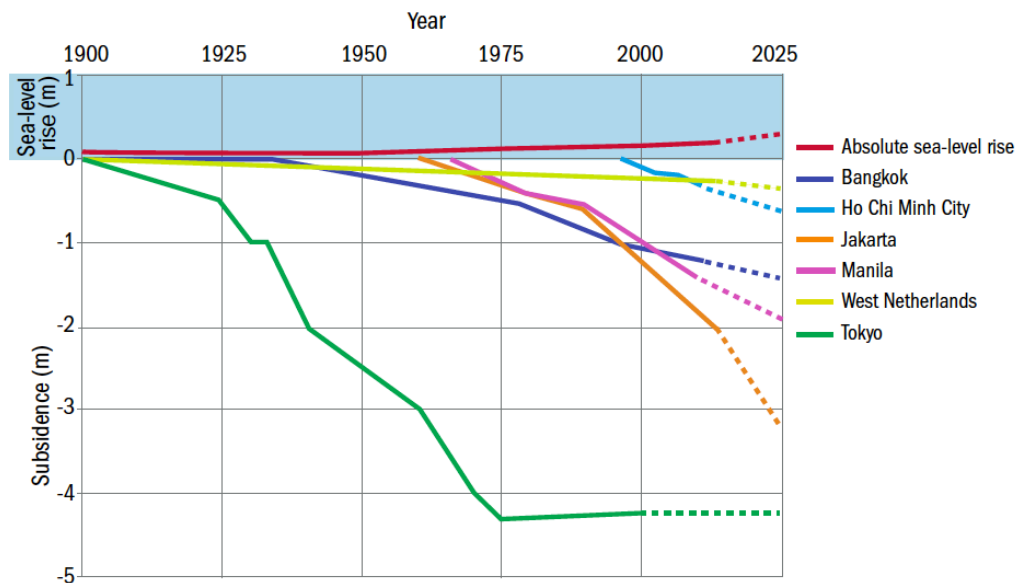


Figure 1.2: Jakarta is leading in land subsidence with more severe rate expected in the future (Deltares, n.d.)

The proposed MRT tunnel is located in the area with active case of land subsidence. This makes the land subsidence an important facet of design and should be anticipated throughout its operational period to prevent disasters. Therefore, the long term impact of this environmental change must be examined to further assure the structural integrity and safety of the underground infrastructure.

1.2 Objective and Scope of Study

In general, the research aims to investigate the engineering challenges posed by land subsidence to tunnel structure and the future rail tunnel of MRT Jakarta is chosen as a case study. The curiosity is formulated in the main thesis objective, phrased as:

“What are the reciprocal impacts of differential land subsidence and bored tunnel in soft soil environment?”

Throughout the study, incremental approach is taken to attain the main objective. Therefore, the main thesis question is divided into five sub-questions presented below.

1. What are the driving factors of the land subsidence in Jakarta?
2. How significant are the additional forces on the tunnel due to differential settlement?
3. Given that the difference in stiffness, how does the presence of the tunnel alter the settlement pattern around it? How significant are the alterations?
4. How do the axial force and bending moment on the tunnel ring of NSL-P2 evolves in time?
5. Departing from the research findings, what design recommendations could be considered in the future to mitigate the consequences?

The study is limited to NSL-P2 project. The research adheres to the local project boundaries and conditions, such as the soft soil environment, the prescribed tunnel dimensions, structural provisions, and the change of groundwater level in time. Furthermore, the study concentrated on the interaction between the bored tunnel and the soil environment and thus the stations are excluded from the analysis. Additionally, the research

focuses more towards the geotechnical aspect rather than the structural, which means that it focuses on the load generation part rather than the structural design.

1.3 Research Methodology

A set of strategy was devised to provide answers for the research questions. Even though the research centers on computer-assisted numerical analysis, adequate comprehension about the topic is important to correctly establish the numerical model and interpret the result. Furthermore, these steps are taken:

1. The research is initiated with literature study about relevant topics. It is immensely essential to document sufficient scientific materials to support the following research sequences. Additionally, the documentation of relevant topics helps to provide explanations about the geotechnical phenomena simulated with the software.
2. The second step is to elaborate the land subsidence phenomenon in Jakarta, including its driving factors and the mechanism of the land subsidence. This activity is performed through series of literature research. The result is important to establish the numerical model.
3. The next step is data collection which was performed in Jakarta. The data was collected from the online archives, MRT Jakarta as the project owner, and related public offices. Necessary information to conduct the research, includes the soil data, structural provision, and settlement report.
4. The fourth step is the establishment of numerical model and execution of analysis. This step is divided into more parts as listed below.
 - a. Soil model, without the tunnel structure, will be established based on obtained and interpreted data. Local and general empirical findings will be used to help the data interpretation process.
 - b. The model will undergo a calibration process, which spans over a 14-year period between the year 2000 to 2014. This decision is made based on the data availability. The calibration is used to ensure that the soil properties in the model are able to produce similar amount of settlement as reported.
 - c. When the soil model is ready, tunnel structure will be added into the model. The insertion of tunnel structure is in accordance with real project timeline, which is in year 2020.
 - d. The change in groundwater level in time will be modeled with four scenarios to anticipate future uncertainties.
 - e. The numerical analysis will be performed in two perspectives, which are the longitudinal and cross sectional. The longitudinal analysis is used to study the macro behavior of tunnel due to differential settlement, while the cross sectional analysis is used to study the reciprocal impact between the structure and local settlement.
5. Next, the findings will be presented and interpreted. Temporal analysis will also be included.

The sequences are presented with more clarity in the research flowchart below.

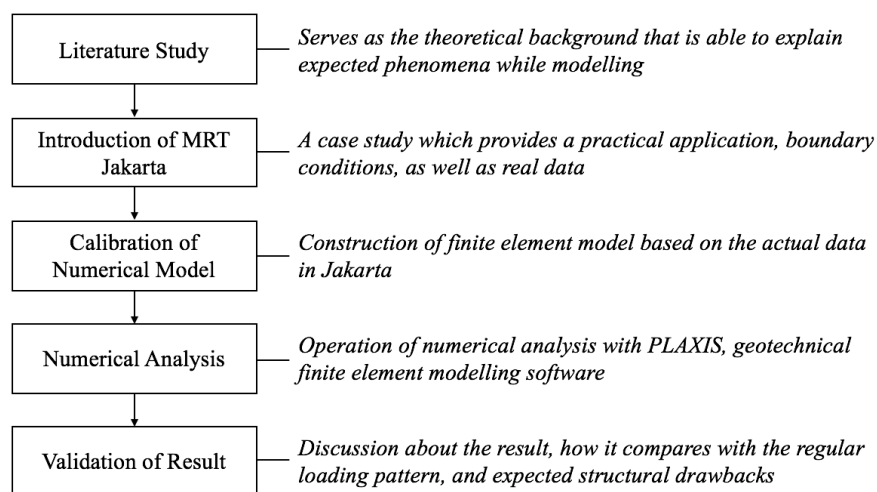


Figure 1.3: Research strategy to attain the objectives

1.4 Report Outline

Chapter 1 presents a general overview of the research. The motivations to proceed with the research topic is presented along with the strategy of pursuit. Additionally, the scope and objectives of study are defined in the chapter.

Chapter 2 provides the conceptual background of land subsidence, tunnel, and soil-structure interaction. These concepts were gathered and summarized from established literatures and past researches. Relevant concepts about soil mechanics, existing load formulation theories, and structural integrity studies are included in this chapter.

Chapter 3 brings reader closer into the case study, which is in Jakarta, Indonesia. This chapter provides general information about the study site and MRT Jakarta. Furthermore, this chapter also presents the response to the first thesis sub-question.

Chapter 4 simplifies Jakarta's complex geotechnical condition in order to construct the numerical model. The simplification procedures are elaborated accordingly in this segment. Additionally, this chapter shows how soil and structural materials are defined.

Chapter 5 delineates the development of the numerical model. This segment discusses about the selected soil constitutive model, calibration, and the construction of the numerical model.

Chapter 6 discusses the result of the numerical analysis. Impacts of differential settlement on longitudinal as well as cross sectional profile of the tunnel are presented based on the result of the numerical analysis. Given that the three remaining thesis sub-questions relies on the numerical analysis, the answers of those sub-questions are presented in this segment.

Chapter 7 provides further assessment on the numerical analysis outcomes. This chapter uses the analysis results to generate design recommendations for NSL-P2 tunnel.

Chapter 8 concludes the study. A summary of findings and recommendation of further studies are conferred in this chapter.

2. LITERATURE REVIEW

2.1 Basic Soil Mechanics

2.1.1 Stress and Strain on Soil

Stress (σ) on soil is defined by the accumulation of gravitational loading from the overburden measured a certain point of interest. As a porous element, stresses on soil are not always constituted wholly to the soil skeleton. Instead, a portion of the stress is sustained by porous fluid, which in this study is always assumed to be water. The principles of stresses on porous media was developed by Terzaghi in 1925 (Osipov, 2015).

$$\sigma = \sigma' + \sigma_w$$

where σ' is the effective stress and σ_w is the pore pressure. The effective stress is a portion of total stress that is sustained by the soil skeleton.

As a vector, stress on soil can be categorized based the direction. In general cases, vertical and horizontal are the most commonly used conventions. However, new conventions can be easily established based on necessity through the geometrical conversion, for instance the radial and tangential soil stress. The correlation between the vertical and horizontal stress, σ_v and σ_h respectively, is elucidated by coefficient of lateral earth pressure (K_0), which value depends on the friction angle of the soil (φ) as proposed by Jaky in 1944.

$$K_0 = 1 - \sin \varphi$$

Therefore, the relationship is defined with the equation below.

$$K_0 = \frac{\sigma_h}{\sigma_v}$$

The behavior of soil as a response to present load is also contingent on the stresses that took place in the past. The stress history of soil is evaluated with the over-consolidation ratio (OCR). The OCR is defined below, where σ'_{pc} represents the effective preconsolidation stress and σ'_{v0} represents the effective existing stress.

$$OCR = \frac{\sigma'_{pc}}{\sigma'_{v0}}$$

Strain (ε) in materials is measured through the ratio of the change of length (Δl) to the original length (l). Therefore, strain is a dimensionless parameter.

$$\varepsilon = \frac{\Delta l}{l}$$

Stress and strain in soil are complexly correlated. The correlation will be discussed at the latter stage of the research as it is associated with soil modelling.

2.1.2 Void Ratio and Porosity

Void ratio (e) is one of the soil compaction measures. It is the quotient of the volume of void and the volume of solid within one soil body. Similarly, porosity (n) is also a ratio. However, it is a ratio between the volume of void and the total volume.

$$e = \frac{V_V}{V_S}$$

$$n = \frac{V_V}{V_T}$$

where V_V is the volume of void, V_S is the volume of solid, and V_T is the total volume. From the equations, a value greater than 1.00 can be obtained for void ratio. On the other hand, soil porosity is limited to 1.00. The relationship between porosity and void ratio is shown below.

$$e = \frac{n}{1 - n}$$

2.1.3 Pore Water

Prior to the elaboration of land subsidence, it is essential to understand how the presence of fluid in porous media influence the properties of soil. Especially for this study, the type of fluid is limited to water. The role of pore water is explained in this subchapter, starting from the soil permeability, porous flow, and drainage.

Soil Permeability

The parameter used to measure soil permeability is the intrinsic permeability (k), which dimension is length squared (L^2). Physically, parameter k is proportional to the degree of interconnectedness of voids in the soil. A more popular representation of permeability is by using the coupled parameter hydraulic conductivity (K). Unlike the intrinsic permeability, hydraulic conductivity is not only a property of porous media. Instead, it hinges on the intrinsic permeability of soil and the viscosity of water (μ_w).

$$K = k \frac{\gamma_w}{\mu_w}$$

where γ_w is the unit weight of water. Hydraulic conductivity measures the rate of penetration for water through the voids in the soil matrix, thus dimension is length over time (L/T).

Zhang (n.d.) asserted that intrinsic permeability is often manifested in square centimeters or Darcy, where one Darcy is equal to $9.87 \times 10^{-9} \text{ cm}^2$. Additionally, typical ranges for measure of were proposed in Table 2.1.

Table 2.1: Typical ranges of soil permeability (Zhang, n.d.)

Material	Intrinsic Permeability (Darcy)	Hydraulic Conductivity (cm/s)
Clay	$10^{-6} - 10^{-3}$	$10^{-9} - 10^{-6}$
Silt, sandy silts, clay sands, till	$10^{-3} - 10^{-1}$	$10^{-6} - 10^{-4}$
Silty sands, fine sands	$10^{-2} - 10^0$	$10^{-5} - 10^{-3}$
Well-sorted sands, glacial outwash	$10^0 - 10^2$	$10^{-3} - 10^{-1}$
Well-sorted gravel	$10^1 - 10^3$	$10^{-2} - 10^0$

A pattern is noticeable in Table 2.1. Homogeneous coarse material exhibits larger hydraulic conductivity; thus it is more permeable than fine materials and directly correlated with the porosity within the soil body. With more void spaces, the pores are more interconnected to one another. Hence, water can easily penetrate through it.

Porous Flow

Given that soil is a porous media, the flow of water is referred as porous flow. The porous flow is either gravity-driven or caused by the pressure gradient, the difference of pore pressure between two points.

Henry Darcy, in 1856, published his discovery about porous flow based on an experiment of porous flow in a sand column. Darcy's theory is analogous to transport laws in other disciplines, such as the Ohm's law for electrical conduction and Fourier's for heat transfer (Zimmerman, 2002). The Darcy's law is defined with the following equation.

$$Q = -KA \left(\frac{h_a - h_b}{L} \right)$$

On the equation, the dependency of flow rate to pressure difference is evident. Q is the flow rate, A is the cross sectional area, $h_{a/b}$ is the hydraulic heads at point a/b, and L is the distance between point a and b. The equation can also be expressed with flow per unit area (q).

$$q = K \cdot i$$

On the equation above, q has the dimensions of L/T , which is commonly expressed in $m^3/year/m^2$. Meanwhile, i is the non-dimensional pressure gradient equivalent to the change of pressure head divided by distance.

$$i = \frac{\Delta h}{L}$$

A direct proportionality between the flow rate with the hydraulic conductivity and pressure gradient is found in Darcy's equation. Thus, considering an identical gradient in environment with high or low hydraulic conductivity, flow rate is expected to be greater in high K -value environment. In the real situation, a similar comparison is portrayed by sand and clay layer, where high and low K -value respectively are apparent. Consequently, drainage, defined by the Darcy equation, is a time-dependent mechanism. The dependency is discussed in the next section.

2.2 Soil Consolidation

Soil deforms upon loading and the deformation is referred as consolidation. Consolidation depends on internal properties, such as soil stiffness and drainage, and external properties, such as the magnitude of the load. The consolidation process is divided into three phases, namely the immediate settlement or initial compression, primary consolidation, and secondary consolidation. The progression of consolidation in time is shown in Figure 2.1.

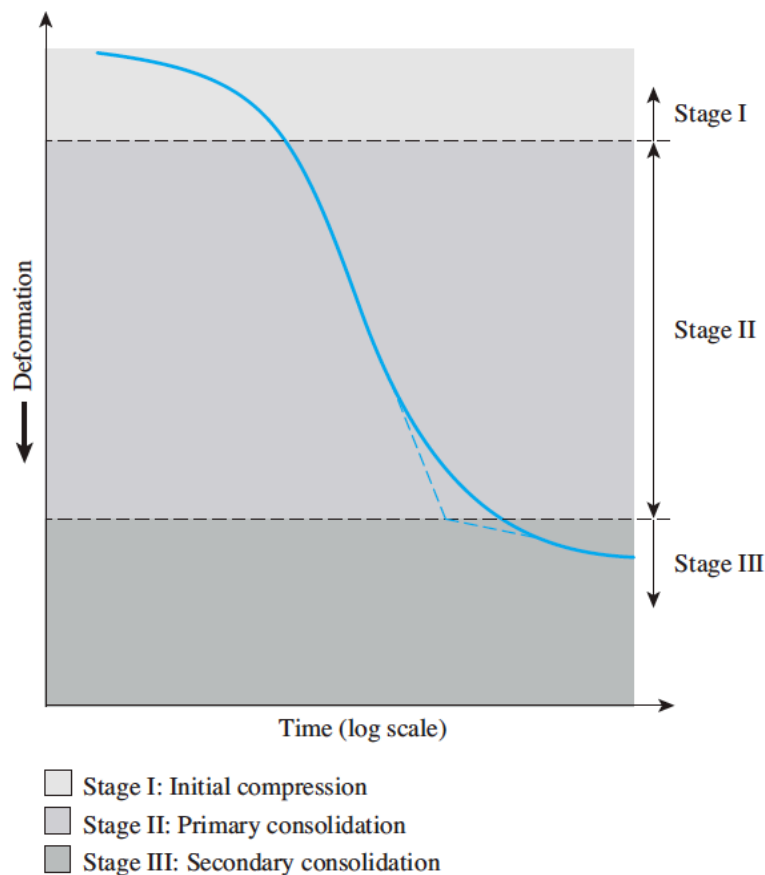


Figure 2.1: Stages of soil consolidation with respect to time (Das, 2011)

Consolidation in time is represented by the blue curve in Figure 2.1. The slope of the curve shows the rate of consolidation. The initial compression takes place instantly as a response to external loading. The highest

settlement rate is observed in the primary consolidation compared to the other two phases. However, secondary compression cannot be disregarded especially in compressible soil as it extends for a long time.

2.2.1 Primary Consolidation

Primary consolidation is the gradual volumetric reduction of a soil body due to the increase in effective stress. Volumetric reduction is often associated with the change of void ratio. Furthermore, the rate of increase is associated with drainage, which is affected by natural causes, for example the permeability of soil, and mechanical causes, such as the implementation of water pump (Knappett and Craig, 2012). Additionally, the opposite mechanism, volumetric increase, could also occur due to the decrease in effective stress. This mechanism is known as swelling. Presented in Figure 2.2, consolidation can follow either of the two curves, referred as the normally consolidated and the overly consolidated.

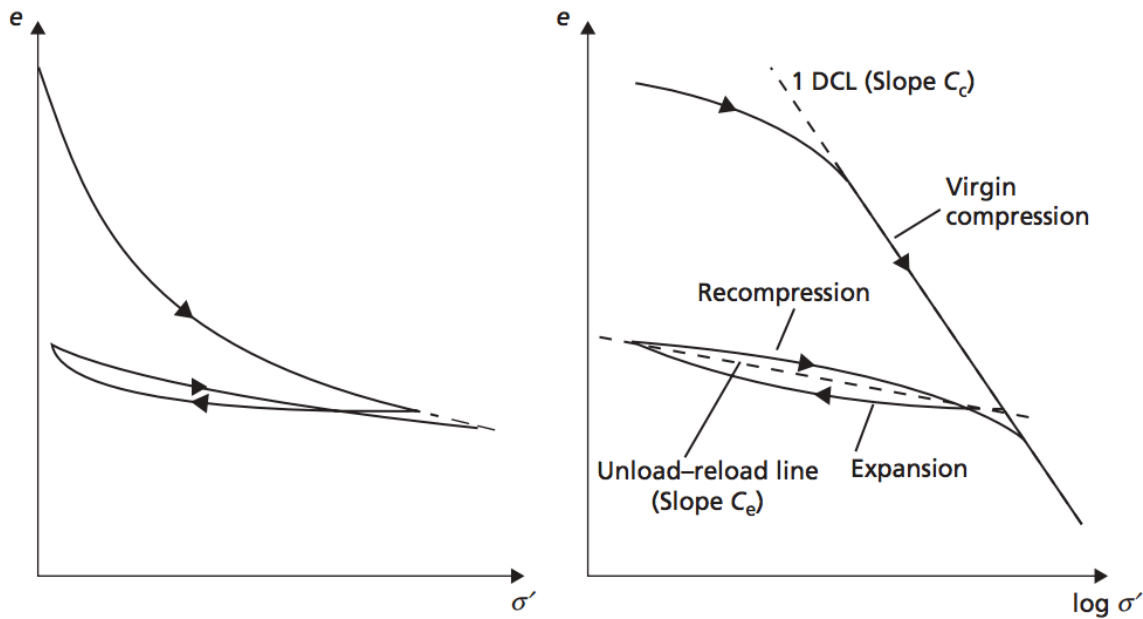


Figure 2.2: Primary consolidation presented in (Left) void ratio and stress graph and (Right) void ratio and stress in logarithmic scale (Knappett and Craig, 2012)

One of the alternatives to quantify soil compressibility is with the compression coefficient (C_c) or swelling coefficient (C_s). These coefficients are the gradient of the virgin compression line and the unload-reload line respectively, see Figure 2.2. Thus, these coefficients are determined with the following formula.

$$C_{c/s} = \frac{e_0 - e_1}{\log(\sigma'_1/\sigma'_0)}$$

Another alternative is with the coefficient of volume compressibility (m_v), which is the volumetric strain per unit increase in effective stress. The volumetric strain is often expressed in the change in void ratio. As a result, the coefficient is calculated with the following formula.

$$m_v = \frac{1}{1 + e_0} \left(\frac{e_0 - e_1}{\sigma'_1 - \sigma'_0} \right)$$

Departing from m_v , the one-dimensional settlement due to primary consolidation (S_c) can be estimated. As mentioned earlier, the consolidation relies on drainage and load. Both are represented in the formula below by the layer thickness (H) and the change of effective stress ($\Delta\sigma'$).

$$S_c = m_v \cdot \Delta\sigma' \cdot H$$

Combining the previous equations with other compressibility measures, the settlement is estimated with the formula below.

$$S_c = \frac{C_c H}{1 + e_0} \log \left(\frac{\sigma'_1}{\sigma'_0} \right)$$

This equation is valid along the normal consolidation line. For stress changes along the unloading-reloading line, C_s should be in place instead of C_c as suggested below.

$$S_c = \frac{C_s H}{1 + e_0} \log \left(\frac{\sigma'_1}{\sigma'_0} \right)$$

In cases where the new stress exceeds the pre-consolidation stress (σ'_{pc}), the deformation must follow two lines. Thus, the settlement should be an accumulation of the two.

$$S_c = \frac{C_s H}{1 + e_0} \log \left(\frac{\sigma'_c}{\sigma'_0} \right) + \frac{C_c H}{1 + e_0} \log \left(\frac{\sigma'_1}{\sigma'_{pc}} \right)$$

2.2.2 Secondary Compression

Secondary compression, also known as creep, is the deformation of soil body due to constant effective stress. With regards to the timeframe of which it occurs, Buisman (1936) asserted that the secondary compression occurs after the excess pore pressure had been completely relieved. On the other hand, Sulkje (1957) and Bjerrum (1967) proposed a different idea, which explains that the primary consolidation and secondary compression might take place simultaneously. The difference of opinions, however, has little to no effects on the consolidation analysis and thus can be disregarded.

In secondary compression, settlement is caused by material deformation, plastic changes of soil fabric, and not because of reorientation of granular material. At this stage, milder deformation rate is apparent compared to the the primary consolidation. Secondary compression is often presented in void ratio and time graph, or $e - \log(t)$ graph, rather than in $e - \log(\sigma)$ graph, as it is a time-dependent process. The $e - \log(t)$ graph is shown in Figure 2.3.

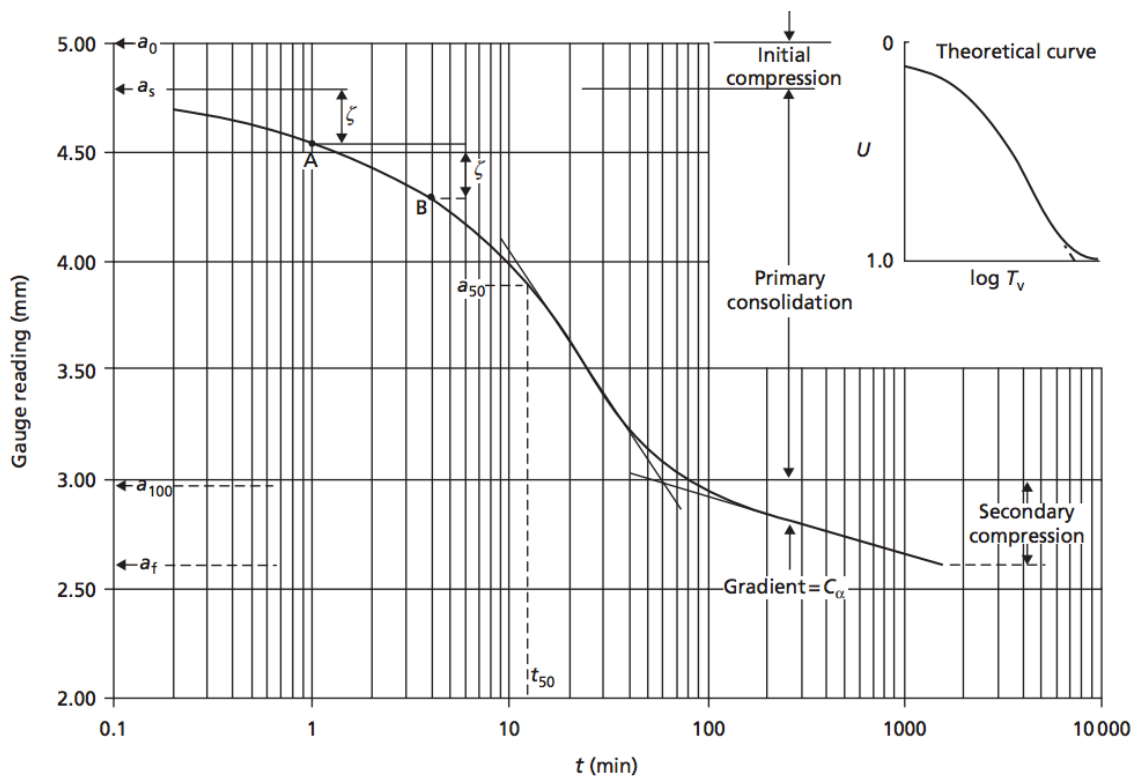


Figure 2.3: Secondary compression portrayed on the result of oedometer test, which plotted the gauge reading and time in logarithmic scale (Knappett and Craig, 2012)

The start of secondary compression is marked by the inflection point at the curve shown in Figure 2.3. The compressibility of soil in secondary compression is defined by the curve gradient, the change of void ratio in time ($t_{0,1}$). The gradient is represented by C_α , which is determined with the formula below.

$$C_\alpha = \frac{e_0 - e_1}{\log\left(\frac{t_1}{t_0}\right)}$$

Unlike in the primary consolidation, the coefficient of volume compressibility (m_v) is now a relevant measure of volumetric strain, represented by the change in void ratio, in time. The coefficient is calculated with the formula shown below.

$$m_v = \frac{1}{1 + e_p} \left(\frac{e_0 - e_1}{t_1 - t_0} \right)$$

where e_p is the void ratio at the end of primary consolidation. Similarly, the amount of settlement due to secondary compression is calculated with the following formula.

$$S_s = m_v \cdot \Delta t \cdot H$$

As it is a stress-independent process, the change in time (Δt) is in place of $\Delta\sigma$. In combination with soil compressibility, the formula is produced.

$$S_s = \frac{C_\alpha H}{1 + e_p} \log(t_1/t_0)$$

2.2.3 Time Rate Consolidation

Drainage of soil layer has significant role in settlement calculation as it defines the dissipation rate of excess pore pressure. In the soft soil environment, more dissipation time is required given the dominance of clay, peat, or other low permeability materials in the stratigraphy. Therefore, the amount of settlement must be able to presented as a function of time. A process diagram, proposed in Figure 2.4, helps to explain about the role of time in the consolidation process.

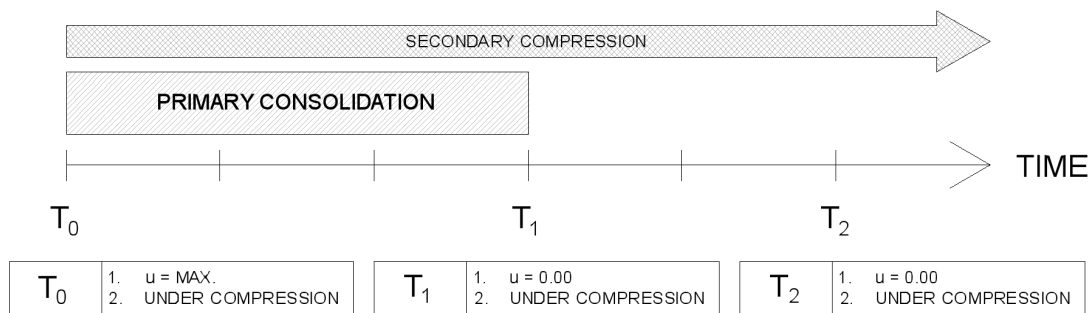


Figure 2.4: Undrained consolidation process diagram

Figure 2.4 suggests that primary consolidation and secondary compression are functions of time. In addition to that, the primary consolidation is also a function of excess pore water pressure (u). The difference between T_0 and T_1 depends on the drainage property of the soil, which means that the two epochs will be more separated in undrained condition. Meanwhile, the secondary compression is a continuous process in time due to the compressive loading and extends beyond the primary consolidation period.

The development of primary consolidation in time can be measured with the degree of consolidation (U_V), which is a ratio of temporary and total change in soil void ratio. Thus, it can be expressed with the following equation.

$$U_V = \frac{e_i - e_t}{e_i - e_f}$$

where e_i is the initial void ratio, e_f is the final void ratio at the end of consolidation, and e_t is the void ratio at a particular time. The degree of consolidation has the value between 0 and 1, with $U_V = 0$ being the beginning of consolidation and $U_V = 1$ being the end of consolidation process. Alternatively, it can also be expressed as a function of stress on a linear portion at the $e - \sigma'$ graph.

$$U_V = \frac{\sigma' - \sigma'_0}{\sigma'_1 - \sigma'_0} = \frac{u_i - u_e}{u_i} = 1 - \frac{u_e}{u_i}$$

where σ'_0 is the initial effective stress, σ'_1 is the final effective stress, and σ' is the effective stress at particular time. The end of primary consolidation is signified with the complete drainage of pore water, thus the difference between the final and initial effective stress difference should be the initial excess pore water pressure (u_i).

The dissipation of excess pore water pressure in time is expressed with the dimensionless time factor (T_V), which is defined with the following equation.

$$T_V = \frac{k t}{m_v \gamma_w d^2}$$

where k is the hydraulic conductivity, t is the time, m_v is the coefficient of volume compressibility, γ_w is the unit weight of water, and d is the drainage length. Stemmed from the differential equation which correlates porous flow velocity and volumetric change, the excess pore water pressure is defined as depth and time function with the equation shown below.

$$u_e(z, t) = \sum_{m=0}^{m=\infty} \frac{2u_i}{M} \left(\sin \frac{Mz}{d} \right) e^{-M^2 T_V}$$

$$M = \frac{\pi}{2} (2m + 1)$$

The excess pore water pressure is depicted with curves referred as isochrones as displayed in Figure 2.5. Figure 2.5 shows the isochrones of the double drainage condition. In other drainage situations, different isochrones will appear and might not be symmetric.

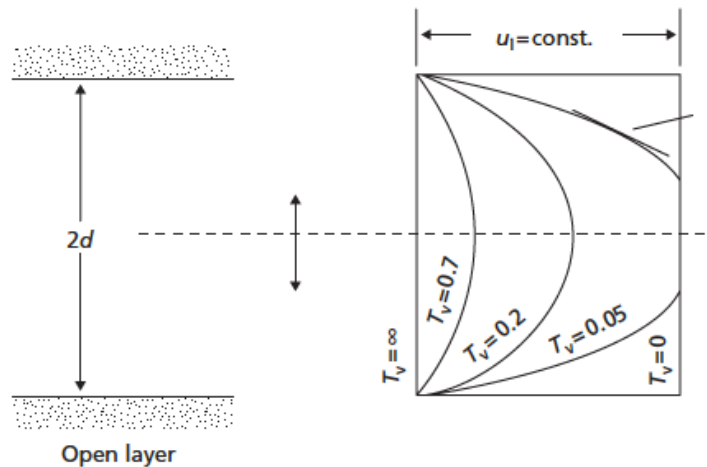


Figure 2.5: Example of isochrones in a double-drainage condition (Knappett & Craig, 2012)

Knappett and Craig provided empirical equations that relate T_V with U_V , shown below.

$$T_V = \begin{cases} \frac{\pi}{4} U_V^2 & U_V < 0.60 \\ -0.933 \log(1 - U_V) - 0.085 & U_V > 0.60 \end{cases}$$

T_V and U_V can be presented graphically as displayed in Figure 2.6. Three drainage cases are shown and represented with each curve. Curve 1 elaborates the development of consolidation in time on a double-drainage scheme and groundwater table change in half-closed layer. Curve 2 explains the virgin consolidation in half-closed layer, while curve 3 resembles the consolidation due to surface loading.

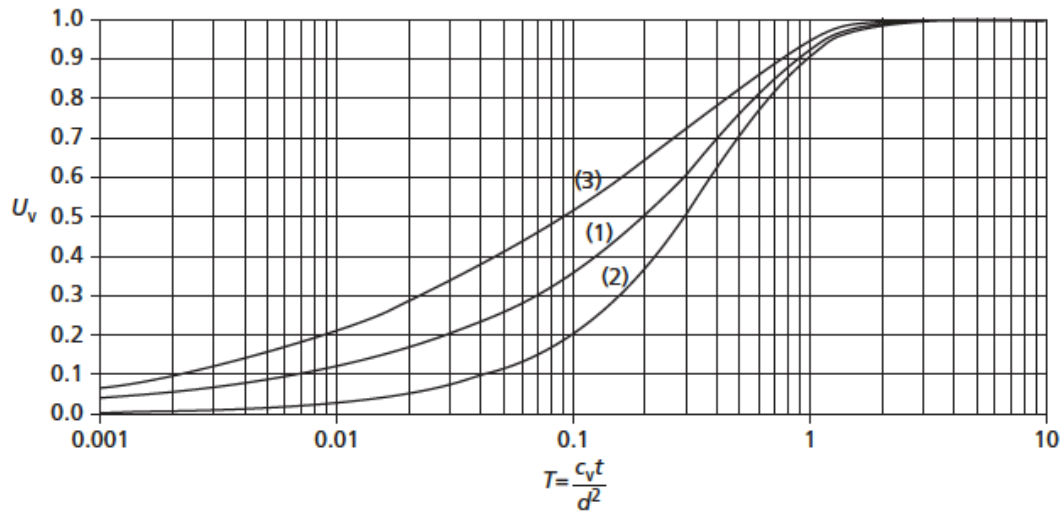


Figure 2.6: Development of degree of consolidation in time (Knappett & Craig, 2012)

Based on the rules of thumb, soil is said to retain undrained behavior when T_V is less than 10^{-4} , which corresponds to the degree of consolidation of less than 1%. In contrast, a perfectly drained system can be claimed if the value of T_V exceeds 2, which corresponds to the degree of consolidation of approximately 99%. In between the two T values, consolidation must always be considered.

2.3 Material Properties

2.3.1 Soft Soil

A property of soil that defines its softness/hardness is the compressibility. Generally, soft soil is defined as earth material that is high in compressibility (Gregory, 2006). Therefore, when load is applied to soft soil, major deformations are expected. Nevertheless, it is a relative measure and there is no absolute threshold on which soil can be identified as soft or hard soil. One of multiple ways to compare the elasticity of material is by comparing the elasticity moduli, which are listed in Table 2.2.

Table 2.2: Elasticity moduli of various materials (Das, 2010)

Materials	Modulus of Elasticity (MPa)
Soft clay	1.8 – 3.5
Hard clay	6.0 – 14.0
Loose sand	10.0 – 28.0
Dense sand	35.0 – 70.0
Steel	200.0

2.3.2 Interpretation of Field Investigation

The type of field investigation relevant to this study is the standard penetration test (SPT). Characterization of a soil profile with SPT is based on the blow counts, later denoted as N , that the instrument must make to a prescribed penetration. Therefore, soft soil will return less blow counts and stiffer soil will return more blow counts. Further information about SPT is provided in Appendix A.1.2.

A lot of studies has been done in the past to correlate N and other soil properties. Even though these correlations are based on empirical studies, they are able to provide sufficient and consistent information about the soil characteristics. General correlations that will be useful for the study are presented below.

SPT to Soil Elasticity

An empirical finding presented the range of blow count multiplier to determine the elasticity modulus of soil. The determination of the multiplier is contingent to the type and consistency of soil, such that the lowest boundary is designated for normally consolidated soil, while the highest boundary is designated for cohesionless soil. The range is displayed in the equation below.

$$E' (kPa) = 750 N_{(60)} \quad \text{for unaged, normally consolidated soil}$$

$$E' (kPa) = 1500 N_{(60)} \quad \text{for stiff clays}$$

$$E' (kPa) = 2500 N_{(60)} \quad \text{for most natural cohesionless soil}$$

SPT to Strength Parameters (ϕ' and C_u)

Peck, Hanson, Thornburn (1974), and Meyerhof approximated the friction angle based on the SPT blow counts. The SPT result was also related to the relative density of soil as less blow counts are usually manifested by loose soil. The approximations were presented in ranges as shown in Table 2.3.

Table 2.3: Approximation of friction angle based on SPT (Peck, Hanson & Thornburn, 1974; Meyerhof, n.d.)

N	Relative Density	ϕ' (°)	
		Peck, Hanson, & Thornburn	Meyerhof
0 - 4	Very loose	< 28	< 30
4 - 10	Loose	28 - 30	30 - 35
10 - 30	Medium	30 - 36	35 - 40
30 - 50	Dense	36 - 41	40 - 45
> 50	Very dense	> 41	> 45

Based on Table 2.3, effective friction angle of soil ranges from 28° to 45°. The correlation shows a direct proportionality between the blow counts and the effective friction angle. Soil layers with small blow counts tend to exhibit smaller effective friction angle and on the contrary, larger angles are exhibited by layers with greater blow counts.

Furthermore, the strength of soil material is also defined by the undrained cohesion (c_u). The method to derive clay undrained cohesion from the SPT blow counts was initiated by Terzaghi and Peck (1967), later modified by Kulhawy and Mayne (1990). The equation is shown below.

$$\frac{c_u}{p_a} = 0.06 N_{1(60)}$$

where p_a is the atmospheric pressure of approximately 100 kPa.

Sowers (1979) proposed correlations between blow counts and undrained shear strength, a function of friction angle and cohesion. The correlations are presented Figure 2.7, which also relates the correlations with the classification of soil.

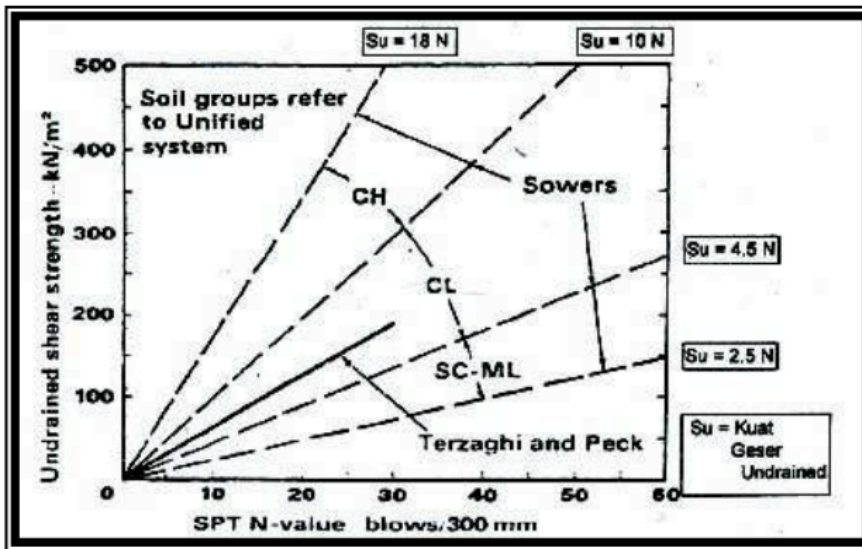


Figure 2.7: Correlation of N-SPT and S_u (Terzaghi & Peck, 1967; Sowers, 1979)

Stress History

An empirical correlation between the preconsolidation pressure and the SPT blow counts was proposed by Mayne and Kemper (1988). The investigation involved 106 data points from North America and aimed to establish the OCR profile based on SPT and CPT. The correlation is displayed below.

$$\sigma'_{pc} = 67 N^{0.83}$$

2.3.3 Other Soil Properties

Unit Weight and Void Ratio

US Federal Highway Administration (2015), after Peck, Hanson, and Thornburn (1974), provided the the unit weight of several soil types in their natural state, presented in Table 2.4. The table helps to rationalize the data obtained from the field measurement.

Table 2.4: Unit weight of soil based on the classification (FHWA, 2015; Peck, Hanson, and Thornburn, 1974)

Soil Type	Unit Weight (kN/m^3)	
	γ_{Dry}	γ_{Sat}
Uniform sand (loose)	14.10	18.50
Uniform sand (dense)	17.10	20.40
Well-graded sand (loose)	15.60	19.50
Well-graded sand (dense)	18.20	21.20
Windblown silt	13.40	18.20
Glacial till	20.70	22.80
Soft glacial clay	11.90	17.30
Stiff glacial clay	16.70	20.30
Soft slightly organic clay	9.10	15.40
Soft very organic clay	6.80	14.00
Soft montmorillonitic clay	4.20	12.60

The estimation of void ratio for the numerical analysis can also be based on the typical void ratio of certain soil types. The ranges of void ratio were selectively gathered from multiple sources and presented in Table 2.5.

Table 2.5: Typical void ratio for sand, silt, and clay (Association of Swiss Road and Traffic Engineers, n.d.; Das, 2008; Hough, 1969; Geotechdata.info, 2013)

Description	USCS	Void ratio [-]	
		min	max
Coarse sand	SW	0.35	0.75
Fine sand	SW	0.4	0.85
Silty sands	SM	0.33	0.98
Clayey sands	SC	0.17	0.59
Low plasticity silt	ML	0.26	1.28
High plasticity silt	MH	1.14	2.1
Low plasticity clay	CL	0.41	0.69
High plasticity clay	CH	0.63	1.45
High plasticity organic clay	OH	1.06	3.34

2.3.4 Creep in Concrete

For numerical analysis that extends for a long time, creep in concrete should not be neglected. The elasticity modulus of concrete alters in time as a result of creep. The development in time should be estimated with the formula below.

$$E(t) = \frac{E_0}{(1 + \phi(t))}$$

where E_t represents the elasticity modulus in time, E_0 is the initial elasticity modulus, ϕ is the time-dependent creep coefficient. The creep coefficient, which is not only dependent on time but also on concrete strength and environment, can be determined by following the diagram below.

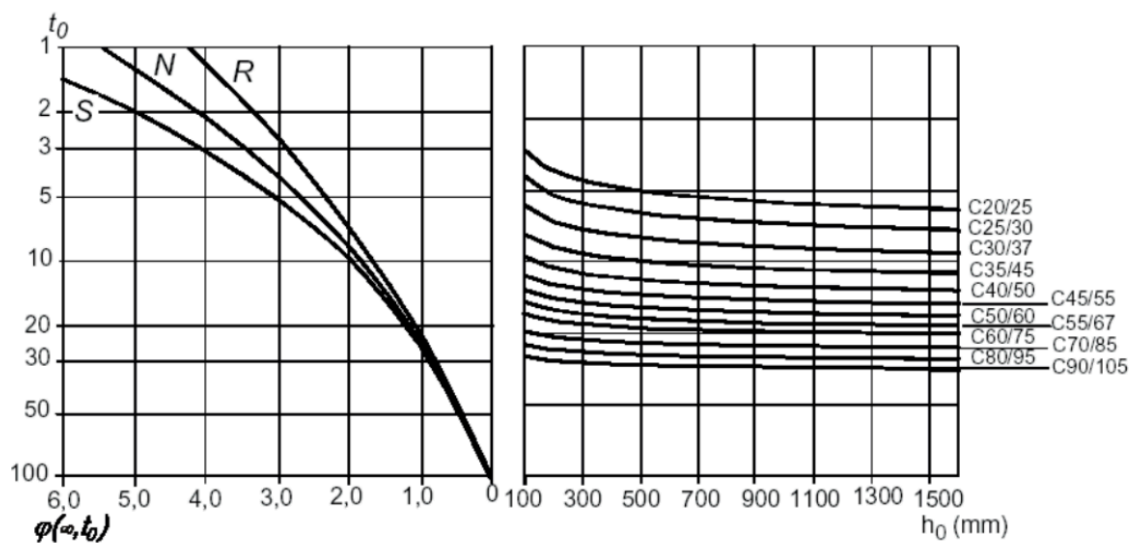


Figure 2.8: Time-dependent time coefficient (Walraven & Braam, 2015)

2.4 Soil Constitutive Models

Soil model, or referred as material model in Plaxis, defines the relationship between stress rate ($\dot{\sigma}$) and strain rate ($\dot{\epsilon}$). The constitutive model is represented by matrix M and what is contained in the matrix defines the behavior of the material in response of loading. The relationship is displayed in the equation below.

$$\dot{\sigma} = M \cdot \dot{\epsilon}$$

The finite element modelling software used for the research, Plaxis, offers a variety of soil models and the suitability of these models depends on the phenomena which are expected to be the center of the computer simulation. Among them, four soil models are considered for the research. These are the Mohr-Coulomb model, soil hardening model, and soft soil creep model. This subchapter summarizes each model. Furthermore, the selection of soil models is discussed at the end of this subchapter.

2.4.1 Mohr-Coulomb Model

The Mohr-Coulomb model is a first-order model. The model recognizes plastic and elastic strain separated by the yield function (f) in the stress-strain diagram. Additionally, the Mohr-Coulomb model is also referred as the elastic perfectly plastic model. A perfectly plastic model assumes that the yield function is constant and not stress dependent. The main concept of Mohr-Coulomb model is presented on the stress-strain diagram in Figure 2.9.

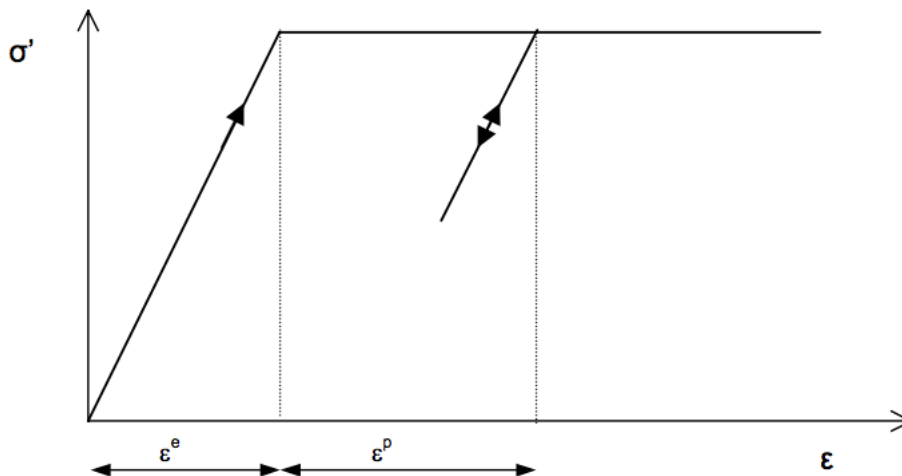


Figure 2.9: Elastic - perfectly plastic stress-strain diagram (Plaxis 8 Manual, n.d.)

The model is based on the Hooke's law of isotropic linear elasticity and it assumed a single stiffness modulus for strains due to loading, unloading, and reloading. As a result, the model has an issue with soil dilatancy. Other than the stiffness modulus, Plaxis required four more parameters, which are the Poisson's ratio, friction angle, dilatancy angle, and cohesion. Given the numbers of simplification, this model is unable to produce accurate results and thus only useful for a first order analysis of a geotechnical problem because the simulation does not require a lot of processing power.

2.4.2 Soil Hardening Model

Compared to the Mohr-Coulomb soil model, the soil hardening model recognizes changes in soil properties due to applied stress. There are two types of hardening which are shear hardening and compression hardening (Plaxis 8 Manual, n.d.). The model requires three stiffness moduli inputs, which are the triaxial stiffness (E_{50}), oedometer stiffness (E_{OED}), and unload-reloading stiffness (E_{UR}). The stiffness of a material is assumed to follow a power law formulation, which is associated with Duncan-Chang (1970) hyperbolic model (Kok et al., 2009) portrayed in Figure 2.10.

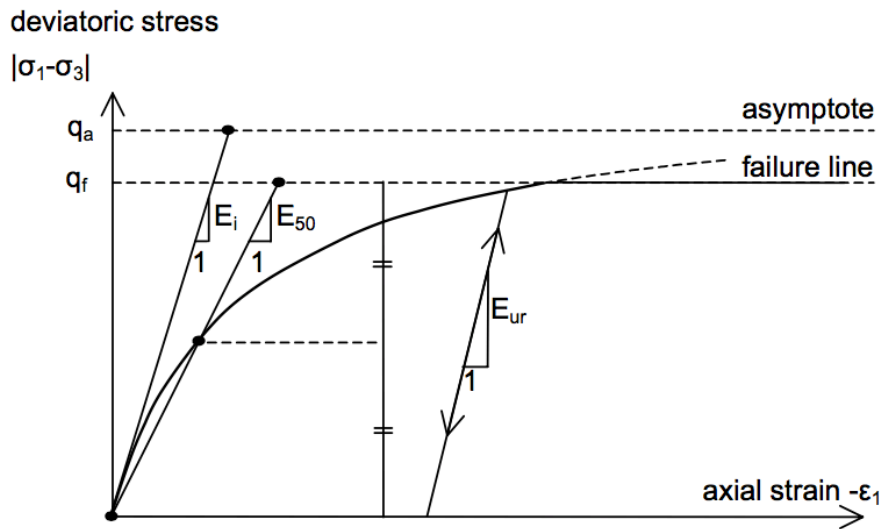


Figure 2.10: Hyperbolic function as suggested by Duncan and Chang (Plaxis 8 Manual, n.d.)

The soil hardening model takes account of stress-dependent modulus of stiffness (Jalali et al., 2012). When soil experiences unloading and reloading, it will follow the stress path that is governed by greater stiffness E_{UR} , roughly equivalent to three times E_{50} . The additional considerations show that this model, compared to the Mohr-Coulomb model, is more capable to provide accuracy for the simulation with the cost of higher computation effort. Kok et al. (2009) added that the soil hardening model is suitable to predict displacement and failure. Meanwhile, the model is not suitable to model creep as it contains no time-dependent behavior.

2.4.3 Soft Soil Creep Model

Compared to other soil constitutive models, the soft soil creep model recognizes the time-dependent secondary compression. In other words, the constitutive model allows material to deform upon constant effective stress, which is the limitation of other models.

Similar to other models, the failure criterion of this model is based on the Mohr-Coulomb model. Thus, inputs of cohesion, friction angle, and dilatancy angle are necessary. Furthermore, Plaxis requires user to describe the behavior of material, which is now defined by the modified compression index (λ^*), modified swelling index (κ^*), and modified creep index (μ^*). In relation to the indices used in Cam-Clay model, the modified indices are interpreted as follows.

$$\lambda^* = \frac{\lambda}{1 + e} \quad \kappa^* = \frac{\kappa}{1 + e}$$

These stiffness parameters should be available from oedometer test and isotropic compression test. Plaxis 8 Manual (n.d.) suggested to use a general observation-based correlation between the values of λ^* , κ^* , and μ^* for rough estimation. Alternatively, the stiffness of soil can also be defined with C_c , C_s , and C_α . These parameters are then translated into the modified indices with the correlations below.

$$\lambda^* = \frac{C_c}{2.3(1 + e)} \quad \kappa^* = \frac{2 C_R}{2.3(1 + e)} \quad \mu^* = \frac{C_\alpha}{2.3(1 + e)}$$

Additional advanced parameters of this model are the Poisson's ratio of unloading and reloading (ν_{ur}) and the vertical – horizontal stress ratio in normally consolidated soil (K_0^{NC}).

2.5 Bored Tunnels

2.5.1 Tunnel Orientation

Despite of multiple interpretations about the orientations and conventions in past studies, the orientations presented in Figure 2.11 are used consistently throughout the document. Furthermore, features in and around

the tunnel will be angularly referred, where $\varphi = 0^\circ$ is denoted as the crown, $\varphi = 90^\circ$ and 270° are called the springlines, and $\varphi = 180^\circ$ is the invert.

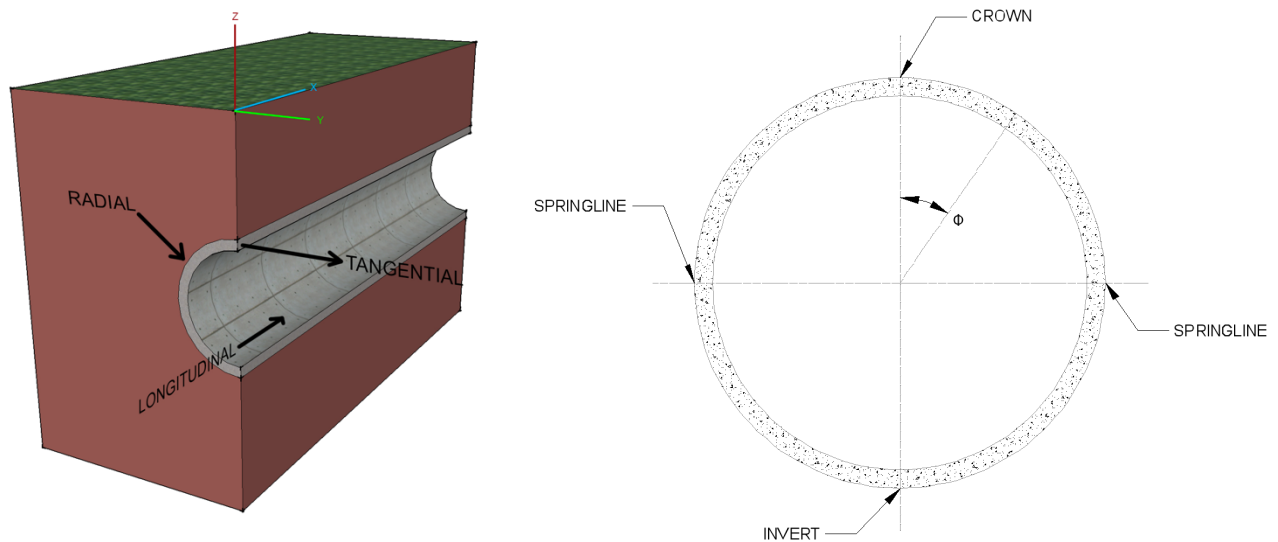


Figure 2.11: (Left) 3D and (right) cross sectional orientation

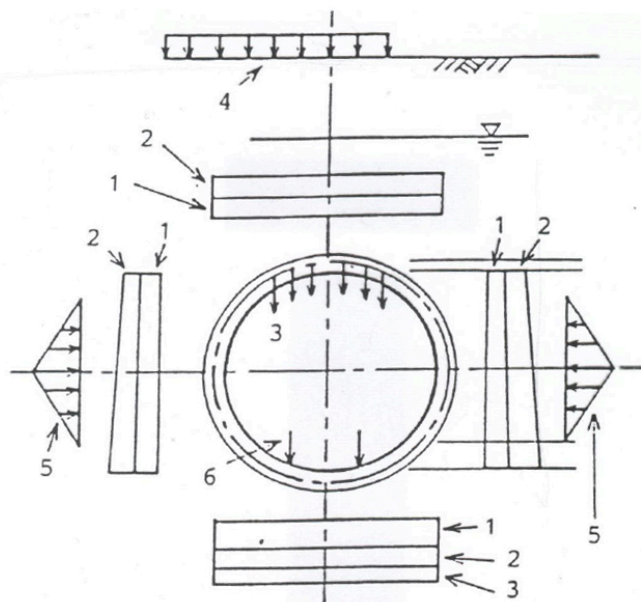
2.5.2 Beam Model

There are two common methods to model bored tunnel as embedded hollow cylinder beam, namely the beam-spring model and longitudinal continuous model. The distinction between the two models lies on the accuracy of the model in emulating the behavior of segmented bored tunnel. In the beam-spring model, the longitudinal joints are modeled with axial, shear, and rotational springs. With that amount of details, the beam-spring model requires high computational power. The longitudinal continuous model is the simplification of the former model. This model does not recognize the effects of joints and thus tends to overestimate the global stiffness of the beam. However, the longitudinal continuous model requires less computational power, which makes it the most popular model to obtain internal forces and deformation (Wu et al., 2015).

2.5.3 Loads on Tunnel Structure

An underground structure, especially tunnel, is constantly associated with soil and if groundwater is present, hydrostatic load. The construction process of underground structure follows a general concept, which includes removal of earth material and replacement with material of greater strength, such as pipelines, tunnels, or culverts. Removal of earth material can be performed with either excavation, for example open-cut immersed tunnel, or by forced deformation, for instance pile penetration. Hence, underground structures are expected to exhibit the strength of the replaced soil as well as perform its functional purpose.

The International Tunneling Association (ITA) identified at least 6 load sources, which are the vertical and horizontal earth pressure, hydrostatic pressure, self weight of the lining, ground surcharge, additional stress due to vertical ovalisation, and loads coming from inside the tunnel. These load sources are displayed in Figure 2.12. Furthermore, other load sources that were not mentioned include the seismic loads and dynamic loads from the operations.



- Remarks:
1. Vertical and horizontal earth pressure
 2. Water pressure
 3. Dead load of the lining
 4. Components of surcharge
 5. Reaction caused by deformation by the lining
 6. Loads acting on the inside of the lining

Figure 2.12: Loads on tunnel (ITA, 2000; Bakker, 2015)

The directions of the aforementioned loads are mostly either vertical or horizontal. The calculation of these loads is simplified with geometrical conversion to comply with the circular shape of the structure. Therefore, the loads displayed in the previous figure are presented in uniform radial load and ovalisation load, instead of vertical and horizontal load, as shown in Figure 2.13

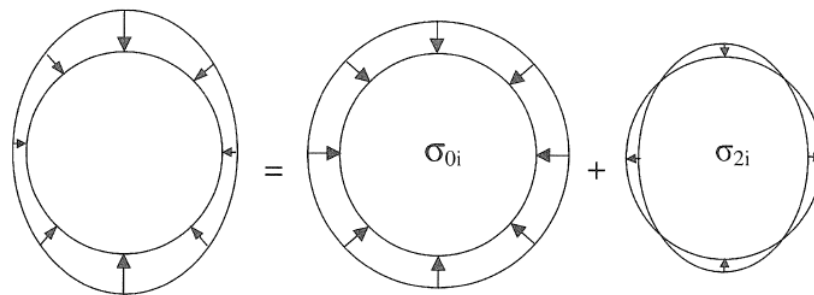


Figure 2.13: (Left) The total radial loading is the accumulation of (middle) uniform radial loading and (right) the ovalisation loading (Blom, 2003)

Furthermore, the load sources are elaborated below based on the tunnel lining design guidelines published by the ITA (2000).

Earth Pressure

The earth pressure is the aggregate of gravitational load from the overlying soil layers. The earth pressure acting on the vertical direction is simply a product of layer thickness and unit weight. On the other hand, the horizontal directed load is associated with the vertical earth pressure by the earth pressure coefficient. Furthermore, the horizontal and vertical earth pressure will be geometrically converted into radial load.

Hydrostatic Pressure

Hydrostatic pressure on tunnel exists if the structure is constructed under or around the water table. Similarly, the water pressure is a product of material unit weight and the height of water table to the point of interest. However, unlike the earth pressure, the hydrostatic pressure is isotropic.

Self Weight of Tunnel Lining

To calculate the distributed weight of the tunnel lining, the total weight of the tunnel lining is divided over its circumference. The distributed weight is often assumed to be equal as the unit weight of reinforced concrete, 25 kN/m^3 .

Ground Surcharge

Surface loading is originated from any kind of land occupation, such as: buildings, roads, or rails.

Subgrade Reaction

The substitution of soil with other structural materials is rarely perfect in terms of exerting the exact same initial stress. Thus, alterations of stress around the structure is inevitable. The archaic theory which explains about soil-structure interaction was developed by Winkler. Winkler (1867) suggested that soil deformation acts locally. Chandra (2014) suggested that Winkler's theory has been constantly opposed and improved by more modern studies which include soil's elasticity, such as Filonenko-Borodich model, Hetenyi, Pasternak, Kerr, and Rhines. Considering its continuum, soil is often modeled as a system of infinitely many interconnected springs. Thus, a disruption at one location can result chain reactions in a different location. One of the evidences of this argument is the deformation of pile foundation due to nearby subsurface construction.

2.5.4 Structural Response

The combination of radial and ovalisation loading results normal force and bending moment at the tunnel lining, which are essential in the design of the tunnel segment. For preliminary calculation purpose, the two reactions can be calculated with the equations below.

$$N = -\frac{(\sigma_v + \sigma_h)}{2}r + \frac{(\sigma_v - \sigma_h)}{2}r \cos(2\varphi) \qquad M = -\frac{(\sigma_v - \sigma_h)}{4}r^2 \cos(2\varphi)$$

where σ_v is soil vertical stress at the crown, σ_h is soil horizontal stress at the springline, r represents the radius of tunnel, and φ is the angular position of observation point with respect to the tunnel crown as $\varphi = 0^\circ$. Furthermore, the interaction between structure and soil is included in the calculation with additional coefficients for each component as shown in the revised equations below.

$$N = -C_{n0} \frac{(\sigma_v + \sigma_h)}{2}r + C_{n2} \frac{(\sigma_v - \sigma_h)}{2}r \cos(2\varphi) \qquad M = -C_M \frac{(\sigma_v - \sigma_h)}{4}r^2 \cos(2\varphi)$$

where C_{n0} , C_{n2} , and C_M are the coefficients devised from soil-structure stiffness ratio and geometrical properties, such as A for cross sectional area and I for second moment of area. The determination of these coefficients should be in accordance with the equations shown below.

$$\alpha = \frac{E_S \cdot r^3}{E_T \cdot I} \qquad \beta = \frac{E_S \cdot r}{E_T \cdot A}$$

$$C_{n0} = \frac{2}{2 + 1.54\beta} \qquad C_{n2} = \frac{2(1 + 0.064\alpha)}{2 + 0.171\alpha} \qquad C_M = \frac{4}{4 + 0.032\alpha}$$

Schulze and Duddeck (1964) also translated the external stresses to the internal structural reactions with the two well-known diagrams in Figure 2.14. The diagrams put forward the correlation between internal load and the stiffness ratio between soil and structure. That being mentioned, the diagrams offer more precision in estimating the internal reactions.

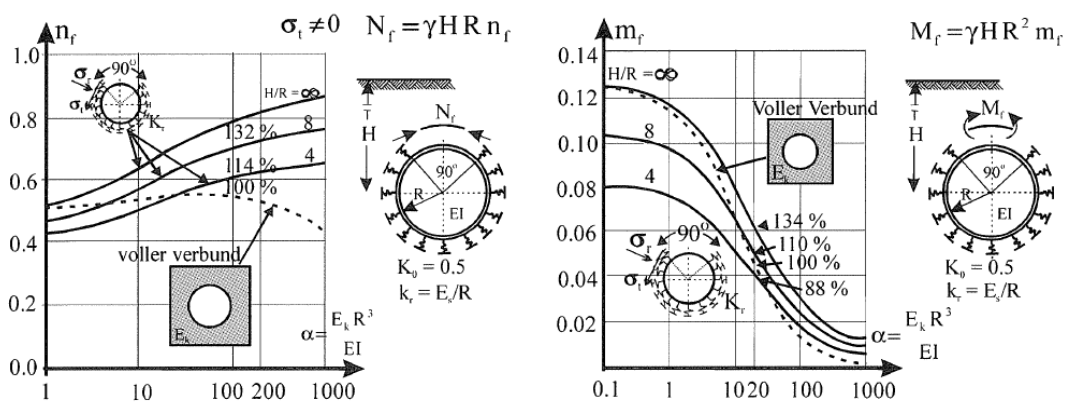


Figure 2.14: Normal force and bending moment of tunnel lining based on the soil - structure interaction (Duddeck & Schulze, 1964)

The stiffness ratio is represented with α . Lesser value of α can be obtained if the structure possesses significantly greater stiffness than the soil. In this situation, the structure will be subjected to less normal force

but more bending moment. The opposite situation generates the reversed. Waart (2010) asserted that these diagrams are still used in practice for first order calculation.

So far, the tunnel ring is modeled as a homogenous circular frame which contradicts to the real situation as bored tunnels are usually constructed with prefabricated segments. Blom (2002) incorporated the tunnel joints into the analytical calculation. Blom considered longitudinal and segmental joints of the tunnel structure and identified them as the weakest point within the structure in terms of stiffness. As a result, the presence of joints reduces the equivalent overall stiffness for the tunnel. In Blom's analytical model, the joints are modeled with springs; rotational spring for the segmental joint and axial spring for longitudinal joint. The inclusion of segmental joints, located in between packing materials, in the model allowed interaction between one ring with another and thus constituted bending and shear stiffness for the tunnel as a whole. The setup is presented in Figure 2.15.

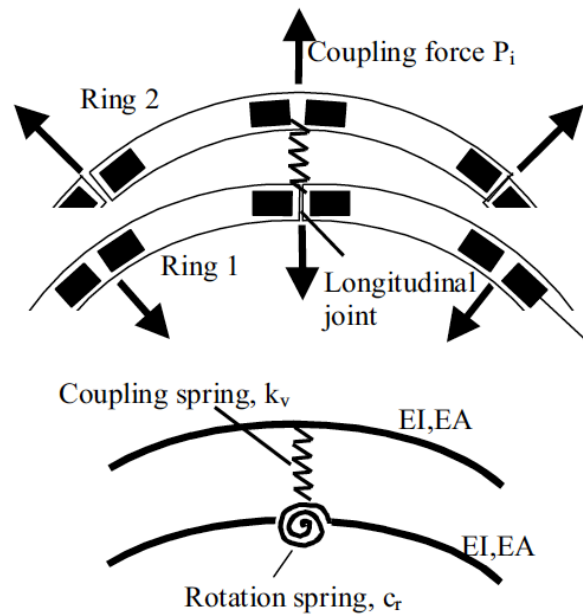


Figure 2.15: Setup for analytical model (Blom, 2002)

Other than Duddeck and Schulze's method, ITA (2000) recognizes four more computation methods, namely the bedded frame model, finite element, elastic equation, and Muir Wood model. The selected computation method must match the model conditions as each method was generated for certain circumstances. Being the least robust model, the elastic equation model method is only suitable to compute reactions due to symmetrical loads. Therefore, the method could be performed without a computer. On the other hand, the bedded frame model method and finite element method require the assistance of computer to solve the complex matrices operations in the calculation. In the present, the use of computer software in tunnel design has become a requirement in the practice. The finite element method helps engineers to simulate soil and structural reactions upon different load cases and enables the engineers predict the forthcoming events or setbacks.

2.5.5 Longitudinal Beam Stiffness

In the longitudinal direction, the tunnel is often modeled as a slender beam due to its dimensional ratio. Also in that direction, tunnel rings are connected with longitudinal joints to simplify and accelerate the construction process.

In general, the beam equivalence of shield tunnel is derived based on Euler-Bernoulli or Timoshenko beam theory. With the presence of longitudinal joints, the beam is not only capable in bending, which was the main concept of Euler-Bernoulli beam, but can also manifest shear deformation. Therefore, Timoshenko-based derivation provides more accuracy in mimicking the behavior of the tunnel. However, Euler-Bernoulli beam theory has been used widely in research and in the industry. One of the reasons behind its popularity is the simplicity of the theory.

Another motive to opt for Euler-Bernoulli instead of Timoshenko is that the former theory produces more conservative result compared to the latter in the stress-control design ideology. The distinction between Euler-Bernoulli and Timoshenko beam theory lies on the recognition of shear stiffness. The recognition of shear stiffness brings an extra failure mode, which then reduces the overall stiffness of the beam. As a result, Timoshenko beam exhibits smaller internal loads but greater deformation. Consequently, the underestimation of internal load could lead to inadequate structural provision.

Inclusion of Longitudinal Joints

Rather than modelling the joints with alternating rotational springs, the integration of this element is accomplished through the assignment of reduced overall longitudinal bending stiffness. Bao et al. (2015) investigated the contribution of bolted longitudinal joints in reducing the global stiffness of the tunnel by comparing the uniform and segmented models. Bao et al. introduced a factor η , which was referred as the efficiency factor of bending rigidity, to incorporate the weak longitudinal joints. The complete formula they developed is presented below.

$$(EI)_{Eq} = \eta EI$$

where $(EI)_{Eq}$ represents the effective global bending stiffness of the beam model and EI stands for the bending stiffness of the longitudinal continuous structure. Other than a comparison between uniform and segmented tunnel, Bao et al. also investigated the influence of different concrete segment configurations, such as staggered and straight, to the value of η .

Furthermore, Bao et al. provided the typical values of η based on series of examinations, including analytical solution, numerical solution, and model tests. The analytical solution estimated a value of 0.042. The numerical solution returned a value of 0.092 for straight and 0.106 for staggered configuration. Additionally, the model tests yielded the range of 0.18 to 0.39 for straight configuration and 0.20 to 0.40 for staggered configuration. Finally, Bao et al. concluded with an estimated value of 0.371 for staggered configuration tunnel and 0.345 for straight jointed tunnel.

Liao et al. (2008) derived analytically the equations to determine the value of η based on the assumption that compressive force at the cross section is fully sustained by concrete, while the tensile force is sustained by the bolts. Additionally, Liao et al. added an angle ψ to locate the neutral axis as displayed in Figure 2.16 below.

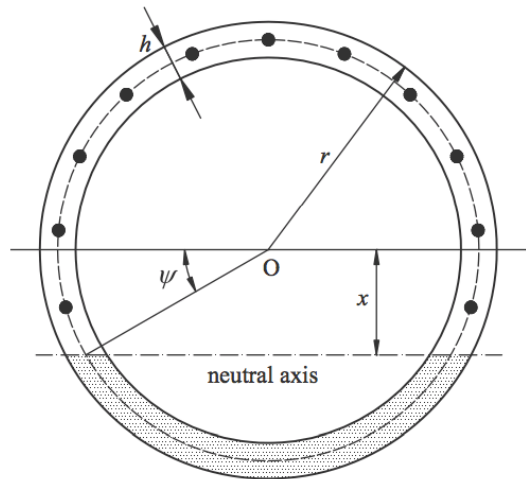


Figure 2.16: Tensile area (unshaded) and compressive area (shaded) of a tunnel cross section (Liao et al., 2008; Wu et al., 2015)

Figure 2.16 suggests that compressive and tensile stress at the cross section are carried by the shaded and unshaded area respectively. Additionally, the fraction of shaded and unshaded area is governed by the position of neutral axis, which is regulated by angle ψ . Furthermore, the series of aforementioned equations to determine η are presented below.

$$\eta = \frac{\zeta \cdot l_s}{\zeta(l_s - \lambda l_b) + \lambda l_b} \quad \zeta = \frac{\cos^3(\psi)}{\cos \psi + (\psi + \pi/2) \sin \psi} \quad \psi + \cot \psi = \pi \left(\frac{1}{2} + \frac{K_b l_b}{E_c A_c} \right)$$

The variable K_b represents the total axial stiffness of the bolts, E_c is the elasticity modulus of concrete, A_c is the cross sectional area of the tunnel, l_s represents the length of ring in the longitudinal direction, l_b is the length of bolt connection, and λ is the influencing factor of joints, which value is greater than 1.0.

The analytical method is selected to determine the equivalent longitudinal beam bending stiffness. To attain the objective of this study, the analytical method is regarded as sufficient as it requires less computational power but is able to include the details of joints to reduce the overall bending stiffness. However, the η -value it produces should concur with Bao et al.'s findings.

2.5.6 Segmental Joint Stiffness

Segmental joint is the tangential connection between one concrete segment with another. In general, there are two methods to incorporate joint stiffness into the tunnel model. The first method is referred as the homogenous approach, which argues that the presence of joints reduces the homogenous ring stiffness. Another method to model the segmental joint is through the assignment of rotational stiffness. This method is referred as the spring approach.

Homogeneous Approach

The method to include segmental joints was proposed by Muir Wood (1975). Knowing that segmental joints are the weakest component of a tunnel ring, Muir Wood developed a theory to calculate the reduced second moment of area which is shown below.

$$I = I_s + I_n \left(\frac{4}{m} \right)^2$$

where I is the reduced second moment of area, I_s is the second moment of area at the force transmission zone, I_n is the second moment of area at the complete section, and m is the number of joints. The reduction of second moment of area does not follow a linear trend as m^2 is positioned at the denominator. The final result, I , represents the second moment of area for the whole ring. Thus, uniform bending stiffness can be assumed if the material is homogeneous. Figure 2.17 shows the joint interface used in Muir Wood's model where segmental thickness is represented with h and reduced joint thickness is represented with h' .

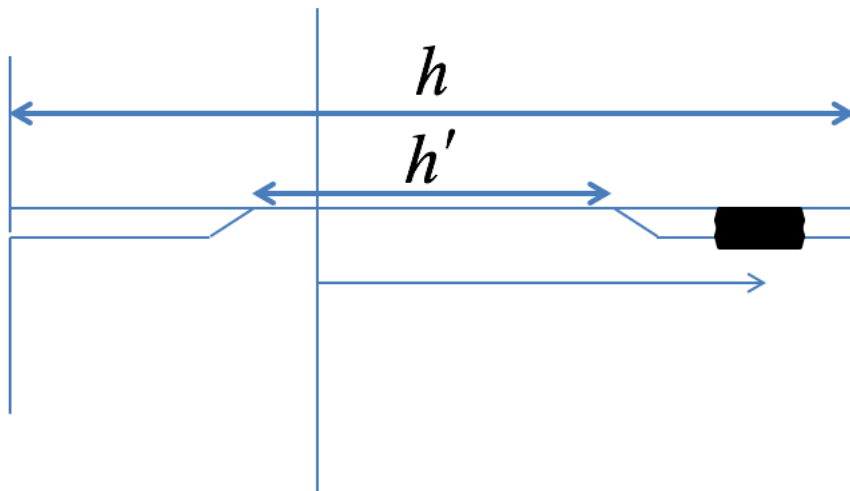


Figure 2.17: Interaction of segmental joints used in the Muir Wood's derivation (Muir Wood, 1975; Bakker, 2015)

Instead of using the reduced second moment of area, Blom (2002) proposed factor ξ to reduce the homogenous bending stiffness. The reduction factor is a function of reduced width of the segment (l_r), tunnel radius (r), and segmental thickness (d). Blom's empirical finding is presented in Figure 2.18.

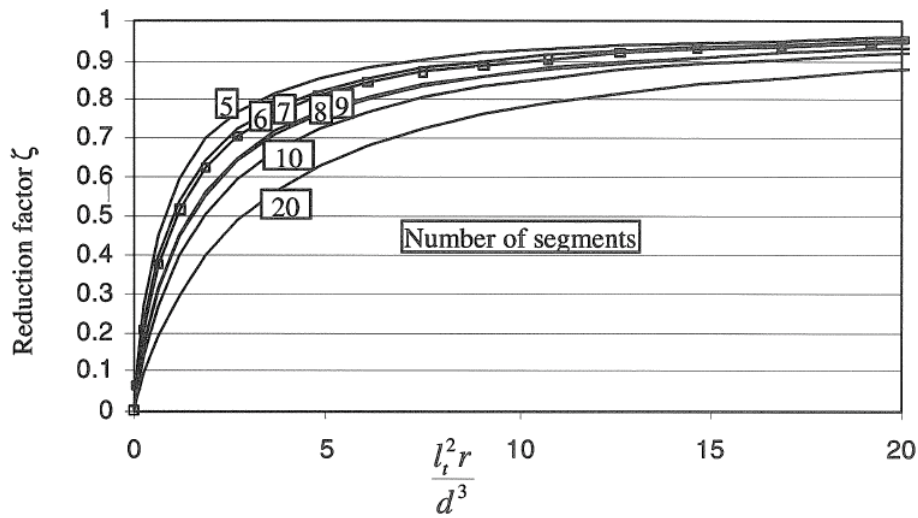


Figure 2.18: Correlation between geometrical properties of tunnel joints and reduction factor of bending stiffness (Blom, 2003)

The dependency of the reduction factor to the number of segments is clearly shown in Figure 2.18, as the reduction factor tends to be smaller with the increase of number of segments. In other words, a more segmented tunnel ring constitutes less homogeneous bending stiffness.

Spring Approach

A method to quantify the stiffness of a segmental joint was proposed by Janssen (1983) along with Figure 2.18. Later in time, Janssen's theory was improved by taking account of Gladwell's (1980) theory about the bilinearity of concrete at the interface. Furthermore, Blom (2002) recognized three stages and each stage constituted different rotational spring stiffness.

1. For $M \leq (N \cdot l_t)/6$, where l_t is the height of the contact area, the rotational stiffness is defined with this formula, $c_R = \frac{b l_t^2 E_C}{12}$. In this region, the stiffness remains linear.
2. As soon the tangential moment exceeds the $(N \cdot l_t)/6$ limit, the compressive stress has entered the elastic stage. Thus, the stiffness is determined with the following equation, $c_R = \frac{9 b l_t E_C M (2M / (N \cdot l_t) - 1)^2}{8 N}$. The upper limit of this region is $\varepsilon = \varepsilon'_c$.
3. In the plastic region, the stiffness can be estimated with the previous formula until it reaches the ultimate yield strain, $\varepsilon = \varepsilon_{cu}$ (Blom, 2002).

The three regions are presented in the $\theta - M$ graph as displayed in Figure 2.19. These two components are interrelated with the rotational spring stiffness where $M = \theta \cdot c_R$. In the first region, a steep increase in tangential moment immediately follows the increase in rotation. The rate of change decreases as it enters the second region. Not a lot of information is known for the third region (Jusoh et al., 2015).

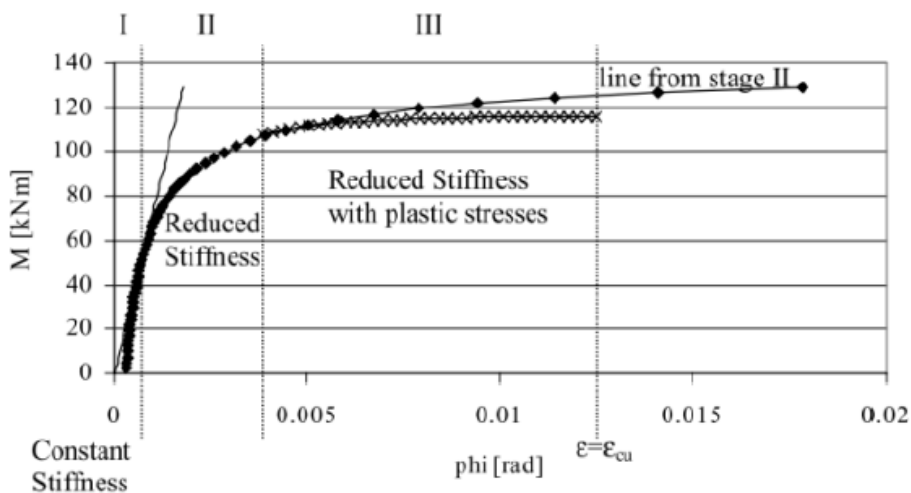


Figure 2.19: Three stages of segmental joint rigidity (Blom, 2002; Jusoh et al., 2015)

Lee et al. (2001) investigated the influence of segmental joints to the structural aspect of the tunnel. The study was conducted on the soft soil environment of Shanghai Metro tunnel. Additionally, the study took account of five cases and each case describes a unique setup of the tunnel in terms of the depth, diameter, number of joints, type of soil, and others. In the study, Lee et al. introduced the joint stiffness ratio (λ). The joint stiffness ratio represents the rotational stiffness of joint relative to the bending stiffness of the concrete segment, depicted in the formula below.

$$\lambda = \frac{K_{\theta} l}{EI}$$

where K_{θ} is the spring stiffness, l is the length of tunnel segment and usually considered as 1 m to produce the unit stiffness, and EI is the bending stiffness of the segment. For tunnels in soft soil environment, the typical λ was claimed to fall within the range of 0.03 – 0.30.

Among the two aforementioned approaches, the spring approach is selected. Unlike the homogeneous approach, the spring approach provides more realistic situation where the segmental joints are the weakest points within the tunnel ring. Upon loading, the rotation will be concentrated on the joints and not in the concrete segment. As a result, the tunnel ring will not deform into a perfect oval shape. Instead, the contrast difference in stiffness will retain the shape of the tunnel lining.

2.5.7 Internal Bending Moment

In the construction process, initial longitudinal stresses are transferred into the tunnel. Due to the eccentricity of these stresses, bored tunnel structure behaves similarly to pre-stressed beam. The stresses are exerted from these sources listed below:

1. Distributed buoyancy load
2. Shear force due to the weight of the TBM
3. Eccentric axial load produced by the TBM to advances into the soil

The resulting moment is calculated with the subgrade reaction model, where the buoyancy load is modeled as uniform load q , the shear force is represented with Q , and the eccentric axial load is modeled as external moment M (Bakker, 2015). The subgrade reaction model is presented in Figure 2.20.

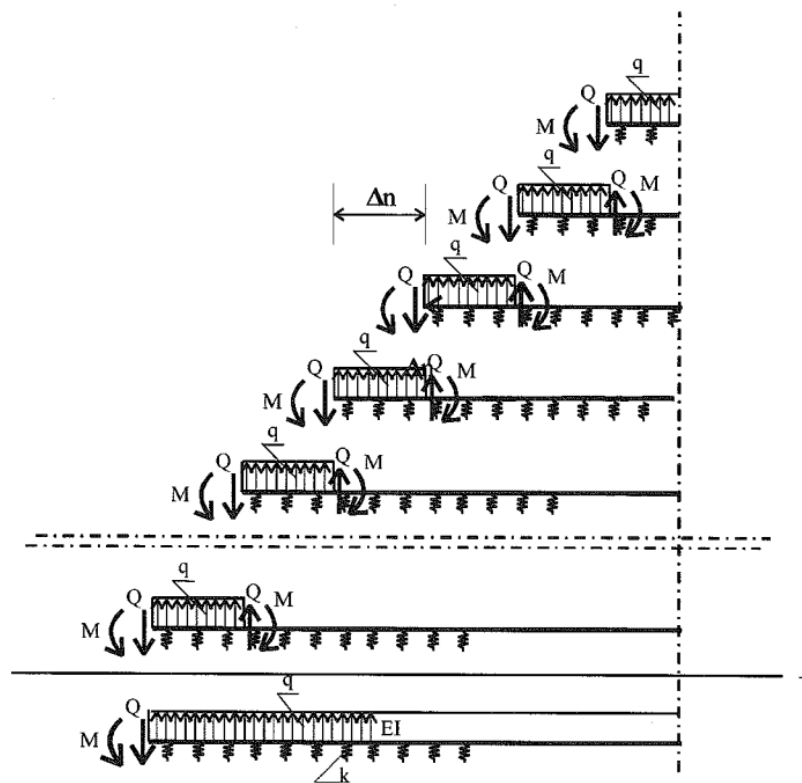


Figure 2.20: Subgrade reaction model to determine the longitudinal stress and internal bending moment (Bakker, 2015)

The subgrade reaction model was used to determine the internal bending moment of the Second *Heinenoord* tunnel. Then, the calculation outcome is compared with the monitored bending moment as presented in Figure 2.21. The graph shows an increase of bending moment from the TBM face to a maximum of approximately 22500 *kNm*, before it declines and stabilizes at 15000 *kNm*.

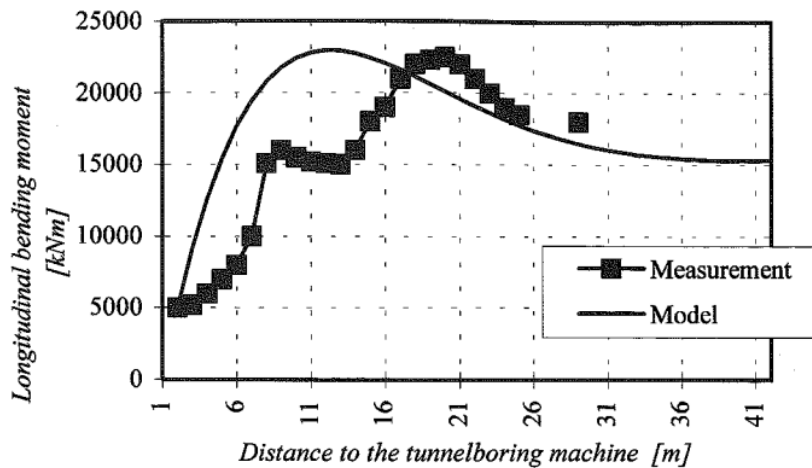


Figure 2.21: Internal bending moment of the Second *Heinenoord* tunnel (Bakker, 2015)

2.5.8 Water Tightness

Segmented tunnel is prone to water leakage especially at the joints. Therefore, rubber gasket is commonly installed and casted with the prefabricated concrete segment as illustrated in Figure 2.22. To serve its purpose, the rubber gasket should be compressed to a certain degree throughout the service life of the tunnel, which is governed by the hydrostatic pressure at the environment. The water tightness test diagram in Figure 2.22 shows that greater compressive stress, which is indicated with smaller gap, leads to increase in water proofing capability. Furthermore, construction errors and deformation could develop an offset between the adjoining gasket and thus reduce the water proofing capacity.

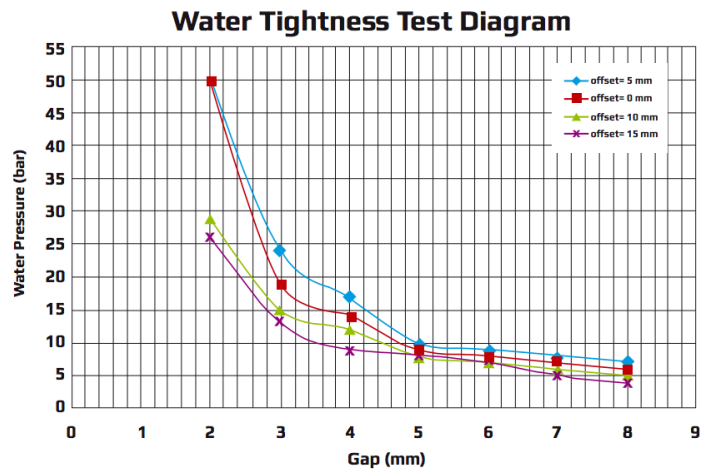
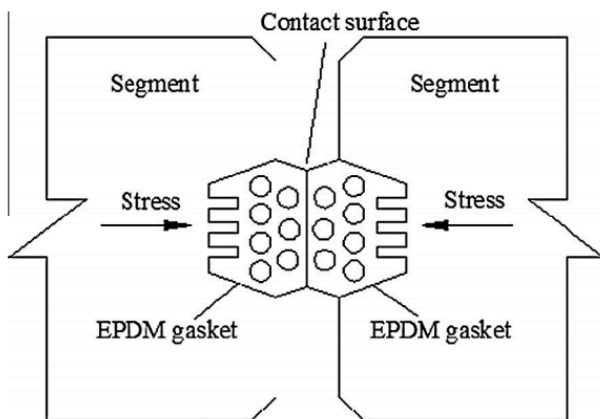


Figure 2.22: (Left) EPDM gasket at the joints of tunnel segment and (right) water tightness test diagram (Shi et al., 2015; Arsan Kaucuk, 2016)

The rubber gasket is manufactured from EPDM (*ethylene-propylene-diene monomer*) with elasticity modulus of 17.0 *GPa* (Shi et al. 2015).

2.6 Soil Arching

A horizontal soil layer under a uniform vertical load constitutes uniform consolidation and compression rate. Additionally, vertical and horizontal soil stress will be identical on the horizontal direction, which then resulted uniform settlement. In the real situation, such deformation does not take place on a large scale given the

spatial variation of soil profile. In this case, ground surcharge is opposed by varying subgrade stiffness, hence the deformation will not be at the same rate. The subgrade stiffness is usually modeled with spring with varying axial stiffness.

The presence of structure in the stratigraphy disrupts the equivalent subgrade stiffness and thus alters the associated deformation of surrounding soil. Differences in compressibility and stiffness between the soil and structure changes the load path and settlement pattern. The differential surface settlement was studied by Anson Marston, in 1913, and it is then referred as soil arching. Marston recognized two types of soil arching namely active and passive, illustrated in Figure 2.23. The distinction of active and passive soil arching is based on structure and soil stiffness ratio.

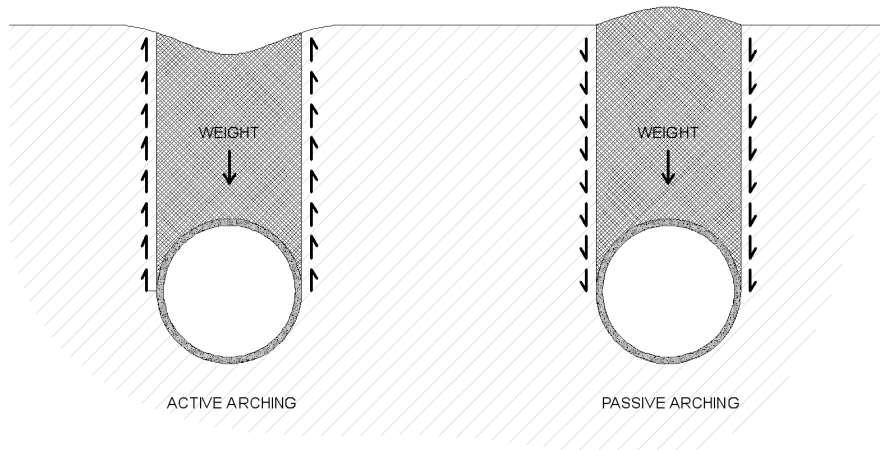


Figure 2.23: (Left) Active and (right) passive arching of soil

In active arching, settlement of soil column over the structure is observed to be larger than its surroundings, which is illustrated in Figure 2.23. This arching process is caused by the presence of relatively more flexible structure than the soil within the profile, thus reduces the overall stiffness of the soil column. On the other hand, the presence of rigid structure increases the overall stiffness of the column. Consequently, less settlement is found at this section compared to its surroundings upon similar loading. This phenomenon is identified as passive arching.

Soil arch is predominantly motivated by the uneven settlement between the soil column on top of the structure with the adjacent. Along with cohesion, the difference in vertical shift induces shear stress along the interface, which resists the movement and deforms the soil column. Marston studied the arching process by fitting the soil column in a free body diagram illustrated in Figure 2.24.

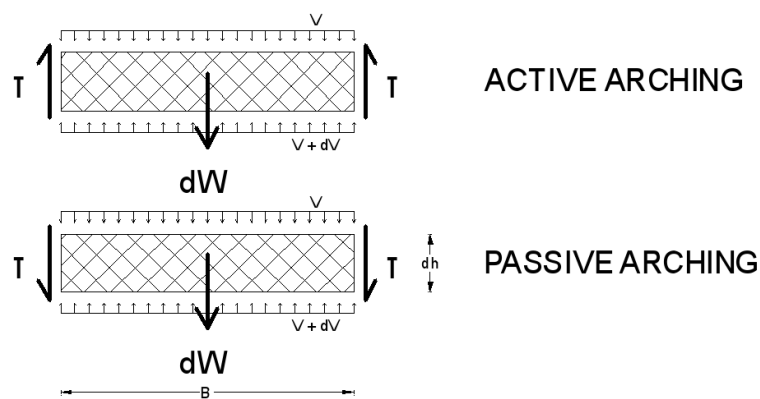


Figure 2.24: Free body diagram of soil column due to arching mechanism

The shear stress along the interface affects the earth pressure acting on the structure. Referring to Figure 2.24, the direction of shear stress differs between active and passive arching. Consider a thin layer of soil with a thickness dh and width B in the active arching profile, the vertical force equilibrium is presented below.

$$V + dV + 2 \cdot \tau \cdot dh = V + \gamma \cdot B \cdot dh$$

where V is the vertical soil force, dV is the discrete change in vertical soil force, τ is the shear stress, and γ is the soil unit weight. The shear stress of soil, as suggested by Mohr-Coulomb, can be defined as:

$$\tau = C + \frac{KV\mu}{B}$$

where K is Rankine's coefficient, C is soil's cohesion, and μ is friction factor. By integrating the vertical force equilibrium of the discrete layer from the soil surface to a designated depth, the pressure at that depth can be obtained. Thus, the earth pressure of active soil arching profile at depth z is:

$$V_A = \frac{B \cdot (\gamma B - 2C)}{2K\mu} \cdot \left(1 - e^{-\frac{2K\mu z}{B}}\right)$$

For the passive soil arching, the earth pressure is defined with the formula below.

$$V_P = \frac{B \cdot (\gamma B + 2C)}{2K\mu} \cdot \left(e^{\frac{2K\mu z}{B}} - 1\right)$$

Implementation in Tunneling

In response to areal settlements, tunnel in soft soil reacts similarly and can be treated as a conduit. Unlike sewage pipes or other conduits, deformation of tunnels is more strictly limited, especially if the structure bears the risk of human lives inside it or at the surface. That being said, tunnel structure must be designed to possess sufficient stiffness to limit deformations in all direction, which makes reinforced concrete a popular material for this type of structure.

However, stiffer tunnel is not always beneficial. As mentioned before, stiffer structures attract more load. The load path around the tunnel is determined by a ratio of structural stiffness and soil stiffness. As a result, the structural requirement of tunnel differs based on the type of environment where the tunnel is designed to sit in. Considering the same magnitude of vertical load applied on the surface, the portion of load that is borne by the tunnel around a rocky soil environment would not be as much as the tunnel that sits in soft compressible soil. Therefore, the increase of stiffness ratio can be an indicator of the growth of tunnel's significance to the structural properties of the soil.

Concrete tunnel within soft soil layers increases the stiffness of the soil profile. A substantial stiffness ratio shows that the tunnel bending stiffness governs. Following the principles of soil arching, the response of designed MRT tunnel in Jakarta with respect to the land subsidence can be deduced. The soil profile on top of the tunnel trace will no longer follow the settlement rate as previously predicted and published by the Government office. Instead, gentler settlement rate can be predicted. That being said, a dominant soil deformation process for tunnel structure is passive arching.

3. CASE STUDY: JAKARTA

3.1 General Information

Aside from its role as the national capital, Jakarta is also the largest and most populous city in Indonesia. Jakarta saw significantly more development compared to other cities in Indonesia as it was a Dutch port city during the colonial era. Hence, it turned into the economic center as it facilitated a lot of trading in the past. Formerly named Batavia, Jakarta successfully enticed merchants from China, Middle Eastern, and Europe.

The city is divided into six administrative areas, which includes North Jakarta, East Jakarta, South Jakarta, West Jakarta, Central Jakarta, and the Thousand Islands. Throughout this research, claims about geological and geotechnical features of Jakarta exclude the Thousand Islands administrative area as it comprises small islands separated from the main Java island.

3.1.1 Geographical Features

Jakarta is located on the northwest coast of Java, one of the five main islands of Indonesia, with the latitude of $6^{\circ}12'S$ and the longitude, $106^{\circ}49'E$ (Google Maps, 2017). The north side of Jakarta, with the exception of the Thousand Island district, is bordered by Java Sea and also known as the Bay of Jakarta. Furthermore, the eastern, southern, and western side are bordered by other districts, namely *Tangerang*, *Bogor*, and *Bekasi* respectively. These districts are known to be the urban spills of Jakarta and it is continuously expanding across the administrative boundary.

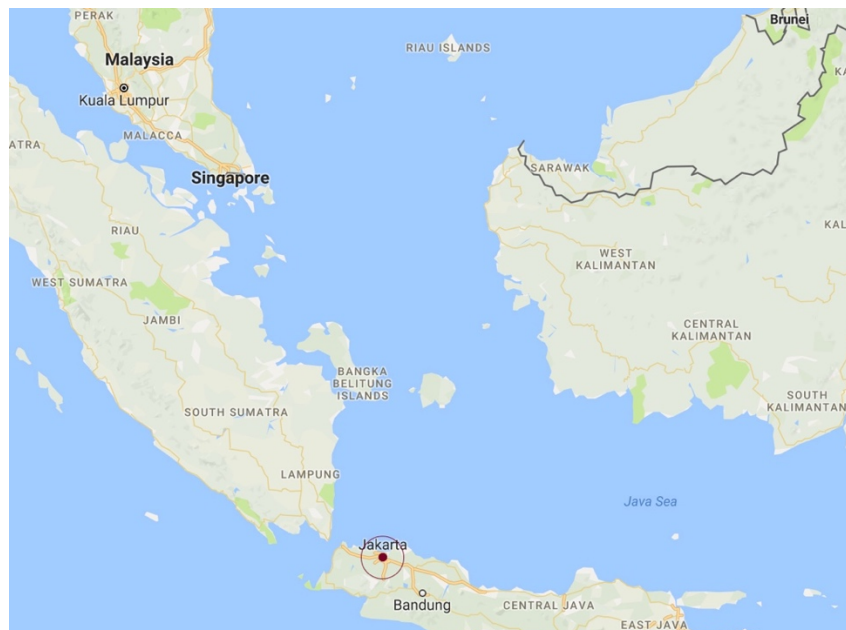


Figure 3.1: Geographical position of Jakarta (Google Maps, 2017 - with adaptations)

3.1.2 Population

Per 2015, approximately 25 million people were reported to reside in Greater Jakarta area (Dzikowitzky et al., 2015). Over the last 15 years, population growth is approximately 1 to 2% (BPS Jakarta, 2016).

3.1.3 Topography

The city of Jakarta lies on top of a flat surface. Slopes in the range of 0° to 2° are evident in Central and North Jakarta. Djaja et al. (2004) reported a maximum slope of 5° in South Jakarta, where the highest point can reach 50 meters above the mean sea level.

3.1.4 Subsurface Profile

Jakarta sits on top of an alluvial basin, which contains a combination of volcanic origin deposit, quaternary, and tertiary sediment. The basin extends to an average depth of 300 meter and was reported to contain multiple aquifers (Djaja, 2004; ESDM, 2014). The alluvial plain gets thinner towards the southern boundary, which then limited by the Miocene impermeable layer (Fauzi et al., 2014).

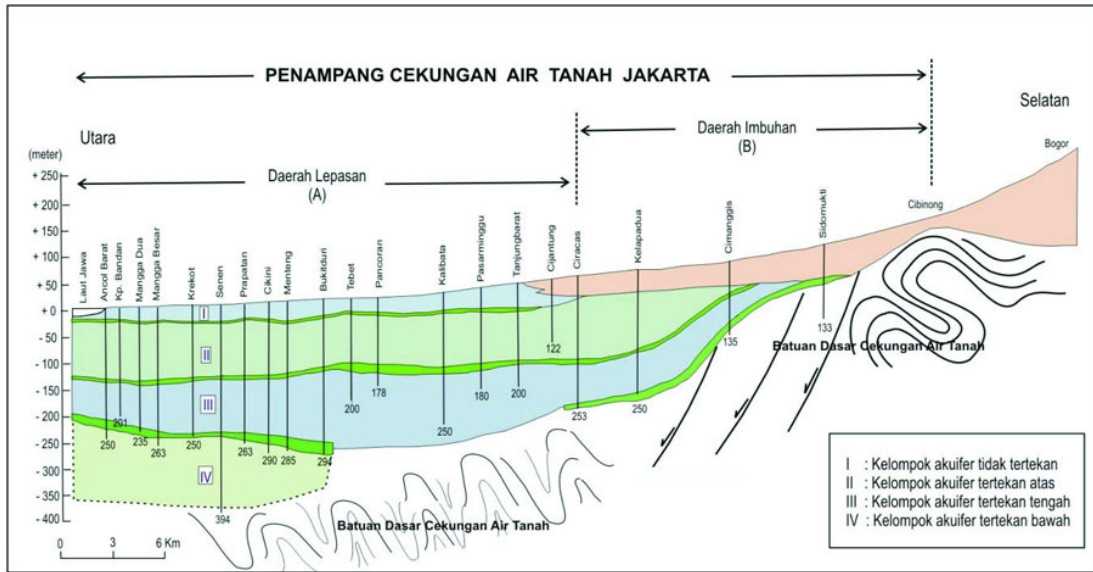


Figure 3.2: Cross section of Jakarta basin and classification of aquifers (ESDM, 2014)

Furthermore, Figure 3.2 dissects Jakarta stratigraphy into four dominant aquifers, consisting of one unconfined and three confined aquifers. A similar four-aquifer system was also proposed by Bakr (2014) for his numerical analysis. This finding was also supported by Abidin (2008), who recognized three aquifers over 250 m depth, categorized them into shallow (0 – 40 m), middle (40 – 140 m), and deep aquifer (140 – 250 m), and asserted that there is another aquifer on the tertiary layer, which depth is more than 250 m.

On a smaller scale, Avanti (2013) proposed a typical Jakarta subsoil profile which consists five main layers and presented in Figure 3.3. Soft soil layers, for instance clay and silt, are apparent in approximately 12 to 18-meter depth. It is then continued with alternation of harder sand and silt layers. Beyond the 35-meter depth mark, silt layer with lenses of sand was identified.

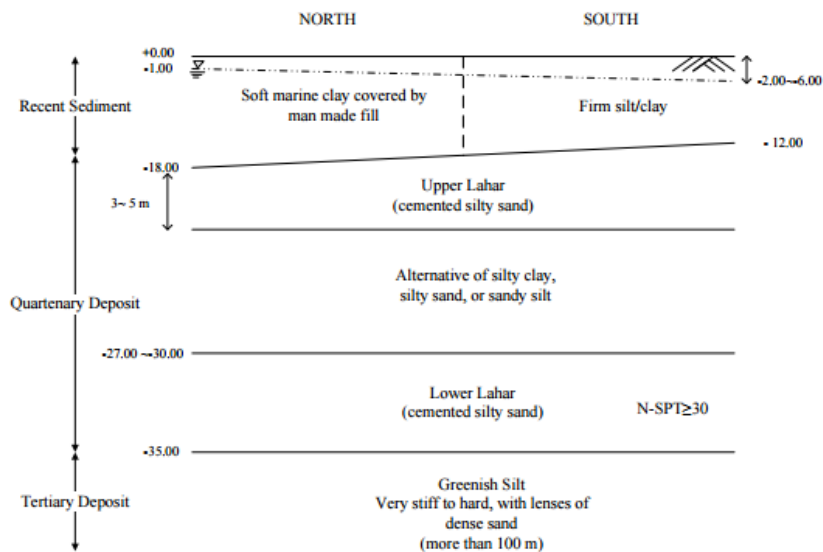


Figure 3.3: Typical subsoil condition of Jakarta (Avanti, 2013; Firmansyah and Sukamta, 2000)

3.2 Groundwater Extraction Issue

This subchapter elaborates the prevalent groundwater extraction issue in Jakarta. Additionally, this section provides a brief history about the early use of groundwater. Then, it is followed by the modern trend of groundwater extraction. These subjects are written based on the information obtained from the online archives and government officials.

3.2.1 History

The introduction of artesian well in Jakarta dates back to the colonialism era. Prior to the installation of pipe networks, artesian wells were exclusively implemented for the area of the city inhabited by the colonials, while local people relied on surface water. When artesian well was replaced by piped water network, local people began to construct artesian well. The exclusivity of pipe networks in this era is subconsciously conserved to the modern era.

According to Colbran (2009), consecutive errors in governmental practices and decision-making processes are the root of Jakarta's groundwater exploitation issue. Despite Soekarno's, the first President of Indonesia, emphasis that water must be managed by the state to provide greater benefits for people, political interest and corruption have tainted this intention. For example, the expansion of pipe networks in Soeharto's administration was only designated for industrial area and the residences of political supporters.

In 2005, only 46% to 56% of registered households connected with pipes. If informal settlers are included, the number dives down to 25%. Colbran (2009) pointed out that multiple zero-used records were found, with cost being one of the reasons for a household to opt for other water sources. Additionally, Colbran added that piped water service and installation were priced more than regional average income. In agreement with Colbran, Kooy et al. (2016) asserted that the 60% of domestic, industrial, and agricultural clean water demand is met by the groundwater. Consequential to the unreliable pressure of piped water, most households combine piped and groundwater system to maintain water supply stability.

3.2.2 Present Trend

The data presented in Figure 3.4 was obtained from the Department of Industry and Energy Jakarta, which one of their responsibilities is to monitor the annual groundwater extraction. Based on Figure 3.4, a reduction of groundwater abstraction is obvious. On a side not, the investigation only considered licensed shallow and deep pumps. Thus, the outcome of the investigation cannot represent the current situation.

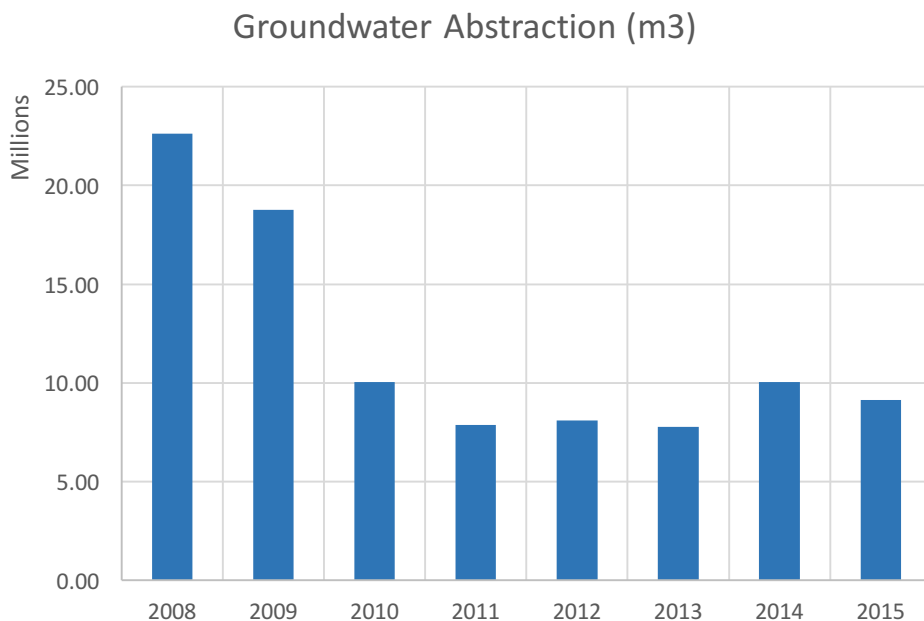


Figure 3.4: Groundwater abstraction based on registered shallow and deep wells (Department of Industry and Energy Jakarta, 2015)

Delinom (2011) provided the groundwater abstraction trend over a longer period of time, shown in Figure 3.5. The graph shows a rapid annual increase of groundwater abstraction between the 1950s to the 1990s. Then, a sharp declination of groundwater extraction is displayed at the end of 20th century. In the final 5 years of the investigation, the graph displays a more stable withdrawal rate which revolves around $22 \cdot 10^6 m^3$ per year.

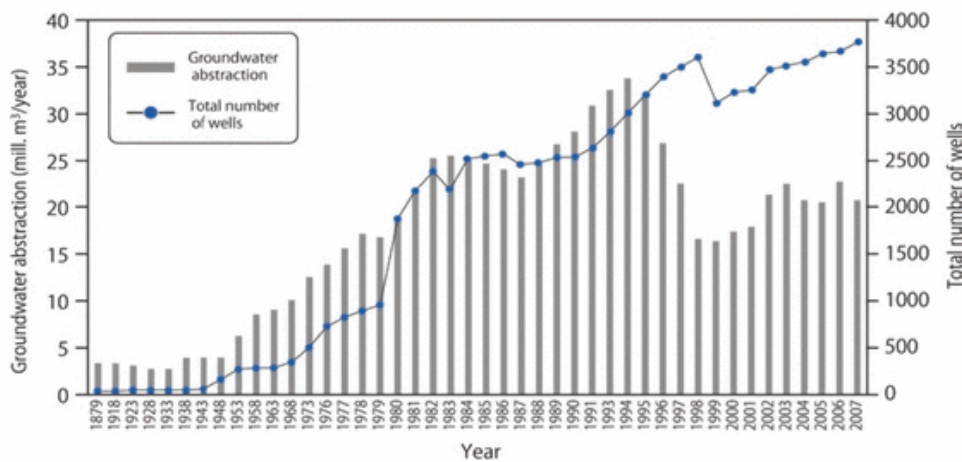


Figure 3.5: Groundwater abstraction in Jakarta (Delinom, 2011)

3.2.3 Groundwater Table

Sutanudjaja and Erkens (2016) conducted a 10-km resolution simulation using *PCRaster Global Water Balance* (PCR-GLOBWB) model to determine the declination of the groundwater table. The simulation concluded a 26 cm/year declination of the groundwater head.

Tirtomihardjo (2011) presented the result of groundwater table depth observation over the span of 27 years in South and East Jakarta. The observation was performed not only on the shallow unconfined aquifer but also on the deeper confined aquifer. The result is displayed in Figure 3.6.

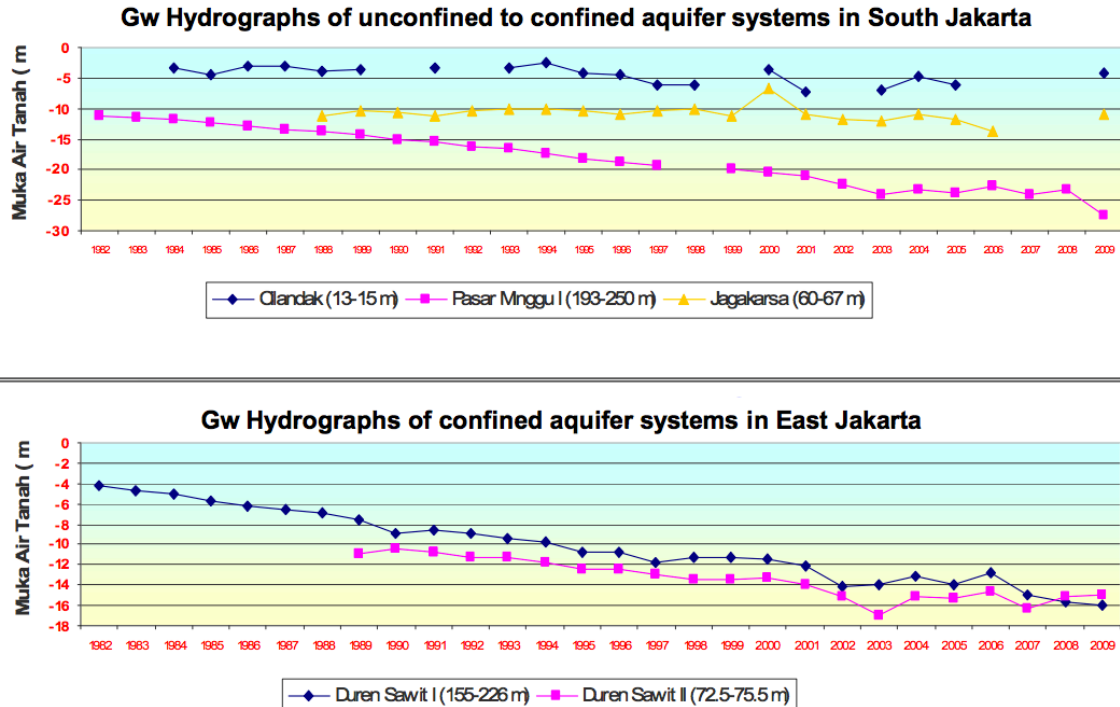


Figure 3.6: Monitored groundwater table depth from 1982 to 2009 of South and East Jakarta (Tirtomihardjo, 2011)

According to Figure 3.6, groundwater head declination is apparent in both confined and unconfined aquifer. Additionally, Figure 3.6 provides indication about the spatial aspect of the declination, given that declination was observed in both South and East Jakarta.

Makarim (2009) staged the groundwater table declination trend between 1971 to 1997, shown in Figure 3.7. As the groundwater table fluctuates, the annual maximum and minimum were recorded and presented in red and blue respectively. The maximum depth is defined as the deepest elevation where the groundwater table was observed and vice versa.

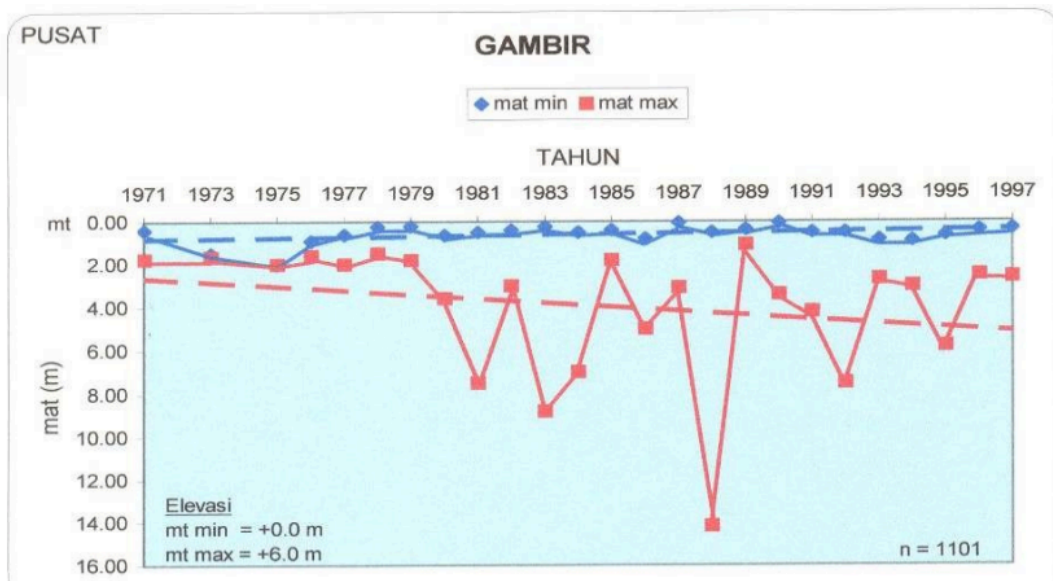


Figure 3.7: Depth of groundwater table in Gambir, Central Jakarta, over the years (Makarim, 2009)

Based on Figure 3.7, the separation between the maximum and minimum groundwater table grows in time. In other words, greater fluctuations are expected in the future. Figure 3.7 shows the declination of the maximum groundwater table. Additionally, it also shows the rise of the minimum groundwater table on a slower rate than the change of the maximum.

Ali (2007) provided the change in average groundwater level from the year 1993 to 2005. Ali's finding shows the groundwater table in Central Jakarta was at +3.42 m PP in 1993 and declined to +2.40 m PP in 2005. If a linear pattern is adopted, the rate of decline is 0.08 m/year.

3.3 Land Subsidence

Land subsidence is defined as the declination of ground level due to natural or anthropogenic cause. Given that land subsidence phenomenon could cause horrendous damage, the decline is usually monitored with extensometer. Early indication of land subsidence in Jakarta was apparent on the pedestrian bridges, where concrete cracks started to appear in the 1970s (Abidin, 2008). In addition to that, the expansion of inundated area during flood also verifies the phenomenon.

This subchapter explains the phenomena of land subsidence in Jakarta by recollecting the knowledge about land consolidation. The elaboration, subsidence rate, and future estimations are based on previous studies.

3.3.1 Mechanism of Land Subsidence

Previous studies (Abidin et al., 2008; Park, 2013) asserted four main causes of land subsidence in Jakarta, which are the excessive groundwater extraction, increase of ground surcharge due to surface construction, natural consolidation, and tectonic activities. Abidin et al. (2008) claimed the first three causes govern, while Park (2013) singled out groundwater extraction as the dominant factor of subsidence. In fact, land subsidence is the accumulation of soil consolidation over the soil the first three factors explained above have influence. The phenomenon itself is not more than the result of uneven interaction between load and resistance. When loads exceed the soil resistance, land subsidence are imminent.

In accordance with Chapter 2, the three factors mentioned earlier can be incorporated with the consolidation formulas. Two of the three factors, namely the increase of ground surcharge and groundwater extraction, directly increase the effective stress on soil. Substantial urban growth, increase of land occupation density,

and large population influx are several sources of additional ground surcharge. Within the soft soil layers, pore water pressure builds up because pore water drainage is a lengthy process. Water can thus slowly escape the soil layer and based on Terzaghi's effective soil stress theory, the stress will be transferred to the soil matrix.

In Jakarta, this process is intervened by the extensive groundwater extraction for domestic and industrial uses. Due to pumping, the excess pore water pressure dissipates quicker and consolidation process is accelerated. Unsustainable groundwater extraction from the aquifers lowers the groundwater table at the shallow aquifer or the piezometric level of the deeper aquifers. As a function of $\Delta\sigma'$, settlement due to primary consolidation increases with the increase in surface loading and the decline of pore pressure.

Other than because of the increase in effective stress, secondary compression contributes to the surface settlement. As explained in Section 2.2.2, secondary compression occurs in areas where groundwater level is stagnant and minimum change in the occupation layer.

The presence of more than one soil layers complicates the process. These layers have their own unique characteristics, thus different reactions to loads of each layer are expected. That being said, multiple consolidation rates exist at one point and accumulates to the surface settlement rate. In order to determine the cumulative subsidence rate, the consolidation in each layer is usually monitored.

3.3.2 Rate of Subsidence

The rate of subsidence is determined by comparing the elevation of different years and find the change in elevation. The maps shown in Figure 3.8 and Figure 3.9 are the products of GPS surveys taken between 2009 and 2011 which present the ground level differences over the period (Bimantara, 2012).

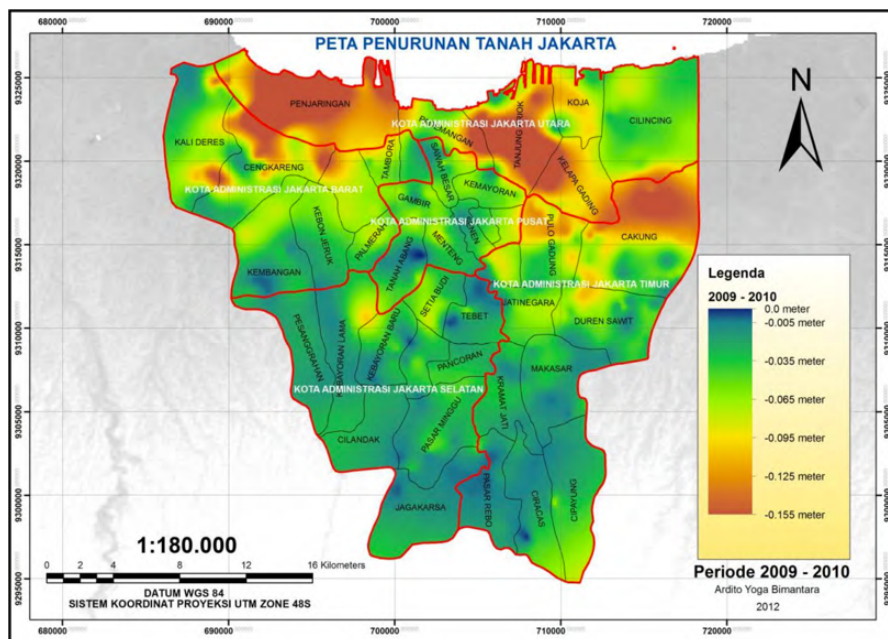


Figure 3.8: Surface settlement of 2009-2010 period (Bimantara, 2012)

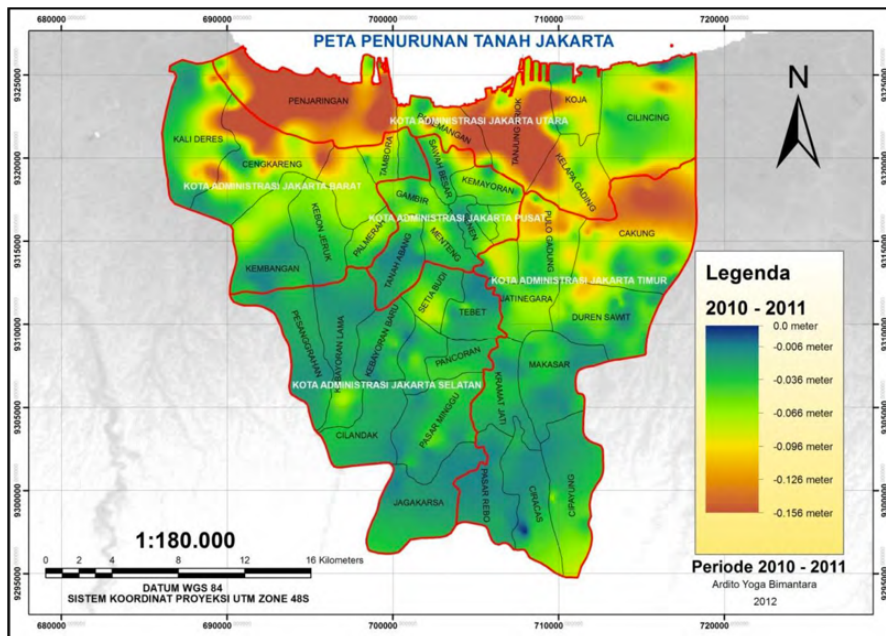


Figure 3.9: Surface settlement of 2010-2011 period (Bimantara, 2012)

Three hotspots are clearly represented in each map and the spatial pattern remains consistent in the two-year period. Greater land subsidence was observed at on the north side of Jakarta compared to the southern side. The maximum subsidence recorded was 15.6 cm in an area referred as *Penjaringan*, North Jakarta. The aforementioned hotspots were found to be correlated with the large amount of groundwater level drop. Figure 3.10 shows the juxtaposition of the subsidence map and the groundwater table map, where the groundwater table in 1995 is represented in blue while the groundwater table in 2005 is represented in red.

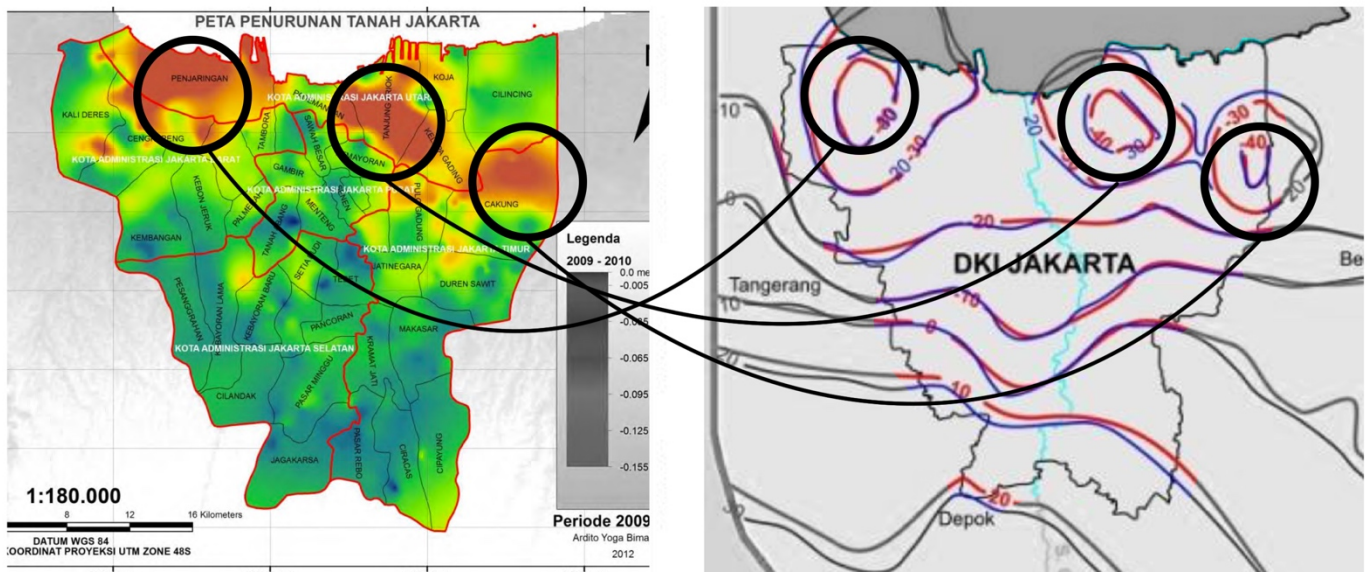


Figure 3.10: (Left) Settlement of 2009-2010 (Bimantara, 2012) shows spatial agreement with decline of groundwater table from 1995 to 2005 (Puradimaja et al., 2008)

In addition, Abidin et al. (2007) presented the subsidence rate that was gathered from 27 proxies scattered around Jakarta. The study concluded an average of 1 – 10 cm/year over December 1997 to September 2005. Abidin et al. emphasized on the spatial and temporal variations of the subsidence rate as a 60-centimeter decline within a 6-month period was recorded in East Jakarta in 2002.

3.4 Mass Rapid Transit Jakarta

3.4.1 General Information

To solve the standing transportation issue, DKI Jakarta Provincial Government, funded and assisted by JICA (Japan International Cooperation Agency), reinstated the MRT Jakarta (MRTJ) project, which was previously stalled due to financial reason. The megaproject is divided into sub-projects and is now being constructed following the sequences based on the priority scale. These smaller projects share a common long-term goal, which is to provide a reliable urban transportation system with intricate network comparable to urban rail in Singapore, Kuala Lumpur, and Bangkok.

3.4.2 Project Sequence

The MRTJ project is divided into three sub-project categories. These are the two phases of North-South line and the East-West line. As of present, the first phase of the North-South line is under construction, while the second phase is still being studied. On the other hand, works for the East-West line will not start before 2020. The three sub-projects are presented in Figure 3.11.

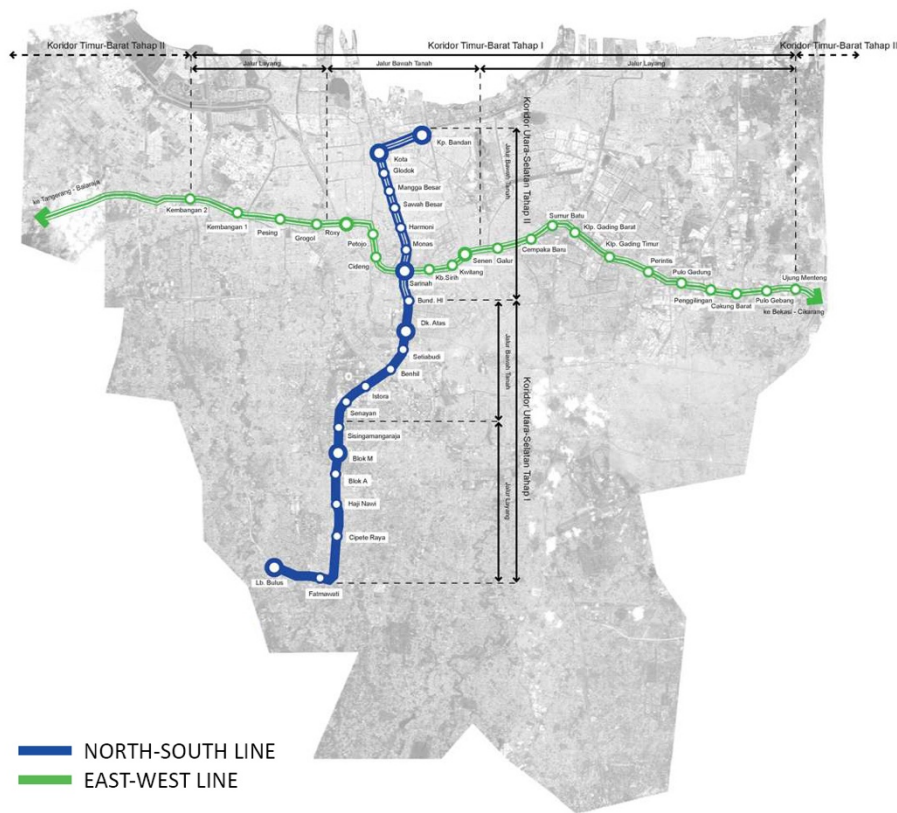


Figure 3.11: MRT Jakarta planned network (MRT Jakarta, 2014 - with adaptations)

The first phase of North-South line inaugurated with route that spans from *Lebak Bulus*, South Jakarta, to *Bundaran HI*, Central Jakarta. The total length is 15.7 km punctuated by 7 elevated and 6 underground stations. The project was commenced in 2013 and expected to be fully operating in 2018, just in time for the sport event. However, the project experienced delays caused by construction complications and it is now estimated to finish in 2019.

The second phase of the North-South line is the project used in this study. Aside from the project being temporally relevant to the study, this project is positioned at the north side of the first phase, in the area where more severe land subsidence transpires. Based on the project proposal, 8 stations are planned along the approximately 8.0-kilometer line. However, it is still unclear whether all 8 stations will be underground. This matter is discussed later in the study.

3.4.3 NSL-P1 Tunnel Properties

Limited information requires this study to adopt MRTJ North-South line Phase 1 tunnel design. To minimize alterations, the geometrical and structural design used in this research is adapted from the tunnel which connects *Dukuh Atas* to *Bundaran HI* station, which is closest to the NSL-P2 project.

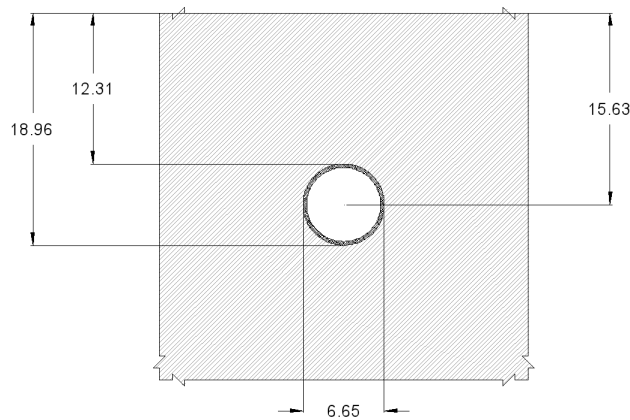


Figure 3.12: Geometry based on MRTJ North-South Phase 1, all measurements are in meter

The amount of overburden at this section is 12300 mm of soil. The inner diameter of the tunnel is 6050 mm. The thickness of the tunnel lining is 300 mm and uniform along its perimeter, which makes the outer diameter of 6650 mm. The segment is 1500 mm in width and comprises 6 reinforced concrete segments, which include 5 regular segments and 1 key segment. Among the 5 regular segments, two geometrical designs were developed to incorporate the trimmed width of the key segment. The complete technical drawing is available in Appendix D (Technical Report MRT Jakarta). The position of joints is shown in Figure 3.13.

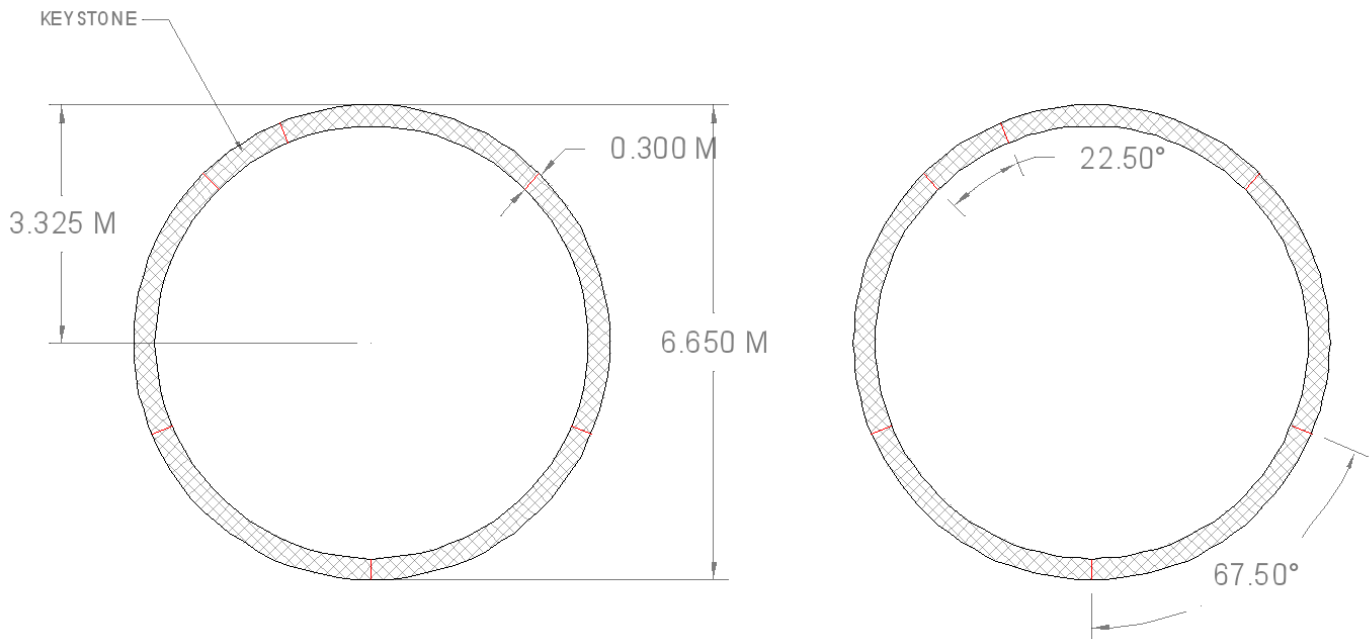


Figure 3.13: Geometry and segmental joints configuration of MRTJ North-South Phase 1 tunnel

Furthermore, steel bolts were implemented to strengthened the connection between one tunnel segment with the other in the longitudinal and radial direction. The type of connection used in the project is curved bolt M27 JIS B1180-Grade 8.8 with yield strength of 380 MPa (SMCC-HK JO, 2015).

4. SITE CHARACTERIZATION

Before the model enters the calibration stage, it must follow the two-part site characterization process as presented in Figure 4.1. The first part defines the size and the boundaries of the numerical model based on the data availability and relevancy to the research interest. The boundary definition is done in two steps, namely the vertical profile and spatial selection. In the second part, material properties of soil and its behaviors are defined, which are based on data interpretation and established local parameters from the past researches.

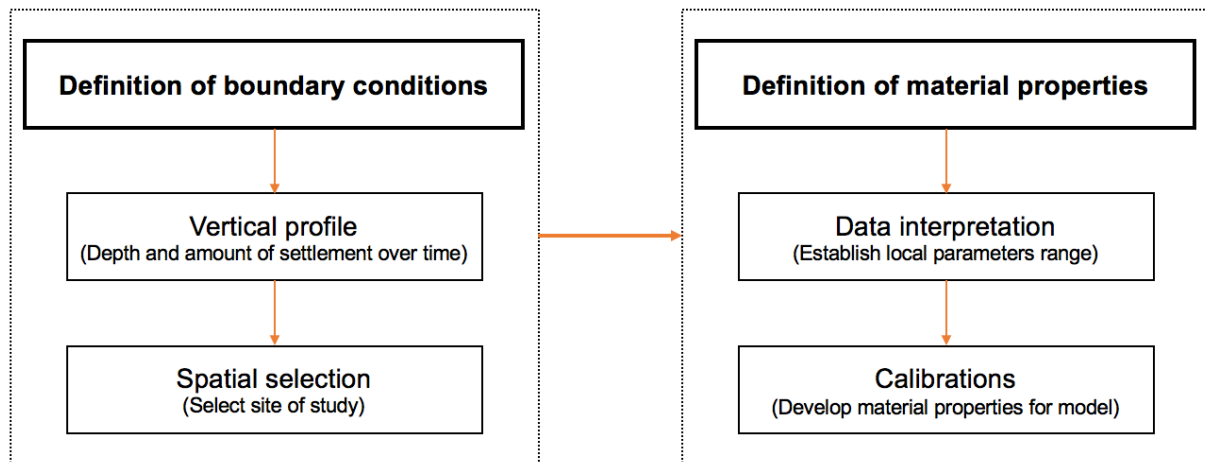


Figure 4.1: Characterization flowchart

In the definition of boundary condition process, a site of study along with its depth limitation is selected. Therefore, the size and the amount of settlement that the model needs to replicate should be available at the end of the first process. The second process, definition of material properties, is performed through calibrations and according to the guidelines presented in Subchapter 2.3 as well as the local parameters. The site characterization process is elaborated in a more detailed manner in the following subchapters.

4.1 Collected Information

Fundamental information regarding the site was successfully obtained from the affiliation with PT. MRT Jakarta. The information is available in these documents:

1. SPT data bank comprised of 462 investigation results scattered all over Jakarta. These investigations were previously collected from numerous geotechnical consultants of diverse projects and were initially intended for seismic analysis.
2. Surface settlement rate based on GPS survey of 2000 – 2014 and 2013 – 2014
3. Feasibility study of MRTJ NSL-P2 project
4. Structural technical specifications for MRTJ NSL-P1 tunnel
5. Geotechnical interpretations of contract package (CP) 106, which consisted of *Bundaran HI* and *Dukuh Atas* station.

Further necessary information that is not provided in the documents stated above is obtained from online archives and cited accordingly.

4.2 Boundary Conditions

4.2.1 Site Selection

The site of study is selected through considerations of multiple factors which is not only comprised of technical factors but also include non-technical factors, such as the likelihood to have an underground rail line rather than an elevated one as it is directly related to the scope of research. On this section, the considerations are discussed to justify the selected site.

Geotechnical Information Availability

At the time of writing, geotechnical information for MRTJ NSL-P2 project is still very limited. Despite the project is surrounded by developed area, geotechnical investigations or surveys went undocumented. If it is documented, most of them are unpublished.

Relevant SPT results were drawn from the SPT data bank. The relevancy of an SPT data is determined by whether or not the datum could represent the characteristics of the soil, which depends largely on the investigation location with respect to project site. Departing from the high variations of Jakarta's stratigraphy, priority is given to boreholes closest to the project site. In other words, section that has the most relevant investigations will be selected.

Preliminary boreholes selection was based on the GPS coordinates and rough spatial description. As a result, 14 out of 462 boreholes were then mapped, as seen in Figure 4.2, to undergo further examination.

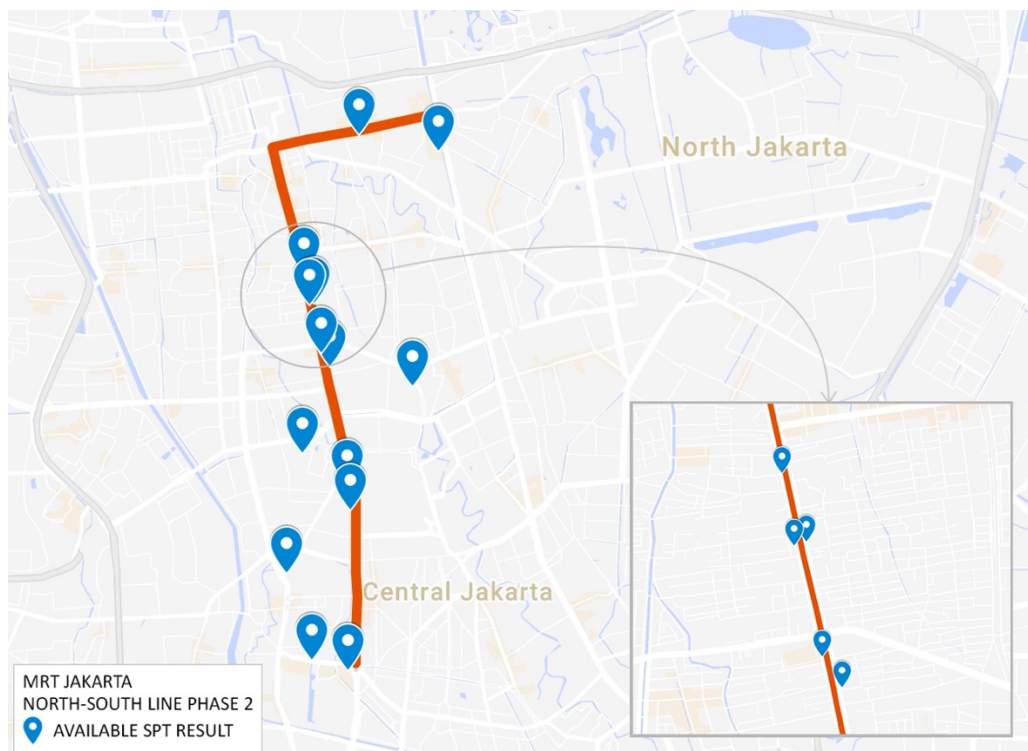


Figure 4.2: Fourteen investigation results were considered after the preliminary selection based on their positions. At the inset, section with the highest information density is shown.

Only 8 out of 11 boreholes fall within the relevancy criteria, in which 5 of them are positioned along *Jalan Hayam Wuruk / Gajah Mada* displayed in the inset of Figure 4.2.

Soil Settlement Rate

Aligning with the research interest, contrast spatial difference in settlement rate would be ideal to produce obvious results. Through the projection of the proposed trace to the surface settlement map, the settlement rate around the tunnel can be approximated. The contoured surface settlement rate maps, presented in Figure 4.3, show an agreement that the variation of settlement rate increases in the northern area. High differential settlement is signified by the cramped contour lines, clearly represented in Figure 4.3B.

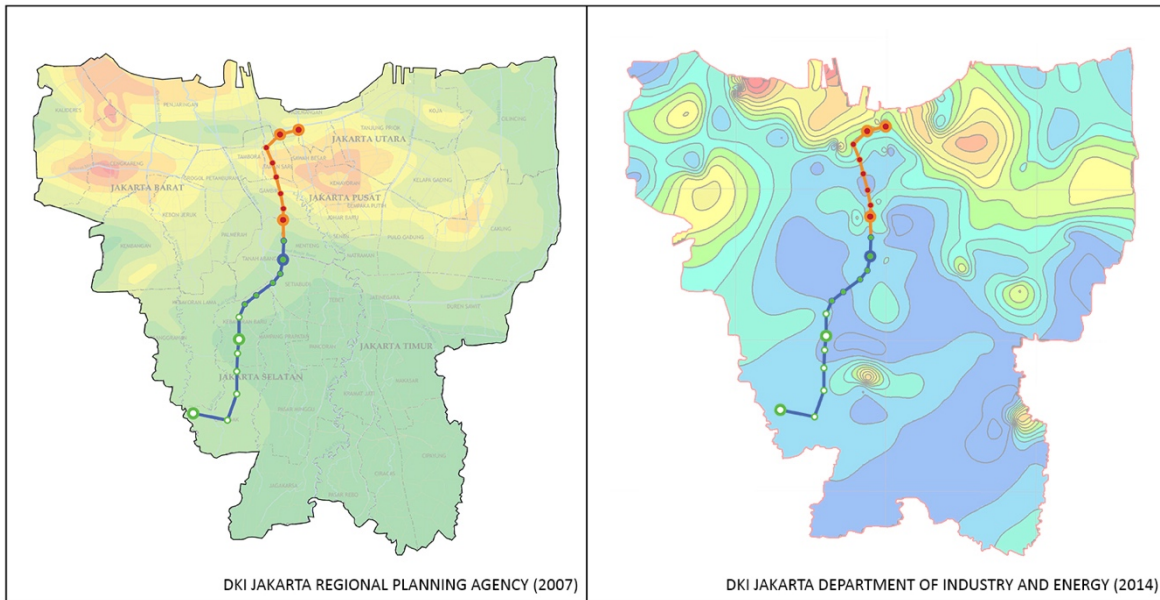


Figure 4.3: Settlement rate contour maps produced by (left) DKI Jakarta Regional Planning Agency (2007) and (right) DKI Jakarta Department of Industry and Energy (2014)

It can be concluded from Figure 4.3 that the southern reach of MRTJ NSL-P2 tunnel is not as exposed to differential settlement as the northern reach. The straight-northbound section, prior to an eastward alignment, experiences the most differential settlement by crossing at least 6 contour lines.

Prevalent Discussion

The research is conducted simultaneously to the completion of MRTJ NSL-P2 feasibility study. The study suggested that the project includes 8.6 km of underground rail and 0.3 km at-grade segment at the end. However, uncertainties were pulled out from an interview session with PT. MRT Jakarta as a the most recent proposal claimed that the underground section could end at *Ancol Barat* station, as annotated in Figure 4.4, and the remaining will be an elevated or at-grade segment eastward.

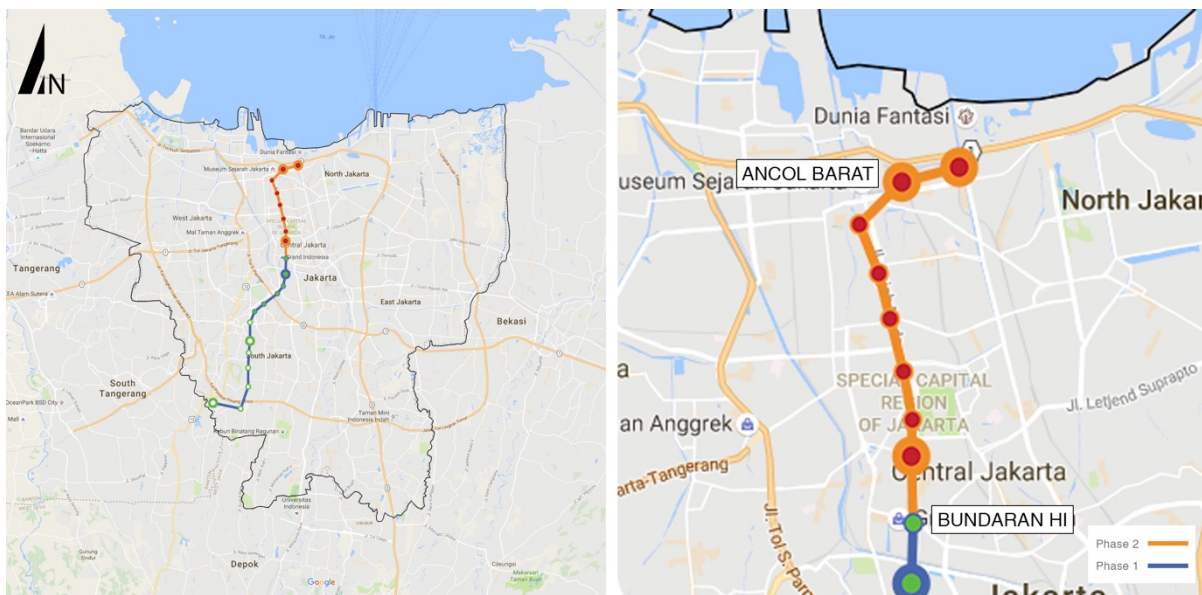


Figure 4.4: (Left) MRTJ Phase 1 and Phase 2, (Right) MRTJ Phase 2 tunnel starts at Bundaran HI and could end at the Ancol Barat station

The rail line between *Bundaran HI* station and *Ancol Barat* station is obliged to be underground given that it is an area of heavy occupancy, hence more certainty. In addition, two tunnel soft eyes have been prepared at the end of *Bundaran HI* station, which increases the certainty to have the tunnel underground, as seen in Figure 4.6.



Figure 4.5: NSL-P2 tunnel soft-eye at the end of NSL-P1

Ideal Reach

For the numerical analysis, the length of the tunnel model should be limited. Stemming from the previous consideration, a 1160 m section from point A to point B, as annotated in Figure 4.6, is selected. Consequently, 5 SPT results are used for the numerical model.

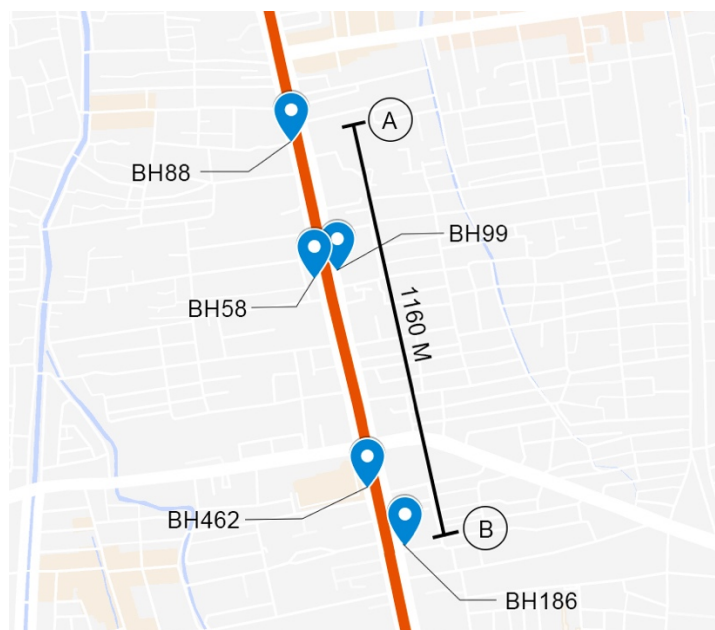


Figure 4.6: Selected underground segment for numerical modelling

Other than the adequate amount of available information, segment A – B experiences differential settlement. Segment A – B spans over 3 different settlement rates as shown in Figure 4.7 and Figure 4.8.

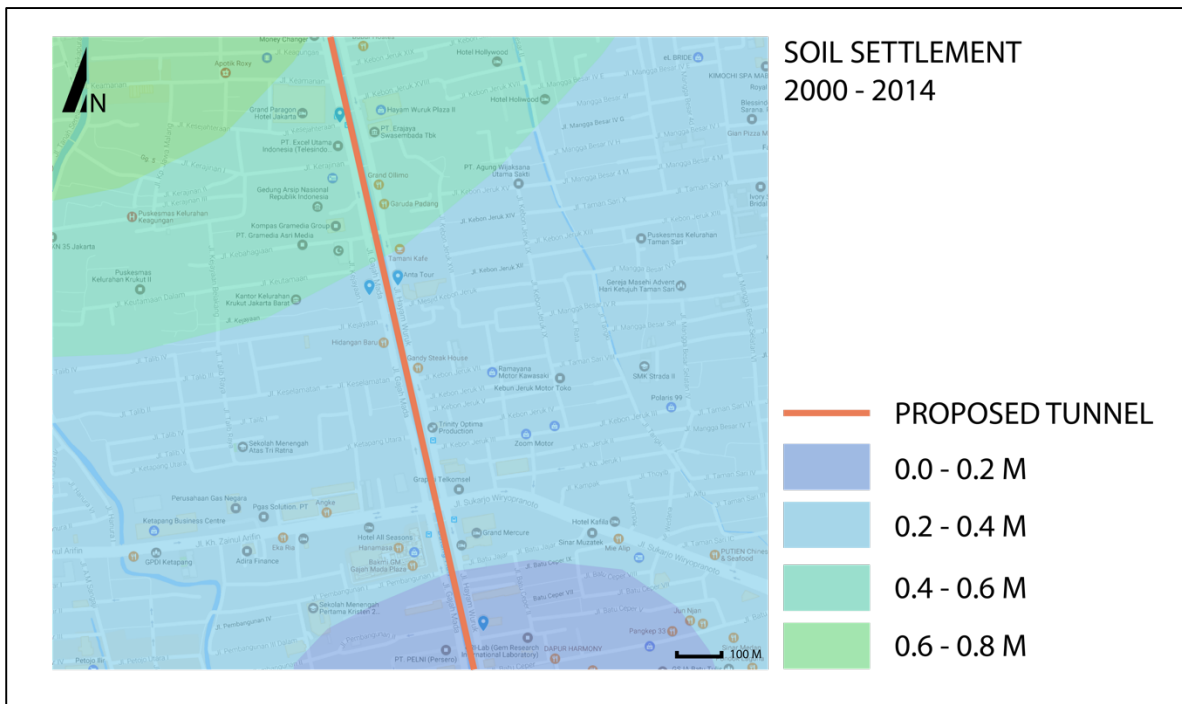


Figure 4.7: Surface settlement of 2010-2014 around the selected reach

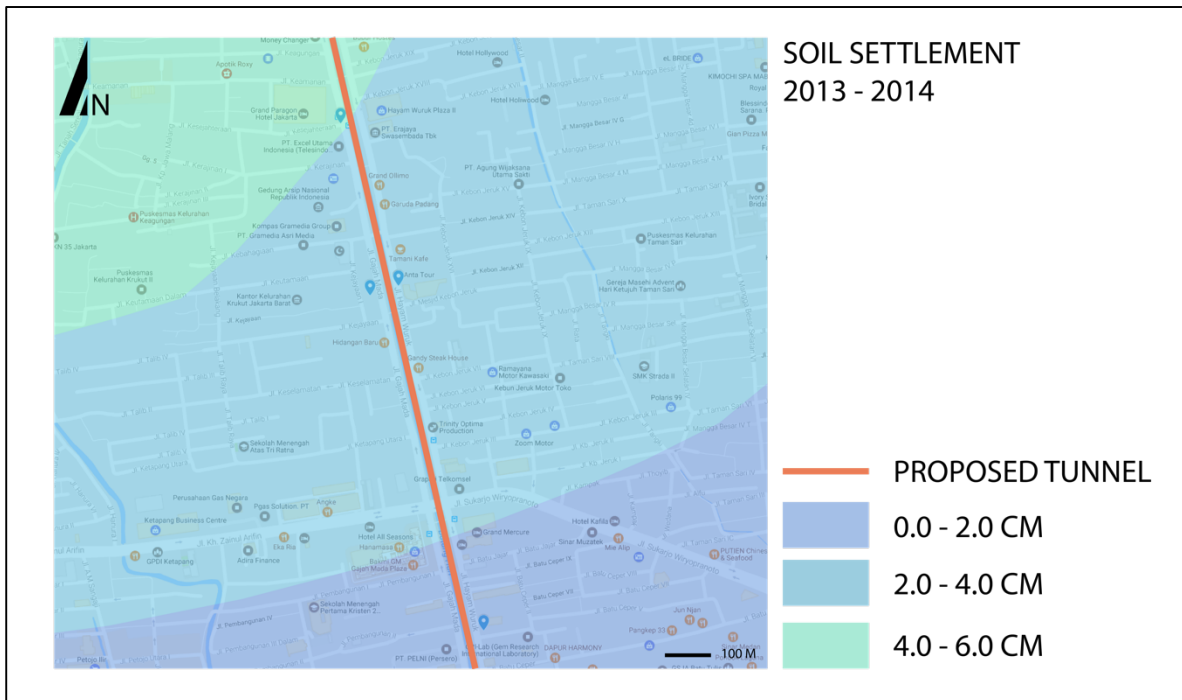


Figure 4.8: Surface settlement of 2013-2014 around the selected reach

The maximum of 60.0 cm settlement difference could occur between point A and point B from the year 2000 to 2014. In the year 2013 to 2014 itself, a potential of 6.0 cm settlement difference is reported. Additionally, segment A-B is located in between *Bundaran HI* station and *Ancol Barat*, where underground construction is required.

4.2.2 Estimation of Consolidation in The Shallow Aquifer

As of this point, the obtained SPT data, whose reach is only to the end of shallow aquifer, is still unable to be aligned with the surface settlement data as it is also the accumulation of consolidations occurred in even deeper soil layers. Therefore, the fraction of settlement occurred in the shallow layers must be estimated to establish the numerical model. The estimation is performed with the past study carried out by Bakr (2015).

Bakr (2015) simulated Jakarta land subsidence due to the decline in piezometric head level with numerical model. Four aquifers were acknowledged within 249-meter depth, located between four aquitards displayed in Figure 4.9.

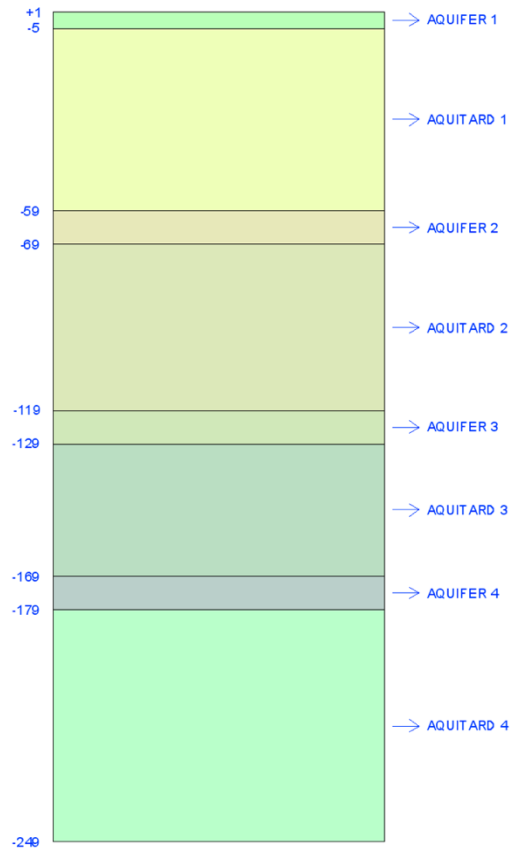


Figure 4.9: Bakr's geological profile for dewatering simulation (Bakr, 2015)

The proposed geological profile is very coarse and highly simplified. However, it was sufficient to provide ideas on how much Jakarta aquitards consolidate in response to change in piezometric head. Aside from the total surface settlement, Bakr also monitored to consolidation of each aquitard. Therefore, the contribution of each soil layer to the total surface settlement can be discovered.

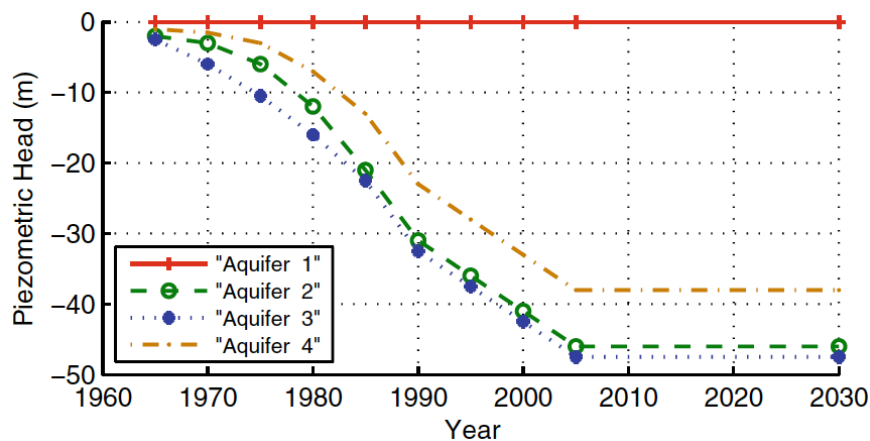


Figure 4.10: Scenario 1 of groundwater management proposed in the simulation (Bakr, 2015)

Four groundwater management scenarios were included in Bakr's research. Unfortunately, only the result of Scenario 1, displayed in Figure 4.10, was made available in the research report. The dewatering process, as explained by Scenario 1, started in the 1960s and maintained the average of 1 m/year declination for 40 years. The extraction was halted in 2005, resulted a stagnant piezometric head towards the end of the simulation. The simulation outcome based on Scenario 1 is presented in Figure 4.11.

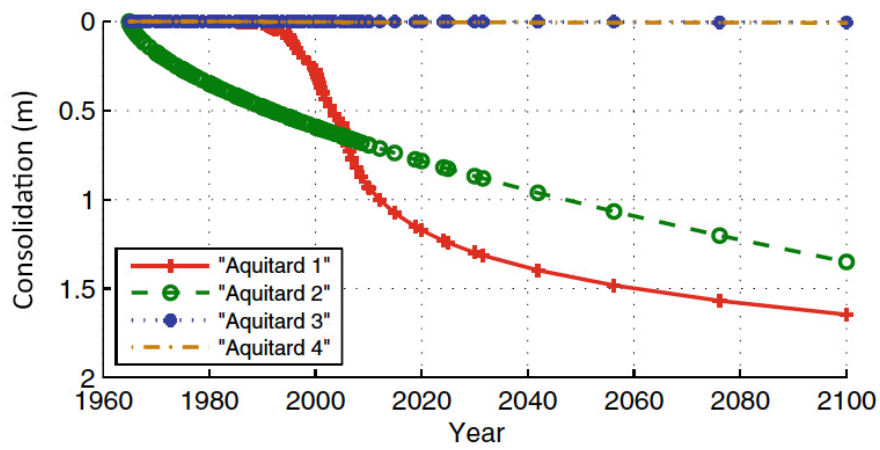


Figure 4.11: Consolidation in each soil layer based on the first scenario of piezometric head function (Bakr, 2015)

From the four aquitards included in the model, only the two shallowest aquitards consolidated, namely Aquitard 1 and 2. No volumetric changes were exhibited in deeper aquitard, referred as Aquitard 3 and 4. Given that the changes in piezometric head only took place in Aquitard 1, this phenomenon is down to the coefficient of creep consolidation assigned to Aquitard 3 and 4, which were roughly an order smaller than Aquitard 1 and 2. Furthermore, primary and secondary compression process were able to be identified in Aquitard 1. On the other hand, secondary compression appeared to be the only source of deformation in Aquitard 2. Another interesting feature to look out from Figure 4.11 is the time lag between the start of groundwater extraction and the start of consolidation of Aquitard 1. The slow excess pore water pressure dissipation process, a product of virtually impermeable aquitards, is responsible for the delay (Bakr, 2015).

The outcome of Bakr's research is used to calibrate the numerical model for this study. The calibration of the numerical model is based on the surface settlement data provided in the previous section, ranging from 2000 to 2014. As it has been concluded that only Aquitard 1 and 2 contribute to the settlement, the deeper aquitards are omitted from the analysis. However, Aquitard 2 must also be excluded from the analysis to comply with the available information. In order to do so, the contribution of Aquitard 1 should be known beforehand.

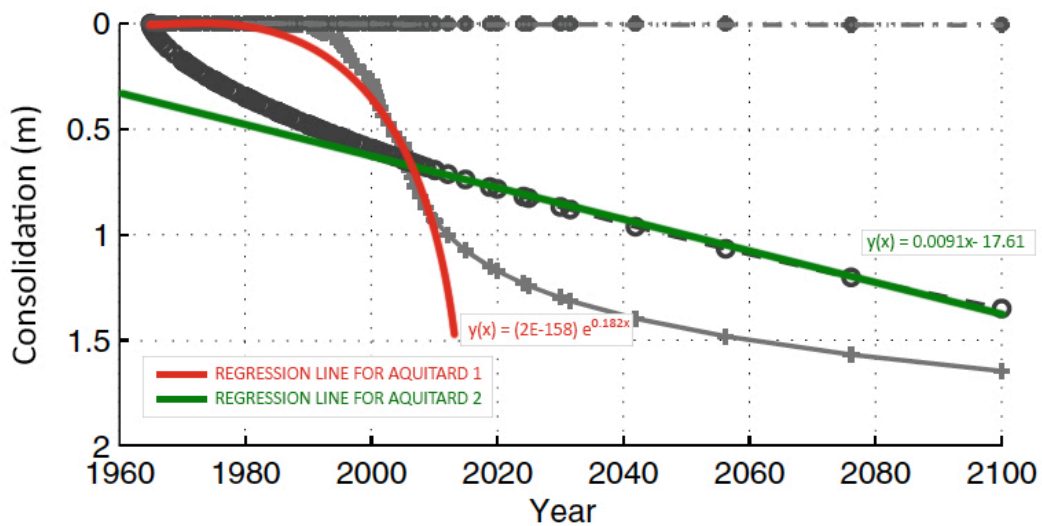


Figure 4.12: Fitted trend lines on Bakr's study outcome to estimate consolidation

Different groundwater management scenario, in alignment with the real situation, necessitates new consolidation progression curve. One exponentially fitted and one linearly fitted trend lines were added to estimate the consolidation of Aquitard 1 and 2 had the dewatering process carries on, presented in Figure 4.12. Two time-functions, derived from the trend lines, reveal an approximately even distribution between the two participating aquitards from the year 2000 to 2014. The estimated consolidation in each aquitard are presented in Table 4.1.

Table 4.1: Consolidation in each aquitard (aqt) from 2000 to 2014 for calibration purposes

Time	Consolidation			Contribution	
	Aqt1 [m]	Aqt2 [m]	Total [m]	Aqt1	Aqt2
2000	0.20	0.59	0.79	25%	75%
2001	0.24	0.60	0.83	28%	72%
2002	0.29	0.61	0.89	32%	68%
2003	0.34	0.62	0.96	36%	64%
2004	0.41	0.62	1.03	40%	60%
2005	0.49	0.63	1.13	44%	56%
2006	0.59	0.64	1.23	48%	52%
2007	0.71	0.65	1.36	52%	48%
2008	0.85	0.66	1.51	56%	44%
2009	1.02	0.67	1.69	60%	40%
2010	1.22	0.68	1.90	64%	36%
2011	1.47	0.69	2.15	68%	32%
2012	1.76	0.70	2.46	72%	28%
2013	2.11	0.71	2.82	75%	25%
2014	2.53	0.72	3.25	78%	22%

Departing from this assessment, the numerical model will be adjusted accordingly to manifest the same amount of settlement as much as 50% of the monitored surface settlement. This amount of settlement will be used in the latter stages to iteratively determine the soil properties.

4.3 Recapitulation of SPT Result

Four sets of SPT results were used to represent soil environment around the selected range. The SPT results were gathered from *BH88* (Borehole 88), *BH58*, *BH186*, and *BH462*, indexed with respect to the sheet order of the SPT data bank. Based on these sets, the environment is characterized by means of soil stratification. The locations of these borehole are presented in Figure 4.13.

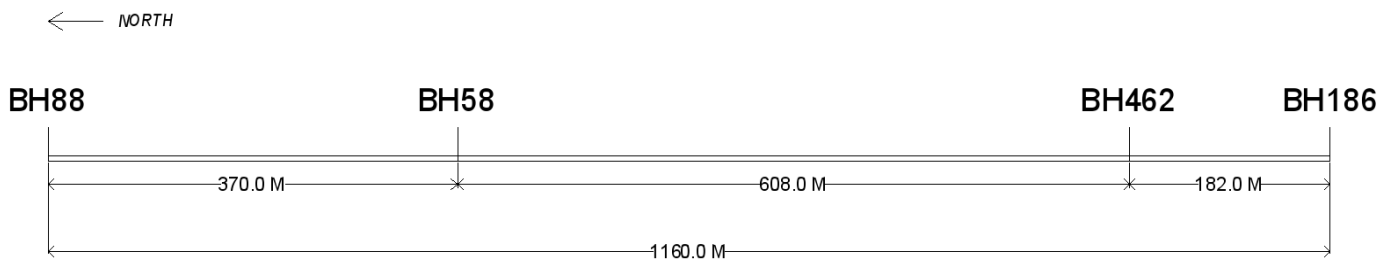


Figure 4.13: Boreholes used for SPT along Jalan Hayam Wuruk / Gajah Mada

The northern boundary of the selected segment sits at +5.3 m PP (Priok Peil) and the southern boundary sits at +10.2 m PP. Additionally, *BH462* was claimed to sit at the highest point, which is +14.8 m PP. However, the information seems to be inaccurate caused by errors in measurement. Two hundred and fifty meters to the south side of *BH186*, the ground level returns to approximately +6.4 m PP. According to the Regional Disaster Management Agency, *Jalan Hayam Wuruk* is located in between two contour lines, which signifies the absence significance elevation difference. Considering that the whole city is located on a flat plain, the altitude of these boreholes can be estimated with linear interpolation and they are presented in Table 4.2.

Table 4.2: Elevations of considered boreholes

ID	Elevation (+m PP)
<i>BH88</i>	5.30
<i>BH58</i>	5.60
<i>BH462</i>	6.06
<i>BH186</i>	6.21

The study used four out of five boreholes, presented before. The omission of *BH99* is based on graphical observation, in which *BH99* causes local and abrupt disruption to the continuity of the soil profile. As the local distortion is rather insignificant compared to the total length of the selected segment, the omission of *BH99* is justified.

4.3.1 Overall Observation

The SPT investigated at least 25.5-meters of soil column and returned the minimum of 18 increments per borehole. As the investigations were conducted by multiple contractors, the incremental length varies from 1.5 to 2 meters. The simplification of soil stratigraphy yielded at least 5 layers, and 7 at most, with different properties. Then, The SPT result is plotted based on its location to devise a spatial pattern. The spatial pattern shows the continuity or discontinuity of soil layers along the selected segment.

The first soil layer is on average 6 meters thick, ranging from the first 4.5 to 11-meter depth. This clay layer has an average N-SPT of 4 blow counts, thus can be considered as compressible soil, and was identified in all four investigation sites. Observing these boreholes spatially, the thickness of this layer decreases towards the southward direction.

The second soil layer extends for 3 meters on average reaching the depth of 9 to 14 meter. The second layer showed more strength than the first layer with N-SPT value averaging on 12 blow counts. No spatial pattern can be recognized pertaining to its thickness. Nevertheless, the second layer was found to be thinnest at *BH58* and deepest at *BH462*.

From 4 out of 5 SPT results, the third layer was situated at 12 to 14 meters below the ground surface. The thickness of the third layer grows larger towards the southward direction with the average of 3.4 meters. This layer is even stiffer than the first two layers with an average N-SPT value of 22 blow counts.

The fourth layer shows significant difference in stiffness. The fourth layer ranges from 6 to 8 meters in thickness and located at a depth of approximately 14 meters, but it is 4 meters deeper at *BH462*. An average N-SPT of 49 blow count was concluded. Additionally, the field measurement reached the maximum value of 50 blow counts in all four boreholes. The investigation reports that this layer is predominantly occupied by coarse sand.

Underneath the sand layer, a weaker layer exists. The fifth layer has an average thickness of 6 meters, ranging from the depth of 20 to 30 meter. Thicker layer, roughly 8 meters thick, is apparent on the north side of the selected segment and the thinnest layer is observed at *BH462* with merely 1.5 meters of thickness. The average N-SPT value of this layer is 29 blow counts and classified as clayey silt in most boreholes.

Three SPT results show that stiffer layer is found below the clayey silt layer as the SPT at *BH462* ended at 25.5-meter depth. This sixth layer extends to 40-meter depth in *BH186* and *BH58*, but not in the two others, which are positioned on the north. Maximum N-SPT of 50 blow counts was reached multiple times, which indicates a soil layer with high stiffness.

Only *BH88* reported two additional silt layers underneath the stiff sand layer. The first layer, or the seventh in total, is 2-meters thick and has the average N-SPT of 21 blow counts, while the second silt layer, the eighth, is 4-meters thick and returned 36 blow counts.

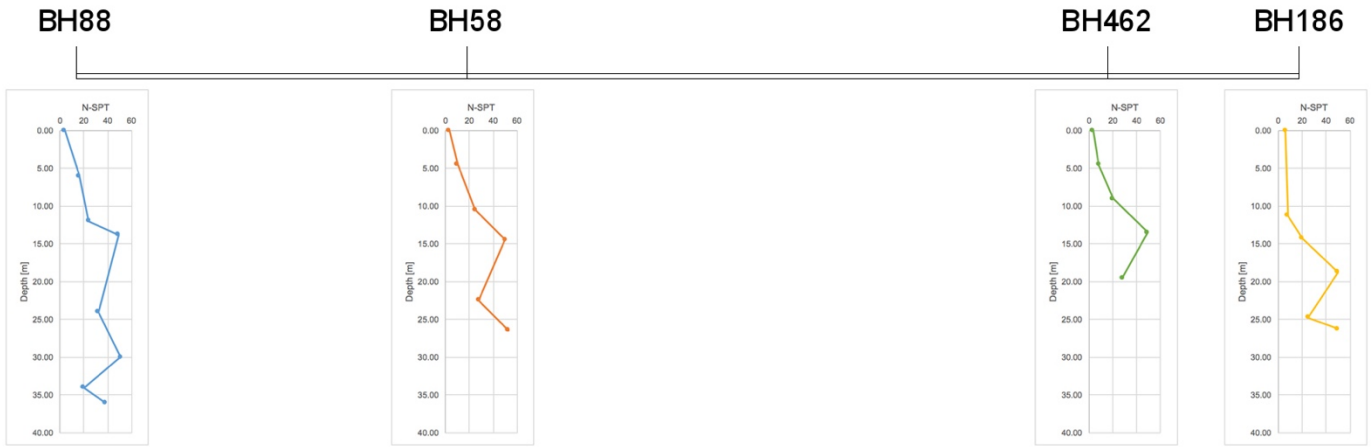


Figure 4.14: Distribution of N-SPT with respect to depth

Figure 4.14 displays the distribution of N-SPT as a function of depth with the average N-SPT for each layer. The graphical observation shows an agreement between the four boreholes, where compressible soil is evident at the first 10-meters of depth. As it goes deeper, the soil layers are found to be stiffer. The complete SPT results is presented in Appendix A.1.1.

4.3.2 N-SPT Corrections

Little information could be found about the common adaptation of SPT method in Indonesia as the procedures of SPT are often undocumented. In order to apply reasonable corrections for the field measurement, the method and the type of instrument must be assumed based on earlier studies.

Using the SPT results on Jakarta soil, Vidayanti (2013) performed corrections with the setup as follows:

1. Borehole diameter is within the range of 60 – 120 mm, thus $\eta_B = 1.00$.
2. Automatic trip hammer is used, $\eta_H = 72\%$ is prescribed.
3. Length of the rod is 6 to 10 meters, thus $\eta_R = 0.95$.
4. Standard sampler is used, which resulted $\eta_S = 1.00$.

Implementing the correction factors into the formula presented in Appendix A.1.2 yields the accumulated correction factor according to Youd and Idriss (2001).

$$N_{60} = N \frac{\eta_H \eta_B \eta_S \eta_R}{60} = N \frac{72 \cdot 1 \cdot 1 \cdot 0.95}{60} = 1.14 N$$

$$N_{1(60)} = \frac{2.2 N_{60}}{(1.2 + 0.01 \sigma'_0)}$$

Combining the two equations, following equation must be valid. On a side note, the post-corrections values must be brought to the nearest integer.

$$N_{1(60)} = \frac{2.51 N_{60}}{(1.2 + 0.01 \sigma'_0)}$$

4.3.3 Simplified Soil Types

After the corrections, the three-dimensional soil profile must be simplified to limit the computation cost of the numerical analysis. Soil layers were categorized based on the characteristics, depicted by the $N_{1(60)}$, and the field classifications provided on the SPT report. As a result, six material types, comprised of two types of clay, two types of silt, and two types of sand, were generated and presented in Table 4.3.

Table 4.3: Soil types for the numerical analysis

Soil Type	Classification	$N_{1(60)}$
C1	Soft Clay	4
C2	Hard Clay	12
Si1	Hard Silt	20
Si2	Soft Silt	10
SA1	Dense Sand	40
SA2	Loose Sand	25

The average value of $N_{1(60)}$ from a continuous layer of the same material classification, e.g. soft clay, over the four boreholes was assumed to be sufficient in describing the strength and elasticity characteristic. The simplified soil profile for the selected segment is shown below.

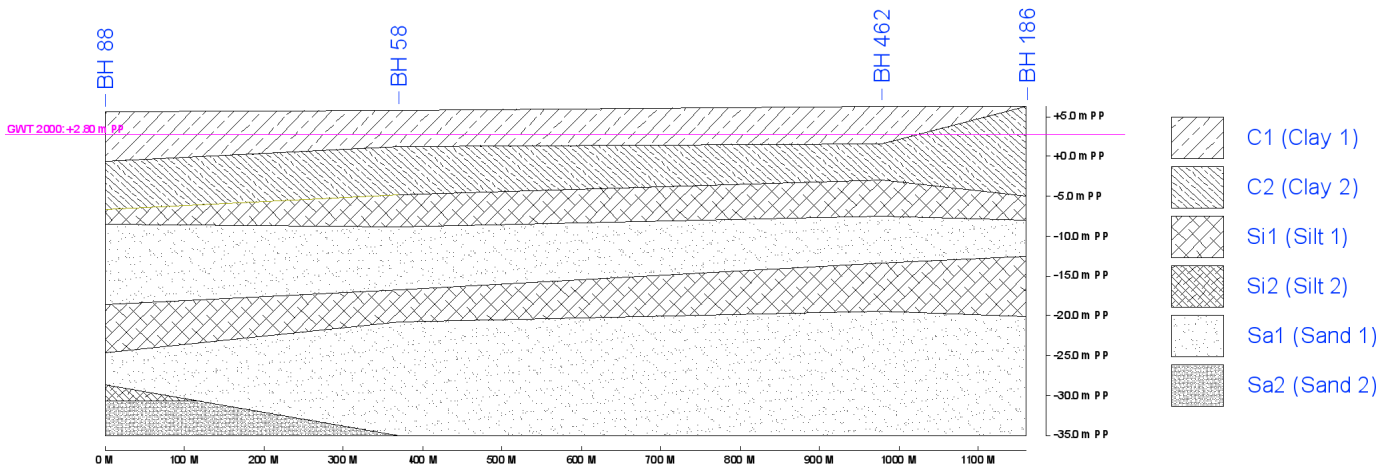


Figure 4.15: Simplified soil profile

As these soil types are the results of aggregation based on property similarities, the fact that there are still two types of clay means that despite they share the same classification, they do not share the same strength or elasticity characteristics which is reflected by the N-SPT values. Five of the six layers are consistently appear in all five considered boreholes and the remaining one layer is only evident at the northern boundary of the tunnel segment. The unprocessed SPT data is presented in Appendix A.1.1.

4.4 SPT Correlations

4.4.1 SPT to Elasticity Moduli

Given the SPT being the most popular soil investigation method locally, correlations between physical properties and mechanical properties of soil are crucial in soil characterization. Hiasinta and Gouw (2012) proposed an empirical link between SPT results with stiffness moduli of Jakarta clayey soil.

Gouw and Hiasinta gathered the soil samples from North and Central Jakarta area, which is within the proximity of NSL-P2 project. The soil samples underwent laboratory investigations, comprised of oedometer, triaxial, pressure-meter, and SPT. The outcome of the investigation includes the oedometer stiffness (E_{oed}), pressure-meter stiffness (E_{PMT}), and triaxial stiffness (E_{50}^{ref}). Next, the stiffness moduli were plotted against the SPT result and statistical method was conducted to establish linear correlations. The results are presented in Figure 4.16.

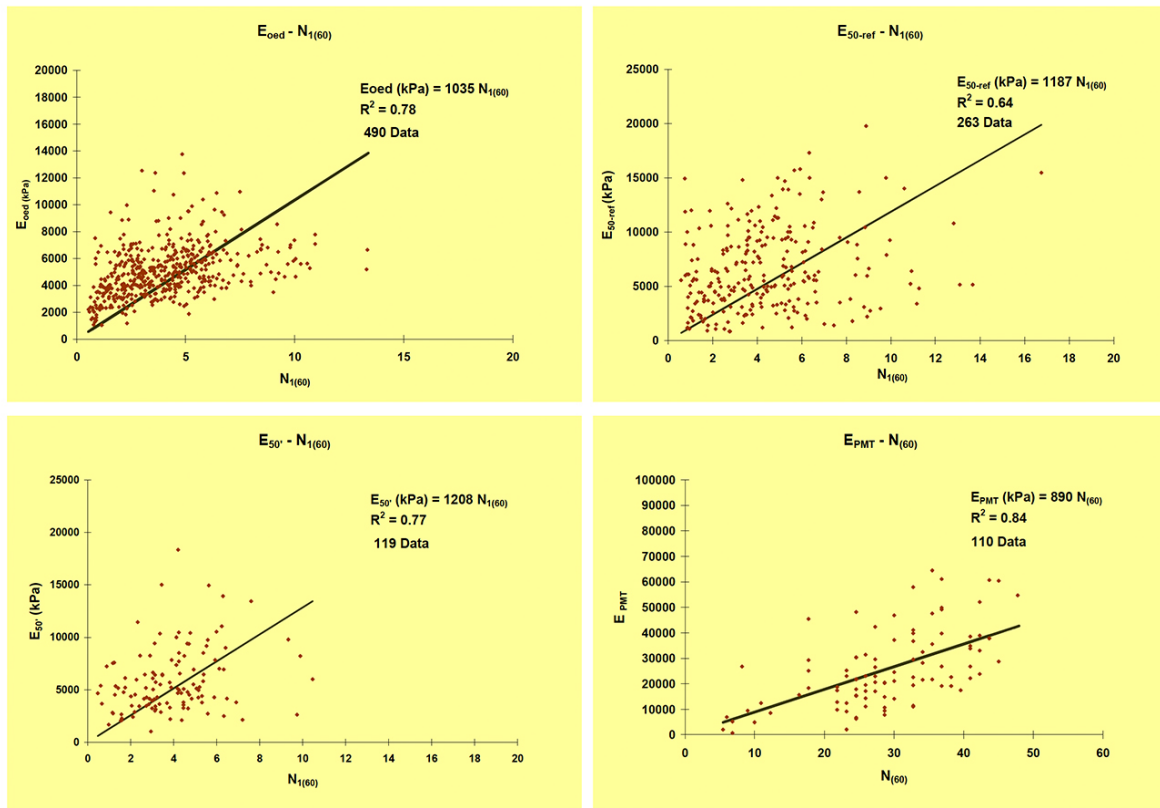


Figure 4.16: Empirical correlation between $N_{1(60)}$ and stiffness moduli (Gouw and Hiasinta, 2012)

Good agreement between the corrected SPT result and E_{PMT} is apparent with R^2 value of 0.84. However, the SPT- E_{PMT} correlation was developed with the least information, 110 data. On the contrary, consistency was also shown in the correlation with most data, SPT- E_{oed} , which yielded lesser but convincing R^2 value of 0.78. The outcome of the investigation is used to define the soil parameters for the finite element method in the next stage of this research.

$$E_{oed} (kPa) = 1035 N_{1(60)}$$

$$E_{50}^{ref} (kPa) = [1187 \sim 1208] N_{1(60)}$$

$$E_{PMT} (kPa) = 890 N_{1(60)}$$

The established correlation, presented in Section 2.3.2, uses $N_{(60)}$ instead of $N_{1(60)}$. With the $N_{1(60)}/N_{(60)}$ ratio ranges from 0.47 to 1.33, the agreement between Gouw's and the established range starts at the lower boundary and extends to the intermediate level. Based on the previous finding, Gouw and Hiasinta's correlation is chosen. Additionally, Gouw and Hiasinta's correlations are more relevant to the study site.

4.4.2 SPT to Strength Parameters

Friction Angle

The conversion from SPT to friction angle was performed in the study of NSL-P1 project. In the report, Avanti (2013) presented multiple ranges from various sources for the friction angle of Jakarta clayey soil. A range of 20° to 30° was gathered from a soil investigation in Thamrin, Central Jakarta. Due to similarities with Singapore Marine Clay, the range was narrowed down to 22° to 25° . Furthermore, Irawan and Sukamta (2000) approximated a value of 24° .

Correlation that leads to wider distribution was proposed by Vidayanti, Simatupang, and Silalahi (2013). The correlation was developed for Jakarta soil and in accordance with other established correlations, such as Osaki's (1959) and Japan Road Association's (1990), which are shown below.

$$\varphi' = (20 N_{1(60)})^{0.5} + 15^\circ \quad (\text{Osaki, 1959})$$

$$\varphi' = (15 N_{1(60)})^{0.5} + 15^\circ \quad (\text{Japan Road Association, 1990})$$

Vidayanti et al. used statistical approach to improve the accuracy of the correlation. Hence, it yielded the correlation which exhibits slight deviation from the previous theory in exchange of better representation of local soil properties. The correlation is presented as follow.

$$\varphi' = (13 N_{1(60)})^{0.5} + 15^\circ \quad (\text{Vidayanti et al., 2013})$$

The determination of friction angle derived by Vidayanti is adopted for this study. Compared to the same correlation asserted by Aila, the outcomes from Vidayanti's show better agreement with Avanti's findings. Additionally, Vidayanti's finding is based on established theories.

Shear Capacity

Vidayanti et al. affirmed the agreement between Jakarta soil with Terzaghi-Peck's findings and strongly recommended the adoption of Terzaghi-Peck's correlation. Furthermore, Aila (2014) conducted similar study but included wider range of soil types. The study showed that more deviations transpire as N exceeds 20 blow counts. Thus, the adoption of Terzaghi-Peck's correlation must pay attention to this remark.

For the numerical model, the shear capacity of each soil layer is assigned in accordance with the corridor that was developed by the established as well as the local correlations.

4.5 Consolidation Coefficients

With limited information about the local soil properties, the numerical model is obliged to use assumed values which adhere to the values used in the past studies. An earlier investigation conducted by Avanti (2013) has collected the consolidation coefficients from multiple sources in Central Jakarta. Avanti's finding with necessary additions are summarized on the list below:

1. The C_c , as reported by Affandi, ranges from 0.39 to 0.89. An investigation in Central Jakarta informed a similar C_c range of 0.28 – 0.81. Firmansyah and Sukamta provided a narrower C_c range of 0.19 to 0.37. Additionally, an investigation from *BH462* resulted a range of 0.47 to 0.49.
2. In addition, *BH462* also resulted the reconsolidation or swelling coefficient (C_R or C_S) ranges from 0.029 to 0.055.
3. Bakr (2014) proposed the secondary compaction coefficient (C_α) to fall within 0.005 – 0.03 range for different aquitards in Jakarta. Specifically, Bakr used the coefficient of 0.013 for the shallow aquitard, located not deeper than 59 meters underground.

Considering a typical liquid limit (LL) of 50 to 70%, the reported C_c values are found to be in the right ballpark. Additionally, the reported C_S values are also reasonable. However, a wider range should be accepted.

Moreover, the correlation between N-SPT with m_v is incorporated to justify the consolidation indices assignment. The correlation was developed by Stroud (1974) and explained that m_v is inversely proportional with N_{60} , conveyed in the equation below.

$$m_v = \frac{1}{f_2 N_{60}}$$

where f_2 is a coefficient which is a function of soil's plastic index (PI). The equation provides a clear insight that soil layer with more blow counts tends to be less compressible than the layer with less blow counts, assuming a consistent PI .

For the soft soil layers, the range of $C_c = 0.30 \sim 0.60$ is selected. Considering the location where these samples were taken from, which is directly on top of the selected tunnel segment, these parameters should suffice. The chosen range also falls within other wider ranges presented earlier. The swelling/reloading characteristics of soil should follow the range of $C_S = 0.029 \sim 0.05$. Furthermore, the creep coefficient for all soft soil layers shall fall within 0.02~0.04 range. The range is chosen because it falls under the right category based on Craig and Knappett's classification.

Given the importance of consolidation coefficients to the analysis, the assignment of these parameters are based on the calibration. Additionally, the calibration increases the accuracy of the model. The benchmark of the calibration is the recorded consolidation between 2000 and 2014. In other words, the numerical model must be able to transpire similar consolidation in the calibration period. Furthermore, the calibration is also used to determine the compressibility of the soft soil layers.

The calibration requires iterations. There, the simulated consolidation of each soil profile, defined by the borehole, is monitored and compared with the actual consolidation. Deformation-defining parameters of the soft soil layers were assigned and adjusted in accordance to the ranges until the simulated consolidation matches the actual consolidation. The 2D calibration compared two dewatering rates, $\Delta h = -0.5 \text{ m/year}$ and -1.0 m/year . These rates were assumed to be consistent throughout the 14-year period. Finally, the selected consolidation coefficient, a result of the iterations, should fall within the aforementioned ranges.

4.6 Unit Weight and Void Ratio

Theoretically, the saturated unit weight of Jakarta soft soil should be approximately 14.00 to 21.20 kN/m^3 , recognizing the presence of sand, silt, and clay layers. The actual unit weight of soil was obtained from soil investigations of three boreholes, *BH88*, *BH58*, and *BH186*. The result shows that soil unit weight in Jakarta perfectly concurs with the theoretical range. Figure 4.17 presents the distribution of unit weight with respect to depth. Furthermore, the graph manifests the uniformity between one boreholes and the other, hence it is safe to assume that the distribution is valid for the full length of selected segment. The minimum of 15 kN/m^3 is apparent at the surface and a maximum of 18 kN/m^3 is situated below the 10-meter depth.

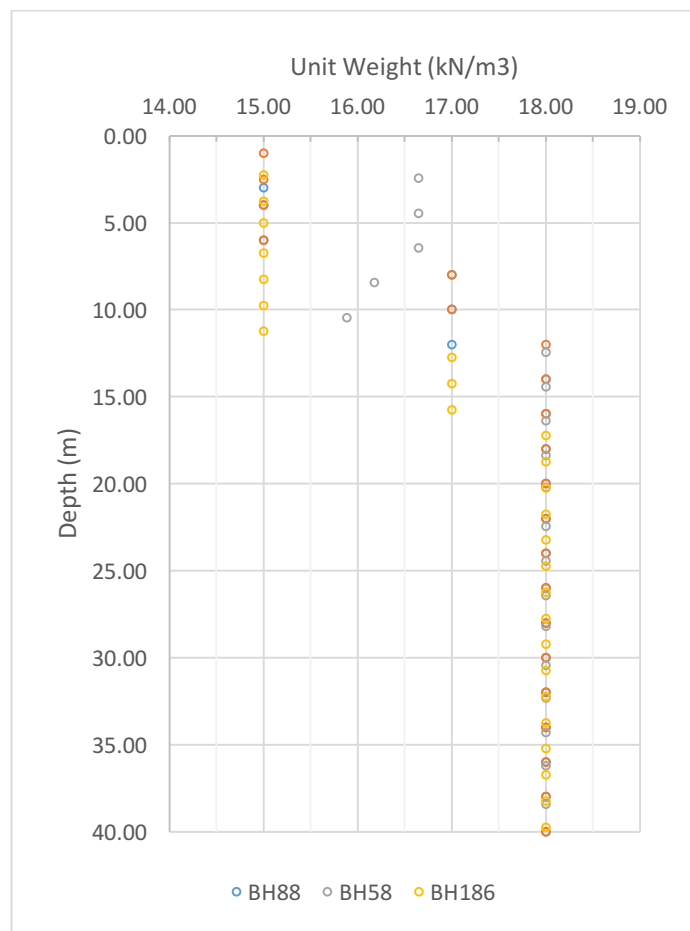


Figure 4.17: Distribution of unit weight with respect to depth

A further soil investigation which contains the void ratio was only performed on *BH462*, shown in Figure 4.18. The report suggested the void ratio increases with depth and stay at the range of 1.32 to 2.22. Other than the five boreholes within the selected tunnels segment, investigation located at the south of the selected segment

returned a value of 1.94 to 2.64 for the void ratio and agreed with the progression as it goes deeper into the soil. However, the investigation was based on shallow soil sample of 3-meter depth.

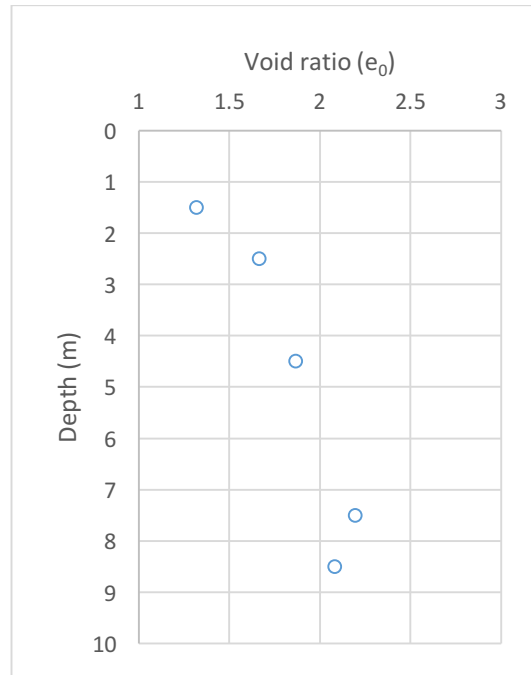


Figure 4.18: Void ratio (e) as a depth function at BH462

Based on the clear trend on the distribution of unit weight with respect to depth, the unit weight of each soil type is assigned accordingly. Furthermore, the initial void ratio of soil element is determined based on the typical void ratio, presented in Table 2.5, but still under the presumption of the trend shown in Figure 4.18.

4.7 Stress History

Geotechnical investigation for the first phase of MRTJ North-South line estimated the OCR with the comparison of maximum and current effective stress based on historical groundwater level. The deepest groundwater table in Jakarta was 14 meters below the surface and thus exerted the largest effective stress (Aila, 2016). Considering the recent flooding events, the current groundwater table was assumed to be at the surface level. The OCR is calculated according to Subchapter 2.1.1 and a profile can be developed as follows.

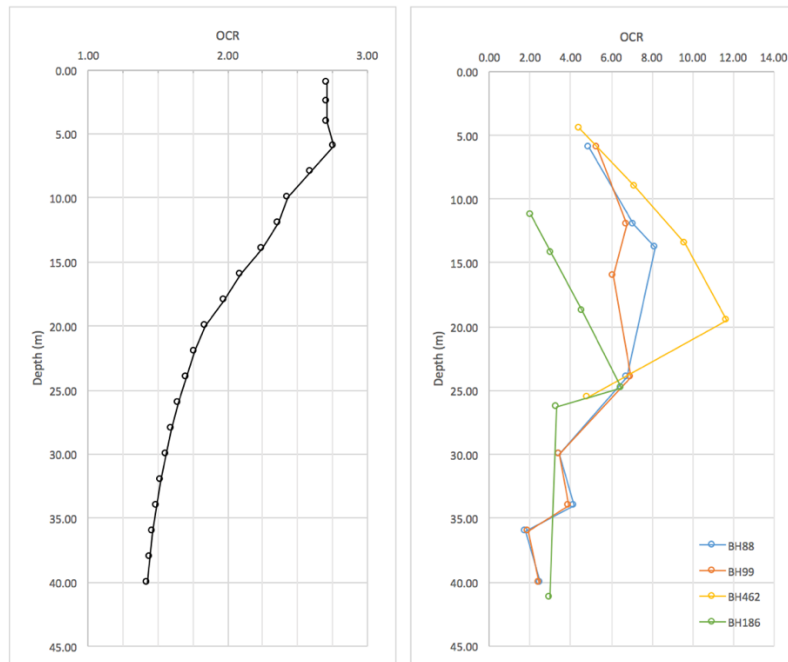


Figure 4.19: The OCR profile as proposed by (Left) Aila and (Right) Mayne and Kemper method

Based on Figure 4.19, the OCR of the study site ranges from 1.42 to the maximum of 2.76. A linear regression fits rightly into the data sets and describes that the OCR decreases in deeper soil layer. The calculation of OCR with the preconsolidation pressure function above yields significantly different result, presented by the the image in the left of Figure 4.19. Nevertheless, it is aligned with the OCR reported by Damoerin (2009), who claimed a range of 2.0 to 8.0 for Jakarta soil.

Furthermore, Mayne and Kamper’s proposal is selected to define the stress history. Aside from its agreement with Darmoein’s finding, Mayne and Kamper used a more robust analysis in developing the OCR profile rather than a comparison of maximum and minimum groundwater level. The average OCR for each soil type is used as the input parameter. The OCR calculation for each borehole with Mayne and Kamper method is provided in Appendix A.1.6.

4.8 Hydraulic Aspects

4.8.1 Head Functions

Changes in groundwater level can be predicted based on current trends. However, if the trend shifts in the future, for instance the implementations of groundwater extraction regulations, the future groundwater level can be far off the predicted level. With that reason, the numerical analysis of this study considers more than one scenario.

Four scenarios were derived from the findings in Section 3.2.3 and considered in the study. These scenarios included several mechanisms, such as slow and rapid drawdown, static level, and groundwater restoration. The scenarios are displayed in Figure 4.20 below.

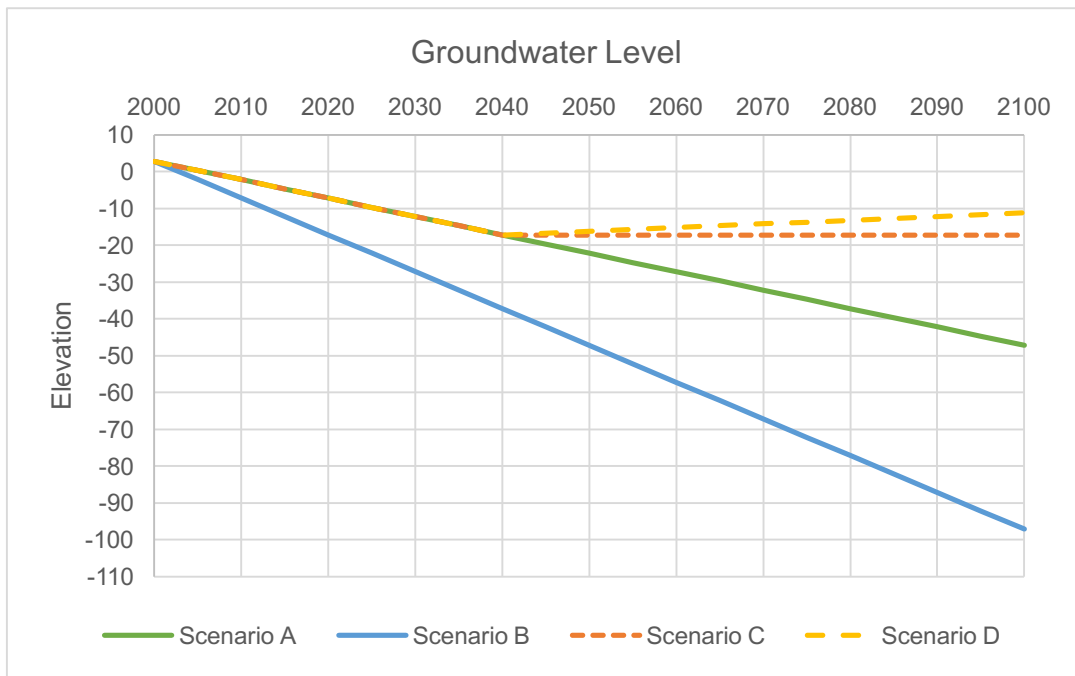


Figure 4.20: Groundwater management scenarios

4.8.2 Permeability

The permeability of clay-silt dominated Jakarta soil profile is considered low, which lengthen the subsidence period as settlement will not occur at an instant (Hoogeveen and van Leeuwen, 1996). Avanti (2013), based on the pumping test results, declared that the permeability of Jakarta soil is approximately on a scale of 10^{-5} to 10^{-7} m/s. Permeability of two order lesser than the average is apparent in silty clay, while higher order is apparent in sandy clay. Avanti's proposal was confirmed by Aila (2016), who conducted the field permeability test for her study. Based on that consideration, the assigned parameters are shown in

Table 4.4.

Table 4.4: Permeability of soil types

Soil Type		Permeability
		[m/day]
Clay 1	C1	0.0085
Clay 2	C2	0.0085
Silt 1	Si1	0.0100
Silt 2	Si2	0.0100
Sand 1	Sa1	0.8500
Sand 2	Sa2	0.8500

4.9 Interface Coefficient

The R_{inter} values used in the analysis are provided in the table below following suggestions from Brinkgreve and Shen (2011). To obtain exaggerated behaviors, the deformation of soil is exaggerated by selecting the minimum value of R_{inter} for each interaction. The coefficients are presented in Table 4.5.

Table 4.5: Interface coefficient used in the numerical model

Interaction	R_{inter} range	R_{inter} used
Sand – Concrete	0.8 – 1.0	0.80
Clay/Silt – Concrete	0.7 – 1.0	0.70

4.10 Structural Aspect

4.10.1 Concrete Material and Capacity

Throughout the analysis, high strength C40 concrete is used as advised in the NSL-P1 technical document. The elasticity modulus of concrete used in the calculation was 31.4 GPa . Referring to the analysis duration, creep effect in concrete must be taken into consideration. Therefore, an elasticity modulus of 13.6 GPa is assigned in the numerical model. The detailed calculation is provided in Appendix A.2.1.

The capacity of concrete under compression is also affected by creep. The maximum allowable compressive stress on concrete is 40.86 MPa . The calculation of the section's bending moment capacity is presented in Appendix A.2.4.

4.10.2 Tunnel Lining and Segmental Joints

Information about the structural features of the tunnel and the segments were provided in the technical design report gathered from MRT Jakarta. On top of that, simple calculations based on the technical drawing were performed when necessary. An example of that is the flexural stiffness of the tunnel segment.

The tunnel segment and its reinforcement is depicted in Figure 4.21. The 300-mm thick profile is reinforced with 12 D16 and 8 D19 bars. Departing from that information, the longitudinal bending stiffness (EI_L) of the segment is $4.6 \cdot 10^4 \text{ kNm}^2$. In the other direction, the segment is reinforced with 28 D13 bars and to simplify the simulation, it is assumed to be very rigid.

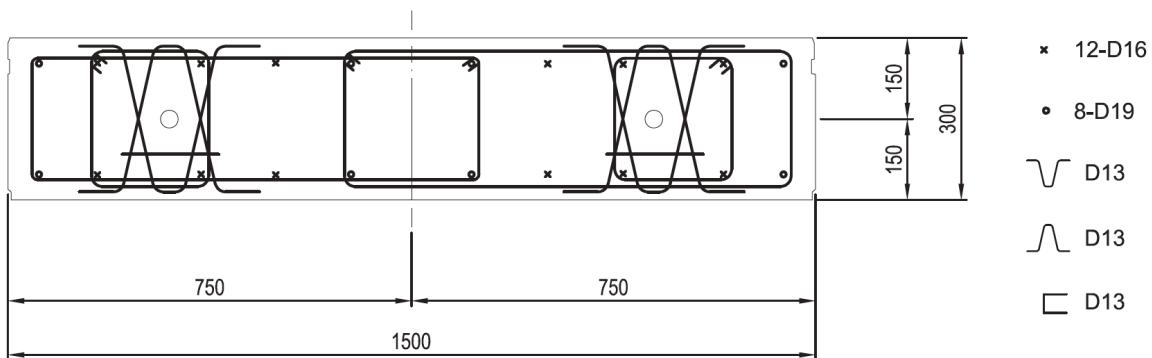


Figure 4.21: Typical reinforcement of tunnel segment (MRT Jakarta, 2015)

As presented in Section 2.5.6, the spring approach is selected to model the segmental joints. The determination of spring stiffness for the segmental joints involved two theories, Lee et al.'s and Blom's. Mentioned before, Lee et al. suggested a reduction factor λ which value is constant and ranges between 0.03 to 0.3. On the contrary, Blom introduced a more accurate method that includes concrete's bilinearity to determine the spring stiffness.

At first, Lee et al.'s method seemed to suitable for the analysis as Plaxis can only recognize a constant value of spring stiffness for the tunnel. However, a representative value of λ must be selected. Therefore, an analysis of joint stiffness based on Blom's theory was performed and presented to a greater detail in Appendix A.2.3. The analysis returned a spring stiffness ranges from $4 \cdot 10^3 \text{ kNm/rad}$ to $80 \cdot 10^3 \text{ kNm/rad}$ in the first 0.015 rad of rotation. Furthermore, an inversely proportional correlation between spring stiffness was observed. A compromise to the bilinearity was required to align with Plaxis and thus the average of the

aforementioned range was taken. Hence, a value of $14 \cdot 10^3 \text{ kNm/rad}$ was assigned as the spring stiffness. With respect to Lee et al.'s theory, the assigned value of spring stiffness is equivalent to $\lambda = 0.3$, which concurs with the proposed range.

4.10.3 Longitudinal Properties

Aside from the segmental stiffness, tunnel exhibits longitudinal stiffness. As mentioned in Section 2.5.5, the determination of longitudinal stiffness must consider the presence of joints to prevent overestimation. Additionally, it is also important to keep in mind that the tunnel behaves differently towards compression and tension. The technical design report gathered from MRT Jakarta reported an equivalent axial rigidity (EA) of $1.8 \cdot 10^8 \text{ kN/m}$ for compression and $9.2 \cdot 10^5 \text{ kN/m}$ for tension. Additionally, the technical report provides a bending stiffness (EI) of $1.3 \cdot 10^7 \text{ kNm}^2/\text{rad}$.

As mentioned before, 16 units of M27 bolts Grade 8.8 were provided to tie one tunnel ring and the other. Each of the bolts has an area of 459 mm^2 , shearing yield strength of 380 MPa , and allowable tensile stress of 290 MPa . In addition to the bolts, creep of concrete must be incorporated to the determine the equivalent stiffness. Therefore, smaller axial compressive stiffness of $8.17 \cdot 10^7 \text{ kN/m}$ should be assigned. The equivalent beam bending stiffness was recalculated to include the effects of joints and creep which returned a stiffness of $1.14 \cdot 10^8 \text{ kNm}^2/\text{rad}$. Furthermore, Euler-Bernoulli and Timoshenko beam theory were considered in the derivations. However, the inclusion of shear stiffness is expected to be insignificant in the determination of beam displacement as it is mostly governed by soil condition. The complete calculation is provided in Appendix A.2.2.

Despite the apparent discrepancy, the reported bending stiffness, $1.3 \cdot 10^7 \text{ kNm}^2/\text{rad}$, is selected for the initial assessment to display the maximum beam deformation. However, later in the research, the impact of stiffer running tunnel will be discussed.

4.10.4 Tunnel Boring Machine Thrust Force

The technical report suggested the TBM advances with the help of 20 hydraulic jacks. Each hydraulic jack is reported to be able to exert a maximum 200 ton-force ($1.96 \cdot 10^3 \text{ kN}$), which then transferred to the tunnel ring. Therefore, the uniformly distributed areal axial stress on the tunnel ring from the TBM (σ_{TBM}) is calculated with the method below.

$$P_{TBM} := 20 \cdot 200 \text{ ton} \cdot 9.81 \frac{\text{m}}{\text{s}^2} = 3.56 \times 10^4 \cdot \text{kN}$$

$$\text{Area} := \pi \cdot (r_{\text{Out}}^2 - r_{\text{In}}^2) = 5.985 \text{ m}^2$$

$$\sigma_{TBM} := \frac{P_{TBM}}{\text{Area}} = 5.948 \times 10^3 \cdot \text{kPa}$$

Based on interviews with the engineers at MRTJ, approximately only a third of the maximum capacity was exerted during the construction. Therefore, the working TBM force averages around 10^4 kN and it is equivalent to the stress calculation as shown below.

$$P_{\text{Effective}} := 10^4 \text{ kN}$$

$$\sigma_{TBM\text{Effective}} := \frac{P_{\text{Effective}}}{\text{Area}} = 1.671 \times 10^3 \cdot \text{kPa}$$

4.11 Ground Surcharge

As of present, the ground surface is covered by traffic lanes, referred as *Jalan Gajah Mada* and *Jalan Hayam Wuruk*. Therefore, a surcharge of 12 kN/m^2 or 250 lb/ft^2 as prescribed by the International Code Council

(2007). The aforementioned surcharge includes the weight of road pavement and utilities. However, the dynamic load due to traffic is not included nor regarded in this research.

4.12 Proposed Parameters for Numerical Model

The preceding subchapters developed corridors for the parameter assignment. Through trial-and-errors and iterations on Plaxis, the parameters, presented in Table 4.6, are assigned to each soil type. Furthermore, Table 4.6 also outlines the constitutive models that will be used in the numerical analysis, which are: hardening soil (HS) and soft soil creep (SSC). Comparison between assigned parameter with the established ranges are presented in Appendix A.1.7.

Table 4.6: Material properties of numerical model soil types

Soil Type	C1	C2	Si1	Si2	SA1	SA2
Classification	Soft clay	Hard clay	Silt	Silt	Sand	Sand
$N_{1(60)}$	4	12	20	10	40	25
Cons. Model	SSC	SSC	SSC	SSC	HS	HS
γ (kN/m ³)	15	17	18	18	18	18
e_0	2.00	2.30	1.80	1.50	0.50	0.40
OCR	3.50	5.00	5.00	6.00	2.00	2.50
C_u (kN/m ²)	24.0	72.0	120.0	60.0	140.0	87.5
c' (kN/m ²)	10	10	15	12	0.2	0.2
ϕ (°)	22	27	31	26	38	33
C_c	0.60	0.40	0.30	0.50	-	-
C_s	0.08	0.07	0.06	0.07	-	-
C_α	0.05	0.03	0.02	0.02	-	-
E_{50} (kN/m ²)	-	-	-	-	48000	30000
E_{OED} (kN/m ²)	-	-	-	-	41400	25875
E_{PMT} (kN/m ²)	-	-	-	-	35600	22250

Similarly, the material properties of the tunnel structure are summarized in the table below.

Table 4.7: Material properties of tunnel for numerical analysis

Longitudinal Parameters	
$EA_{\text{Compression}}$ (kN)	$8.17 \cdot 10^7$
EA_{Tension} (kN)	$9.2 \cdot 10^5$
EI (kNm ²)	$1.3 \cdot 10^7$
Segmental Parameters	
EA (kN)	$6.14 \cdot 10^6$
EI (kNm ²)	$4.61 \cdot 10^4$
$K\theta$ (kNm/rad)	$1.4 \cdot 10^4$

5. NUMERICAL STUDY DETAILS

5.1 Software

The numerical analysis of this study is performed in Plaxis 2016. Plaxis 2016 is a finite element program that specializes in geotechnical engineering computations, including deformation, groundwater flow, and stability. A structural analysis software, SAP2000, was also used in several instances in the study to complement the numerical analysis built up and outcome.

5.2 Setup and Phasing

5.2.1 Constitutive Models

The assignment of constitutive model to soil elements is motivated by the research interest and expected outcomes as the constitutive model defines the behavior of soil elements in the simulation. Departing from the predominantly soft soil environment in Jakarta, two constitutive models were selected, namely the hardening soil and soft soil creep model. In this section, the motivation behind the assignment is elaborated.

Hardening Soil Model

Hardening soil model is assigned to the sand layers for the numerical analysis. The model is selected because it has the ability to describe the behavior of sand layer with the right amount of details. In other words, the model is able to yield the important outcome for analysis without consuming large computation cost. As asserted in Subchapter 4.5, sand is less susceptible to secondary compression compared to clay or silt layers. Therefore, the creep feature is omitted for the sand layers.

Soft Soil Creep Model

The behavior of clay and silt layers is defined by the soft soil creep model. Unlike the granular soil, creep in clay and silt has significant contribution to the total consolidation. The soft soil creep model is chosen, ahead of soft soil or hardening soil model to accommodate the secondary compression.

5.2.2 Simulation Phases

In general, the simulation is divided into two main periods and one transitional period. The first main period is the aforementioned calibration period and the second main period is the analysis period. As mentioned before, the calibration period starts at the year 2000 and extends to 2014. The calibration period is used to iteratively assign the soil parameters and to ensure that the model works as desired while running the real analysis.

The transitional period comes after the calibration period and extends to the year 2020. At this stage, the consolidation as well as the dewatering process continues. The transitional period ends with the analysis period.

The analysis period included the tunnel into the model and simultaneously disregarded the soil mass that occupied the space before. It extends until 2100, which signifies the end of the analysis. To simulate the decline of ground water level, the analysis period is divided into 16 phases of five-year increments and each time step has its own groundwater level. These timeline is shown in Figure 5.1 below.

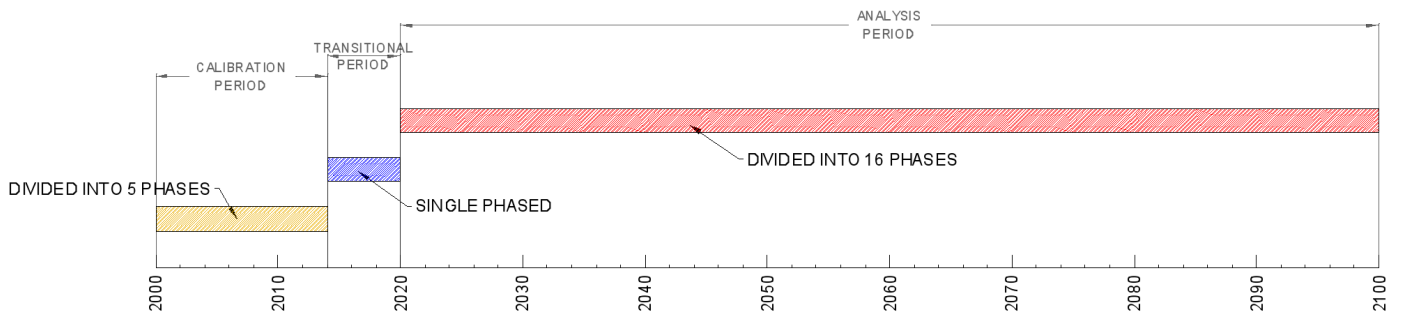


Figure 5.1: Simulation timeline

To comply with the model limitation, the decline of groundwater level is discretely modeled as displayed in the diagram below.

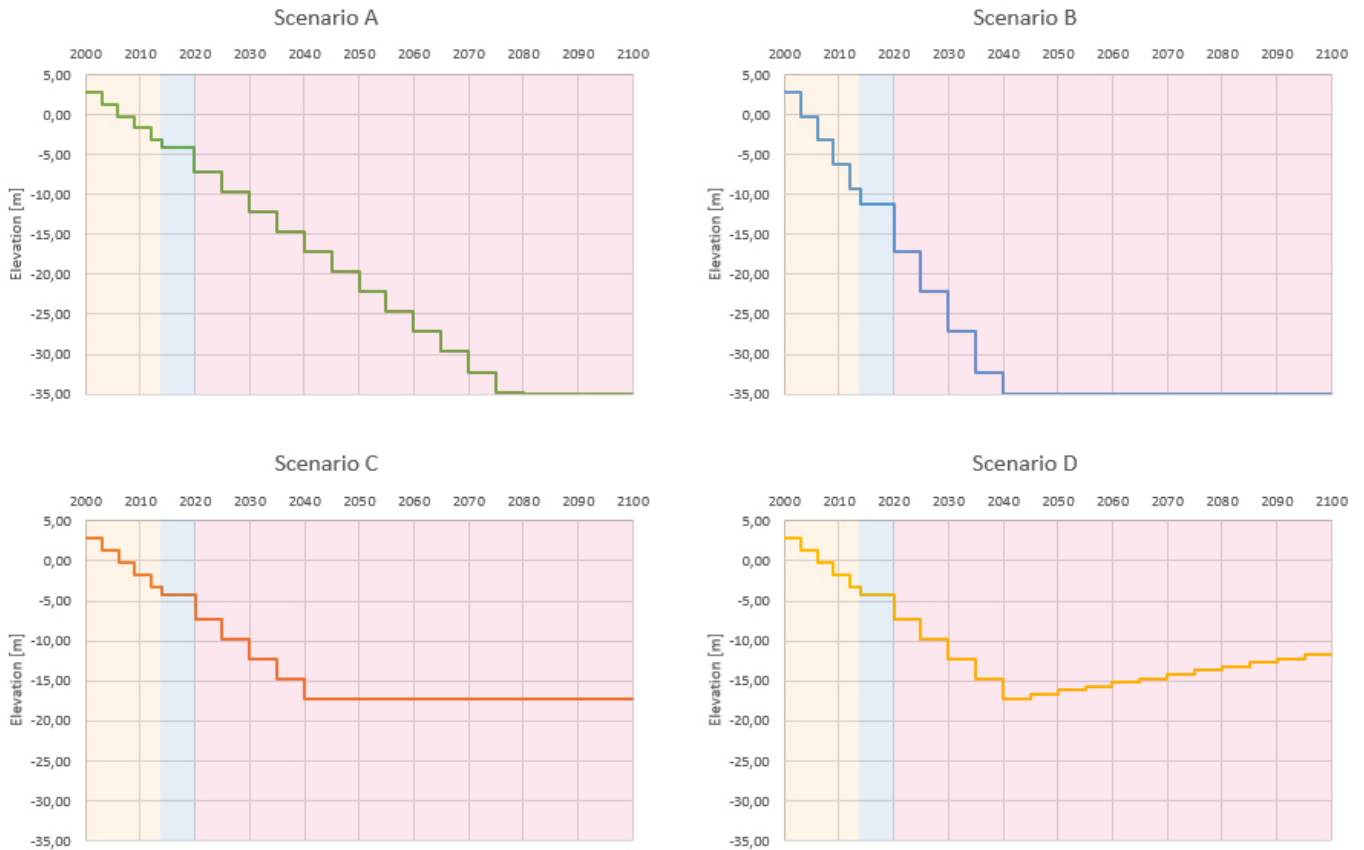


Figure 5.2: Discrete groundwater level scenarios for the numerical model. The yellow, blue, and red colored regions represent the calibration, transition, and analysis period.

5.2.3 Calculation and Loading Type

For all phases, the calculation type is set to consolidation and the loading type is set to staged construction.

5.3 Numerical Model

5.3.1 Structural Model

From the longitudinal point of view, the length of the tunnel is significantly larger to compared to its diameter. Consequentially and as mentioned previously, the tunnel can be modeled as a slender beam which constitutes the actual homogenous stiffness. The beam is embedded at a depth of approximately -10 m PP. Additionally, as much as 0.1 m was taken from each end of the tunnel to avoid the structure being fixedly jointed by the edges of the model.

On the contrary, the tunnel is modeled as a circular frame with connections in the cross sectional point of view. These perspectives are shown in the following sections.

5.3.2 Longitudinal Model

The longitudinal model used in the study is displayed in Figure 5.3 below. The red line in the figure represents the beam equivalent of the tunnel. As shown on the figure, positive and negative interface are assigned on the two sides of the tunnel. On the top of the model, the surface load is depicted by the blue arrows. Further information about the longitudinal model is provided in Appendix E.1 and E.2. Additionally, finer mesh was generated on the soft soil layers.

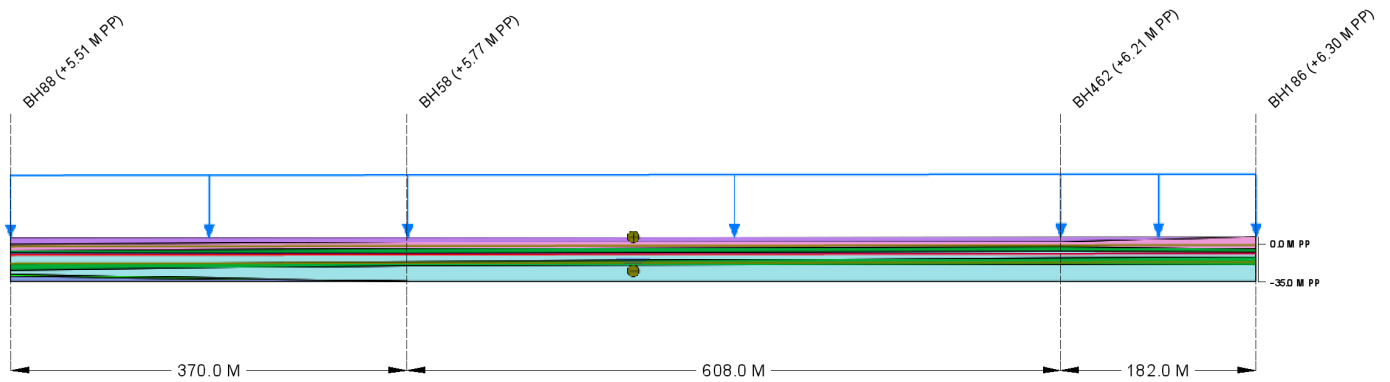


Figure 5.3: Longitudinal 2D model, snapshot at 2030

5.3.3 Cross Sectional Model

The cross sectional numerical model is presented in Figure 5.4 and Figure 5.5. Likewise, a more elaborative drawing of the cross sectional model is provided in Appendix E.3. Likewise, finer mesh was generated on the soft soil layers.

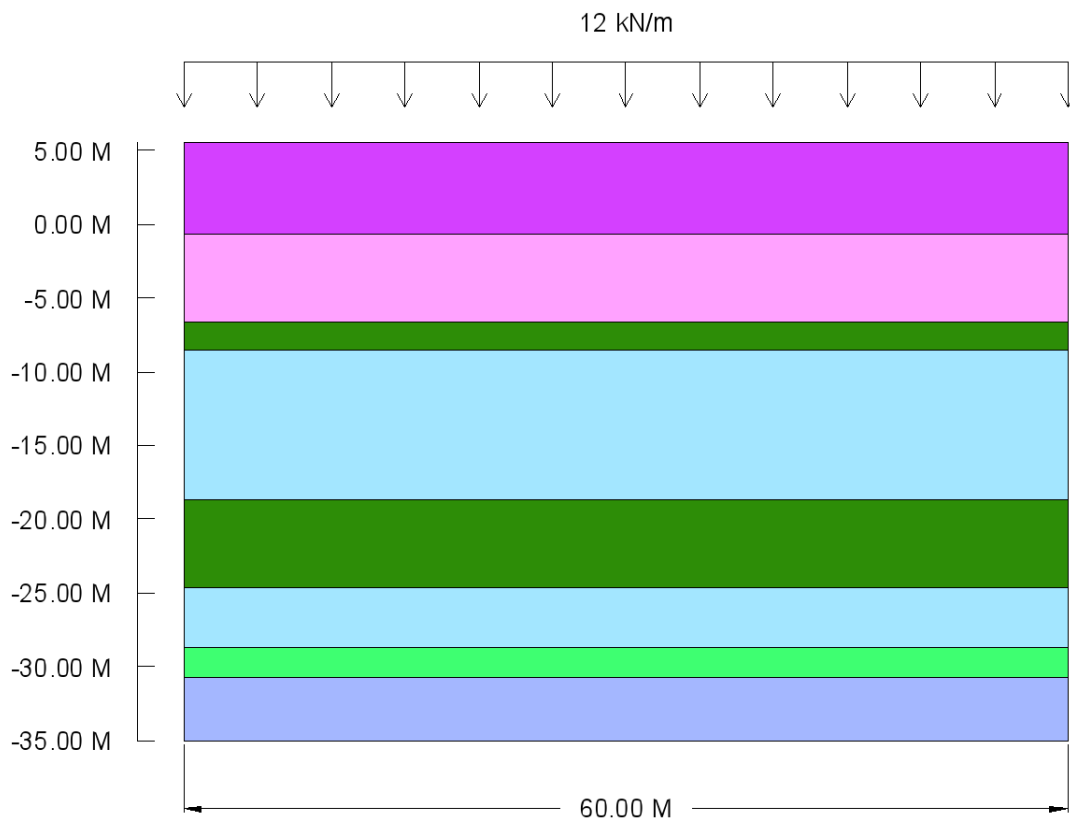


Figure 5.4: Cross section model of BH88

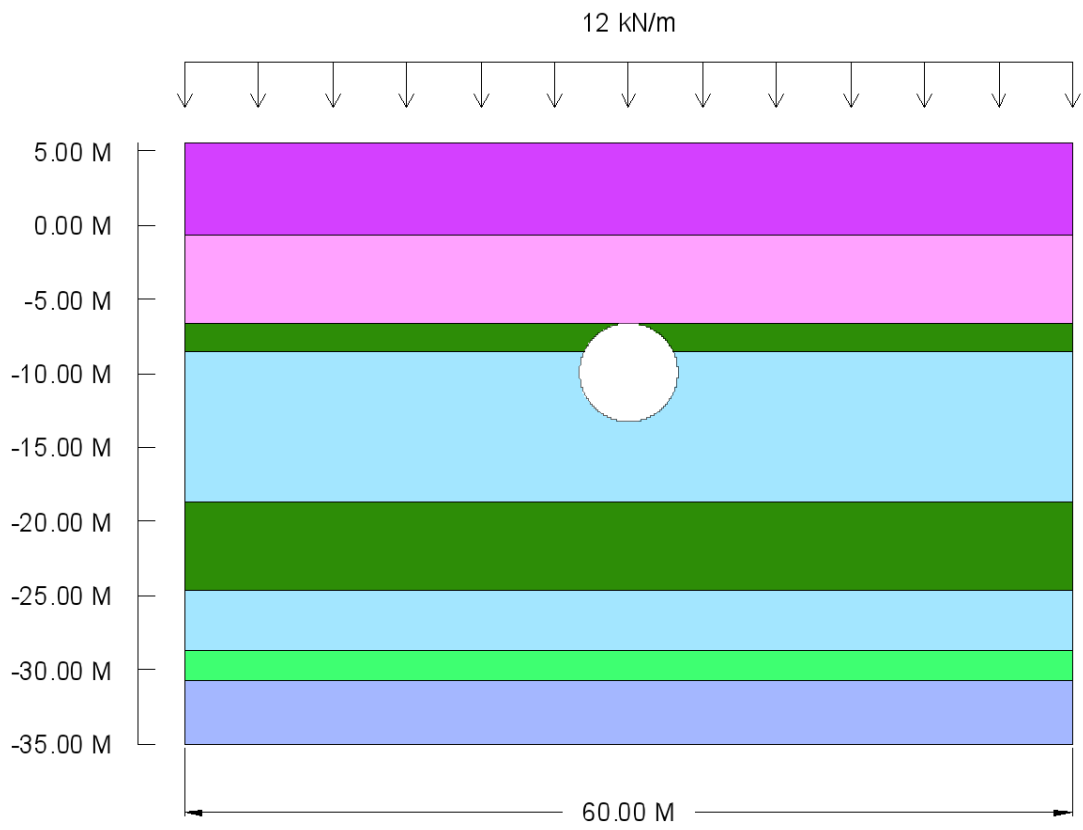


Figure 5.5: Cross section model of BH88 with the tunnel

6. RESULTS AND DISCUSSION

6.1 Forces in Longitudinal Perspective

6.1.1 Vertical Displacement

Similarities in vertical displacement are evident in all four groundwater management scenarios. The most obvious similarity is the position of minimum vertical displacement, which is located at $x = 370\text{ m}$. This vertical displacement is associated with the variety of soil compressibility along the length of the model, with the most compressible and the least compressible soil profile are situated at $x = 0\text{ m}$ and 370 m respectively. The presence of thick sand layer at $x = 370\text{ m}$ reduces the overall compressibility of the soil profile.

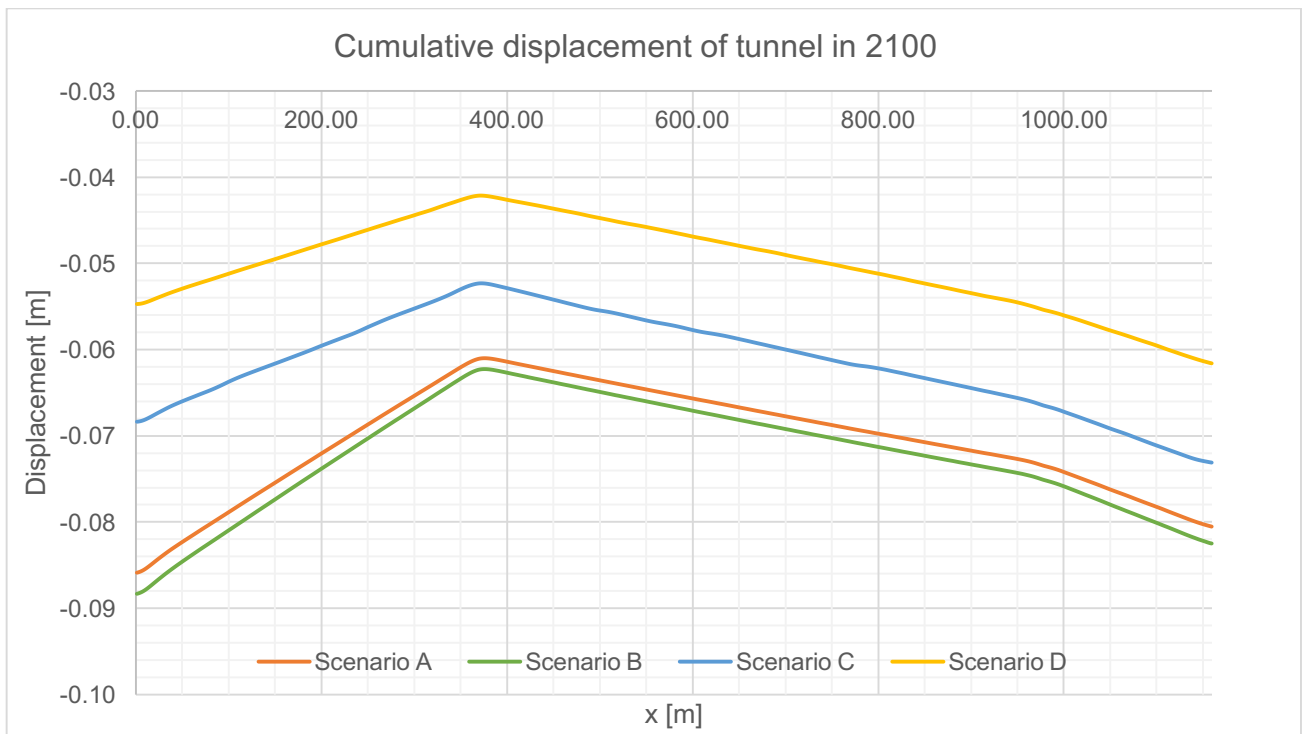


Figure 6.1: Cumulative vertical displacement of tunnel structure in 2100

Additionally, the variation of soil compressibility is responsible for another similarity in the result shown in Figure 6.1. The vertical displacement of tunnel decreased from $x = 0\text{ m}$ to the minimum at $x = 370\text{ m}$ and then increased at a milder rate to the end of the model, $x = 1160\text{ m}$. Figure 6.2 shows that the displacement pattern is in complete agreement with the cumulative thickness of compressible soil underneath the tunnel.

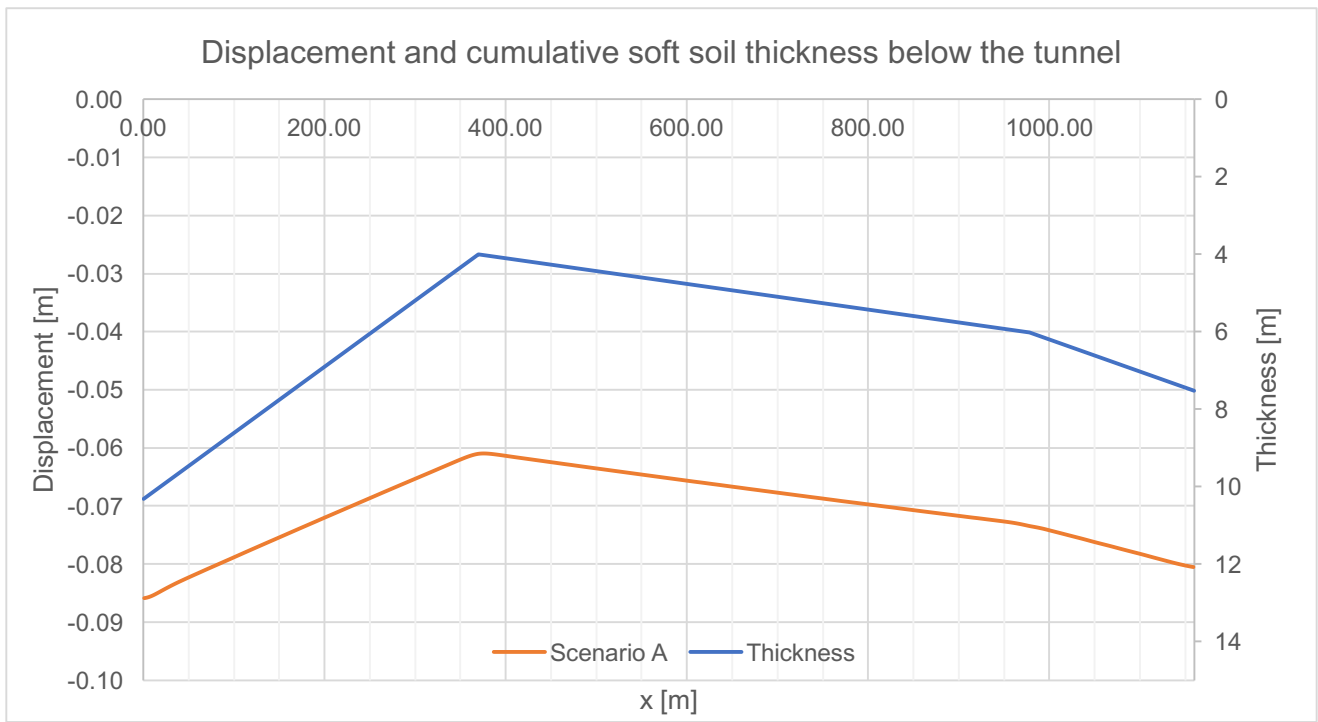


Figure 6.2: The pattern of cumulative displacement compared with the thickness of compressible soil underneath the tunnel

The numerical analysis shows that, for the case of NSL-P2, the vertical displacement of tunnel is not sensitive to the consolidation of the soil over the structure but indeed directly correlated with the consolidation of soil underneath it.

6.1.2 Additional Forces

The uneven vertical displacement is an additional source of shear stress and bending moment. At extreme situations, these additional forces could pose implications on the tunnel. The results of the numerical analysis in terms of additional longitudinal forces are elaborated as follows.

Shear Stress

Figure 6.3 displays the additional shear stress envelope due to inhomogeneous displacement. The maximum additional shear stress is experienced by the tunnel section near BH88, which is caused by the differential deformation close to the borehole.

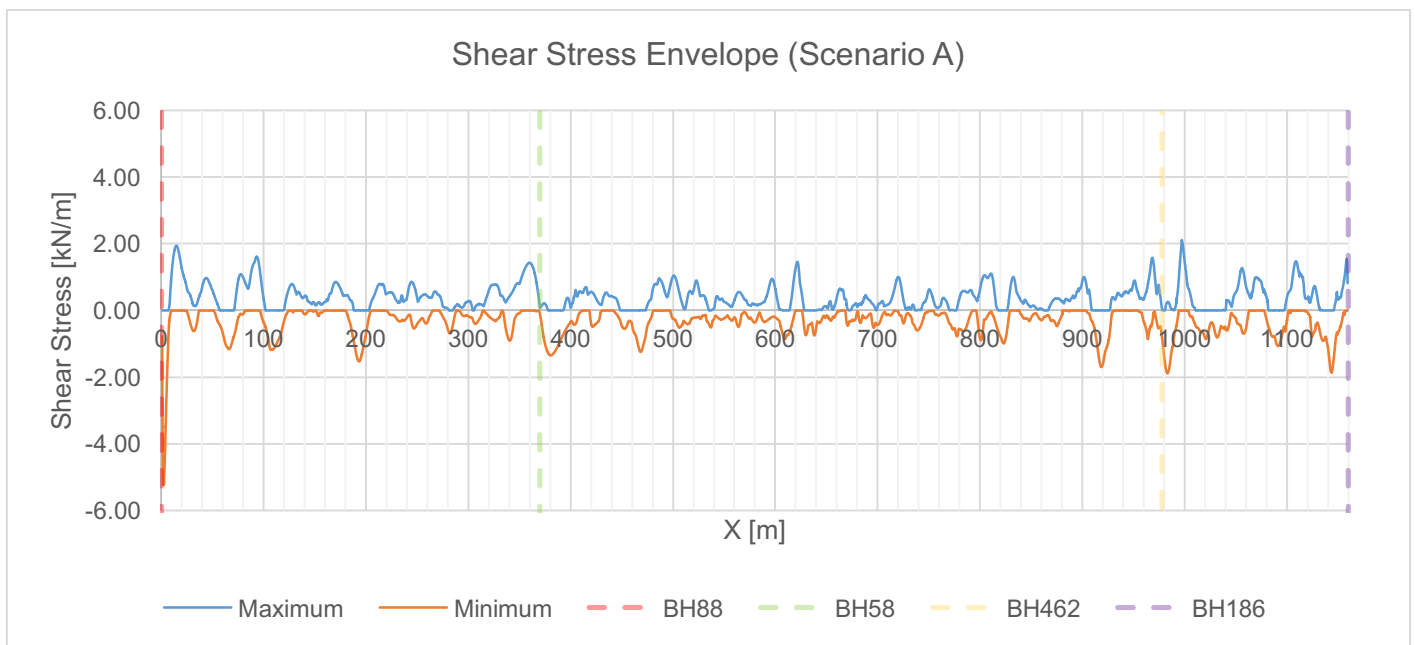


Figure 6.3: Shear force envelope of scenario A in 2100

The additional shear stress due to differential settlement increases in time following the increase in structural displacement. However, the rate of change decreases as it is associated with the consolidation of underlying soft soil, which rate also decreases. The maximum shear stress shown in Figure 6.3 is considerably small compared to the shear capacity of bolt connections. The calculation of related bolt capacity is available in Appendix A.2.5.

Bending Moment

The additional longitudinal bending moment on the structure was derived from the differential displacement of the beam. In all groundwater management scenarios, the maximum bending moment is observed in BH58 ($x = 370\text{ m}$). The largest maximum bending moment is reported in Scenario A, which reached a value of 28.33 kNm/m . A comparison between Scenario A and B shows that the fall of groundwater table below the structure, hence the loss of buoyant force, has a significant impact to the development of bending moment. This finding is also supported with the development of bending moment in Scenario D, in which a decline in bending moment is reported following the rise of groundwater table. The moment envelopes of all four scenarios are presented in Figure 6.4-7.

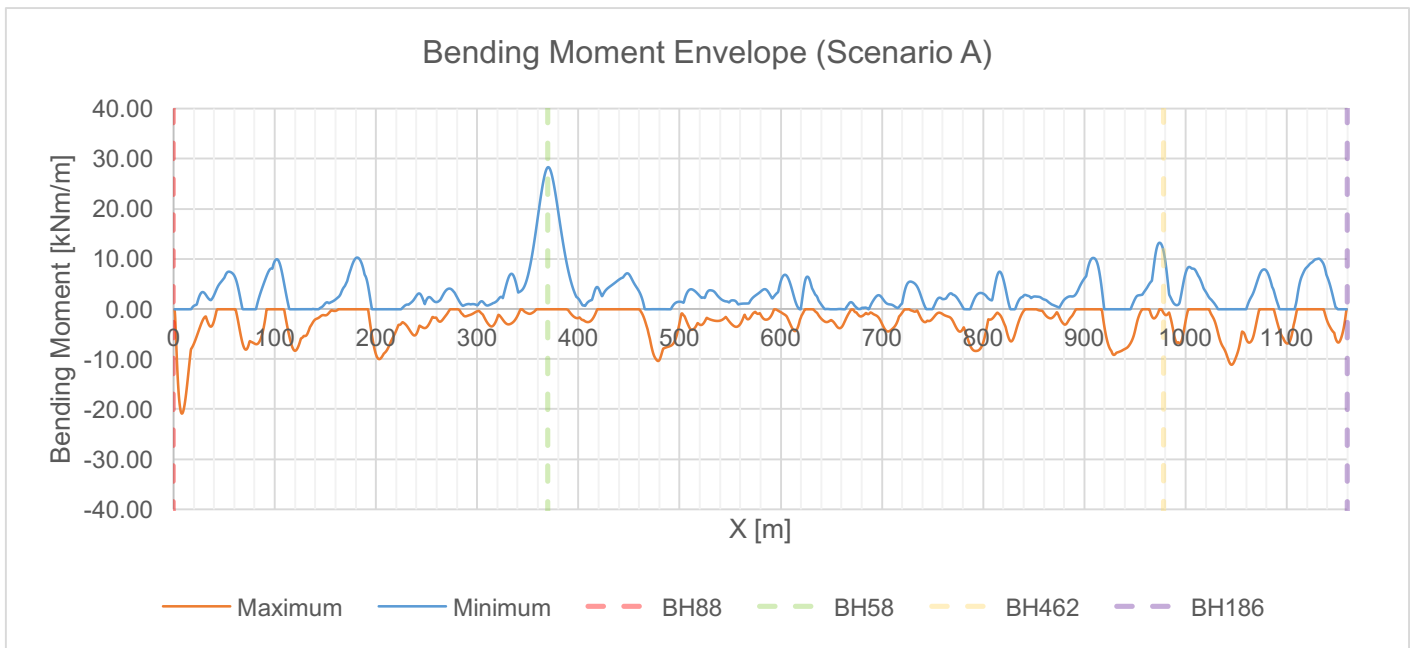


Figure 6.4: Bending moment envelope of scenario A

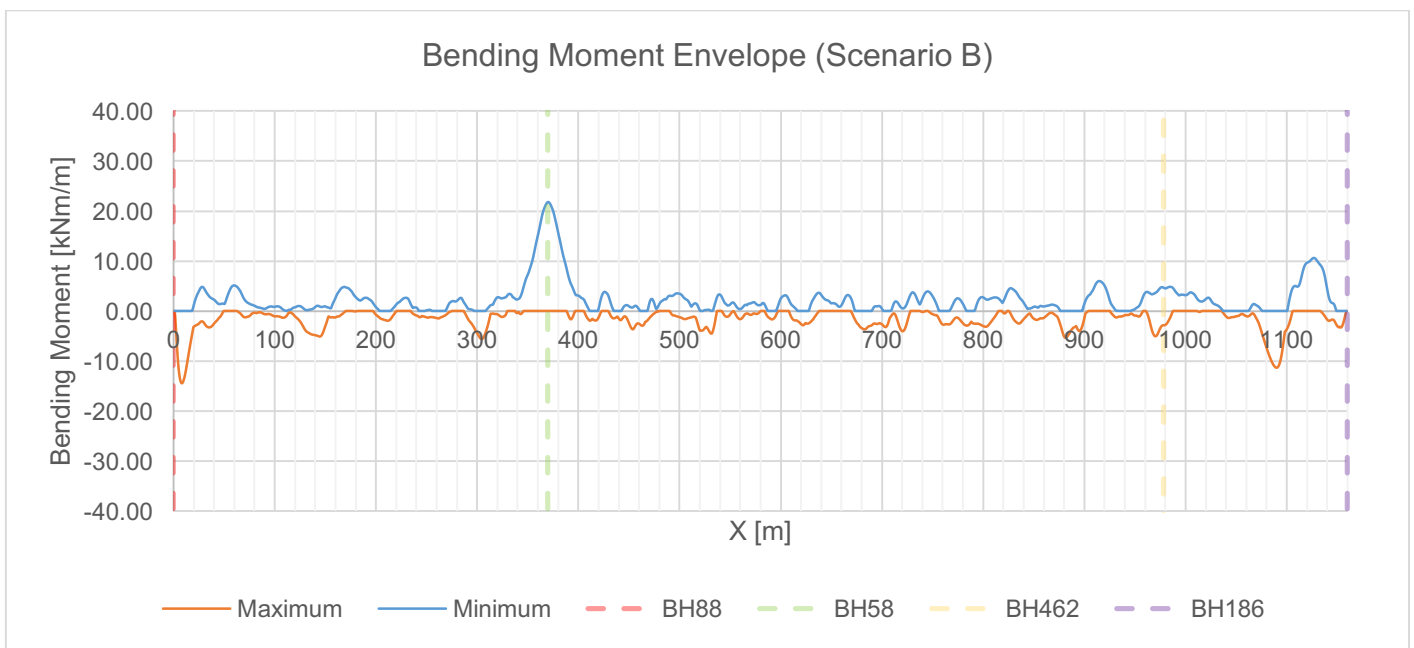


Figure 6.5: Bending moment envelope of scenario B

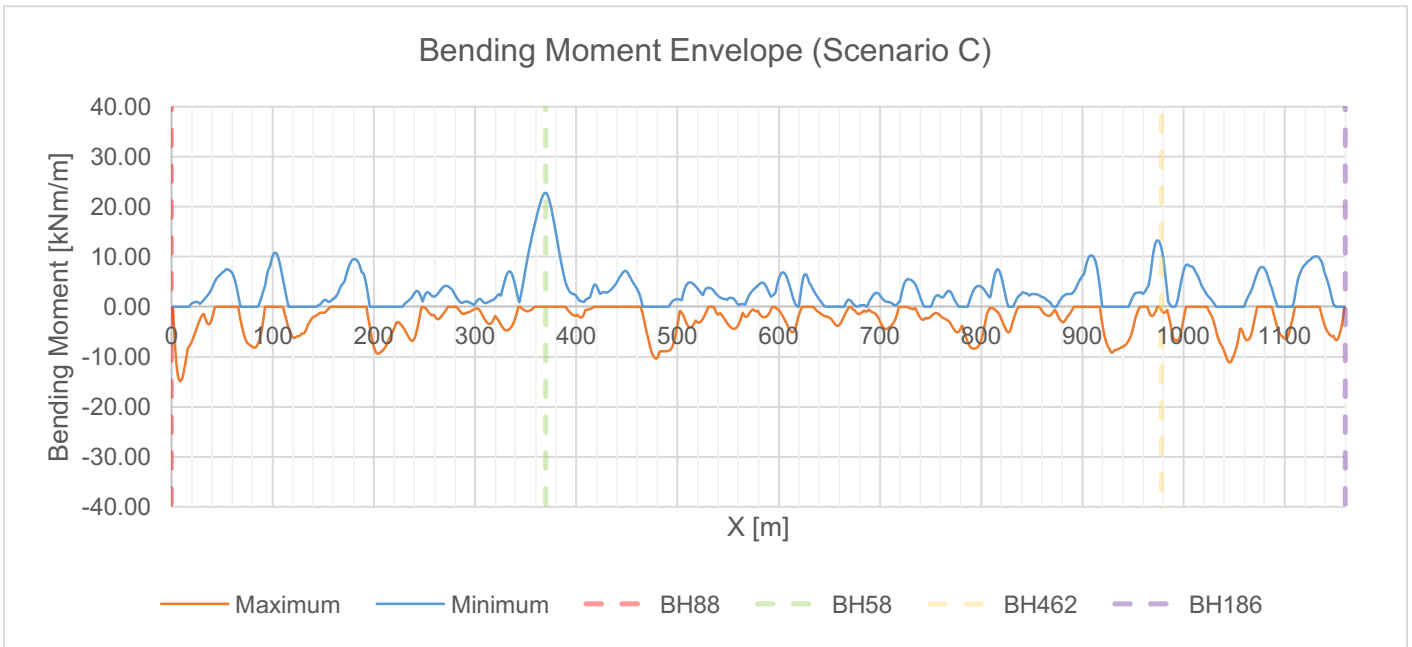


Figure 6.6: Bending moment envelop of scenario C

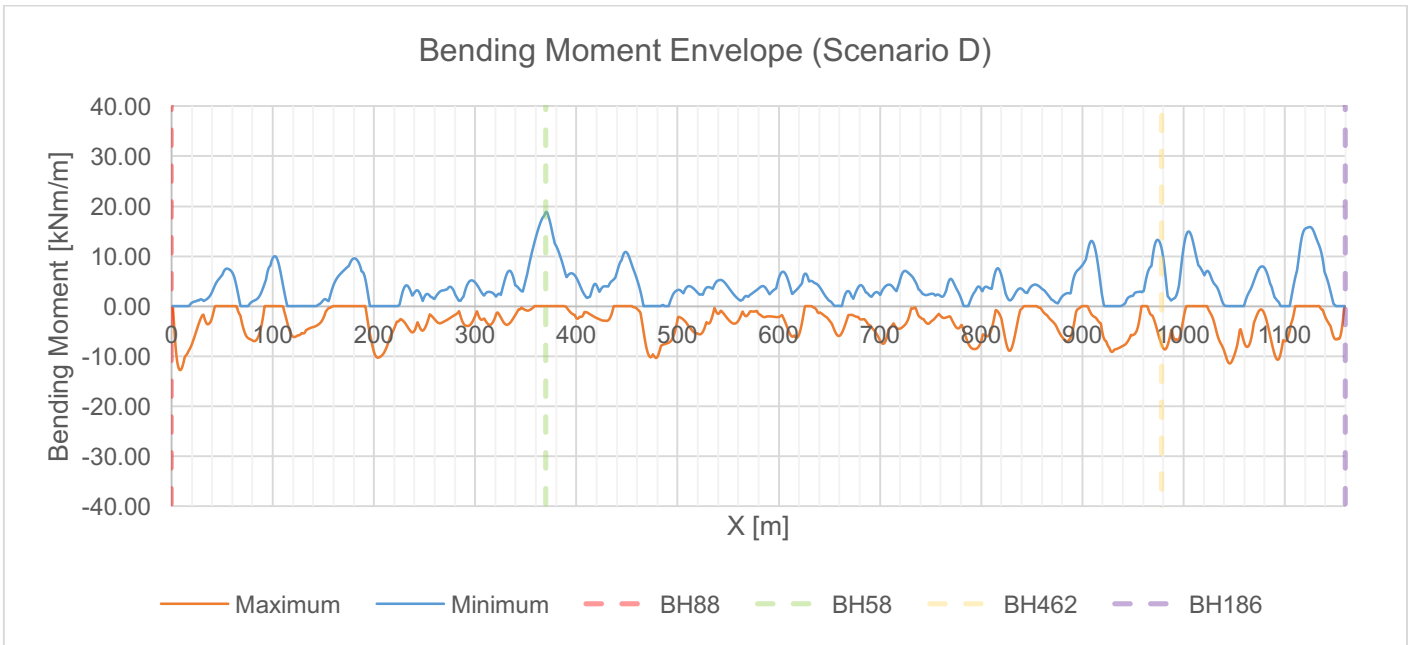


Figure 6.7: Bending moment envelope of scenario D

Unlike in other scenarios, the maximum additional bending moment in Scenario D did not occur at the end of the analysis (2100). In fact, the bending moment at *BH58* in 2100 was reported to be 15.12 *kNm/m*, which is approximately 20% less than the maximum bending moment in Figure 6.7.

The numerical analysis results are aligned with the displacement reported in Section 6.1.1. The maximum additional bending moment is situated at the same position as the obtuse angle at *BH58*. Furthermore, the remaining noises in the diagram along the length of the tunnel is caused by local structural rotation.

The development of extreme longitudinal additional bending moment in time was redacted from the numerical analysis outcome to further learn the influence of groundwater table. Figure 6.8 presents the development of bending moment from scenario A and D. The bending moment of the two scenarios were initially identical in terms of magnitude until 2050, when the groundwater level started to rise. As mentioned before, a decline of bending moment was evident when buoyant force comes into effect. Meanwhile, scenario A shows that the maximum bending moment stabilizes in time as a result of lesser consolidation.

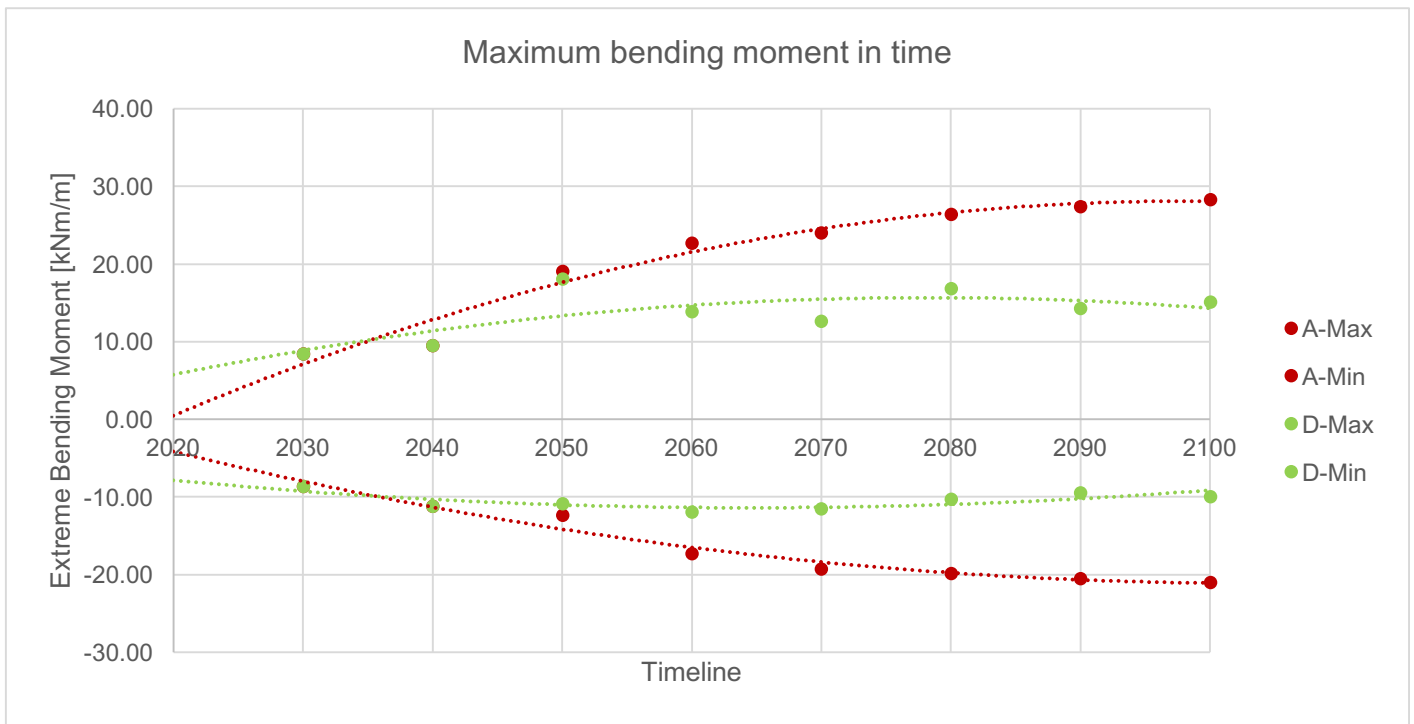


Figure 6.8: Development of maximum bending moment in time

To determine the significance of the additional bending moment, it should be compared with the internal bending moment in the tunnel due to the construction process. However, because of limited information, the Second *Heinenoord* tunnel, mentioned in Section 2.5.7, in the Netherlands is considered as reference. The reported internal bending moment due to the tunneling process of the Second *Heinenoord* and stored in the tunnel is in the order of 10^4 *kNm*, which is nearly 3 orders of magnitude larger than the additional bending moment due to differential settlement. Hence, it can be concluded that the additional bending moment due to differential settlement in NSL-P2 project is not significant.

The maximum bending moment resulted a change of tensile stress by 3.12 *kPa* at the extreme fiber. Furthermore, assuming that the additional tensile stress is acting on the bolt connection, the aforementioned tensile stress is significantly small relative to the bolt tensile capacity. On the other hand, the additional compressive stress, also 3.12 *kPa*, is 4 orders of magnitude smaller than the concrete capacity. Therefore, this finding shows that the additional tensile and compressive stress are unable to provide significant implications to the structure.

The calculation of concrete and bolt capacity can be found in Appendix A.2.4 and A.2.5 respectively.

6.2 Soil and Structural Stresses in the Tunnel Ring

In this sub-chapter, the results of *BH88* is chosen to represent the outcome of the analysis. The selection is motivated by the maximum amount of consolidation occurred in the respective borehole. The change in soil stress in time are presented in Appendix B.3 and B.4.

6.2.1 Progression of Soil Stress

The development of effective soil stress in time is presented in Figure 6.9. In all time intervals, the maximum σ'_{xx} is situated at the two sides of tunnel. Minimum σ'_{xx} is found at the tunnel invert. Furthermore, the maximum σ'_{yy} is located at the tunnel springlines and the minimum is also at the invert. These stresses increase in time but the pattern remains the same. Additionally, this pattern is also observed in other groundwater management scenarios.

The development of vertical soil stress on a slowly drained and rapidly drained environment are directed towards similar end results. However, quicker development of stress is evident in the rapidly drained

environment. Groundwater level stagnation did not affect the progression of soil stress around the tunnel as the groundwater level stays under the tunnel. Finally, as expected, the restoration of groundwater level relieved the stress with buoyancy.

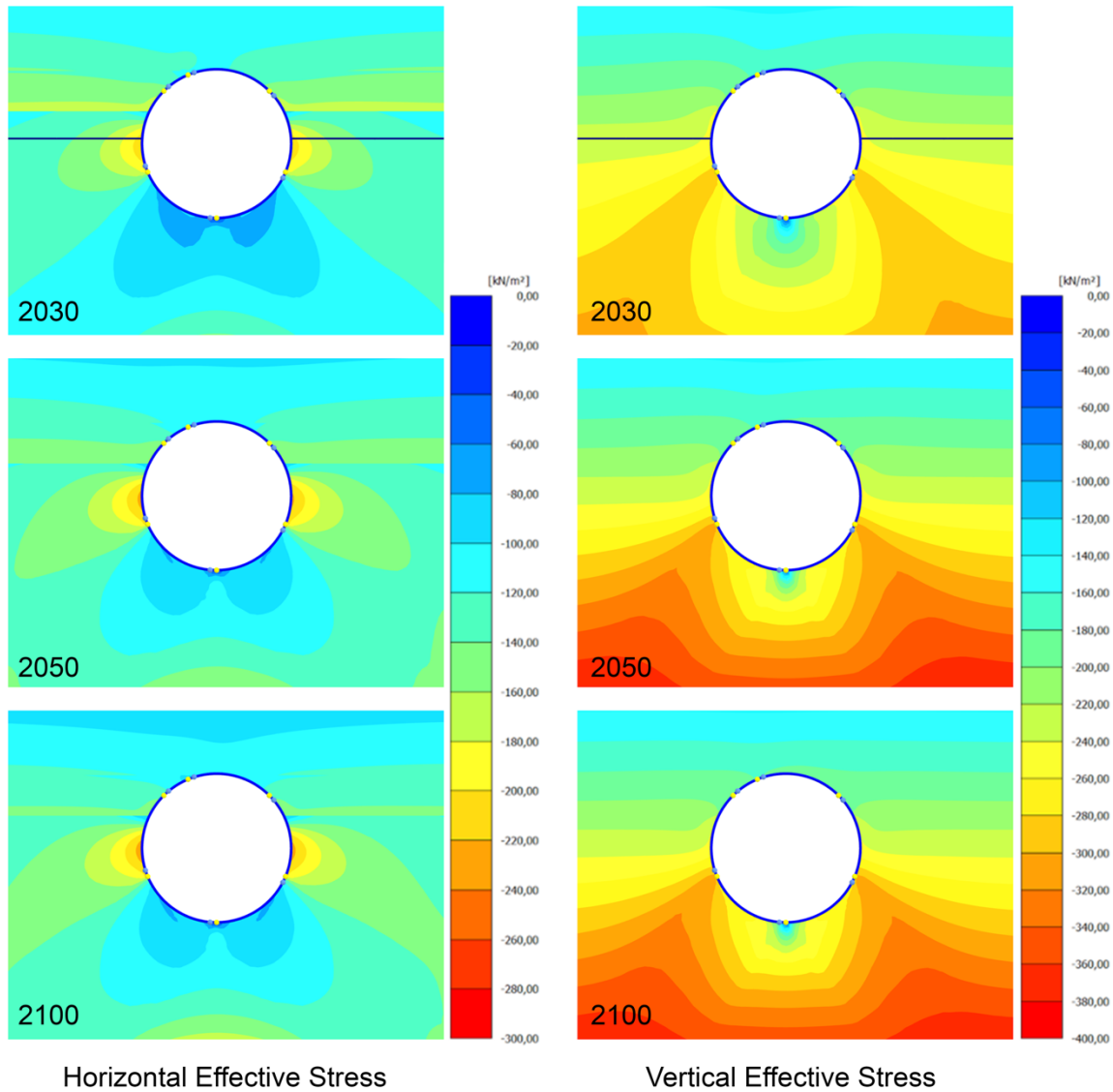


Figure 6.9: (Left) Effective horizontal stress around the structure and (right) effective vertical stress around the structure in time

The increase of stress around the tunnel is caused by the vertical ovalisation of tunnel and the dewatering. The expansion of tunnel horizontal diameter increases σ'_{xx} as it deforms towards the soil. Moreover, as explained in Chapter 2, the loss of groundwater transfers the load into the soil and as a result increase the σ_{xx} . Most alterations of stress occur during the dewatering process and in the absence of groundwater, both vertical and horizontal stress underneath the tunnel structure increases less significantly in time due to the creep in soil and ovalisation. This observation is depicted in Figure 6.10.

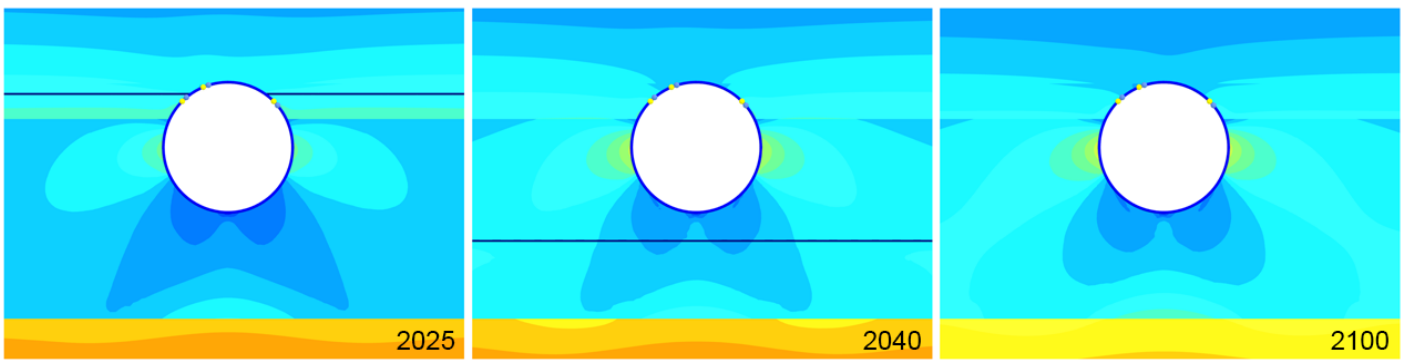


Figure 6.10: Development of effective horizontal stress in time due to (2025-2040) primary and (2040-2100) secondary compression

Furthermore, the hardening and cap points around the structure were identified and displayed in Figure 6.11. The brown points indicate the component of soil that experiences hardening and cap. The green points signify the component of soil that experiences hardening process. Finally, the blue points represent the cap points.

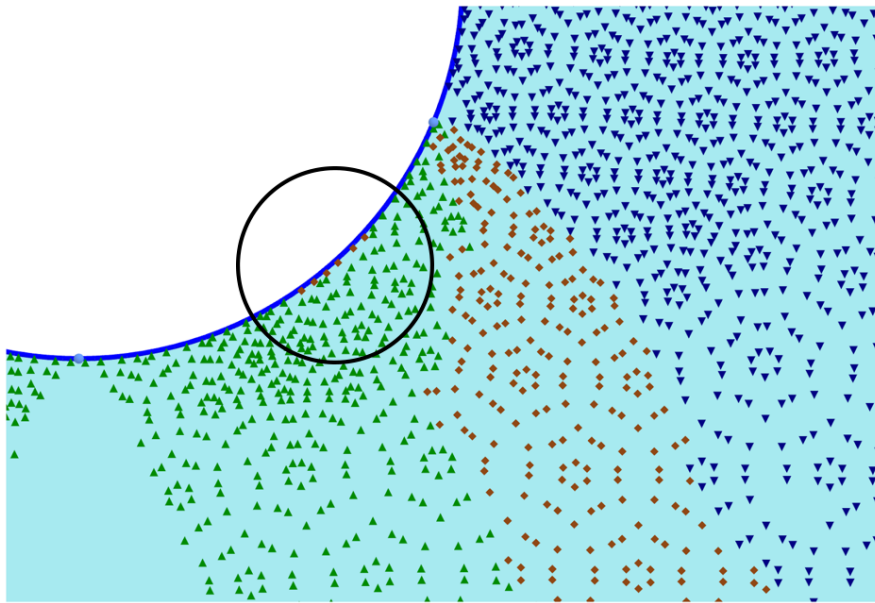


Figure 6.11: Hardening and cap points were observed at the tunnel

Figure 6.11 shows that the stress along the perimeter of the tunnel segments below the springlines are deviatoric. On the other hand, the stress at the springline was more isotropic. The black circle in the figure shows hardening and cap points at the concrete interface and if larger interface coefficient is assigned, the aforementioned points reached failure.

6.2.2 Ring Deformation

Two deformation mechanisms were identified from the numerical analysis, which are vertical translation and vertical ovalisation. The translation reported on the cross sectional perspective agrees with the translation reported on the longitudinal perspective. For this numerical analysis, there is no horizontal shift as the model was made to be symmetrical. The deformation process of the tunnel in time is presented in Figure 6.12 below.

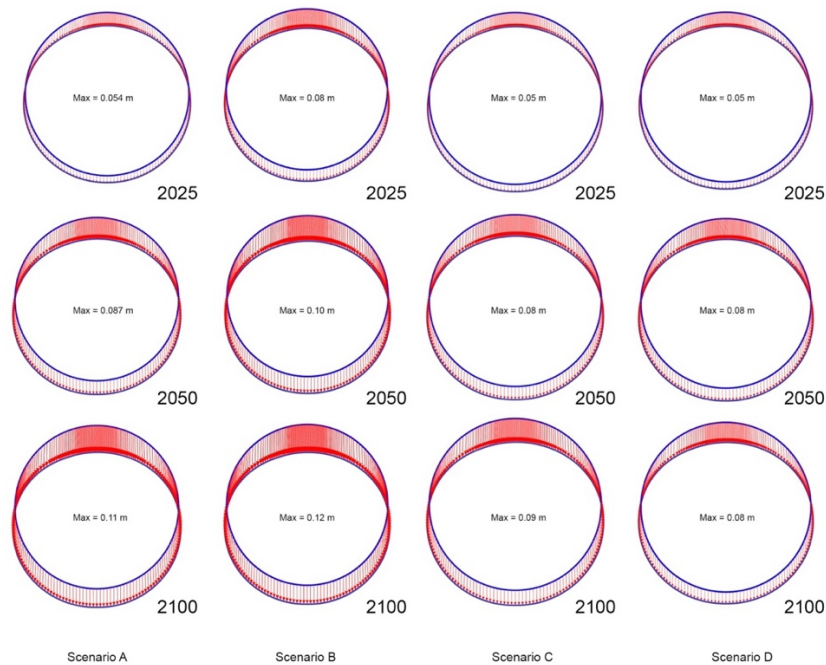


Figure 6.12: Deformation of tunnel ring in time

From the comparison, it can be concluded that the most deformation occurred if the dewatering rate is increased. However, the difference between one scenario with the other is not very significant.

Vertical ovalisation increased the horizontal diameter and reduces the vertical diameter. The change in diameter of tunnel ring at BH88 in time is shown in Figure 6.13 below. As the deviations are very small, a factor of 20 was included to show the deformation. At the end of the analysis, the the increase of horizontal diameter was claimed to be 18 mm and the reduction of vertical diameter to be 34 mm. While in Scenario B, the horizontal diameter increased by 16 mm and the vertical diameter reduced by 37 mm.

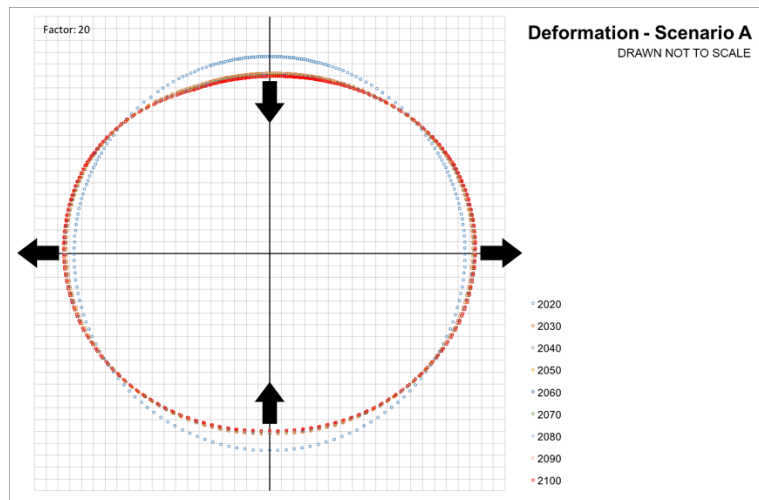


Figure 6.13: Tunnel ring deformation at BH88 in time (Scenario A)

6.2.3 Axial Force at Lining

The development of normal force on the tunnel lining of NSL-P2 in time is shown in Figure 6.14.

Axial Force

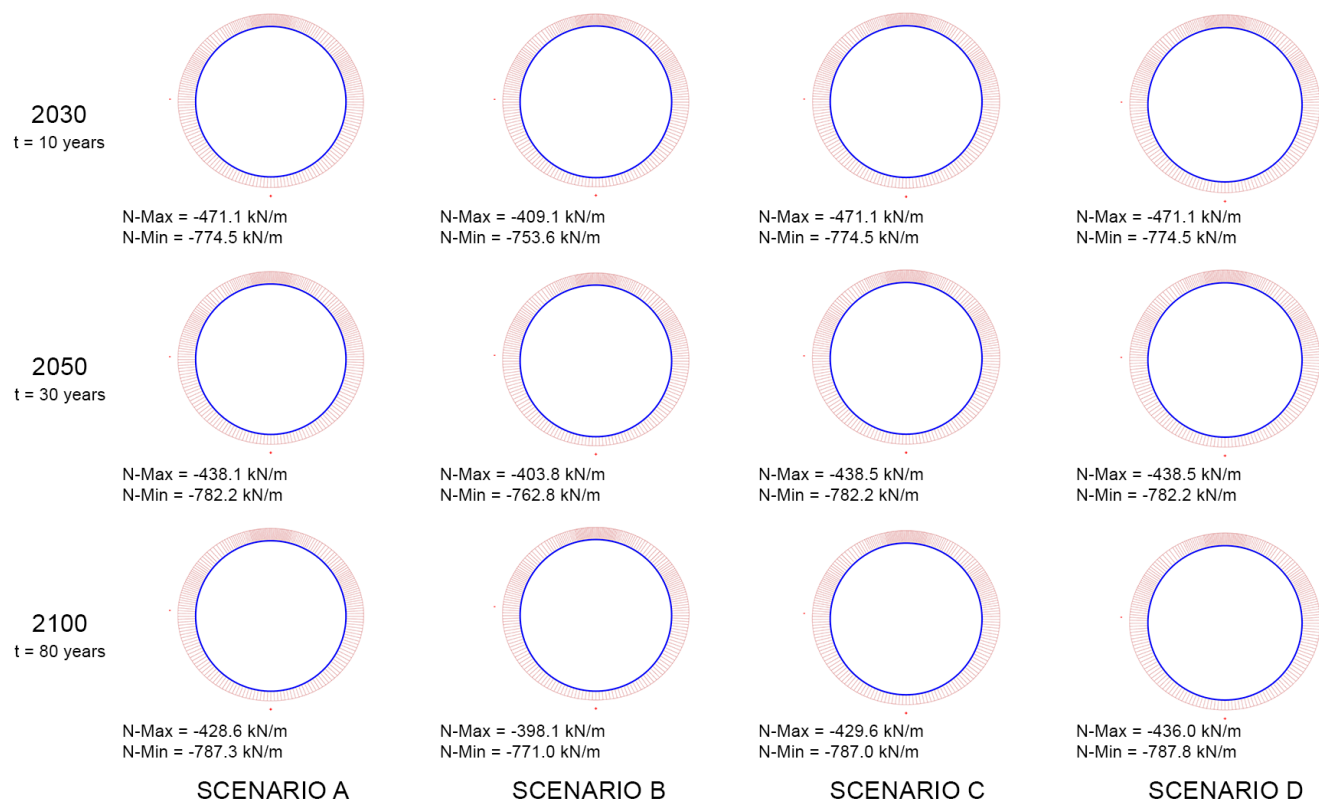


Figure 6.14: Development of axial force on lining in time

In all scenarios, the maximum and minimum axial force are situated at identical angular positions. The maximum is consistently found at the invert, while the minimum at the springline. Throughout the analytical 80-year period, the distribution of axial force along the tunnel ring does not show significant deviations. Due to the ovalisation, the axial force at the crown and invert decreases, while the axial force at the springline increases. The maximum deviation of axial force is as small as 9% in Scenario A.

The presence of groundwater increases the axial force at the tunnel ring as it must withstand not only the effective soil stress, but the total soil stress. Therefore, as portrayed in Scenario D, larger axial force is expected if groundwater level bounces back in the future.

The development of axial force is proportional to change in vertical or horizontal diameter. Compared to Scenario B, greater horizontal deformation in Scenario A, as reported in the previous section, led to greater reduction in axial force at tunnel crown and invert. Similarly, more vertical deformation manifested by the tunnel ring in Scenario B resulted in larger increase in stress at the springlines.

The numerical outcome agrees with the analytical calculation provided in Appendix A.1.5.

6.2.4 Bending Moment

The development of bending moment on the tunnel lining of NSL-P2 in time is presented in Figure 6.15.

Moment Diagram

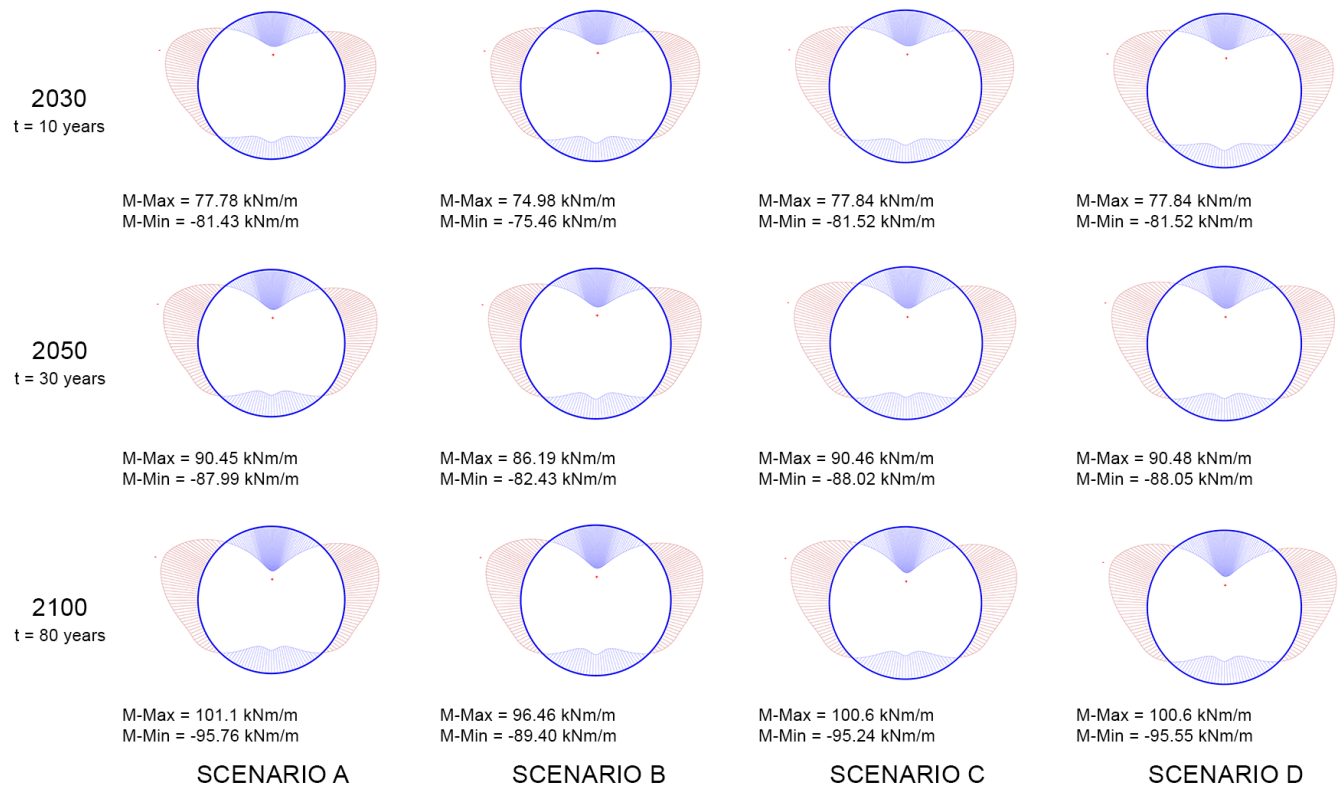


Figure 6.15: Development of bending moment on lining in time

As depicted in Figure 6.15, the bending moment on the lining at the end of the numerical analysis in all scenarios are within the same order of magnitude. This shows that the variety of groundwater management scenario has little to no effect to the development of bending moment. Furthermore, unlike the development of axial force, more substantial increase was found in all scenarios with an average of 30% at the tunnel crown and 17% just above the springlines.

The development of bending moment is predominantly caused by the deformation of the tunnel ring. The bottom part of the tunnel, being confined by stiffer sand layer, consistently showed smaller absolute bending moment than the upper side of the tunnel, where the tunnel is surrounded with more compressible soil. This finding is aligned with Duddeck's theory presented in Subchapter 2.5.4. The theory suggested a proportional correlation between the soil-structure stiffness ratio and the bending moment acting on the tunnel lining.

The numerical analysis outcome falls in the same ballpark with the calculation based on Duddeck's, provided in Appendix A.1.5. However, the analytical calculation overestimated the bending moment because of the homogenous profile. Due to the presence of joints along the tunnel ring, smaller bending moment was reported in the numerical analysis.

6.2.5 Normal Stress

The normal stress around the tunnel ring is directed in the radial direction, towards the center of the circular shape. The stress, which originates from the surrounding soil and ground surcharge, is an alternative to validate the numerical analysis outcomes, which is available in the appendix. The development of normal stress in time is presented in Figure 6.16.

Normal Stress

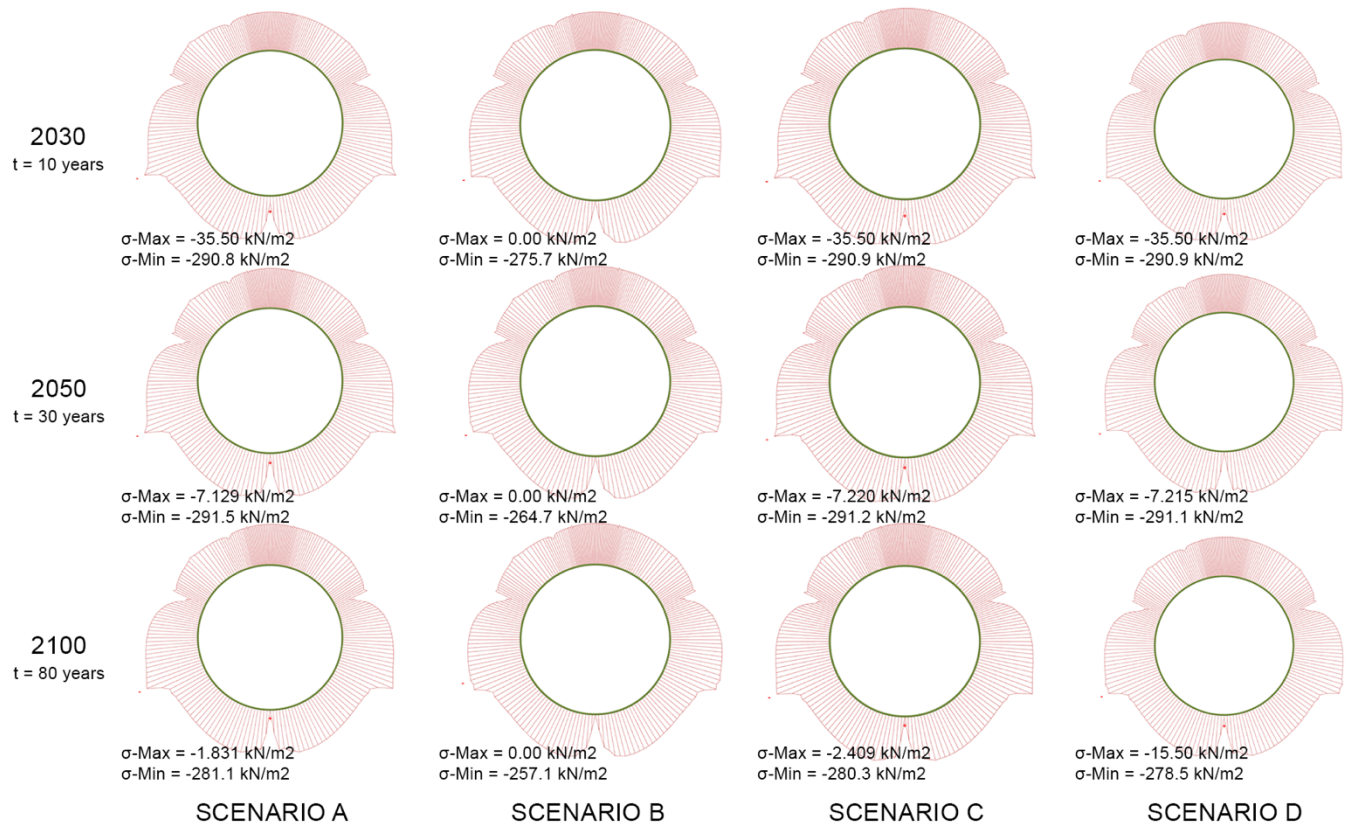


Figure 6.16: Development of normal stress in time

A minimum compressive stress of 0 kPa was reported at the tunnel invert in scenario B throughout the simulation. The finding asserts that groundwater is the only load source at the tunnel invert. Being a point of rotation, the tunnel invert shifted towards the positive Z-axis direction with respect to other points in the frame and away from the soil. In response to the shift, the soil at the invert reduces the compressive stress to the tunnel. That being said, the normal stress at the invert in other scenarios is also dictated by the decline or rise of the groundwater level.

On the other hand, the normal stress at the springlines continuously increased in time following the deformation. Alike, the slight decrease of minimum (absolute maximum) normal force at the two joints below the springlines in time is predominantly by tunnel deformation, especially the rotation of joints.

6.3 Behavior of Surrounding Soil

The development of settlement in time are presented in Appendix B.1 and B.2.

6.3.1 Consolidation in Calibration and Transitional Period

The consolidation in the calibration and transitional period is as expected. Due to the uniformity of the cross section, the model consolidated uniformly over its width. The total of 220 mm of consolidation was reported for the slow drainage (Scenario A, C, D) and 248 cm of consolidation was reported for the rapid drainage (Scenario B). The consolidation profile is presented in Figure 6.17.

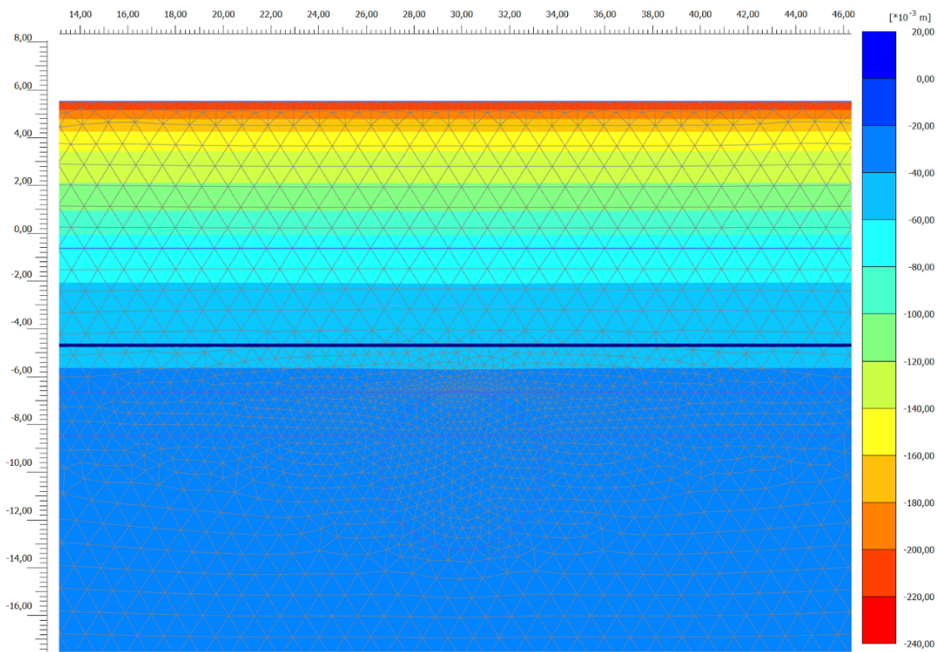


Figure 6.17: Uniform vertical displacement in calibration period at BH88 in 2020 (Scenario A)

6.3.2 Consolidation in Analysis Period

The consolidation in analysis period shows a different pattern. The deformation of the tunnel induces small degree alteration to the consolidation pattern and thus uniform consolidation is no longer the case. Based on the numerical analysis, more settlement occurred right on the top of the tunnel. The maximum recorded difference is only 2 mm. On the opposite, less settlement is evident underneath the tunnel as illustrated in Figure 6.18. The maximum recorded difference at the material boundary is 5 mm.

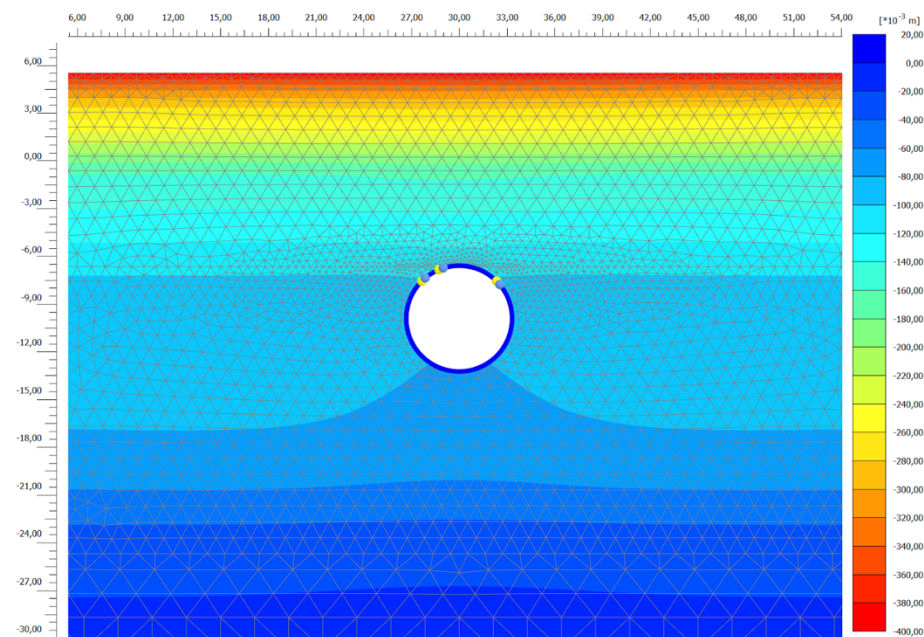


Figure 6.18: Total vertical soil displacement (u_y) pattern around the NSL-P2 tunnel at BH88 in 2100 (Scenario A)

Furthermore, the consolidation of silt layer at the top part of the tunnel continued but manifested more pronounced horizontal deformation. The presence of a stiffer structure forced the compressible soil to flow around it. Additionally, this phenomenon is also caused by the ovalisation of the tunnel, which increased the horizontal diameter and decreased the vertical diameter. As a consequence, it increased the stress at both sides of the tunnel and relieved the stress on top. This phenomenon is displayed in Figure 6.19.

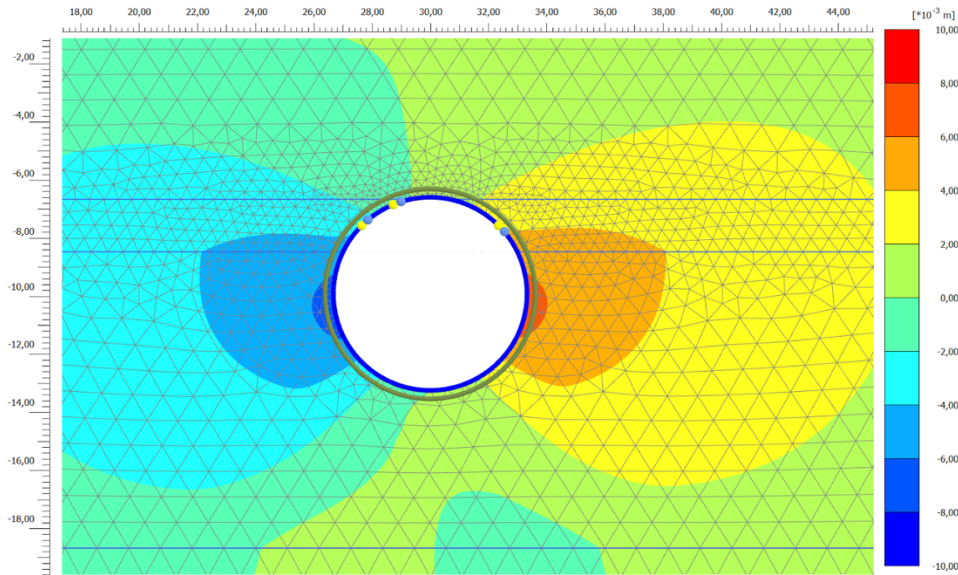


Figure 6.19: Horizontal soil movement around the NSL-P2 tunnel at BH88 in 2100

An average reduction of overburden depth as much as 30 cm is apparent directly above the tunnel crown in all four scenarios after the 80-year period. This phenomenon is a product of consolidation and horizontal movement of soil around the tunnel. The reduction of overburden thickness in time is presented in the graph below.

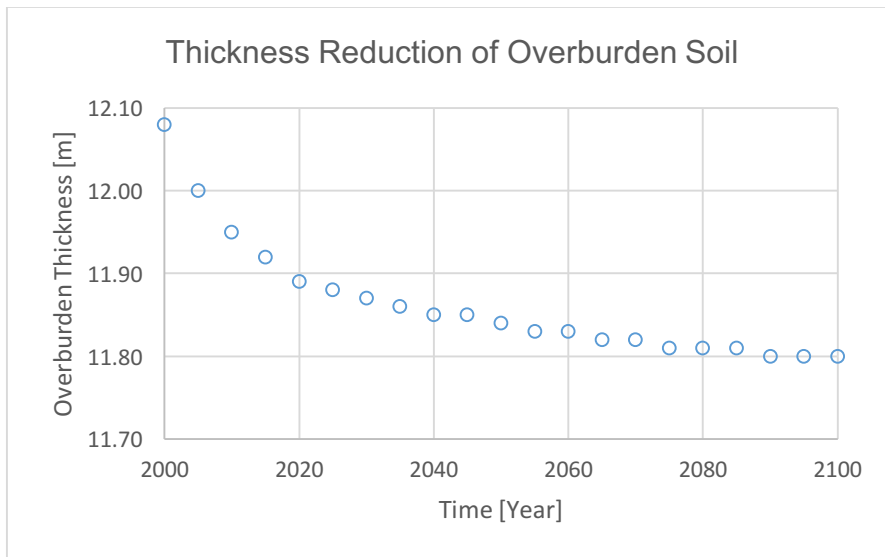


Figure 6.20: The reduction of overburden thickness over time – Scenario A

6.3.3 Influence of Tunnel on Total Settlement

In NSL-P2, the numerical analysis suggests that the tunnel did not significantly impact the cumulative settlement nor significantly change the settlement pattern. This finding is caused by the majority of consolidation, nearly 75%, took place in the first three compressible soil layers (Appendix B.5). Within the small changes itself, the vertical ovalisation of the structure is responsible for the majority. The largest surface settlement was observed directly over the tunnel axis as much as 392 mm at the end of the numerical analysis. This value is 3 mm more than the settlement at the point furthest from the tunnel, which demonstrated a total settlement of 389 mm in 2100. The progression of surface settlement profile is presented in Figure 6.21 below.

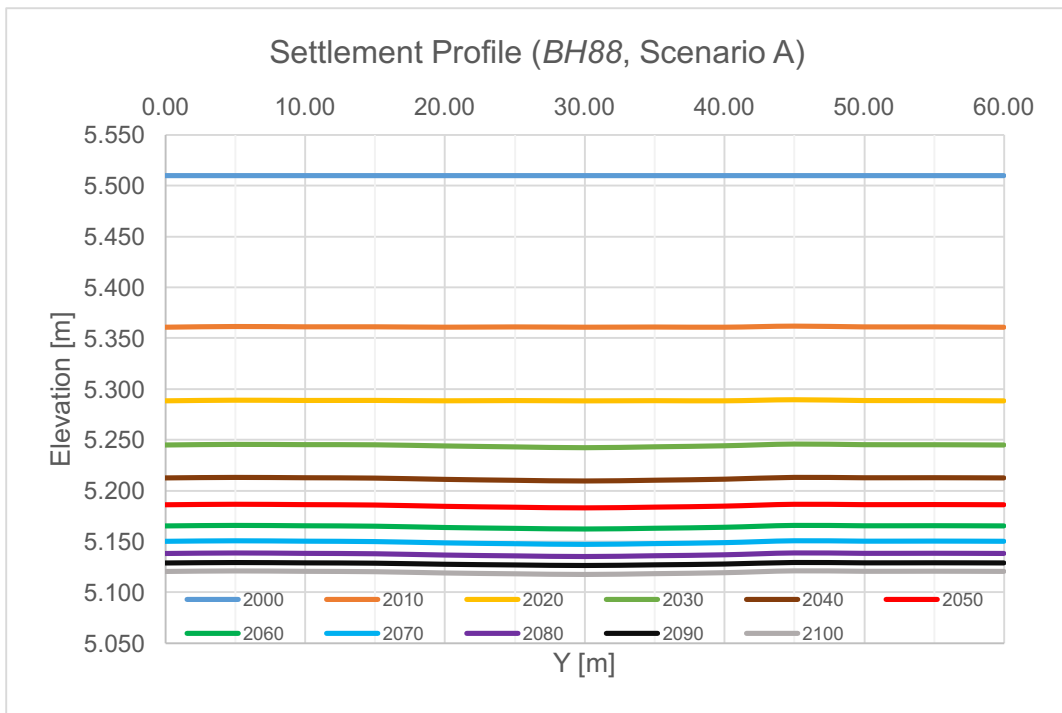


Figure 6.21: Progression of settlement at BH88 (Scenario A)

The numerical analysis recognizes two settlement mechanisms. These are the settlement due to soil consolidation and settlement due to structural deformation. The development of trench over the tunnel is an interesting point that was observed in the progression of surface settlement in time. The trench development started immediately, reached an extreme relative depth, which then reduced. This argument can be demonstrated by comparing the settlement of point A and B. Points A-B and the differential settlement is presented in Figure 6.22.

Figure 6.22 shows the development of relative settlement at point B with respect to point A in time, taken from Scenario A. Initially, the difference in settlement develops in time before it declines after the year 2040. The immediate settlement over the tunnel axis occurred almost instantly and was the result of tunnel deformation. When structural deformation halts, soil consolidation continues. Furthermore, the structure provided additional stiffness upon loading and formed soil arching, presented in Subchapter 2.6. Even though soil arching is not clearly visible at the surface, it is observable in Figure 6.18, where larger settlements were reported at the sides of the tunnel and least settlement occurred underneath the tunnel.

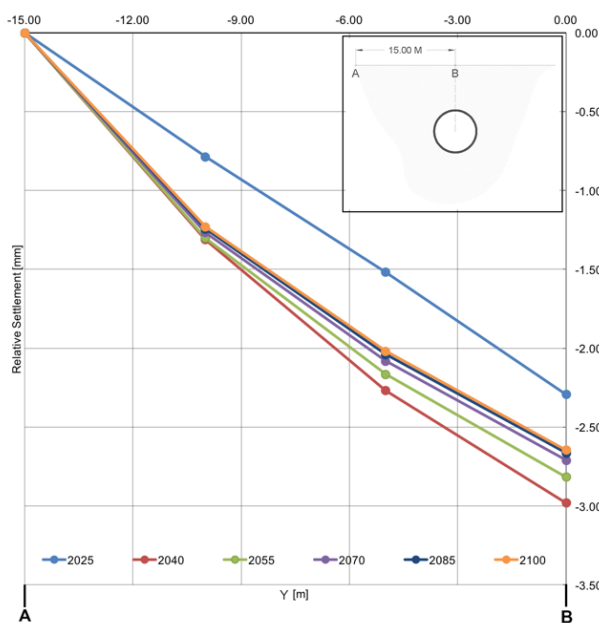


Figure 6.22: The development of relative settlement in time; (Inset) Points A & B with respect to the tunnel

7. FURTHER ANALYSIS

This chapter presents further investigation which departs from the outcomes of the numerical analysis. This investigation helps to derive design recommendations for the future NSL-P2 tunnel with regards to the differential settlement as well as its implications. Two points of discussion about tunnel design are elaborated in the following sections, including the assessment of stiffer tunnels and the possibility of great settlement difference at the station-tunnel interface.

7.1 Stiffer Tunnels

Given that the numerical analysis was based on beam-spring model, the global bending stiffness of the beam itself is known to be influential to its longitudinal deformation. Increasing the global bending stiffness can be attained through one or many ways, such as employing thicker segments, prescribing larger tunnel diameter, or using stiffer longitudinal joints. However, on top of it all, the increase of global stiffness comes with a cost. Therefore, it is important to look into the performance of stiffer tunnels in the settling environment and figure out how stiff the structure should be to significantly minimize the impact of differential settlement.

7.1.1 Equivalent Beam Stiffness

As segmented structure, the equivalent beam stiffness of the tunnel is derived from two axial stiffness moduli, which define its behavior in compression and tension. The axial stiffness in compression is established by the concrete to concrete interaction, while the axial stiffness in tension is defined by the bolt connections. With the properties provided in Section 4.10.3, the stress-strain diagram below was generated.

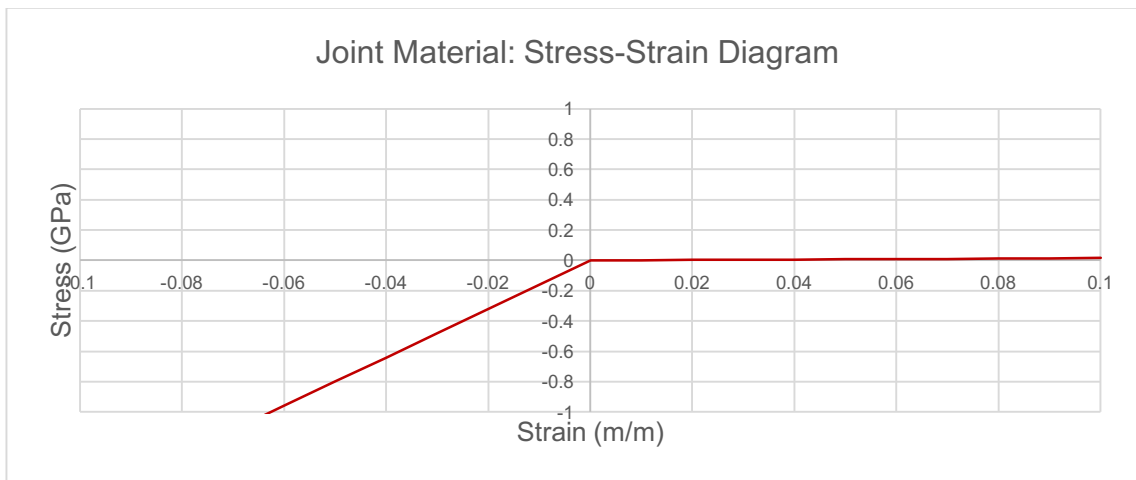


Figure 7.1: Stress-strain diagram of joint material

The equivalent beam stiffness is guided by factor η , a factor which reduces the longitudinal bending stiffness of the homogenous beam because of the presence of longitudinal joints. The aforementioned reduction factor is determined with a model which juxtaposes the performance of homogenous and segmented beam under load. In the model, the maximum deflection of simply supported homogeneous and segmented beam under uniformly distributed load are the main interests. The ratio of the two maximum deflections dictates the value of η . Then, η is used as a multiplier for the homogenous beam bending stiffness to obtain the equivalent beam stiffness. The analysis performed in Appendix A.2.2 suggests a reduction factor of 0.276. Hence, the equivalent beam stiffness is determined as shown below.

$$EI_{Equivalent} = \eta \cdot EI_{Homogenous} = 0.276 \cdot 4.13 \cdot 10^8 = 1.14 \cdot 10^8 \text{ kNm}^2$$

7.1.2 Deformation and Bending Moment

This additional assessment is based on the discrepancy found between the calculated and reported bending stiffness. In this assessment, a longitudinal bending stiffness of $1.14 \cdot 10^8 \text{ kNm}^2$, calculated in the previous section and Appendix A.2.2, was assigned. The aforementioned bending stiffness is approximately 10 times greater than the bending stiffness used in the previous analysis (Chapter 6). To be consistent with the theory, greater bending stiffness of the tunnel should entice greater bending moment as presented in Figure 7.2.

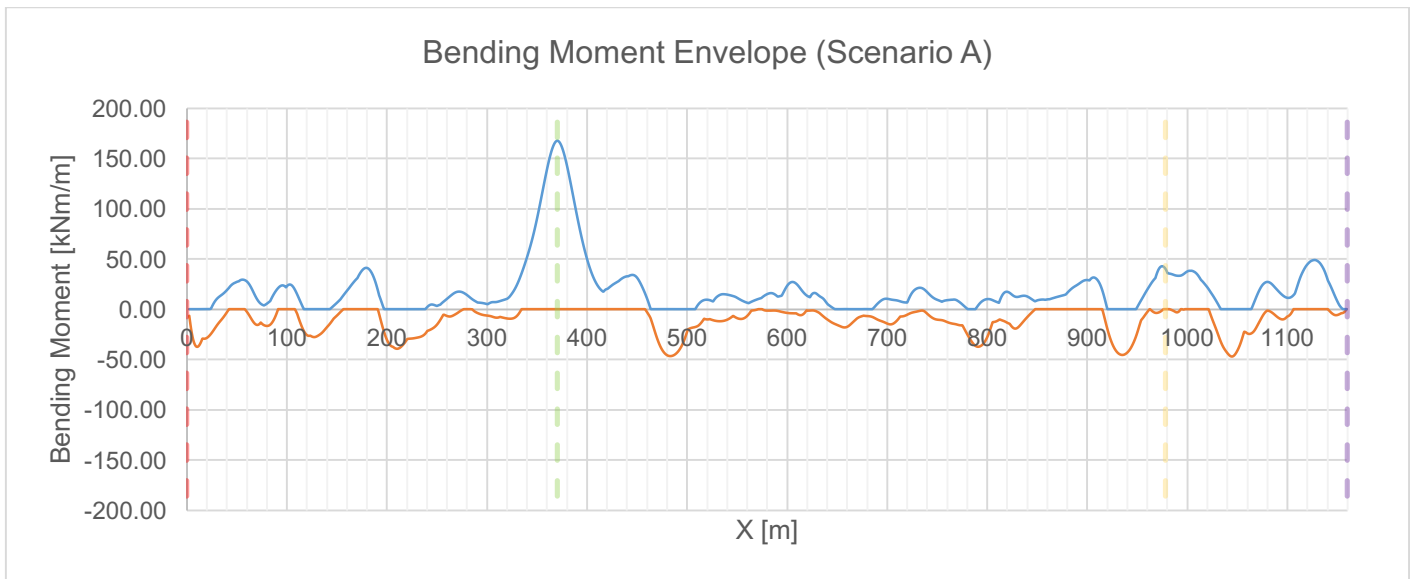


Figure 7.2: Bending moment envelope at year 2100 of a stiffer tunnel (Scenario A)

The numerical model returned amplified bending moment along the studied reach. The maximum bending moment increased by roughly a factor of 6. This finding underlines the importance of equivalent beam stiffness used in the analysis. An underestimation of tunnel bending stiffness leads to smaller design load, inadequate design, and thus can be dangerous for its user. Therefore, maximum, but reasonable, tunnel stiffness should be used in the conservative concrete design phase.

As mentioned before, the increase of tunnel longitudinal stiffness can affect its deformation in the longitudinal direction due to differential settlement. To find out whether or not the alternative should be considered in the future, three tunnels with bending stiffness in three different orders of magnitudes (1x, 10x, and 100x) were assessed to see the influence of stiffness to the deformation. The outcome of the assessment is displayed in Figure 7.3.

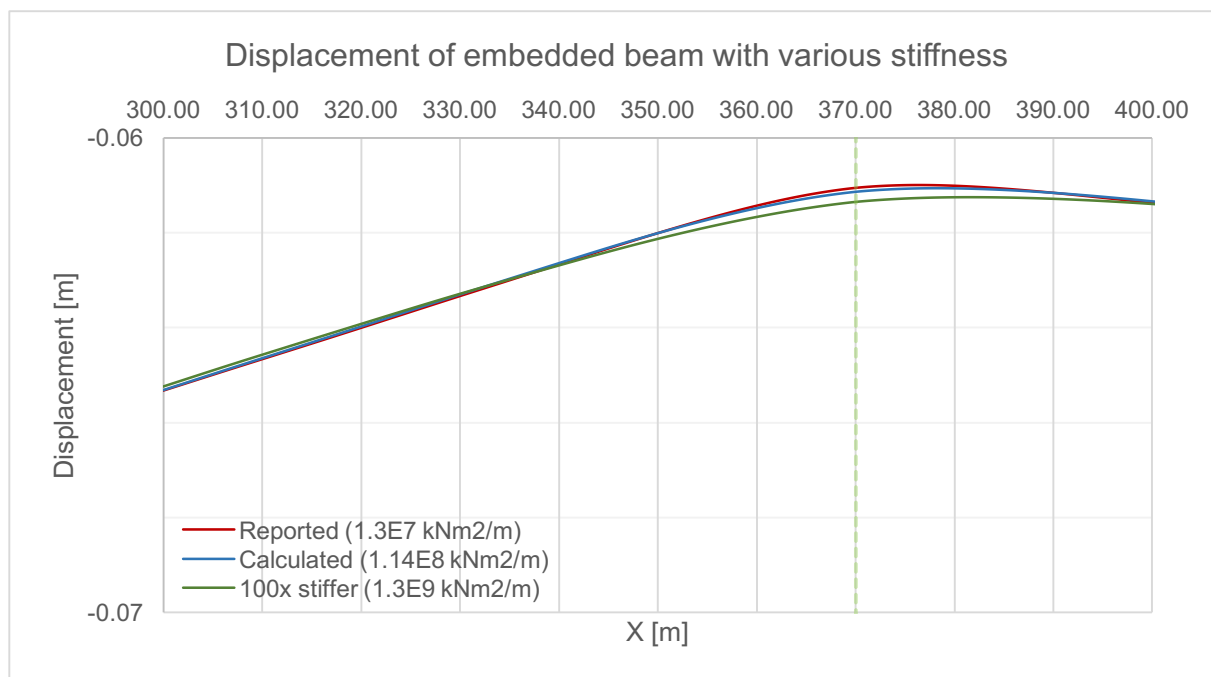


Figure 7.3: Comparison of beams with various stiffness

This particular segment shown in Figure 7.3 showcases the largest discrepancy between the three beams/tunnels. The beam with greatest stiffness (shown in dark green) exhibited the least differential settlement compared to the two ends of the structure. Following the dark green line are the blue and red line which represents the calculated (10x) stiffness and reported (1x) stiffness respectively. The most pronounced deviation between the three beams is evident at $x = 370 \text{ m}$ or at *BH58*. However, it turns out that significant increase in longitudinal stiffness can only produce small deviation. This finding was demonstrated by the beam which is 100 times stiffer than the original at the cost of approximately 40 times larger bending moment. The bending moment diagram is available in Appendix B.6.

The stiffness assessment shows that the increase of structural stiffness has minimal impact to the differential structural settlement. Therefore, it is not advised to employ this alternative as the main solution for the future NSL-P2 tunnel. However, if stiffer tunnel is planned for NSL-P2, material capacity is one of many aspects that demands attention.

7.2 Presence of Stiffer Structures

One feature that is likely to be present in NSL-P2 is the interface between tunnel and stiffer structures along the longitudinal direction. This subchapter investigated the implications of stiffer structures to the tunnel and recommended several design suggestions to minimize the impacts. Stiffer structures are usually required special connection to fasten supplementary structures, such as transit stations and emergency shafts, to the tunnel. But in contrast to the tunnel, these supplementary structures are designed to minimize settlement with the additional vertical support with the help of deep piles, diaphragm wall, or other deep foundations. An example of diaphragm wall is shown in Figure 7.4. Given the contrast in stiffness, differential settlement between the station and adjacent tunnel could transpire and become an extra issue to solve.

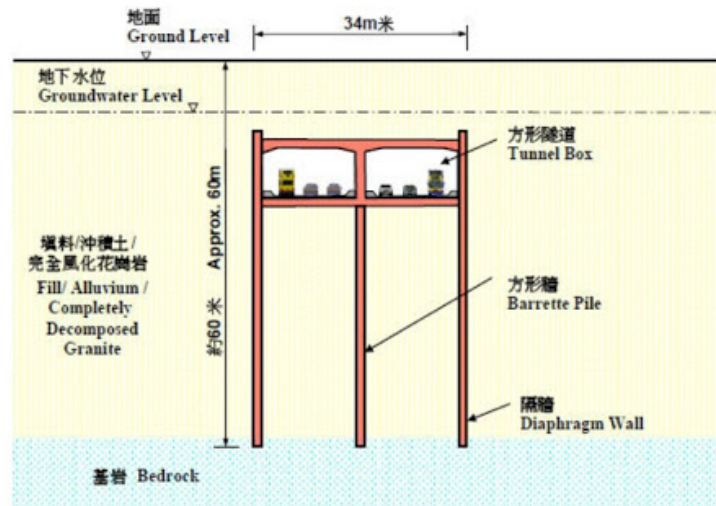


Figure 7.4: Vertical support of an Wan Chai Bypass, Hong Kong (City University of Hong Kong, 2017)

The tunnel displayed in Figure 7.4 is supported by the diaphragm walls at its side and a barrette pile in the middle. Other than its function in retaining horizontal loads, the diaphragm walls are also responsible to extend vertical burden to the hard soil layers below the structure. As a result, the underlying soft soil will receive less stress and thus settlement can be limited.

Similar approach is evident along the NSL-P1, for example: *Bundaran HI* station at the north end of NSL-P1 (or the southern end of NSL-P2). Putting the previous statement into consideration, it is safe to assume that the same approach will be used for the stations along the NSL-P2.

7.2.1 Reflection from Shanghai Subway Tunnel

Even though this subject has not been profoundly studied in Indonesia, the striking differential settlement at the station-tunnel interface was observed in Shanghai Subway Tunnel. According to Xia et al. (2006), Shanghai is located at the downstream reach of *Yangtze* river and on an alluvial floodplain dominated by clay, silt, and sand layers. Zhou et al. (2016) monitored the settlement of the three transit stations and observed a significant difference in settlement between the station and the adjacent tunnel. The monitored displacement of *Yuantong* station, one of the monitored stations, and its adjacent tunnel is presented in Figure 7.5.

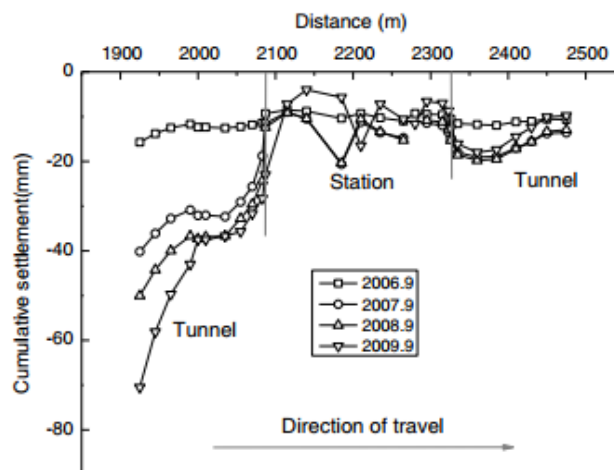


Figure 7.5: Differential displacement between Yuantong Station and adjacent tunnel (Zhou et al., 2016)

Zhou et al. finding shows that the differential settlement at the station-tunnel interface can reach approximately 70 mm. Figure 7.5 clearly shows less settlement occurred at the station compared to the settlement at the tunnel. The differential settlement between the two structures increases in time as the station remained stagnant while the tunnel settled steadily. An even larger differential settlement was reported by Cui et al. (2015), which difference exceeds 100 mm between the tunnel of South *Huangpi* road and the People's Square station.

7.2.2 Analysis of Proposed NSL-P2 stations and Design Recommendations

The numerical analysis in Chapter 6 omitted the presence of stations along the NSL-P2 reach and focused solely on the deformation of the tunnel structure. Reflecting from the Shanghai subway tunnel case, differential settlement at the station-tunnel interface can also transpire in Jakarta. Therefore, an additional assessment regarding the concern is carried out.

A new numerical model was established to incorporate the proposed stations and study the impact of fixities at the tunnel. According to the feasibility study, there are two stations within the proximity of the selected segment, which referred as: *Mangga Besar* station and *Sawah Besar* station. The location of these stations with respect to the boreholes are shown below.

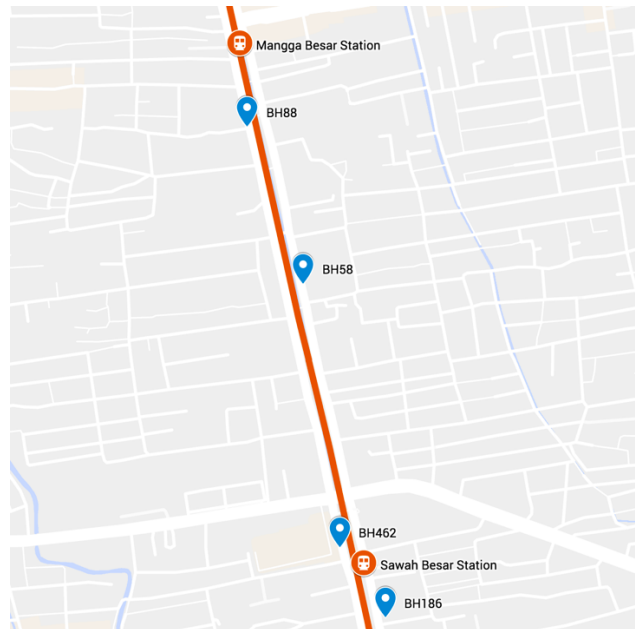


Figure 7.6: Stations around the selected segment

Figure 7.6 displays the aforementioned stations. *Mangga Besar* station is positioned north of the selected segment, close to *BH88*, and *Sawah Besar* station is located at the southern part of the studied reach, squeezed by *BH462* and *BH186*. As simplification is necessary to develop the numerical model, the presence of two stations are modelled as vertical displacement and rotation restrictions at both ends of the studied segment, $x = 0\text{ m}$ and 1160 m . The assumption is based on the differential settlement in Shanghai tunnel case study. To obtain conservative results and produce the worst case scenario, zero, rather than slight, displacement was prescribed at the two points. With such assumption, maximum forces associated differential settlement can be attained. The new numerical model is referred as the fixed-fixed model, which is displayed in Figure 7.7.

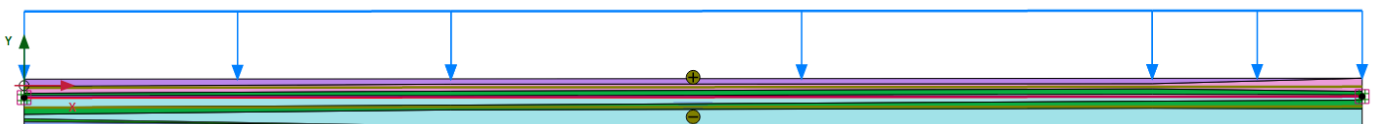


Figure 7.7: Longitudinal model with fixed ends

The presence of constraints at the ends of the segment altered the displacement of the tunnel. Severe differential settlement between the station and the tunnel took place at each fixities. The resulted deformation profile is presented in Figure 7.8.

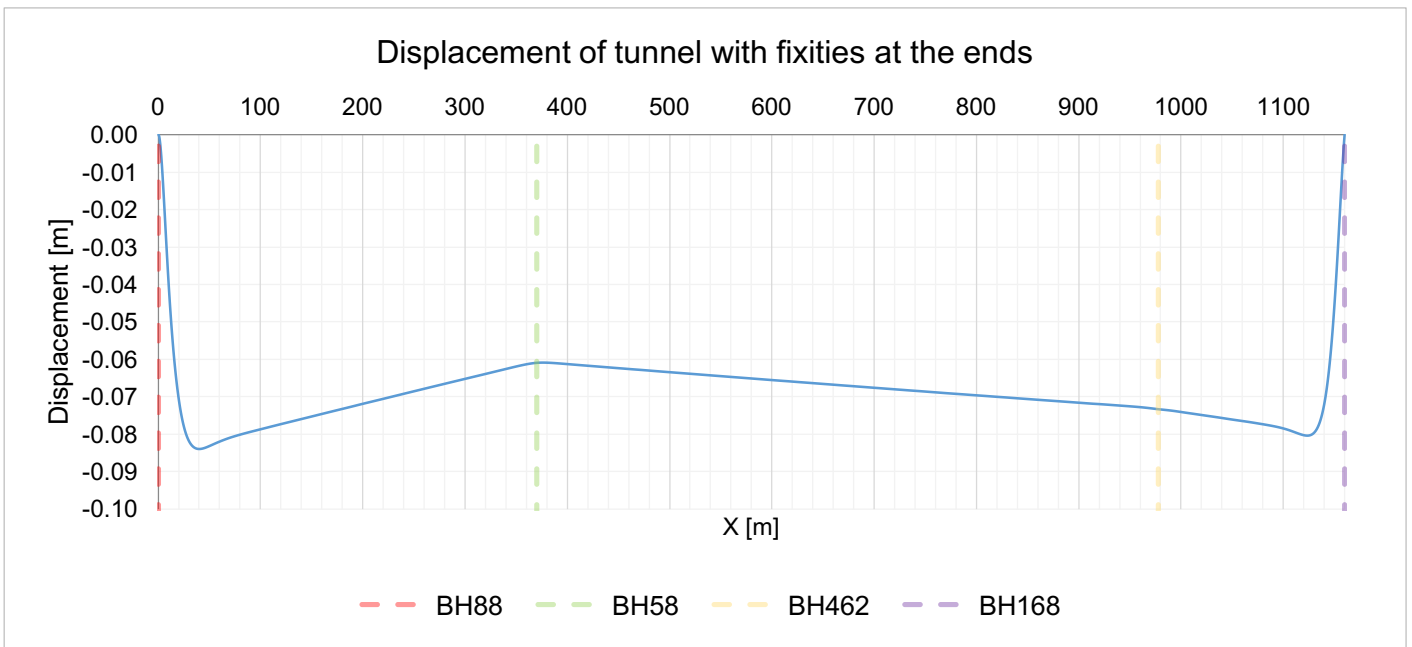


Figure 7.8: Influence of fixities at the ends to the vertical displacement of tunnel

As the tunnel is quite flexible longitudinally, Figure 7.8 suggests that the effect of supplemental structures extends to approximately 40 m away from the fixed point on the longitudinal direction. As it exceeds the 40 m mark, no effects of fixities were observed and displacement profile similar to the previous case (unsupported beam) was found. The maximum of 83 mm settlement difference over a 40 m distance took place in the affected regions. If the differential displacement is assumed to be linear, an average settlement difference of 3 mm between adjoining tunnel rings should be anticipated. Even though simplifications were made in the model, this finding is comparable to the monitoring result in Shanghai.

Furthermore, amplified shear stress and bending moment were reported at the fixities. With the restriction in translation and rotation, the model suggested a bending moment as large as 10800 kNm/m at BH88 and 5400 kNm/m at BH168. These values are 3 orders of magnitude larger than the bending moment at intermediate points. The full-extent bending moment envelopes are presented in Figure 7.9. On the smaller scale, the bending moment at the intermediate reach was reported not to be significantly different compared to the scenario where the tunnel has free ends. Local minima and maxima were discovered along the longitudinal direction and rightly correlated with the deformed curvatures. The bending moment at the intermediate location is presented in Figure 7.8.

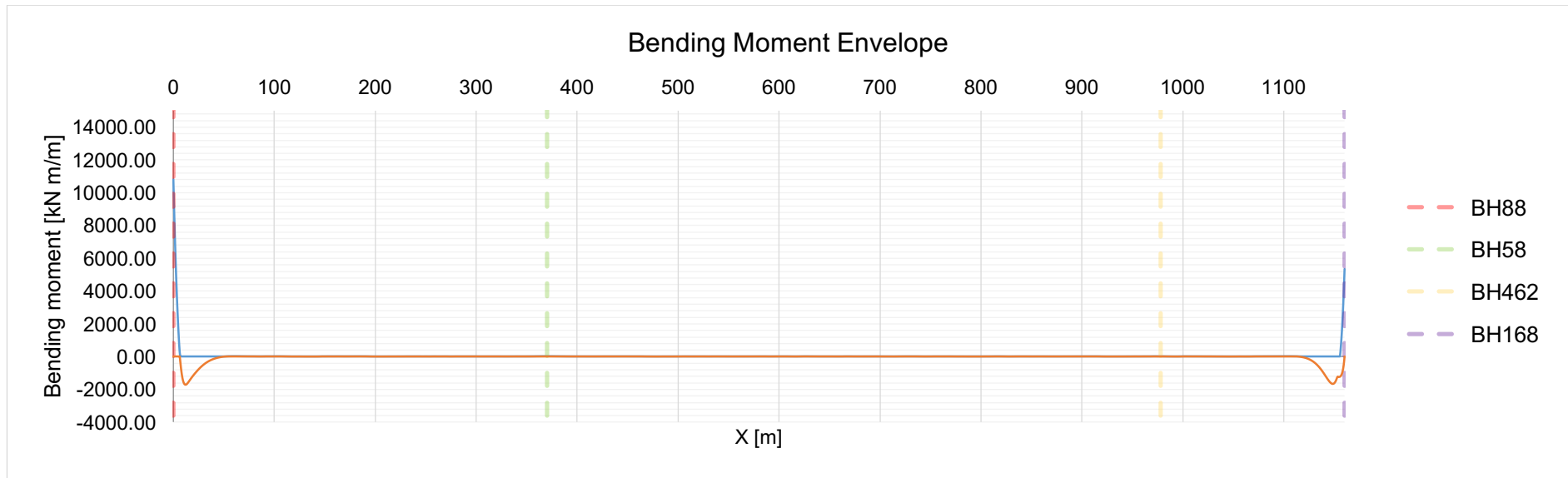


Figure 7.9: Bending moment diagram of fixed-fixed segment

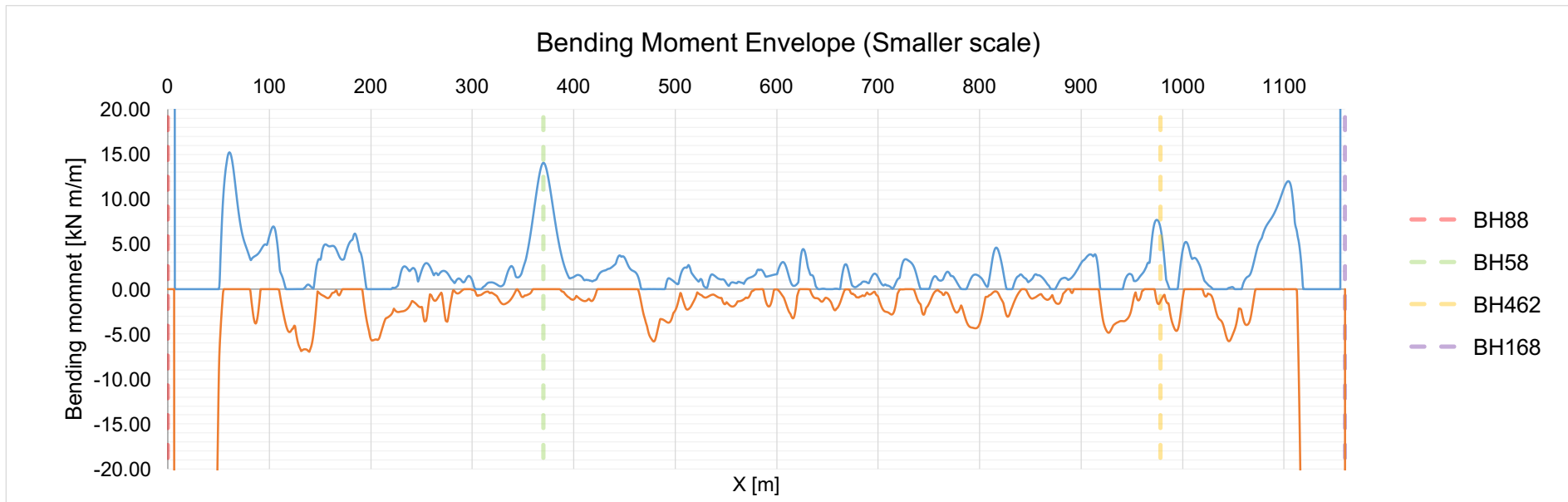


Figure 7.10: Bending moment diagram of fixed-fixed segment on a smaller scale

Impacts on Water Tightness

Bending moments on tunnel structure is known to affect its water tightness. Not only on the longitudinal direction, the bending moments acting along the tunnel lining in the cross sectional perspective also have implications to the water tightness. In fact, Girnau (1978) argued that most leakage occurs at the T-joint, where longitudinal and axial connection meets (Shalabi et al., 2007). As mentioned before, the water tightness of tunnel relies on the compression of rubber joints at the edge of the tunnel segments. The rubber gasket is shown in Figure 7.11.



Figure 7.11: Tunnel segment rubber gaskets (Trelleborg, n.d.)

The earlier statement proves that reduction of axial stress could decrease its capabilities to retain water out of the tunnel. Critical section was determined to be the station-tunnel interface, where large bending moment could transpire due to the constraints. The maximum reported bending moment of 10800 kNm/m was used in the calculation. Assuming a symmetrical stress distribution, the calculation suggests a stress change of $\pm 1188 \text{ kPa}$, where the reduction occurs at the crown and the additional compressive stress transpires at the invert.

As the technical document of NSL-P1 did not specify any water tightness feature, the minimum compressive stress to ensure water tightness is estimated with a simple method suggested by Shalabi et al. (2007). According to Shalabi et al., leakage is expected when hydrostatic pressure exceeds the compressive stress. To be conservative, the greatest hydrostatic pressure along the tunnel was considered to established the required compressive force. The largest hydrostatic pressure is experienced by tunnel invert and occurs when the groundwater table is at the highest point or during flood. The estimation produces a minimum contact stress of 437 kPa . The full length of calculation can be found in Appendix A.3. The model used in the calculation is presented below.

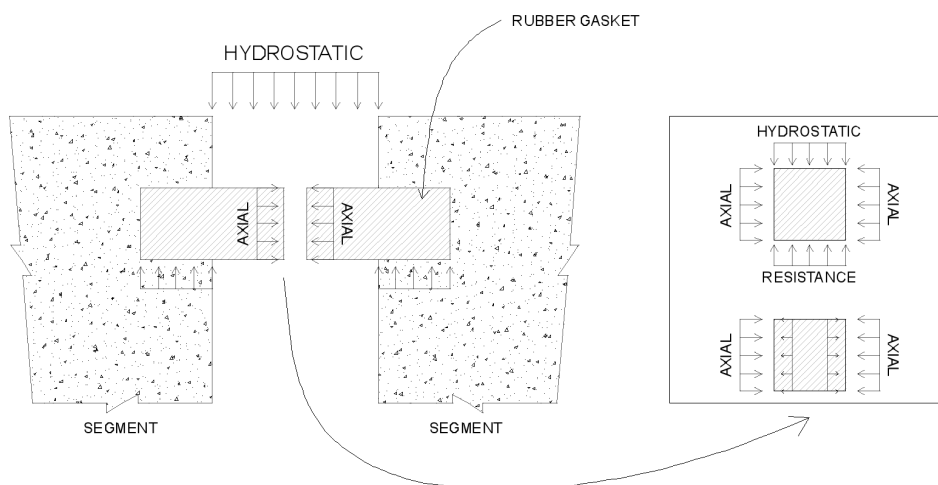


Figure 7.12: Interaction of forces in the rubber gasket

The assessment is carried on with the inclusion of internal axial stress, one that was instilled during the construction phase. The axial stress is originated from the hydraulic jack, which exerted a total of 10^4 kN force. This value was obtained from the engineering team of MRT Jakarta and is equivalent to one-third of the TBM maximum capacity. The calculation involves an interaction between the soliciting load (change in stress due to deformation) and the allowable stress (difference between stress from jack forces with the required stress to maintain water tightness).

The analysis reported that the change in stress at the station-tunnel interface is barely under the allowable stress. The ratio between the change in stress with the allowable stress was reported to be 96.3%. This value can easily increase and exceed the allowable stress if the tunnel turned out to be stiffer. Furthermore, the load-resistance interaction can also be expressed with strain of rubber gasket. The allowable strain, 0.075, was calculated based on the previous model and elasticity modulus of the rubber gasket. On the other side, the maximum bending moment caused by the fixity, 10800 kNm, produced a strain of 0.072. The detailed calculation is available in Appendix A.3.

There are two methods to improve the water tightness of the tunnel reflecting from the stress calculation. The allowable strain is predominantly defined by the jack force and the elasticity of the rubber gasket. The water tightness of the tunnel is proportional to the rubber gasket compression. Therefore, larger stress from jack force can increase the allowable strain. Additionally, the increase of allowable strain can also be attained by using more flexible material for the joints.

Other mitigation measure involves maintenance. The pretension bolt connections of the concrete segments are vulnerable to deterioration in time due to corrosion or fatigue. Hence, periodical maintenance to ensure that the bolt connections are still capable to maintain gasket compression is necessary. Similar treatment is also required to repair cracks on the concrete segments.

Expansion Joints

One alternative to reduce the bending moment at the station-tunnel interface is through the implementation of flexible connection, for example: expansion joint. Expansion joint is a type of connection that allows horizontal and vertical movement of adjoining structural features to a certain degree while maintaining its structural integrity. This type of connection is commonly used in bridge structures as horizontal thermal expansion and differential settlement at the abutments must be anticipated. Furthermore, hydrophilic rubber gasket is installed at the connection to prevent water intrusion following the deformation of joints.

The implementation of expansion joint in bored tunnel can refer to the *Daiba* tunnel, Japan. Constructed on a fresh reclaimed land made of soft alluvial clay, *Daiba* tunnel is subjected to longitudinal settlement and thus require the flexibility of expansion joint. However, in 1984, the deformation of *Daiba* tunnel exceeds the allowable strain, which damaged the joint and caused water leakage (Komiya et al., 2006). Learning from this case, the implementation of expansion joint should be preceded by the assessment of long-term longitudinal deformation. The reinforced joint system of *Daiba* tunnel is presented in Figure 7.13.

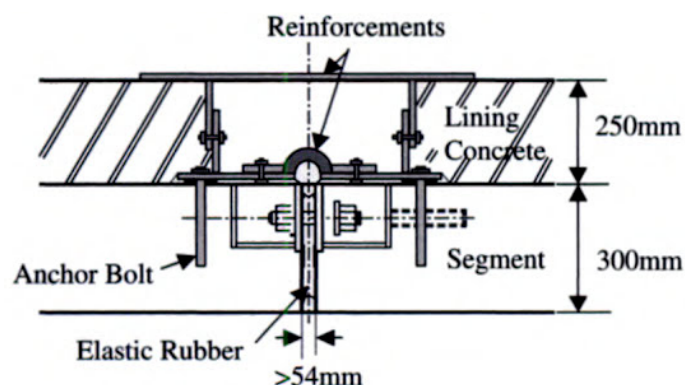


Figure 7.13: Reinforced expansion joint of *Daiba* tunnel, Japan (Komiya et al., 2006)

The difficulty to maintain water tightness at the station-tunnel interface was also experienced by the tunnel in Shanghai. Due to differential settlement between the station and tunnel in Shanghai, Wu et al. (2014) claimed that the gap between the vertical shaft and bored tunnel is more prone to leakage compared to the opening of longitudinal joint. Numerous cases of water leakages in the past shifted the trend of station-tunnel

connection from rigid to flexible. Typical station-tunnel interface of Shanghai newer tunnels is presented in Figure 7.14.

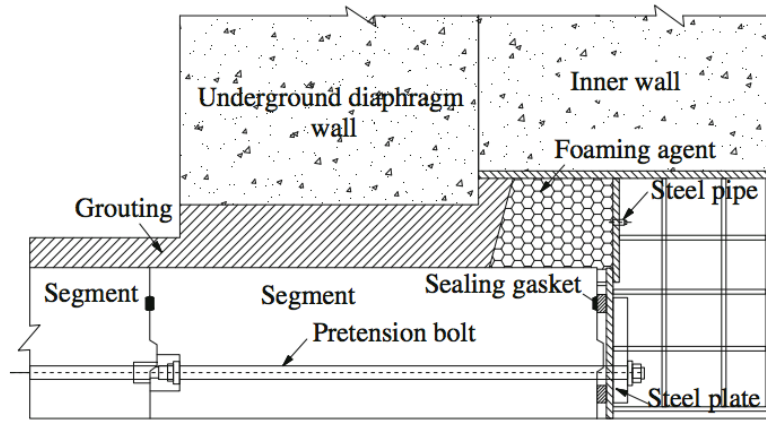


Figure 7.14: Station-tunnel connection of newer Shanghai tunnels (Wu et al., 2014)

7.3 Summary and Design Improvements

The ramifications of differential structural settlement include splitting of train tracks and leakage, which then could lead to operation disturbance and other indirect impacts. Consequentially, regular maintenance will be required to keep the rail operational and thus increases the overall maintenance cost. This could be prevented with an appropriate tunnel design to minimize the difference in settlement. Therefore, design recommendations below should be considered in the planning of NSL-P2 tunnel. The recommendations are:

1. Alterations in tunnel geometry to increase the global stiffness, such as increasing tunnel diameter or segmental thickness, were proven to be not effective in reducing the differential settlement of the tunnel. The numerical analysis, which involves a tunnel with equivalent to ~ 3 times the original diameter, showed that the reduction of differential settlement is in the order of $10^{-2} m$.
2. The differential settlement of NSL-P2 did not pose significant risk to the water tightness of the tunnel. The strain due to maximum longitudinal bending moment is incomparable to the allowable rubber gasket strain. The contribution is even less if it is compared with the internal stress of tunnel that was transferred during the construction. However, rotational and translational fixities at the station-tunnel interface were proven to risk the water tightness. Therefore, flexible joints should be assigned at the station-tunnel interface to accommodate differential settlement as well as to maintain the water tightness.
3. The option of deeper tunnel should be assessed in the future and prior to the planning of NSL-P2 tunnel. At greater depth, there is less probability for the tunnel to be constructed over compressible layers and thus settlement can be minimized.
4. The numerical analysis shows that the decline of groundwater level greatly affected the vertical displacement of tunnel. Therefore, the planning of NSL-P2 should coexist with the enforcement of groundwater extraction regulations.

8. CONCLUSIONS

8.1 Conclusion

Q1: What drives land subsidence in Jakarta?

1. Land subsidence in Jakarta is a result of multiple mechanisms, which include the loss of groundwater, increase of ground surcharge, creep, and tectonic movement. According to past studies, a majority of settlement was conveyed by the first three mechanisms.
2. Settlement due to declining groundwater level and creep was studied with numerical analysis in this research. The numerical analysis successfully demonstrated the significant contribution of groundwater level declination to the surface settlement due to increasing effective stress.
3. Due to continuous groundwater level declination, half of the surface settlement occurred at the shallow aquitard with approximate depth of 40 meters. Furthermore, 75% of the settlement at the shallow aquitard was caused by the deformation of the first three shallow soft soil layers.
4. Assuming that the tunnel will be constructed at 15-meter depth, the structure will not be largely affected by the settlement of top layers. On the other hand, the longitudinal deformation of the structure will be dependent on the differential settlement of the soft soil layers underneath the tunnel in its axial direction.

Q2: How significant is the additional forces on tunnel structure due to differential land subsidence?

1. The additional forces due to differential settlement is not a critical load to the tunnel. Compared to the initial construction loads, the additional forces are less significant.
2. Additional shear force and bending moment were identified due to longitudinal deformation of tunnel. The numerical output indicates inhomogeneous settlement of tunnel in time on the longitudinal direction, which can reach a maximum difference of 25 mm between BH88 and BH58 (370.0 m).
3. However, the corresponding shear force and bending moment were declared to be insignificant compared to the shear and bending moment capacity respectively. Furthermore, it was presented in the research that these additional are three orders of magnitude smaller than the internal concurrent loads.

Q3: Given the difference of stiffness, how does the presence of the tunnel alter the settlement pattern around it? How significant are the alterations?

1. Settlement carries on after the construction of tunnel. The presence of tunnel increased the amount of surface settlement but only as little as 3 mm due to structural deformation.
2. A reduction of overburden thickness as much as 30 centimeters was observed and is a product of consolidation and creep of soil over the tunnel as well as soil flow around it. The flow of soil is shown by the horizontal displacement vectors around the tunnel. However, the amount of reduction is achieved after 80-years of operation and thus can be regarded as insignificant compared to the initial overburden thickness of approximately 12 meters.
3. Vertical ovalisation amplifies soil stress at the springlines and relieves the stress at the invert. A maximum of 100% increase to horizontal soil stress was displayed in Scenario A at BH88.

Q4: How do the axial force and bending moment on the tunnel ring of NSL-P2 evolve in time?

1. In general, the development axial force and bending moment at the tunnel ring are influenced by the deformation of tunnel. Following the vertical ovalisation, the axial force at the springlines increases and the axial force at the crown and invert decreases in time. Likewise, the increase in bending moment in time is also induced by the deformation. The maximum bending moment increase was reported to be 30% at the crown and 17% at the springlines.
2. Larger bending moment is upheld by the top half of the tunnel, where structure is surrounded by soft soil layer. This finding is aligned with the theory which explains that the magnitude of load acting on

structure is dependent on the structure-soil stiffness ratio. However, as the majority of the consolidation in the case study occurred at the overburden layers, the consolidation poses minimal impact to the tunnel is reported.

Q5: Departing from the research findings, what design recommendations could be considered in the future to mitigate the consequences?

1. While the increase of global stiffness remains an option, the assessment shows that the alternative is not as effective as other methods to reduce the settlement difference. Moreover, the stiffer tunnel will be subjected to larger bending moment and thus affect design requirements.
2. The differential settlement at the station-tunnel interface should be accommodated with expansion joints. With its flexibility, the expansion joint will be able to simultaneously keep the tunnel attached to the station and preserve the water tightness.
3. Constructing a deeper tunnel is an option to eliminate soft soil layers underneath the tunnel and thus reduce the differential settlement in the longitudinal direction. With less differential settlement, the cost of maintenance will be less.
4. On top of it all, the study predicted less structural settlement in scenarios where the groundwater experiences stagnancy and rebound. Therefore, simultaneous enforcement of groundwater use regulations is advised.

8.2 Limitations and Further Studies

To comply with the time schedule, the master thesis has limitations in one and other aspects. Fortunately, the limitations of this research are also the opportunities for further research. The limitations and further research recommendations are:

1. The numerical analysis conducted in this study only considered the presence of single tunnel. In reality, the NSL-P2 has a great chance to employ two adjacent tunnels as it is a continuation of the similar system of NSL-P1 tunnel. This limits the analysis outcome from the effects of nearby structural deformation, which is partly influenced by the gap between the tunnels. Furthermore, the ground surcharge in the numerical model was a result of extensive simplification. These simplifications open up opportunities for further research which should involve more realistic configuration.
2. The focal point of this master thesis lies on the long-term development of the tunnel and its surrounding. This perspective restricts the analysis to incorporate the formation of settlement trough during the construction process. The settlement trough is a result of the conical-shape TBM protruding through the soil, where the diameter of the cutter head is larger than the tunnel diameter. Based on the antecedents, the scale of trough is comparable to the structural deformation induced settlement. Therefore, the settlement in the construction process should be investigated to anticipate the shortcomings.
3. One of the limitations of this study is the permeability of the tunnel structure. Throughout the analysis, the structure was modeled as an impermeable structure. This assumption limits the possibility of water flowing into the tunnel and thus increase the rate of groundwater extraction as there have been multiple cases of water leakages from the joints. This phenomenon was seen to have minimal impact for the long-term analysis, thus it was only represented with one of the groundwater management scenarios. However, it is possible for this phenomenon to have an impact to the immediate development of soil stress around the structure. Therefore, it becomes an opportunity for future research to understand the interaction between tunnel and the dewatering process.
4. This research utilized soil parameters based on the SPT results gathered from different sources and not specifically purposed for the NSL-P2 project. With limited information, the research was forced to employ universal correlations to develop the numerical model. Future studies about NSL-P2 should be performed with higher quality information to obtain more accurate results.
5. Seismic and operational cyclic load were not considered in all parts of this study. In reality, seismic load and cyclic load are able to constitute fatigues into the structure and thus reduce the strength. Additionally, past studies suggest that cyclic loads coming from moving trains might have an impact

to longitudinal tunnel deformation. That being said, future research should integrate the outcome of this study with other load sources.

6. The whole analysis was performed in Plaxis, a finite element software that specializes in solving geotechnical engineering cases. Therefore, the model did not have the capability to provide enough structural details and yield structural implications, matters that should concern the structural engineers. To obtain more structural details, the same analysis can be performed in a similar manner on *Abaqus* or other finite element software that is particular for structural engineering.

9. REFERENCES

- Abidin, H. et al. "Land Subsidence Characteristics of the Jakarta Basin (Indonesia) and Its Relation with Groundwater Extraction and Sea Level Rise." IAH - Selected Papers on Hydrogeology Groundwater Response to Changing Climate (2010): 113-30. Print.
- Abidin, H., H. Andreas, R. Djaja, D. Darmawan, and M. Gamal. "Land subsidence characteristics of Jakarta between 1997 and 2005, as estimated using GPS surveys." GPS Solutions 12.1 (2007): 23-32. Web. 22 Feb. 2017.
- Aila, W. "Establishment of Geotechnical Properties and 3D Numerical Models for Deep Excavation in Central Jakarta." Thesis. National Taiwan University of Science and Technology, 2016. NTUST Library. Web. 9 Jan. 2017.
- Ali, F. Implementasi Konsep IUWRM Untuk Keterpaduan Pengelolaan Sumber Daya Air dan Penanganan Kemacetan Lalu Lintas di Wilayah Metropolitan DKI Jakarta. Rep. Engineering Center Universitas Indonesia, 27 Nov. 2007. Web. 8 Apr. 2017.
- Arsan Kaucuk Website. 2016.
- Association of Swiss Road and Traffic Engineers. "Characteristic Coefficients of Soils." *Swiss Standard SN-670-010b*.
- Avanti, A. "Numerical Analysis of Jakarta MRT Deep Excavation Project." Thesis. National Taiwan University of Science and Technology, 2013. NTUST Library. Web. 9 Jan. 2017.
- Bakker, K. CIE5305, TU Delft. 2015.
- Bao, Z., H. Yu, and Y. Yuan. "Longitudinal Rigidity of Shield Tunnels Based on Numerical Investigation." *Conference Paper of ITA WTC Congress (2015)*. Web. 25 March 2017.
- Bimantara, A. "Pemetaan Dampak Akibat Penurunan Muka Tanah di Wilayah Jakarta." Thesis. Institut Teknologi Bandung, 2012. ITB Digital Library. Web. 27 March 2017.
- Bjerrum, L. "Rankine Lecture." *Geotechnique*. Vol.17 (1967): 81-118. Web. 6 March 2017.
- Blom, Cornelis Bernhard Marco. Design philosophy of concrete linings for tunnels in soft soils: proefschrift. Delft: DUP Science, 2002. Print.
- BPS DKI Jakarta. Data Jumlah Penduduk dan Laju Pertumbuhan Penduduk Menurut Kabupaten/Kota Administrasi di Provinsi DKI Jakarta. N.p., n.d. Web. 8 Apr. 2017.
- Buisman, K. "Results of long duration settlement tests." *Proceedings 1st International conference on Soil mechanics and Foundation engineering*, Mass. Vol. 1 (1936): 103-107. Web. 6 March 2017.
- Chandra, S. "Modeling of Soil Behavior." Indian Institute of Technology, Kapuur. 3 Dec. 2014. Peeyush Chandra. Web. 20 Mar. 2017.
- Colbran, Nicola. "Will Jakarta be the next Atlantis? Excessive groundwater use resulting from a failing piped network." *Law Environment and Development Journal* 5.1 (2009): 18. 2009. Web. 03 Jan. 2017.
- Cui, Z., and J. Tan. "Analysis of long-term settlements of Shanghai Subway Line 1 based on the in situ monitoring data." *Natural Hazards* 75.1 (2014): 465-72. Web. 9 June 2017.
- Das, B. M. Principles of Geotechnical Engineering. 7th ed. Stamford, CT: Cengage Learning, 2010. Web. 18 Nov. 2016.
- Delinom, R. Groundwater Management Issues in The Greater Jakarta Area, Indonesia. Proc. of International Workshop on Integrated Watershed Management for Sustainable Water Use in a Humid Tropical Region, University of Tsukuba. N.p., Oct. 2007. Web. 21 Mar. 2017.
- Deltares. Land Subsidence: Causes, impacts, and adaptive measures. Delft: Deltares, n.d. Web.

- Department of Industry and Energy DKI Jakarta. Groundwater Abstraction Report. 2015.
- Djaja R., J. Rais, H. Z. Abidin, K. Wedyanto. Land subsidence of Jakarta Metropolitan Area. Proc. 3rd IG Regional Conference, Jakarta, Indonesia. 2004.
- Dzikowitzky, Larissa et al. "Impacts of Megacities on Tropical Coastal Ecosystems - The Case of Jakarta, Indonesia." *Marine Pollution Bulletin* 110.2 (2016): 621–623. Web.
- Geotechdata Info* Website. 2013.
- Google Maps*. Web. 6 Jan. 2016.
- Gregory, A., W. Whalley, C. Watts, N. Bird, P. Hallett, and A. Whitmore. "Calculation of the compression index and pre-compression stress from soil compression test data." *Soil and Tillage Research* 89.1 (2006): 45-57. Web. 9 Feb. 2017.
- Herrenknecht Website*. 2015.
- Him, N. Wan Chai Bypass Section. Digital image. Central Wanchai Bypass. City University of Hong Kong. Web. 9 June 2017.
- Hoogeveen, R., and B. Van Leeuwen. "The large scale development of land subsidence in Northwest Jakarta and North Tangerang, Indonesia." *International Journal of Rock Mechanics and Mining Sciences & Geomechanics Abstracts* 33.7 (1996). Web. 20 Mar. 2017.
- Hough, B. Basic Soil Engineering. New York City, United States of America: Ronald Press Company, 1969.
- International Tunneling Association. "Guidelines for the design of shield tunnel lining." *Tunneling and Underground Space Technology* 15.3 (2000): 303-31. Web.
- Jalali, M., S. Golmaei, M. Jalali, A. Borthwick, M. Ahmadi, and R. Moradi. "Using Finite Element method for Pile-Soil Interface (through PLAXIS and ANSYS)." *Journal of Civil Engineering and Construction Technology* 3.10 (2014): 256-72. Web. 26 Feb. 2017.
- Kahlström, M. Plaxis 2D Comparison of Mohr-Coulomb and Soft Soil Material Models. Thesis. Luleå University of Technology, 2013. Print.
- Kementrian Energi dan Sumber Daya Mineral. "Air Tanah dan Pembangunan Bawah Tanah Jakarta." *Geomagz*, 28 Jan. 2014. Web. 18 Feb. 2017.
- Knappett, J., and R. Craig. *Craig's Soil Mechanics*. Abingdon, Oxon: Spon Press, 2012. Print.
- Kok, S. T. "A Review of Basic Soil Constitutive Models for Geotechnical Application." *Electronic Journal of Geotechnical Engineering* 14 (2009): n. pag. Universiti Putra Malaysia International Repository. Web. 09 Feb. 2017.
- Komiya, K., H. Akagi, and K. Takiyama. "Settlement behavior of a shield tunnel constructed in subsiding reclaimed area." *Geotechnical Aspects of Underground Construction in Soft Ground* (2006). Web. 4 July 2017.
- Kooy, M., C. Walter, and I. Prabaharyaka. "Inclusive development of urban water services in Jakarta: The role of groundwater." *Habitat International* (2016). 18 Sept. 2016. Web. 05 Jan. 2017.
- Kulhawy, F., and P. Mayne. "Manual on estimating soil properties for foundation design." Electric Power Research Institute, Palo Alto, California (1990). Web. 18 Jan. 2016.
- Liao, S., F. Peng, and S. Shen. "Analysis of shearing effect on tunnel induced by load transfer along longitudinal direction." *Tunneling and Underground Space Technology* 23.4 (2008): 421-30. Web. 6 July 2017.
- Makarim, C. "Sistim Resapan Air Dangkal Kota Jakarta: Suatu Kajian Geoteknik." Lecture at Universitas Tarumanegara. 2011.
- Massachusetts Institute of Technology. "Shallow Foundations on Sand - Bearing Capacity." *Advance Soil Mechanics*. Boston, MA. Fall 2004. Web. 22 Feb. 2017.

- Mayne, P., and J. Kemper. "Profiling OCR in Stiff Clays by CPT and SPT." *Geotechnical Testing Journal* 11.2 (1988): 139. Web. 9 Feb. 2017.
- Mercubuana. <https://goo.gl/k9sKVN>. 2015.
- Meyerhof, G. "Penetration tests and bearing capacity of cohesionless soils." *Journal of Soil Mechanics and Foundations Division* 82.1 (1956): 1-19. Web. 18 Jan. 2016.
- Mitchell, J.K. and K. Soga. *Fundamentals of Soil Behavior - Third Edition*. New York, United States of America: John Wiley & Sons, 2005.
- MRT Jakarta Website*. 2015.
- Niu, W., Z. Wang, F. Chen, and H. Li. "Settlement Analysis of a Confined Sand Aquifer Overlain by a Clay Layer due to Single Well Pumping." *Mathematical Problems in Engineering* (2013): 1-13. Web. 09 Feb. 2017.
- Osipov, V. I. *Physicochemical Theory of Effective Stress in Soils*. Springer Link. Springer International Publishing, 17 Sept. 2015. Web. 22 Mar. 2017.
- Park, H. "Land Subsidence Survey and Analysis Using the Terrestrial LIDAR in Jakarta Bay, Indonesia." *Journal of the Korean Society of Marine Environment & Safety* 19.3 (2013): 233-40. Web. 25 March 2017.
- Peck, R., W. Hanson, and T. Thornburn. "Foundation Engineering." John Wiley & Sons, 1974. Web. 18 Jan. 2016.
- Plaxis Version 8. *Material Models Manual*. Web. 9 Feb. 2017.
- Puradimaja, D. et al. "Sumbang Saran Untuk Penataan Ruang Kawasan Jabotabek Punjur." *Geology Workshop of ITB* (2008). Web. 25 March 2017.
- Schulze, H., and H. Duddeck. "Spannungen in schildvorgetriebenen tunnels." *Beton- und Stahlbetonbau*, 8.59 (1964). Web. 22 Jan. 2017.
- Shalabi, F., E. Cording, and S. Paul. "Sealant behavior of gasketed segmental tunnel lining - Conceptual model." *Geomechanics and Tunneling* 9.4 (2016): 345-55. Web. 29 June 2017.
- Shi, C., C. Cao, M. Lei, L. Peng, and J. Shen. "Time-dependent performance and constitutive model of EPDM rubber gasket used for tunnel segment joints." *Tunneling and Underground Space Technology* 50 (2015): 490-98. Web. 6 July 2017.
- Smith, J., R. Satar, A. Wiryawan, T. Boothman, and Price Waterhouse Coopers. *Indonesian Infrastructure: Stable foundations for growth*. Rep. no. 1. 2nd ed. 2016. Web.
- Sowers, G. *Introductory Soil Mechanics and Foundations: Geotechnical Engineering*. Prentice Hall, 1979. Web. 9 July 2017.
- Suhonen, K. "Creep on Soft Clay." Thesis. Aalto University, 2010. 07 Jan. 2010. Web. 19 Feb. 2017.
- Suklje, L. *Rheological aspects of soil mechanics*. Bath, United Kingdom: Pitman Press, 1969. Web. 5 Feb. 2017.
- Sutanudjaja, E. and G. Erkens. "Modeling falling groundwater tables in major cities of the world." *Paper of EGU General Assembly* (2016). Web. 25 March 2017.
- Terzaghi, K., and R. Peck. *Soil Mechanics in Engineering Practice - Second Edition*. New York City, United States of America: John Wiley & Sons, 1967. Web. 18 Jan. 2016.
- Tirtomihardjo, H. "Groundwater Resource Potential in Indonesia and its Management." Asia Pacific Water Forum (APWF) Regional Water Knowledge Hub for Groundwater Management Launch Meeting. Plaza Athenee, Bangkok. 3 June 2011. IGES Official Website. Web. 21 Mar. 2017.
- United Nations. "World's population increasingly urban with more than half living in urban areas | UN DESA Department of Economic and Social Affairs." United Nations, 10 July 2014. Web. 22 Dec. 2016.

- USFHWA. "Geotechnical Aspects of Pavements Reference Manual." U.S. Department of Transportation/Federal Highway Administration. 19 Oct. 2015. Web. 12 Apr. 2017.
- Van der Waart, T. G. Snap Through of Large Driven Shield Tunnels Reserve Capacity. Thesis. TU Delft, 2010. TU Delft Repository. Web. 20 Mar. 2017.
- Vidayanti, D., P. Simatupang, S. Silalahi. "Korelasi Nilai N-SPT dengan Parameter Kuat Geser Tanah Untuk Wilayah Jakarta dan Sekitarnya." Konferensi Nasional Teknik Sipil 7. 24 Oct. 2013. Web. 22 Jan. 2017.
- Walraven, J., and C. Braam. "Prestressed Concrete". *TU Delft CIE 3150 Dictaat* (2015). Web. 9 Feb. 2017.
- Wazoh, H. N., and S. J. Mallo. "Standard Penetration Test in Engineering Geological Site Investigations – A Review." *The International Journal of Engineering and Science* 3.7 (2014): 40-48. Web. 22 Jan. 2017.
- Wood, A. M. The Circular Tunnel in Elastic Ground. *Geotechnique* 3.1 (1975): 115-127.
- Wu, H., S. Shen, S. Liao, and Z. Yin. "Longitudinal structural modelling of shield tunnels considering shearing dislocation between segmental rings." *Tunneling and Underground Space Technology* 50 (2015): 317-23. Web. 9 May 2017.
- Wu, H., R. Huang, W. Sun, S. Shen et al. "Leaking behavior of shield tunnels under the Huangpu River of Shanghai with induced hazards." *Natural Hazards* 70.2 (2013): 1115-132. Web.
- Xia, J., G. Huang, and S. Yan. "Behaviour and engineering implications of recent floodplain soft soil along lower reaches of the Yangtze River in Western Nanjing, China." *Engineering Geology* 87.1-2 (2006): 48-59. Web. 9 June 2017.
- Zhang, P. "Darcy's Law and Hydraulic Conductivity." EAS 4460 Course. New York City. City University of New York. Web. 18 Jan. 2017.
- Zhou, S., H. Di, J. Xiao, and P. Wang. "Differential Settlement and Induced Structural Damage in a Cut-and-Cover Subway Tunnel in a Soft Deposit." *Journal of Performance of Constructed Facilities* 30.5 (2016). Web. 18 April 2017.
- Zimmerman, R. "Flow in Porous Media". *Imperial College Lecture Material* (2002). Web. 20 Feb. 2017.

Appendix A: REVIEWS AND CALCULATIONS

A.1. Geotechnical Data and Calculation

A.1.1 SPT Data

These three SPT results were extracted from a databank, which contains 461 reports all around Jakarta and was originally used for seismic study. The other one that was used in the analysis, BH 462, was gathered from Mercubuana (2015).

Project Name: Perkantoran 12 Lantai
 Reduce Level: 131DB1
 Bor No.: Jl. Gajah Mada No.27A Jakpus
 Location: 3
 Long.lat: 106.817144
 -6.152155

BH88

No.	Soil Type	Type	Number of sublayers in layer	Thickness (m)	g (kN/m ³)	VS-used	Location of water table	Depth		N-SPT	Ohta and Gohto	Imai and Tonouchi	Vs (m/dt)	Vs (m/dt)	Vs (m/dt)	Vs (m/dt) DHT	Remarks
1	Clay	2	2	3.00	15.00	130.44		0.00	-	3.00	3	124.06	136.82	130.44	Soft	Very Loose	Very Loose
2	Clay	2	1	1.00	15.00	163.61	W	3.00	-	4.00	6	157.14	170.08	163.61	Loose	Loose	Loose
3	Clayey Silt	1	1	2.00	15.00	143.30		4.00	-	6.00	4	136.85	149.75	143.30	Soft	Very Loose	Soft
4	Clay	1	1	1.80	17.00	220.78		6.00	-	7.80	15	214.78	226.79	220.78	Stiff	Medium Dense	Stiff
5	Clayey Silt	1	1	1.60	17.00	230.01		8.00	-	9.60	17	224.15	235.88	230.01	Very Stiff	Medium Dense	Very Stiff
6	Clayey Silt	1	1	2.00	17.00	225.49		10.00	-	12.00	16	219.56	231.43	225.49	Very Stiff	Medium Dense	Very Stiff
7	Silt	1	1	1.80	18.00	257.48		12.00	-	13.80	24	252.12	262.85	257.48	Very Stiff	Medium Dense	Very Stiff
8	Coarse Sand	2	1	1.60	18.00	327.40		14.00	-	15.60	50	323.82	330.98	327.40	Hard	Very Dense	Very Dense
9	Coarse Sand	2	1	2.00	18.00	327.40		16.00	-	18.00	50	323.82	330.98	327.40	Hard	Very Dense	Very Dense
10	Coarse Sand	2	1	0.80	18.00	327.40		18.00	-	18.80	50	323.82	330.98	327.40	Hard	Very Dense	Very Dense
11	Sand	2	1	2.00	18.00	323.05		20.00	-	22.00	48	319.34	326.76	323.05	Hard	Dense	Dense
12	Sand	2	1	2.00	18.00	316.30		22.00	-	24.00	45	312.39	320.21	316.30	Hard	Dense	Dense
13	silt	1	1	1.80	18.00	276.99		24.00	-	25.80	30	272.05	281.93	276.99	Very Stiff	Medium Dense	Very Stiff
14	Silt	1	1	2.00	18.00	296.67		26.00	-	28.00	37	292.22	301.12	296.67	Hard	Dense	Hard
15	Silt	1	1	2.00	18.00	270.81		28.00	-	30.00	28	265.72	275.89	270.81	Very Stiff	Medium Dense	Very Stiff
16	Silt	1	1	2.00	18.00	327.40		30.00	-	32.00	50	323.82	330.98	327.40	Hard	Very Dense	Hard
17	Cemented Sand	2	1	2.00	18.00	329.53		32.00	-	34.00	51	326.01	333.04	329.53	Hard	Very Dense	Very Dense
18	Silt	1	1	2.00	18.00	242.57		34.00	-	36.00	20	236.92	248.23	242.57	Very Stiff	Medium Dense	Very Stiff
19	Silt	1	1	2.00	18.00	311.63		36.00	-	38.00	43	307.58	315.67	311.63	Hard	Dense	Hard
20	Cemented Sand	2	1	2.00	18.00	285.77		38.00	-	40.00	33	281.04	290.49	285.77	Hard	Dense	Dense
21	clay	1	10	30.00	19.00	313.09		40.00	-	70.00							
22	clay	1	10	30.00	19.00	340.99		70.00	-	100.00							
23	clay	1	10	30.00	19.00	368.89		100.00	-	130.00							
24	clay	1	10	30.00	19.00	396.78		130.00	-	160.00							
25	clay	1	10	30.00	19.00	424.68		160.00	-	190.00							
26	clay	1	10	30.00	19.00	452.58		190.00	-	220.00							
27	clay	1	10	30.00	19.00	480.48		220.00	-	250.00							
28	clay	1	10	30.00	19.00	508.37		250.00	-	280.00							
29	clay	1	10	30.00	19.00	536.27		280.00	-	310.00							
30	clay	1	10	30.00	19.00	564.17		310.00	-	340.00							
31	clay	1	10	30.00	19.00	592.06		340.00	-	370.00							
32	clay	1	10	30.00	19.00	619.96		370.00	-	400.00							
33	clay	1	10	30.00	19.00	647.86		400.00	-	430.00							
34	clay	1	10	30.00	19.00	675.75		430.00	-	460.00							
35	clay	1	10	30.00	19.00	703.65		460.00	-	490.00							
36	clay	1	10	30.00	19.00	731.55		490.00	-	520.00							
37	clay	1	10	30.00	19.00	759.45		520.00	-	550.00							
38	Rock	0				760.00		550.00	-								

Project Name: Hayam Wuruk
 Reduce Level: 65DB1
 Bor No.:
 Location: 4.45
 Long.lat: 106.818302
 -6.155379

BH58

No.	Soil Type	Type	Number of sublayers in layer	Thickness (m)	g (kN/m ³)	VS-used	Location of water table	Depth		N-SPT	Ohta and Gohto	Imai and Tonouchi	Vs (m/dt)	Vs (m/dt)	Vs (m/dt)	Vs (m/dt) DHT	Remarks
1	Silty Clay	1	1	2.45	16.65	114.25		0.00	-	2.45	2	108.04	120.46	114.25	Very Soft	Very Loose	Very Soft
2	Silty Clay	1	1	2.00	16.65	130.44		2.45	-	4.45	3	124.06	136.82	130.44	Soft	Very Loose	Soft
3	Silty Clay	1	1	2.00	16.65	154.15	W	4.45	-	6.45	5	147.67	160.62	154.15	Medium Stiff	Loose	Medium Stiff
4	Silty Clay	1	1	2.00	16.18	143.30		6.45	-	8.45	4	136.85	149.75	143.30	Soft	Very Loose	Soft
5	Silty Clay	1	1	2.00	15.89	260.95		8.45	-	10.45	25	255.65	266.24	260.95	Very Stiff	Medium Dense	Very Stiff
6	Clayey Silt	1	1	2.00	18.00	270.81		10.45	-	12.45	28	265.72	275.89	270.81	Very Stiff	Medium Dense	Very Stiff
7	Clayey Silt	1	1	2.00	18.00	225.49		12.45	-	14.45	16	219.56	231.43	225.49	Very Stiff	Medium Dense	Very Stiff
8	Clayey Silt	1	1	1.93	18.00	327.40		14.45	-	16.38	50	323.82	330.98	327.40	Hard	Very Dense	Hard
9	Sandy Silt	1	1	1.98	18.00	327.40		16.38	-	18.36	50	323.82	330.98	327.40	Hard	Very Dense	Hard
10	Sand	2	1	1.84	18.00	327.40		18.36	-	20.2	50	323.82	330.98	327.40	Hard	Very Dense	Very Dense
11	Sand	2	1	2.25	18.00	294.02		20.20	-	22.45	36	289.50	298.54	294.02	Hard	Dense	Dense
12	Sandy Silt	1	1	2.00	18.00	270.81		22.45	-	24.45	28	265.72	275.89	270.81	Very Stiff	Medium Dense	Very Stiff
13	Clayey Silt	1	1	2.00	18.00	242.57		24.45	-	26.45	20	236.92	248.23	242.57	Very Stiff	Medium Dense	Very Stiff
14	Sand	2	1	1.76	18.00	327.40		26.45	-	28.21	50	323.82	330.98	327.40	Hard	Very Dense	Very Dense
15	Sand	2	1	2.24	18.00	335.75		28.21	-	30.45	54	332.43	339.07	335.75	Hard	Very Dense	Very Dense
16	Sand	2	1	1.89	18.00	327.40		30.45	-	32.34	50	323.82	330.98	327.40	Hard	Very Dense	Very Dense
17	Sand	2	1	1.97	18.00	327.40		32.34	-	34.31	50	323.82	330.98	327.40	Hard	Very Dense	Very Dense
18	Sand	2	1	1.92	18.00	327.40		34.31	-	36.23	50	323.82	330.98	327.40	Hard	Very Dense	Very Dense
19	Sand	2	1	2.22	18.00	333.70		36.23	-	38.45	53	330.31	337.09	333.70	Hard	Very Dense	Very Dense
20	Sand	2	1	2.00	18.00	349.42		38.45	-	40.45	61	346.53	352.30	349.42	Hard	Very Dense	Very Dense
21	Clayey Silt	1	1	2.00	18.00	246.48		40.45	-	42.45	21	240.89	252.06	246.48	Very Stiff	Medium Dense	Very Stiff
22	Clayey Silt	1	1	1.91	18.00	225.49		42.45	-	44.36	16	219.56	231.43	225.49	Very Stiff	Medium Dense	Very Stiff
23	Clayey Silt	1	1	2.09	18.00	238.54		44.36	-	46.45	19	232.81	244.26	238.54	Very Stiff	Medium Dense	Very Stiff
24	Clayey Silt	1	1	2.00	18.00	257.48		46.45	-	48.45	24	252.12	262.85	257.48	Very Stiff	Medium Dense	Very Stiff
25	Clayey Silt	1	1	2.00	18.00	253.92		48.45	-	50.45	23	248.48	259.36	253.92	Very Stiff	Medium Dense	Very Stiff
26	Clayey Silt	1	1	1.91	18.00	294.02		50.45	-	52.36	36	289.50	298.54	294.02	Hard	Dense	Hard
27	Clayey Silt	1	1	2.09	17.00	215.86		52.36	-	54.45	14	209.79	221.93	215.86	Stiff	Medium Dense	Stiff
28	Clayey Silt	1	1	2.00	17.00	225.49		54.45	-	56.45	16	219.56	231.43	225.49	Very Stiff	Medium Dense	Very Stiff
29	Sandy Silt	1	1	2.00	17.00	210.69		56.45	-	58.45	13	204.55	216.82	210.69	Stiff	Medium Dense	Stiff
30	Sandy Silt	1	1	-38.45	17.00	220.78		58.45	-	0	15	214.78	226.79	220.78	Stiff	Medium Dense	Stiff

No.	Soil Type	Type	Number of sublayers in layer	Thickness (m)	g (kN/m3)	VS-used	Location of water table	Depth			N-SPT	Ohta and Gohito	Imai and Tonouchi	Vs (m/dt)	Vs (m/dt)	Vs (m/dt)	Vs (m/dt) DHT	Remarks
1	silty clay	1	1	2.25	15.00	163.61		0.00	-	2.25	6	157.14	170.08	163.61	Medium Stiff	Loose		Medium Stiff
2	silty clay	1	1	1.50	15.00	143.30		2.25	-	3.75	4	136.85	149.75	143.30	Soft	Very Loose		Soft
3	silty clay	1	1	1.25	15.00	172.07		3.75	-	5.00	7	165.63	178.52	172.07	Medium Stiff	Loose		Medium Stiff
4	silty clay	1	1	1.75	15.00	179.75	W	5.00	-	6.75	8	173.34	186.16	179.75	Medium Stiff	Loose		Medium Stiff
5	silty clay	1	1	1.50	15.00	193.36		6.75	-	8.25	10	187.05	199.68	193.36	Stiff	Loose		Stiff
6	silty clay	1	1	1.50	15.00	179.75		8.25	-	9.75	8	173.34	186.16	179.75	Medium Stiff	Loose		Medium Stiff
7	silty clay	1	1	1.50	15.00	199.48		9.75	-	11.25	11	193.23	205.74	199.48	Stiff	Medium Dense		Stiff
8	silty clay	1	1	1.50	16.00	179.75		11.25	-	12.75	8	173.34	186.16	179.75	Medium Stiff	Loose		Medium Stiff
9	silty clay	1	1	1.50	16.00	186.81		12.75	-	14.25	9	180.45	193.18	186.81	Stiff	Loose		Stiff
10	clayey silt	1	1	1.50	17.00	238.54		14.25	-	15.75	19	232.81	244.26	238.54	Very Stiff	Medium Dense		Very Stiff
11	clayey silt	1	1	1.50	17.00	242.57		15.75	-	17.25	20	236.92	248.23	242.57	Very Stiff	Medium Dense		Very Stiff
12	clayey silt	1	1	1.50	17.00	246.48		17.25	-	18.75	21	240.89	252.06	246.48	Very Stiff	Medium Dense		Very Stiff
13	silty sand	2	1	1.50	18.00	327.40		18.75	-	20.25	50	323.82	330.98	327.40	Hard	Very Dense		Very Dense
14	silty sand	2	1	1.50	18.00	327.40		20.25	-	21.75	50	323.82	330.98	327.40	Hard	Very Dense		Very Dense
15	silty sand	2	1	1.50	18.00	327.40		21.75	-	23.25	50	323.82	330.98	327.40	Hard	Very Dense		Very Dense
16	silty sand	2	1	1.50	18.00	327.40		23.25	-	24.75	50	323.82	330.98	327.40	Hard	Very Dense		Very Dense
17	clayey silt	1	1	1.50	18.00	260.95		24.75	-	26.25	25	255.65	266.24	260.95	Very Stiff	Medium Dense		Very Stiff
18	clayey silt	1	1	1.50	18.00	327.40		26.25	-	27.75	50	323.82	330.98	327.40	Hard	Very Dense		Hard
19	silty sand	2	1	1.50	18.00	327.40		27.75	-	29.25	50	323.82	330.98	327.40	Hard	Very Dense		Very Dense
20	silty sand	2	1	1.50	18.00	327.40		29.25	-	30.75	50	323.82	330.98	327.40	Hard	Very Dense		Very Dense
21	silty sand	2	1	1.50	18.00	327.40		30.75	-	32.25	50	323.82	330.98	327.40	Hard	Very Dense		Very Dense
22	sand	2	1	1.50	18.00	327.40		32.25	-	33.75	50	323.82	330.98	327.40	Hard	Very Dense		Very Dense
23	sand	2	1	1.50	18.00	327.40		33.75	-	35.25	50	323.82	330.98	327.40	Hard	Very Dense		Very Dense
24	sand	2	1	1.50	18.00	327.40		35.25	-	36.75	50	323.82	330.98	327.40	Hard	Very Dense		Very Dense
25	sand	2	1	1.50	18.00	327.40		36.75	-	38.25	50	323.82	330.98	327.40	Hard	Very Dense		Very Dense
26	sand	2	1	1.50	18.00	327.40		38.25	-	39.75	50	323.82	330.98	327.40	Hard	Very Dense		Very Dense
27	sand	2	1	1.50	18.00	327.40		39.75	-	41.25	50	323.82	330.98	327.40	Hard	Very Dense		Very Dense
28	clayey silt	1	1	1.50	18.00	253.92		41.25	-	42.75	23	248.48	259.36	253.92	Very Stiff	Medium Dense		Very Stiff
29	clayey silt	1	1	1.50	18.00	257.48		42.75	-	44.25	24	252.12	262.85	257.48	Very Stiff	Medium Dense		Very Stiff
30	clayey silt	1	1	1.50	18.00	264.32		44.25	-	45.75	26	259.09	269.54	264.32	Very Stiff	Medium Dense		Very Stiff
31	clayey silt	1	1	1.50	18.00	253.92		45.75	-	47.25	23	248.48	259.36	253.92	Very Stiff	Medium Dense		Very Stiff
32	clayey silt	1	1	1.50	18.00	264.32		47.25	-	48.75	26	259.09	269.54	264.32	Very Stiff	Medium Dense		Very Stiff
33	clayey silt	1	1	0.75	18.00	257.48		48.75	-	49.50	24	252.12	262.85	257.48	Very Stiff	Medium Dense		Very Stiff

A.1.2 Standard Penetration Test

The standard penetration test (SPT) is one of the physical methods of soil investigation and is one of the most popular methods in field measurement. In the SPT, samples of soil layer, extracted with a spoon sampler, are characterized based on the number of blows (N-SPT) the hammer needs to penetrate as far as 150 millimeters. However, due to its popularity, derivations of SPT methods are found around the globe, which stemmed from the local environmental condition and availability of instrument.

The practice of SPT in the field is far from accurate and, as mentioned before, methods may vary. Therefore, corrections must be made to the test results before it is interpreted to other soil characteristics. An example of inaccuracy is the discrepancy between the amount of energy that is transferred from the hammer to the drill rod and from the drill rod to the soil. Apparently, only 60% of the energy input transferred into the soil. Aside, other sources of inaccuracy exist and each of them is represented with correction factor. Finally, the N-SPT should be processed with the equation below.

$$N_{60} = N \frac{\eta_H \eta_B \eta_S \eta_R}{60}$$

$$N_{1(60)} = \frac{2.2 N_{60}}{\left(1.2 + \frac{\sigma'_0}{P_A}\right)}$$

where N_{60} is the corrected blow counts, N is the obtained blow counts from field measurements, η_H is a correction factor related to hammer efficiency, η_B is a correction factor related to the borehole diameter, η_S is a correction factor related to sampler, and η_R is a correction factor related to rod length. Furthermore, correction due to overburden comes next. It is necessary because during the examination, the sample is no longer under effective vertical pressure (σ'_0), instead it is under atmospheric pressure (P_A) of 100 kPa. The corrections are shown in the tables below.

Table A.1: Hammer efficiency correction factor in % (Das, 2011)

Country	Hammer Type	Hammer Release	η_H (%)
Japan	Donut	Free fall	78
	Donut	Rope and pulley	67
United States	Safety	Rope and pulley	60
	Donut	Rope and pulley	45
Argentina	Donut	Rope and pulley	45

China	Donut	Free fall	60
	Donut	Rope and pulley	50

Table A.2: Borehole diameter correction factor (Das, 2011)

Diameter (mm)	η_B
60-120	1
150	1.05
200	1.15

Table A.3: Sampler correction factor (Das, 2011)

Variable	η_S
Standard sampler	1
With liner for dense sand and clay	0.8
With liner for loose sand	0.9

Table A.4: Correction factors due to difference in rod length (Das, 2011)

Rod Length (m)	η_R
>10	1
6-10	0.95
4-6	0.85
0-4	0.75

A.1.3 Stratigraphy Simplification

BH 88 GWT 3

Thickness	Start (m)	End (m)	Classification	γ (kN/m ³)	N-SPT	σ (kN/m ²)	σ' (kN/m ²)	$N_{(60)}$	$N_{(100)}$	$N_{(100)}/N_{(60)}$	σ'_p (kN/m ²)	OCR
6.00	0.00	6.00	Clay	15.00	4	90.00	60.57	5	6	1.20	296.44	4.89
6.00	6.00	12.00	Clay	17.00	16	192.00	103.71	18	18	1.00	737.82	7.11
1.80	12.00	13.80	Silt	18.00	24	224.40	118.45	27	25	0.93	969.09	8.18
10.20	13.80	24.00	Sand	18.00	49	408.00	201.99	56	38	0.68	1371.81	6.79
6.00	24.00	30.00	Silt	18.00	32	516.00	251.13	36	22	0.61	871.54	3.47
4.00	30.00	34.00	Sand	18.00	51	588.00	283.89	58	32	0.55	1189.46	4.19
2.00	34.00	36.00	Silt	18.00	20	624.00	300.27	23	12	0.52	526.98	1.76
4.00	36.00	40.00	Sand	18.00	38	696.00	333.03	43	21	0.49	838.53	2.52

BH 58 GWT 4.45

Thickness	Start (m)	End (m)	Classification	γ (kN/m ³)	N-SPT	σ (kN/m ²)	σ' (kN/m ²)	$N_{(60)}$	$N_{(100)}$	$N_{(100)}/N_{(60)}$	σ'_p (kN/m ²)	OCR
4.45	0.00	4.45	Clay	16.50	3	73.43	73.43	3	4	1.33	211.73	2.88
6.00	4.45	10.45	Clay	15.90	10	168.83	109.97	11	11	1.00	490.26	4.46
4.00	10.45	14.45	Silt	18.00	25	240.83	142.73	29	24	0.83	936.81	6.56
8.00	14.45	22.45	Sand	18.00	50	384.83	208.25	57	38	0.67	1371.81	6.59
4.00	22.45	26.45	Silt	18.00	28	456.83	241.01	32	19	0.59	771.69	3.20
13.55	26.45	40.00	Sand	18.00	53	700.73	351.98	60	28	0.47	1064.67	3.02

BH 462 GWT 2.4

Thickness	Start (m)	End (m)	Classification	γ (kN/m ³)	N-SPT	σ (kN/m ²)	σ' (kN/m ²)	$N_{(60)}$	$N_{(100)}$	$N_{(100)}/N_{(60)}$	σ'_p (kN/m ²)	OCR
4.50	0.00	4.5	Clay	15.2	3	68.40	47.80	3	4	1.33	211.73	4.43
4.50	4.50	9	Clay	14.4	8	133.20	68.45	9	11	1.22	490.26	7.16
4.50	9.00	13.5	Silt	15.5	20	202.95	94.06	23	23	1.00	904.29	9.61
6.00	13.50	19.5	Sand	17.5	49	307.95	140.20	56	47	0.84	1636.50	11.67
6.00	19.50	25.5	Clay	17.5	28	412.95	186.34	32	23	0.72	904.29	4.85

BH 186 GWT 4.61

Thickness	Start (m)	End (m)	Classification	γ (kN/m ³)	N-SPT	σ (kN/m ²)	σ' (kN/m ²)	$N_{(60)}$	$N_{(100)}$	$N_{(100)}/N_{(60)}$	σ'_p (kN/m ²)	OCR
11.25	0.00	11.25	Clay	15.00	6	168.75	103.61	7	7	1.00	336.90	3.25
3.00	11.25	14.25	Clay	17.00	8	219.75	125.18	9	8	0.89	376.39	3.01
4.50	14.25	18.75	Silt	18.00	20	300.75	162.04	23	18	0.78	737.82	4.55
6.00	18.75	24.75	Sand	18.00	50	408.75	211.18	57	38	0.67	1371.81	6.50
1.50	24.75	26.25	Silt	18.00	25	435.75	223.46	29	18	0.62	737.82	3.30
15.00	26.25	41.25	Sand	18.00	50	705.75	346.31	57	27	0.47	1033.02	2.98

Soil Type	Classification	N ₁₍₆₀₎					
		BH 88	BH 58	BH 462	BH 168	Average	Design
C1	Clay	6	4	4	7	5	4
C2	Clay	18	11	11	8	12	12
Si1	Silt	25	24	23	18	22	20
SA1	Sand	38	38	47	38	40	40
Si1	Silt	22	28	23	18	25	20
SA1	Sand	32		-	27		40
Si2	Silt	12		-	-		10
SA2	Sand	21	-	-	-	25	

A.1.4 Earth Pressure Validation

The analytical estimation is required to check the outcome of the numerical analysis, whether or not it makes sense. The cross section in Figure A.1 is used for the analytical calculation of earth pressure.

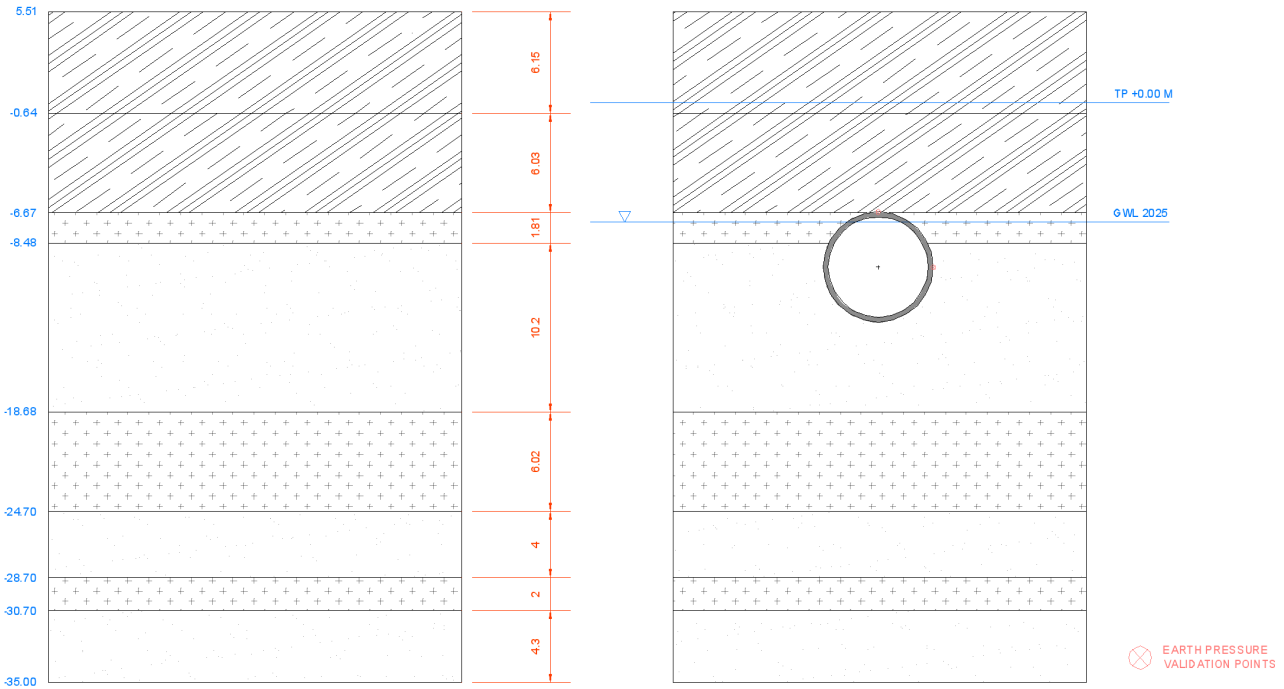


Figure A.1: Simplified soil profile for analytical estimation

Calculation details are presented as follows.

$$\gamma_1 := 15 \frac{\text{kN}}{\text{m}^3} \quad d_{1T} := 6.15\text{m} \quad d_{1S} := 6.15\text{m}$$

$$\gamma_2 := 17 \frac{\text{kN}}{\text{m}^3} \quad d_{2T} := 5.96\text{m} \quad d_{2S} := 6.03\text{m}$$

$$\gamma_3 := 18 \frac{\text{kN}}{\text{m}^3} \quad d_{3S} := 1.81\text{m}$$

$$d_{4S} := 1.45\text{m}$$

$$\gamma_4 := 18 \frac{\text{kN}}{\text{m}^3}$$

$$\gamma_W := 9.81 \frac{\text{kN}}{\text{m}^3}$$

Year 2025

$$h_{W1} := 2.7625\text{m}$$

$$\sigma_{VT} := \gamma_1 \cdot d_{1T} + \gamma_2 \cdot d_{2T} = 193.57\text{ kPa}$$

$$\sigma_{VS} := \gamma_1 \cdot d_{1S} + \gamma_2 \cdot d_{2S} + \gamma_3 \cdot d_{3S} + \gamma_4 \cdot d_{4S} = 253.44\text{ kPa}$$

$$\sigma_{VTeff} := \gamma_1 \cdot d_{1T} + \gamma_2 \cdot d_{2T} = 193.57\text{ kPa}$$

$$\sigma_{VSeff} := \gamma_1 \cdot d_{1S} + \gamma_2 \cdot d_{2S} + \gamma_3 \cdot d_{3S} + \gamma_4 \cdot d_{4S} - \gamma_W \cdot h_{W1} = 226.34\text{ kPa}$$

The calculation results fall within the right ranges on the numerical analysis outcome, shown in Figure A.2.

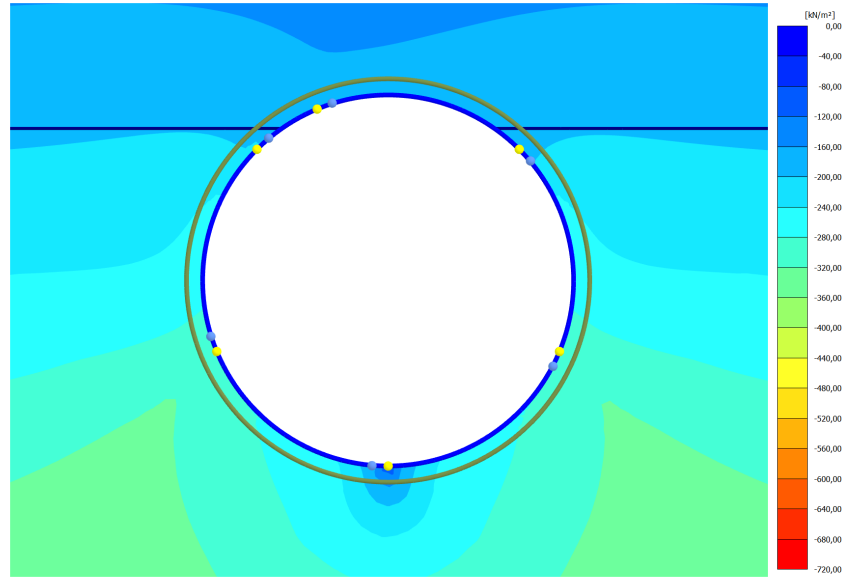


Figure A.2: Total vertical earth pressure profile at year 2025 (Scenario A)

A.1.5 Axial Force and Bending Moment

Furthermore, the axial force and bending moment on the tunnel lining is also checked with the analytical estimate. The estimation is performed with the formulas below.

$$N(\theta) = -C_{n0} \frac{(\sigma_v + \sigma_h)}{2} r + C_{n2} \frac{(\sigma_v - \sigma_h)}{2} r \cos(2\theta)$$

$$M(\theta) = -C_M \frac{(\sigma_v - \sigma_h)}{2} r \cos(2\theta)$$

where N represents axial force, M represents bending moment, σ_v is the vertical pressure at the tunnel crown, σ_h is the horizontal soil pressure at the side, r is the radius, and θ is the angular position with respect to the tunnel crown. Moreover, C_{n0} , C_{n2} , and C_M are the coefficients to accommodate soil and structure interaction. These coefficients are defined as shown below.

$$\alpha = \frac{E_S \cdot r^3}{E_T \cdot I}$$

$$\beta = \frac{E_S \cdot r}{E_T \cdot A}$$

$$C_{n0} = \frac{2}{2 + 1.54\beta}$$

$$C_{n2} = \frac{2(1 + 0.064\alpha)}{2 + 0.171\alpha}$$

$$C_M = \frac{4}{4 + 0.032\alpha}$$

Further calculations are shown below.

$$r_{\text{Out}} := 3.325\text{m}$$

$$r_{\text{In}} := 3.025\text{m}$$

$$r_{\text{Avg}} := 0.5(r_{\text{Out}} + r_{\text{In}}) = 3.175\text{m}$$

$$E_g := 45000 \frac{\text{kN}}{\text{m}^2}$$

$$E_C := 14\text{GPa}$$

$$I := \frac{1}{12} \cdot (r_{\text{Out}} - r_{\text{In}})^3 = 2.25 \times 10^{-3} \frac{\text{m}^4}{\text{m}}$$

$$\text{Area} := (r_{\text{Out}} - r_{\text{In}}) = 0.3 \frac{\text{m}^2}{\text{m}}$$

$$\alpha := \frac{E_g \cdot r_{\text{Avg}}^3}{E_C \cdot I} = 45.723$$

$$\beta := \frac{E_g \cdot r_{\text{Avg}}}{E_C \cdot \text{Area}} = 0.034$$

$$C_{n0} := \frac{2}{2 + 1.54\beta} = 0.974$$

$$C_{n2} := \frac{2(1 + 0.064 \cdot \alpha)}{2 + 0.171 \cdot \alpha} = 0.8$$

$$C_M := \frac{4}{4 + 0.032\alpha} = 0.732$$

$$\theta := 38\text{deg}$$

$$K_0 := 1 - \sin(\theta) = 0.384$$

$$v_{\text{ur}} := 0.2$$

$$\text{OCR} := 2$$

$$K_{0X} := K_0 \cdot \text{OCR} - (\text{OCR} - 1) \cdot \frac{v_{\text{ur}}}{1 - v_{\text{ur}}} = 0.519$$

$$\varphi_{\text{Crown}} := 0\text{deg}$$

$$\sigma_{\text{HS}} := \sigma_{\text{VS}} \cdot K_{0X} = 131.454\text{kPa}$$

$$N_{\text{Crown}} := -r_{\text{Avg}} \cdot C_{n0} \cdot \frac{(\sigma_{\text{VT}} + \sigma_{\text{HS}})}{2} + r_{\text{Avg}} \cdot C_{n2} \cdot \frac{(\sigma_{\text{VT}} - \sigma_{\text{HS}})}{2} \cdot \cos(2\varphi_{\text{Crown}}) = -423.94 \frac{\text{kN}}{\text{m}}$$

$$M_{\text{Crown}} := -r_{\text{Avg}}^2 \cdot C_M \cdot \frac{(\sigma_{\text{VT}} - \sigma_{\text{HS}})}{4} \cdot \cos(2\varphi_{\text{Crown}}) = -114.618 \text{kN} \cdot \frac{\text{m}}{\text{m}}$$

$$\varphi_{\text{Springline}} := 90\text{deg}$$

$$N_{\text{Springline}} := -r_{\text{Avg}} \cdot C_{n0} \cdot \frac{(\sigma_{\text{VT}} + \sigma_{\text{HS}})}{2} + r_{\text{Avg}} \cdot C_{n2} \cdot \frac{(\sigma_{\text{VT}} - \sigma_{\text{HS}})}{2} \cdot \cos(2\varphi_{\text{Springline}}) = -581.669 \frac{\text{kN}}{\text{m}}$$

$$M_{\text{Springline}} := -r_{\text{Avg}}^2 \cdot C_M \cdot \frac{(\sigma_{\text{VT}} - \sigma_{\text{HS}})}{4} \cdot \cos(2\varphi_{\text{Springline}}) = 114.618 \text{kN} \cdot \frac{\text{m}}{\text{m}}$$

Slight discrepancies were found between the outcomes of analytical and numerical results, shown in Figure A.3 and Figure A.4. The analytical calculations did not take into account the presence of segmental joints, which causes the presence of larger bending moments.

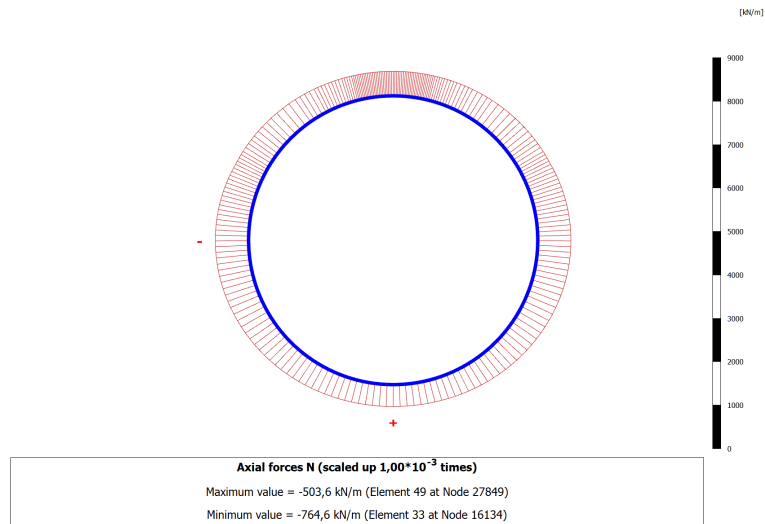


Figure A.3: Axial forces of tunnel lining at 2025 (Scenario A)

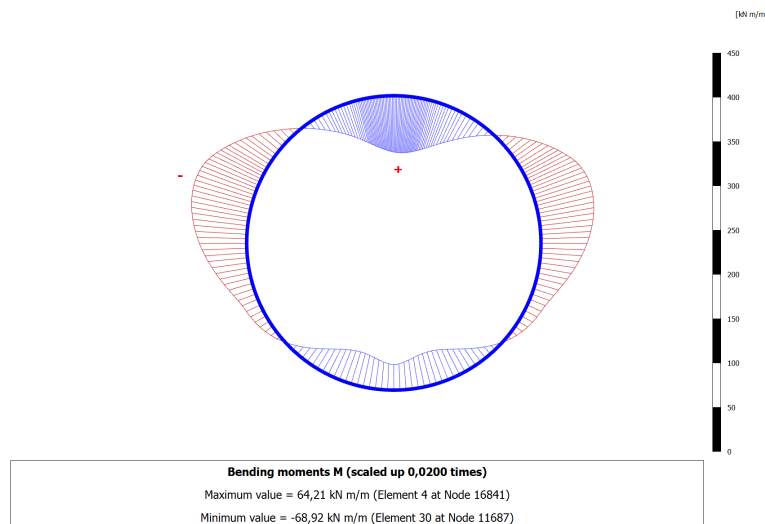


Figure A.4: Bending moment of tunnel lining at 2025 (Scenario A)

A.1.6 SPT Interpretations

BH 88 GWT 3

Thickness	Start (m)	End (m)	Classification	γ (kN/m ³)	N-SPT	σ (kN/m ²)	σ' (kN/m ²)	$N_{(60)}$	$N_{1(60)}$	$N_{1(60)}/N_{(60)}$	σ_p' (kN/m ²)	OCR
6.00	0.00	6.00	Clay	15.00	4	90.00	60.57	5	6	1.20	296.44	4.89
6.00	6.00	12.00	Clay	17.00	16	192.00	103.71	18	18	1.00	737.82	7.11
1.80	12.00	13.80	Silt	18.00	24	224.40	118.45	27	25	0.93	969.09	8.18
10.20	13.80	24.00	Sand	18.00	49	408.00	201.99	56	38	0.68	1371.81	6.79
6.00	24.00	30.00	Silt	18.00	32	516.00	251.13	36	22	0.61	871.54	3.47
4.00	30.00	34.00	Sand	18.00	51	588.00	283.89	58	32	0.55	1189.46	4.19
2.00	34.00	36.00	Silt	18.00	20	624.00	300.27	23	12	0.52	526.98	1.76
4.00	36.00	40.00	Sand	18.00	38	696.00	333.03	43	21	0.49	838.53	2.52

BH 58 GWT 4.45

Thickness	Start (m)	End (m)	Classification	γ (kN/m ³)	N-SPT	σ (kN/m ²)	σ' (kN/m ²)	$N_{(60)}$	$N_{1(60)}$	$N_{1(60)}/N_{(60)}$	σ_p' (kN/m ²)	OCR
4.45	0.00	4.45	Clay	16.50	3	73.43	73.43	3	4	1.33	211.73	2.88
6.00	4.45	10.45	Clay	15.90	10	168.83	109.97	11	11	1.00	490.26	4.46
4.00	10.45	14.45	Silt	18.00	25	240.83	142.73	29	24	0.83	936.81	6.56
8.00	14.45	22.45	Sand	18.00	50	384.83	208.25	57	38	0.67	1371.81	6.59
4.00	22.45	26.45	Silt	18.00	28	456.83	241.01	32	19	0.59	771.69	3.20
13.55	26.45	40.00	Sand	18.00	53	700.73	351.98	60	28	0.47	1064.67	3.02

BH 462 GWT 2.4

Thickness	Start (m)	End (m)	Classification	γ (kN/m ³)	N-SPT	σ (kN/m ²)	σ' (kN/m ²)	$N_{(60)}$	$N_{1(60)}$	$N_{1(60)}/N_{(60)}$	σ_p' (kN/m ²)	OCR
4.50	0.00	4.5	Clay	15.2	3	68.40	47.80	3	4	1.33	211.73	4.43
4.50	4.50	9	Clay	14.4	8	133.20	68.45	9	11	1.22	490.26	7.16
4.50	9.00	13.5	Silt	15.5	20	202.95	94.06	23	23	1.00	904.29	9.61
6.00	13.50	19.5	Sand	17.5	49	307.95	140.20	56	47	0.84	1636.50	11.67
6.00	19.50	25.5	Clay	17.5	28	412.95	186.34	32	23	0.72	904.29	4.85

BH 186 GWT 4.61

Thickness	Start (m)	End (m)	Classification	γ (kN/m ³)	N-SPT	σ (kN/m ²)	σ' (kN/m ²)	$N_{(60)}$	$N_{1(60)}$	$N_{1(60)}/N_{(60)}$	σ_p' (kN/m ²)	OCR
11.25	0.00	11.25	Clay	15.00	6	168.75	103.61	7	7	1.00	336.90	3.25
3.00	11.25	14.25	Clay	17.00	8	219.75	125.18	9	8	0.89	376.39	3.01
4.50	14.25	18.75	Silt	18.00	20	300.75	162.04	23	18	0.78	737.82	4.55
6.00	18.75	24.75	Sand	18.00	50	408.75	211.18	57	38	0.67	1371.81	6.50
1.50	24.75	26.25	Silt	18.00	25	435.75	223.46	29	18	0.62	737.82	3.30
15.00	26.25	41.25	Sand	18.00	50	705.75	346.31	57	27	0.47	1033.02	2.98

A.1.7 Parameter Assignment

Parameter	Established Range	Local Range	Assigned
Consolidation Coefficients (CC, CS, C α)	<p>Most theories (Terzaghi, Peck, Skempton, Skempton, Hong & Onitsuka) linked CC with LL and PI. With LL = 50-70% or PI = 25-45, <u>CC = 0.3-0.7</u>.</p> <p><u>CS = 0.1 to 0.2 CC</u> (Edil & Benson, 2009)</p> <p><u>Cα = 0.03 to 0.1 CC</u> (Knappett & Craig, 2012)</p>	<p>CC = 0.39 to 0.89 (Affandi)</p> <p>CC = 0.28 to 0.81 (Central Jakarta)</p> <p>CC = 0.19 to 0.37 (Firmansyah & Sukamta)</p> <p>CC = 0.471 to 0.491 (BH462)</p> <p>CS = 0.029 to 0.055 (BH462)</p> <p>Cα = 0.005 to 0.03 (Bakr, 2014)</p>	<p><u>Clay 1 (C1)</u> CC = 0.6, CS = 0.08, Cα = 0.05</p> <p><u>Clay 2 (C2)</u> CC = 0.4, CS = 0.07, Cα = 0.03</p> <p><u>Silt 1 (Si1)</u> CC = 0.3, CS = 0.06, Cα = 0.02</p> <p><u>Silt 2 (Si2)</u> CC = 0.5, CS = 0.07, Cα = 0.02</p> <p>Assignment based on Stroud (1974)</p>
Elasticity Moduli (E ₅₀ , E _{OED} , E _{UR})	<p>A lot of empirical correlations between N₆₀ with E.</p> <p><u>E = 750 to 2500 N₆₀</u></p> <p><u>E_{UR} = 3 E_{OED}</u> (Plaxis)</p>	<p>E₅₀ = 1187 to 1208 N₁₍₆₀₎</p> <p>E_{OED} = 1035 N₁₍₆₀₎ (Both by Gouw & Hiasinta, 2012)</p> <p>N₁₍₆₀₎ = 0.47 to 1.33 N₆₀</p>	<p><u>Sand 1 (Sa1)</u> E₅₀ = 4.8E4 kN/m², E_{OED} = 4.14E4 kN/m², E_{UR} = 1.26E5 kN/m²</p> <p><u>Sand 2 (Sa2)</u> E₅₀ = 3.0E4 kN/m², E_{OED} = 2.59E4 kN/m², E_{UR} = 8.28E4 kN/m²</p>
Friction Angle (ϕ)	<p>Correlations between SPT and ϕ were established by Peck, Hanson, Thornburn, and Meyerhof.</p> <p><u>N = 0 to 4, $\phi < 30^\circ$</u> <u>N > 50, $\phi > 45^\circ$</u></p> <p>Furthermore, the empirical study in Japan produced these correlations:</p> <p>$\phi = (20 N_{1(60)})^{0.5} + 15^\circ$ (Osaki, 1959) $\phi = (15 N_{1(60)})^{0.5} + 15^\circ$ (JRA, 1990)</p>	<p>$\phi = (15 N_{1(60)})^{0.5} + 15^\circ$ (Vidayanti, 2013)</p>	<p><u>Clay 1 (C1)</u> $\phi = 22^\circ$</p> <p><u>Clay 2 (C2)</u> $\phi = 27^\circ$</p> <p><u>Silt 1 (Si1)</u> $\phi = 31^\circ$</p> <p><u>Silt 2 (Si2)</u> $\phi = 26^\circ$</p> <p><u>Sand 1 (Sa1)</u> $\phi = 38^\circ$</p> <p><u>Sand 2 (Sa2)</u> $\phi = 33^\circ$</p>
Shear Capacity (S _u)	<p>The correlation derived by Terzaghi-Peck and Kulhawy-Mane is shown below:</p> <p><u>S_u/P_A = 0.06 N₁₍₆₀₎</u></p> <p>Moreover, Terzaghi-Peck and Sowers also provided the range below:</p> <p><u>S_u = 2.5 to 18 N₁₍₆₀₎</u></p>	<p>c_u/P_A = 0.06 N₁₍₆₀₎ (Terzaghi-Peck, Kulhawy-Mane)</p>	<p><u>Clay 1 (C1)</u> c_u = 10 kN/m²</p> <p><u>Clay 2 (C2)</u> c_u = 10 kN/m²</p> <p><u>Silt 1 (Si1)</u> c_u = 15 kN/m²</p> <p><u>Silt 2 (Si2)</u> c_u = 12 kN/m²</p> <p><u>Sand 1 (Sa1)</u> c_u = 0.2 kN/m²</p> <p><u>Sand 2 (Sa2)</u> c_u = 0.2 kN/m²</p>

A.2. Structural Calculations

A.2.1 Concrete Modulus of Elasticity

The accommodation of creep effect starts with the determination of creep coefficient, which follows the diagram shown in Figure A.5.

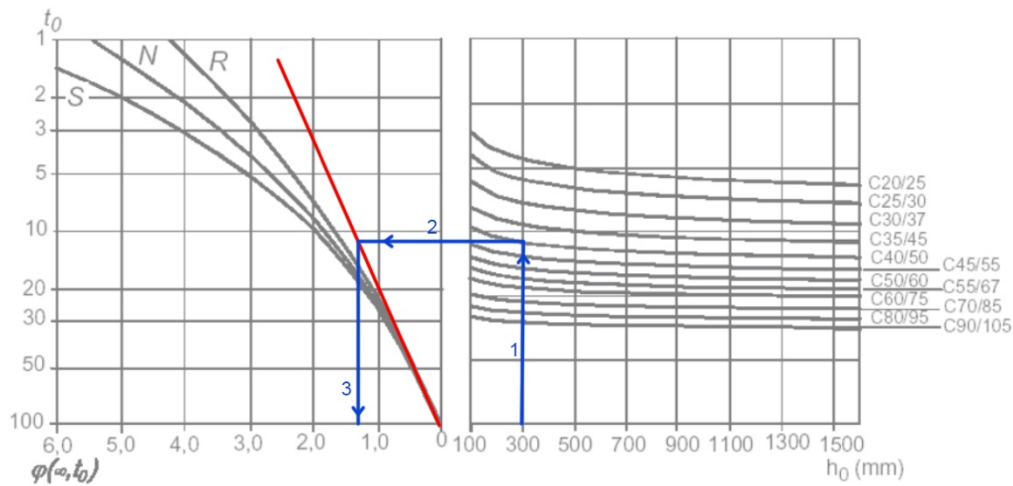


Figure A.5: Creep coefficient as a function of concrete properties (Walraven & Bakker, 2015)

From Figure A.5, the creep coefficient is approximately 1.30. It is then plugged into the formula below to calculate the equivalent elasticity modulus.

$$\phi := 1.30 \quad E_{C0} := 31.4 \text{ GPa} \quad E_{Ct} := \left(\frac{1}{1 + \phi} \right) \cdot E_{C0} = 13.652 \text{ GPa}$$

A.2.2 Longitudinal Joints Analysis

Simple structural analysis was performed to accommodate longitudinal joints and determine the equivalent bending moment. The analysis used the Euler-Bernoulli beam theory and modeled the tunnel as simply-supported beams, one being homogenous and the other one being segmental. These models are shown below.

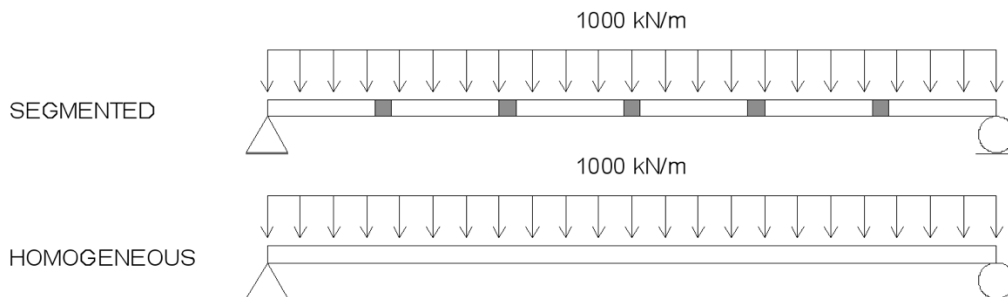


Figure A.6: Beam models to determine equivalent bending moment

The shaded areas along the segmented beam are the locations of joints. Different material was assigned to the joints as it relies on bolt connectors to resist tension force. According to MRTJ technical report, the tunnel has axial stiffness (EA) of $9.2 \cdot 10^5 \text{ kN}$. At a given cross section, the area-averaged elasticity modulus of bolts was calculated to be 0.15 GPa . Thus, the tunnel joints were assumed to manifest $E = 16 \text{ GPa}$ for compression (creep is considered) and $E = 0.15 \text{ GPa}$ for tension. Furthermore, a distributed load was assigned along the beam.

The determination of equivalent EI is based on the ratio between the maximum deflection of homogenous and segmented beam. The maximum deflection (δ) of a beam under a uniform distributed load (q) is calculated with the following equation.

$$\delta = \frac{5}{384} \frac{ql^4}{EI}$$

With identical load, length, and cross section, the equivalent EI is determined as shown below.

$$EI_{Eq} = \frac{\delta_{Homogeneous}}{\delta_{Segmented}} (EI)_{Homogeneous} = \eta (EI)_{Homogeneous}$$

The structural analysis returned $\eta = 0.276$, which then resulted an equivalent EI of $1.14 \cdot 10^8 \text{ kNm}^2$. The outcome of structural analysis is shown in Figure A.7.

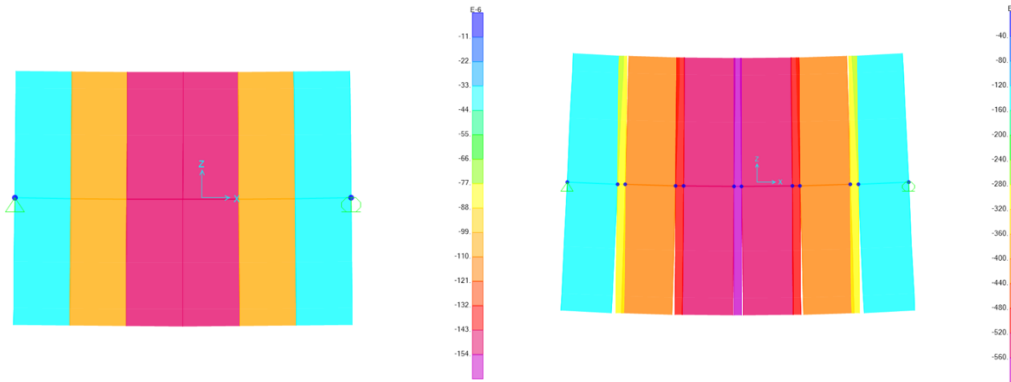


Figure A.7: Deformed profile of (left) homogenous beam and (right) segmented beam

Furthermore, the calculations are presented below.

$$A_{Lg} := \frac{\pi}{4} \cdot (d_{OUT}^2 - d_{IN}^2) = 5.985 \text{ m}^2$$

$$EA_{Compression} := E_{Ct} \cdot A_{Lg} = 8.17 \times 10^7 \text{ kN}$$

$$EA_{Tension} := 9.2 \cdot 10^5 \text{ kN}$$

$$E_{Bolt} := \frac{EA_{Tension}}{A_{Lg}} = 0.154 \text{ GPa}$$

$$\delta_{Homogeneous} := 0.000161 \text{ m}$$

$$\delta_{Segmented} := 0.000584 \text{ m}$$

$$\eta := \frac{\delta_{Homogeneous}}{\delta_{Segmented}} = 0.276$$

$$I_{Lg} := 0.25 \cdot \pi \cdot \left[\left(\frac{d_{OUT}}{2} \right)^4 - \left(\frac{d_{IN}}{2} \right)^4 \right] = 30.232 \text{ m}^4$$

$$EI_{Homogeneous} := E_{Ct} \cdot I_{Lg} = 4.127 \times 10^8 \text{ kN} \cdot \text{m}^2$$

$$EI_{Segmented} := \eta \cdot EI_{Homogeneous} = 1.138 \times 10^8 \text{ kN} \cdot \text{m}^2$$

Instead of using the Euler-Bernoulli beam principles, a more accurate representation of segmented tunnel can be attained with the Timoshenko beam theory. Unlike in Euler-Bernoulli principle, the longitudinal joints of the tunnel, which are susceptible to shear deformation, are acknowledged by the Timoshenko beam theory. Having said that, Timoshenko beam theory yields greater stiffness reduction compared to the Euler-Bernoulli. The following section shows the displacement function derived based on Timoshenko beam theory.

Derivation Based on Timoshenko Beam Theory

The derivation of beam equation based on Timoshenko started with the two following equations.

$$\begin{aligned} \frac{dM}{dx} &= V & \frac{dV}{dx} &= -q \\ -EI\vartheta'' &= GA(v' - \vartheta) & GA(v'' - \vartheta') &= -q \\ EI\vartheta'' + GA(v' - \vartheta) &= 0 & v'' &= \vartheta' - \frac{q}{GA} \\ EI\vartheta''' + GA(v'' - \vartheta') &= 0 & v''' &= \vartheta''; v'''' = \vartheta''' \end{aligned}$$

The combinations of two equations above resulted the following relationship.

$$EIv'''' = q$$

Direct integration of the previous equation brings the series of equations below.

$$\begin{aligned} EIv''' &= qx + C_1 \\ EIv'' &= \frac{1}{2}qx^2 + C_1x + C_2 \\ EIv' &= \frac{1}{6}qx^3 + \frac{1}{2}C_1x^2 + C_2x + C_3 \\ EIv &= \frac{1}{24}qx^4 + \frac{1}{6}C_1x^3 + \frac{1}{2}C_2x^2 + C_3x + C_4 \end{aligned}$$

The four unknown variables (C_1, C_2, C_3, C_4) are solved with four boundary conditions for a simply-supported beam, which are:

$$\begin{aligned} M(0) &= M(L) = 0 \\ v(0) &= v(L) = 0 \end{aligned}$$

As a result, the displacement function of the beam due to uniformly distributed load (q) according to Timoshenko is presented below.

$$v(x) = \frac{qL^4}{24EI} \left(\frac{x^4}{L^4} - \frac{2x^3}{L^3} + \frac{x}{L} \right) + \frac{qL^2}{2GA} \left(\frac{x}{L} - \frac{x^2}{L^2} \right)$$

The displacement function above has an extra component compared to the beam equation derived with Euler-Bernoulli beam theory, which is displayed below.

$$v(x) = \frac{qL^4}{24EI} \left(\frac{x^4}{L^4} - \frac{2x^3}{L^3} + \frac{x}{L} \right)$$

A comparison between the two is displayed in Figure A.8. The curves in Figure A.8 were produced with identical load and beam properties. It is clearly proven that larger displacement can be delivered with Timoshenko beam theory rather than Euler-Bernoulli.

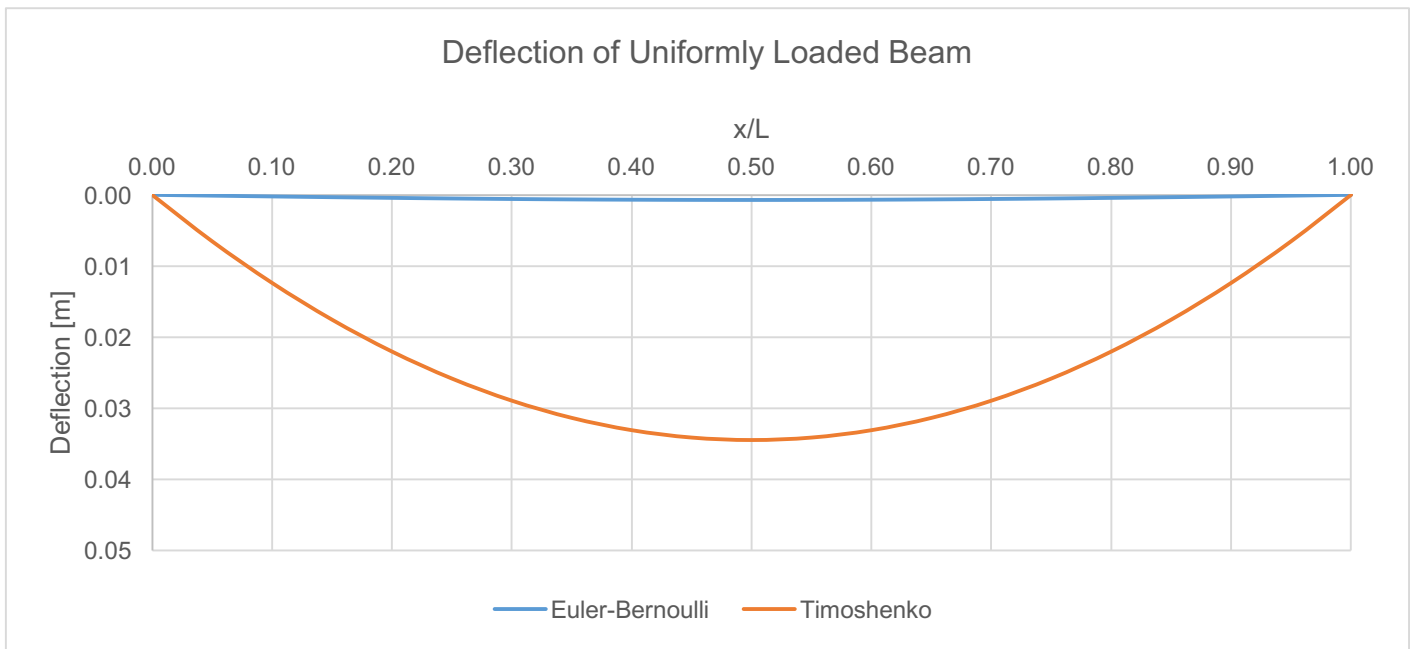


Figure A.8: Deflection of beam based on Euler-Bernoulli and Timoshenko

Despite the recent finding, Euler-Bernoulli beam theory has been widely adopted in tunnel models, including the models in Plaxis, and has proven to be adequate for structural design because it overestimates the internal bending moment.

A.2.3 Segmental Joints Analysis

For this analysis, representative values of normal force and bending moment at the joint are considered. These values were obtained from the 2D cross sectional analysis.

Blom (2002)

The analysis starts with the examination of joints stiffness according to Blom. Throughout the analysis, an average of 550 kN of normal force is assumed. This assumption is based on the average value of normal force as estimated in Section A.1.4.

$$\text{Normal} := 550 \text{ kN} \quad b := 75 \text{ cm} \quad I_t := 25 \text{ cm}^4$$

$$M_{\text{Threshold}} := \text{Normal} \cdot \frac{I_t}{6} = 22.917 \cdot \text{kN} \cdot \text{m}$$

Region 1

$$c_{r1} := b \cdot I_t^2 \cdot \frac{E_{C0}}{12} = 1.227 \times 10^5 \cdot \text{kN} \cdot \text{m}$$

$$\text{Moment}(\theta) := c_{r1} \cdot \theta$$

Region 2

$$\text{Moment}(\theta) := \left(\text{Normal} \cdot \frac{I_t}{2} \right) \cdot \left(1 - \sqrt{\frac{8N}{9\theta \cdot b \cdot I_t \cdot E_{C0}}} \right)$$

The inclusion of non-linearity increases the complexity of rotational stiffness determination. The calculation above was then displayed in a graph that correlates the degree of rotation to bending moment and to rotational stiffness as displayed in Figure A.9. The graph suggested that the rotational stiffness decline upon the growth of the rotation. On the other hand, the bending moment increases with the increase of rotation. However, the

rate of change of both bending moment and rotational stiffness decreases as the rotation increases. Furthermore, the red line on the graph separates region I (left) and II (right).

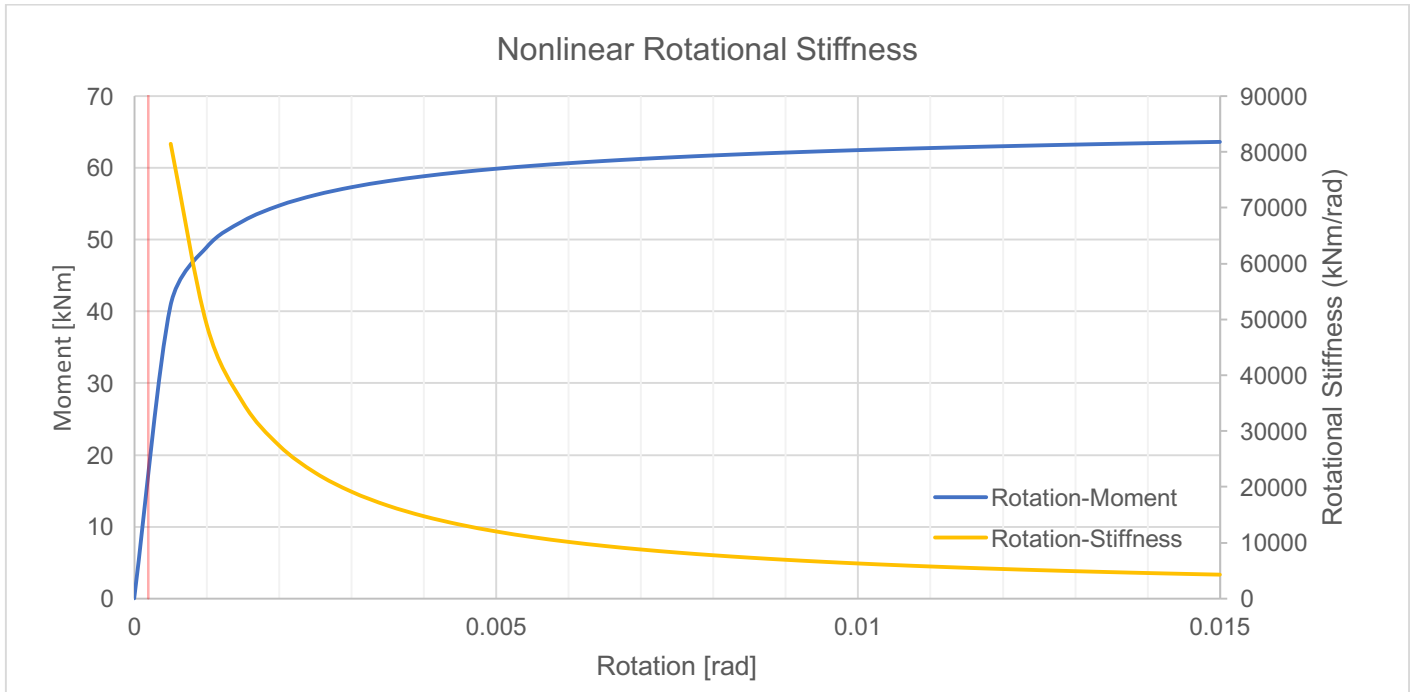


Figure A.9: Non-linearity of rotational stiffness

Lee et al. (2001)

Lee et al. correlated the joint stiffness with the segmental stiffness with a ratio λ . They reported a range of 0.03 to 0.30 for the ratio. With that range, the joint stiffness is calculated as presented below.

$$E_{C0} = 31.4 \cdot \text{GPa} \quad E_{Ct} = 13.652 \cdot \text{GPa}$$

$$b_{\text{Seg}} := 1.5 \text{m}$$

$$d_{\text{Seg}} := 30 \text{cm}$$

$$I_{\text{Seg}} := \frac{1}{12} (b_{\text{Seg}} \cdot d_{\text{Seg}}^3) = 3.375 \times 10^{-3} \text{m}^4$$

$$EI_{\text{Seg}} := (E_{Ct} \cdot I_{\text{Seg}}) = 4.608 \times 10^4 \cdot \text{kN} \cdot \text{m}^2$$

$$A_{\text{Tan}} := b_{\text{Seg}} \cdot d_{\text{Seg}} = 0.45 \text{m}^2$$

$$EA_{\text{Seg}} := E_{Ct} \cdot A_{\text{Tan}} = 6.143 \times 10^6 \cdot \text{kN}$$

$$\lambda_{\text{Min}} := 0.03 \quad \lambda_{\text{Max}} := 0.3$$

$$K_{\Theta \text{Min}} := \lambda_{\text{Min}} \cdot \frac{EI_{\text{Seg}}}{1 \text{m}} = 1.382 \times 10^3 \cdot \frac{\text{kN} \cdot \text{m}}{\text{rad}}$$

$$K_{\Theta \text{Max}} := \lambda_{\text{Max}} \cdot \frac{EI_{\text{Seg}}}{1 \text{m}} = 1.382 \times 10^4 \cdot \frac{\text{kN} \cdot \text{m}}{\text{rad}}$$

Lee et al., 2001

Departing from the agreement between the calculation results of Lee et al. and Blom, a value of 0.3 is selected for λ .

A.2.4 Concrete Compressive Capacity

The capacity of concrete under compressive stress is a product of maximum strain, $\varepsilon = 0.003$, and its modulus of elasticity. Using the previously calculated elasticity modulus, the capacity is calculated as shown below.

$$\sigma_c = \varepsilon \cdot E_c = 0.003 \cdot 13.6 \text{ GPa} = 40.86 \text{ MPa}$$

A.2.5 Bolt Tensile and Shear Capacity

Sixteen units of M27 bolts Grade 8.8 were provided to tie one tunnel ring and the other. Each of the bolts has an area of 459 mm^2 , shearing yield strength of 380 MPa , and allowable tensile stress of 290 MPa . Therefore, the total tensile and shear capacity of the whole tunnel ring is determined with the following method.

M27 bolts Grade 8.8 - 16 units

$$n := 16 \quad \gamma_{M2} := 1.25$$

$$\text{dia} := 27 \text{ mm}$$

$$A_S := 459 \text{ mm}^2$$

$$f_{\text{yield}} := 640 \text{ MPa}$$

$$f_{\text{Ult}} := 800 \text{ MPa}$$

Bolt in shear

$$\tau := \frac{0.6 \cdot f_{\text{Ult}}}{\gamma_{M2}} = 384 \text{ MPa}$$

$$\tau_{\text{Total}} := n \cdot \tau = 6.144 \times 10^3 \text{ MPa}$$

$$F_V := \tau \cdot A_S = 176.256 \text{ kN}$$

$$F_{V\text{Total}} := \tau_{\text{Total}} \cdot A_S = 2.82 \times 10^3 \text{ kN}$$

Bolt in tension

$$\sigma_t := \frac{0.9 \cdot f_{\text{Ult}}}{\gamma_{M2}} = 576 \text{ MPa}$$

$$\sigma_{t\text{Total}} := n \cdot \sigma_t = 9.216 \times 10^3 \text{ MPa}$$

$$F_t := \sigma_t \cdot A_S = 264.384 \text{ kN}$$

$$F_{t\text{Total}} := \sigma_{t\text{Total}} \cdot A_S = 4.23 \times 10^3 \text{ kN}$$

A.3. Water Tightness Calculation

Leakage occurs when water pressure exceeds the contact stress at the rubber joints. Shalabi et al. (2007) suggested the equation below.

$$P_W = m P_C = m (P_{Ci} + \Delta P_C)$$

where P_W is the water pressure, P_C is the total contact pressure, P_{Ci} is the initial contact pressure, ΔP_C is the change in contact pressure, and m is the material coefficient (0.92 for polyisoprene gasket and 0.96 for neoprene). The limit state is a product of the interaction diagram below.

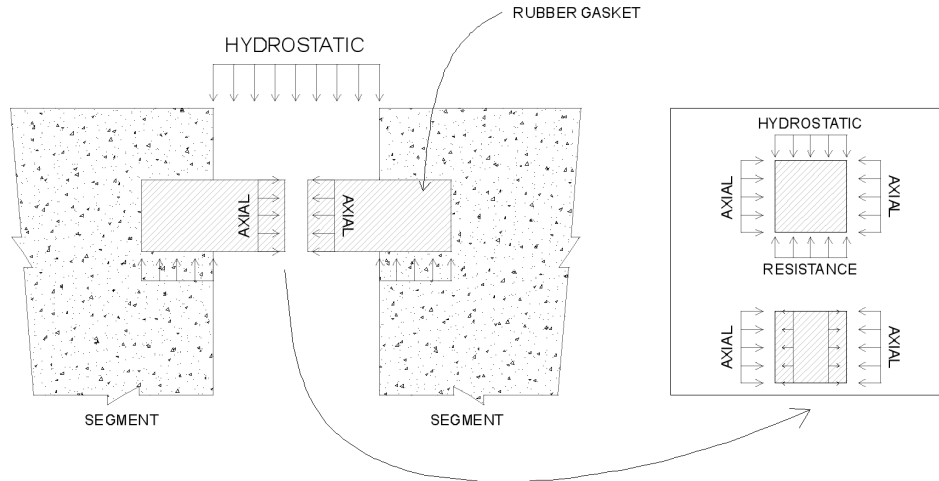


Figure A.10: Interaction of rubber gasket, tunnel segment, and hydrostatic load

Figure A.10 presents the loads acting on the rubber gasket, which are axial and hydrostatic load. The hydrostatic load works perpendicularly to the axial load, on the radial direction, and thus could slightly reduce the axial load. The minimum required contact pressure is calculated as shown below. To stay conservative, the groundwater table was assumed to be at the ground level. Additionally, material and load safety factor were included into the calculation.

$$\zeta_{Res} := 1.1$$

$$\zeta_{Load} := 1.5$$

$$h_{Water} := 18m \quad \gamma_{Water} := 9.81 \frac{kN}{m^3}$$

$$\sigma_{Hydrostatic} := h_{Water} \cdot \gamma_{Water} = 176.58 kPa$$

$$\nu := 0.5$$

$$\sigma_{Minimum} := \zeta_{Res} \cdot \zeta_{Load} \cdot \sigma_{Hydrostatic} \cdot (1 + \nu) = 437.036 kPa$$

Other than the perpendicular hydrostatic pressure, the changes in contact pressure are originated from the additional longitudinal bending moment due to differential land subsidence, which is calculated with the equation below.

$$\Delta\sigma = \frac{M \cdot y}{I}$$

where $\Delta\sigma$ is the change in stress, M is the bending moment, y is the distance from the neutral axis to the extreme fiber, and I is the moment inertia. On the other side, the resistance is provided by the effective jack force. The interaction between the soliciting load and the resistance is calculated with the method shown below.

$$P_{\text{Effective}} := 10^4 \text{ kN}$$

$$\sigma_{\text{TBMEffective}} := \frac{P_{\text{Effective}}}{\text{Area}} = 1.671 \times 10^3 \text{ kPa}$$

$$\Delta\sigma := \sigma_{\text{TBMEffective}} - \sigma_{\text{Minimum}} = 1.234 \times 10^3 \text{ kPa}$$

$$E_{\text{Gasket}} := 16.5 \text{ MPa}$$

$$\varepsilon_{\text{Critical}} := \frac{\Delta\sigma}{E_{\text{Gasket}}} = 0.075$$

The additional soliciting load comes from the deformation of the tunnel following the settlement. For the initial calculation, the maximum longitudinal bending moment reported in Chapter 6 is considered. The calculation is shown below.

$$M := 28.33 \text{ kN}\cdot\text{m}$$

$$r_{\text{Out}} := 3.325 \text{ m} \quad r_{\text{In}} := 3.025 \text{ m}$$

$$I := \frac{\pi}{4} \cdot (r_{\text{Out}}^4 - r_{\text{In}}^4) = 30.232 \text{ m}^4$$

$$y := r_{\text{Out}}$$

$$\Delta\sigma_{\text{Top}} := \frac{M \cdot y}{I} = 3.116 \text{ kPa}$$

The calculation on top shows that the soliciting load due to differential settlement is merely 1% relative to the allowable stress. However, this might not be the same case if the moment at the station-tunnel interface is used. Therefore, bending moment as large as 10800 *kNm* was assigned and the calculation is presented below.

$$M := 10800 \text{ kN}\cdot\text{m}$$

$$r_{\text{Out}} := 3.325 \text{ m} \quad r_{\text{In}} := 3.025 \text{ m}$$

$$I := \frac{\pi}{4} \cdot (r_{\text{Out}}^4 - r_{\text{In}}^4) = 30.232 \text{ m}^4$$

$$y := r_{\text{Out}}$$

$$\Delta\sigma_{\text{Top}} := \frac{M \cdot y}{I} = 1.188 \times 10^3 \text{ kPa}$$

Indeed, greater soliciting stress was generated, which almost reaches the upper limit. This load-resistance interaction can also be presented in terms of strain as shown below.

$$M_{\text{Solicitation}} := 10800 \text{ kN}\cdot\text{m}$$

$$y = 3.325 \text{ m}$$

$$K := \frac{M_{\text{Solicitation}}}{E_{\text{Gasket}} \cdot I} = 0.022 \frac{1}{\text{m}}$$

$$\varepsilon_{xx} := y \cdot K = 0.072$$

$$\text{Ratio} := \frac{\varepsilon_{xx}}{\varepsilon_{\text{Critical}}} = 96.266\%$$

Appendix B: NUMERICAL ANALYSIS RESULTS

In this segment, the outcomes of numerical analysis from Plaxis are presented selectively, which includes the effective vertical and horizontal soil stress, vertical and horizontal displacement, and structural deformation. To portray the significance of groundwater, only the results from the year 2030 ($t = 10 \text{ years}$), 2040 ($t = 20 \text{ years}$), 2050 ($t = 30 \text{ years}$), and 2100 ($t = 80 \text{ years}$) are provided. The selection of timeframes is in accordance with the groundwater management scenarios.

B.1. Vertical Displacement

B.1.1 Scenario A

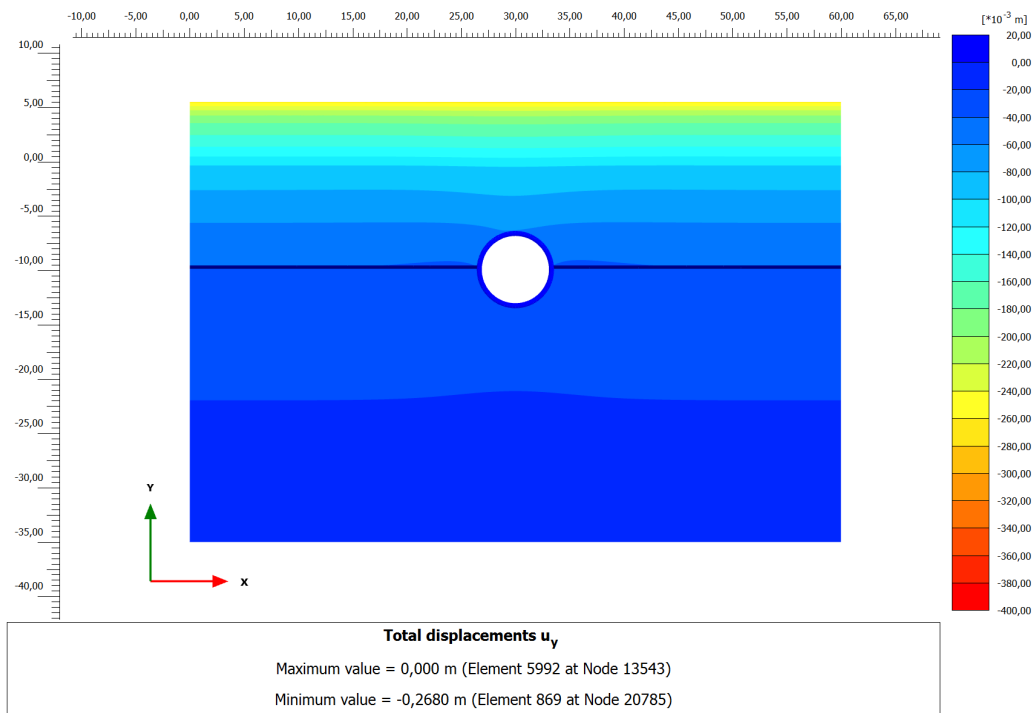


Figure B.1: Vertical displacement (u_y) of BH88 at year 2030

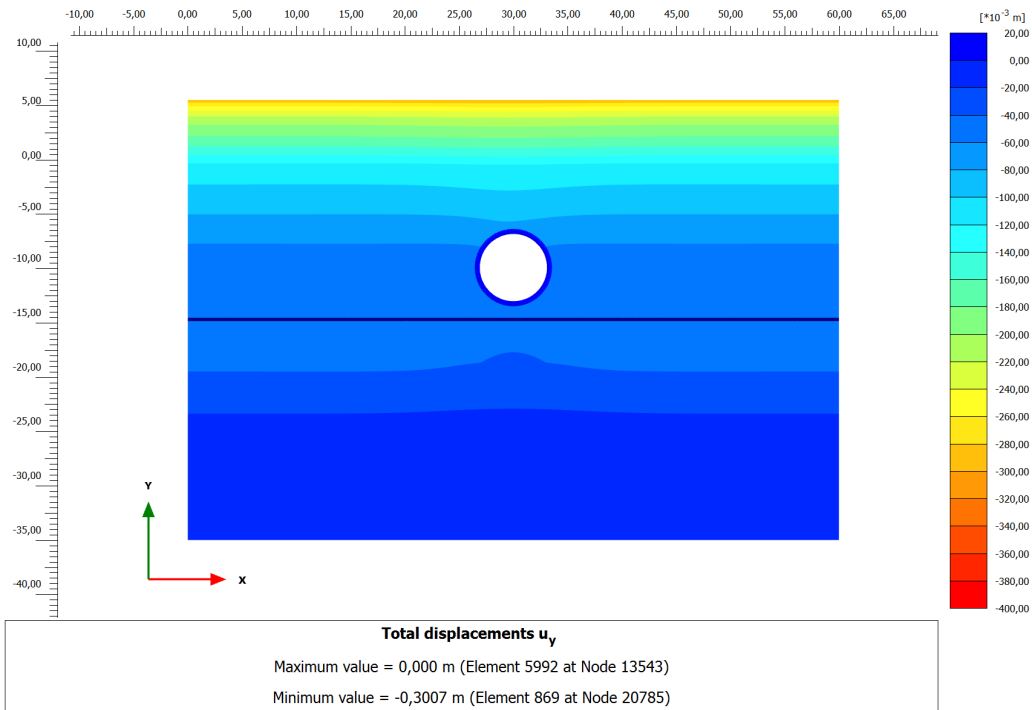


Figure B.2: Vertical displacement (u_y) of BH88 at year 2040

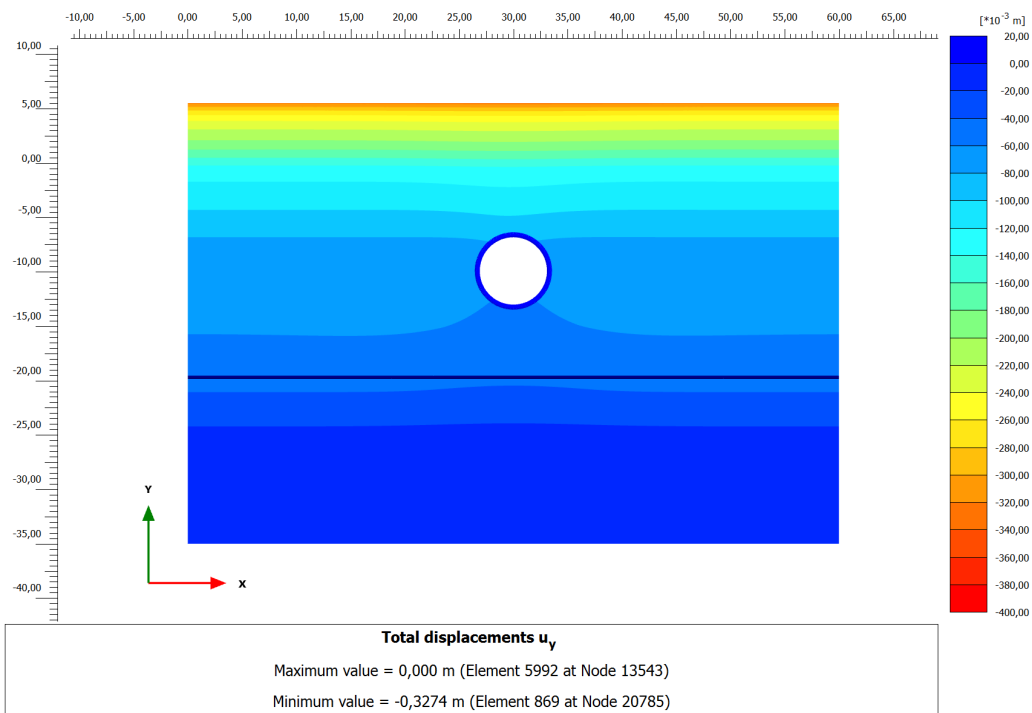


Figure B.3: Vertical displacement (u_y) of BH88 at year 2050

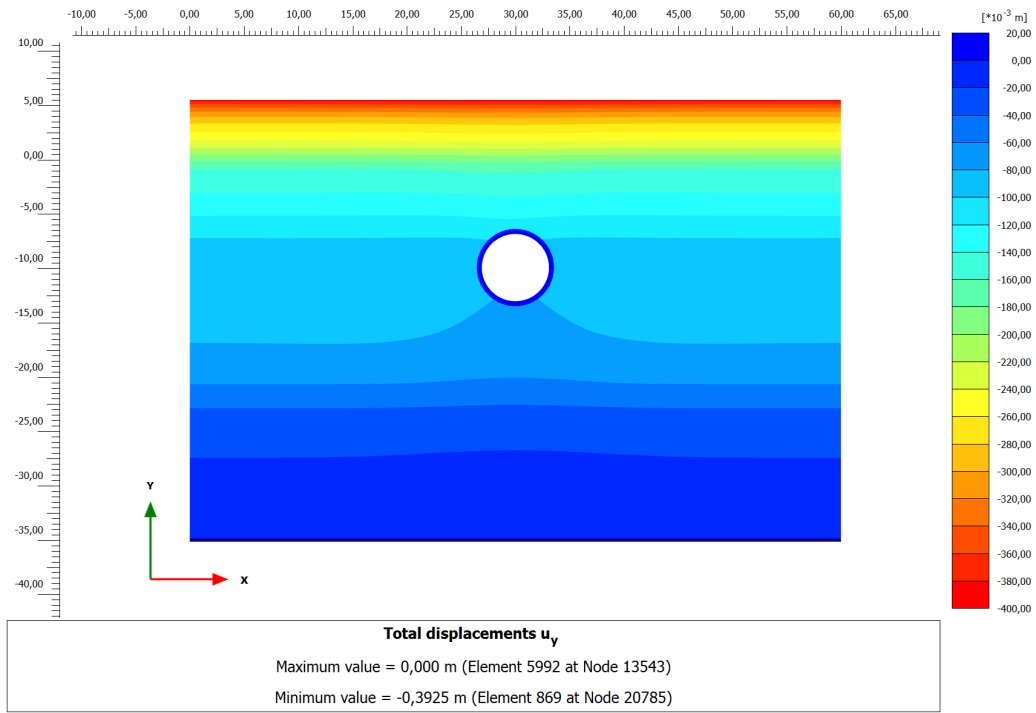


Figure B.4: Vertical displacement (u_y) of BH88 at year 2100

B.1.2 Scenario B

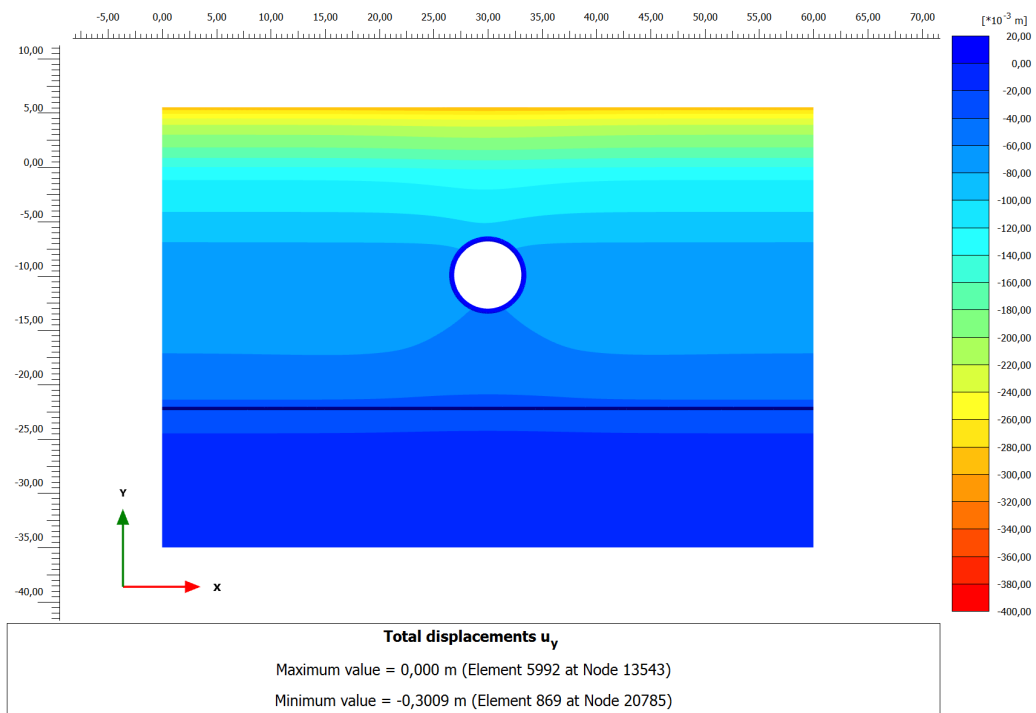


Figure B.5: Vertical displacement (u_y) of BH88 at year 2030

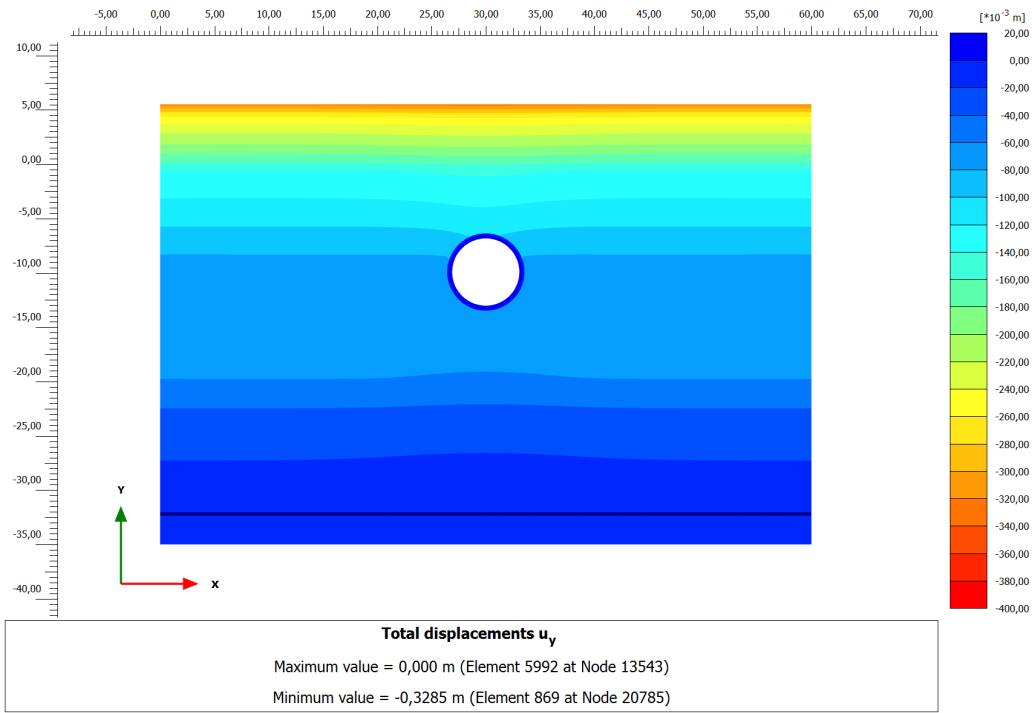


Figure B.6: Vertical displacement (u_y) of BH88 at year 2040

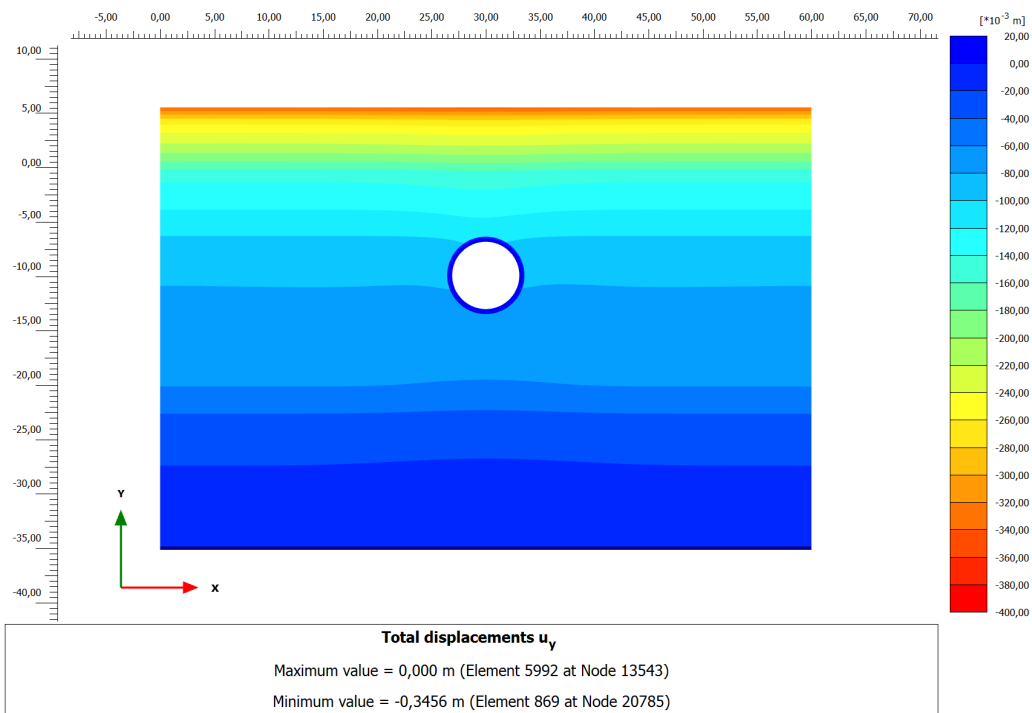


Figure B.7: Vertical displacement (u_y) of BH88 at year 2050

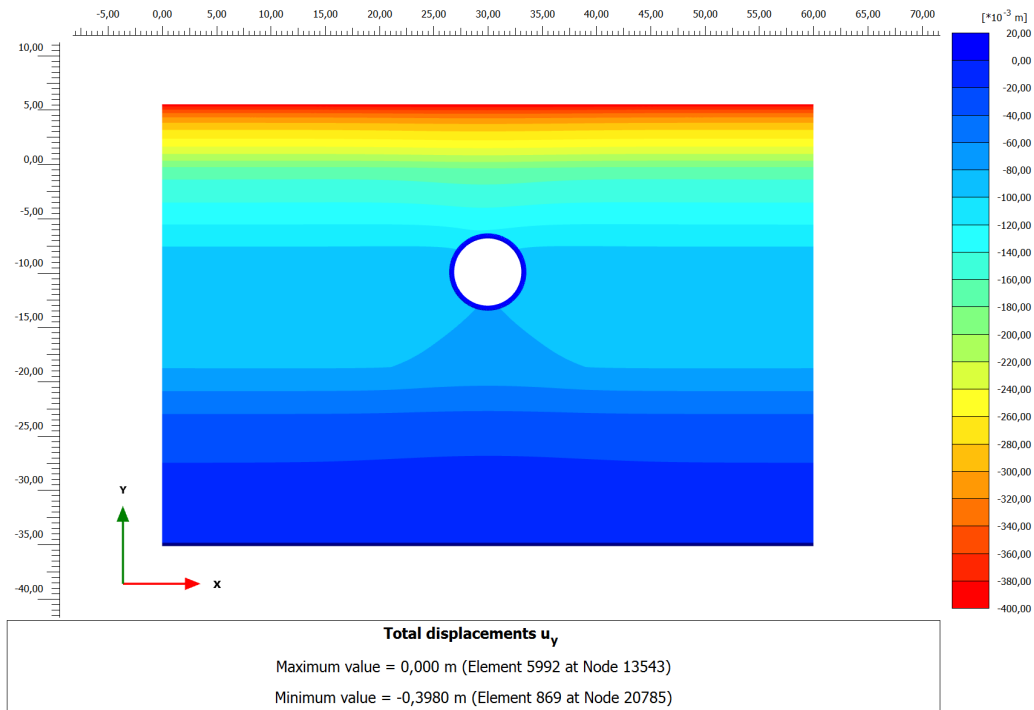


Figure B.8: Vertical displacement (u_y) of BH88 at year 2100

B.1.3 Scenario C

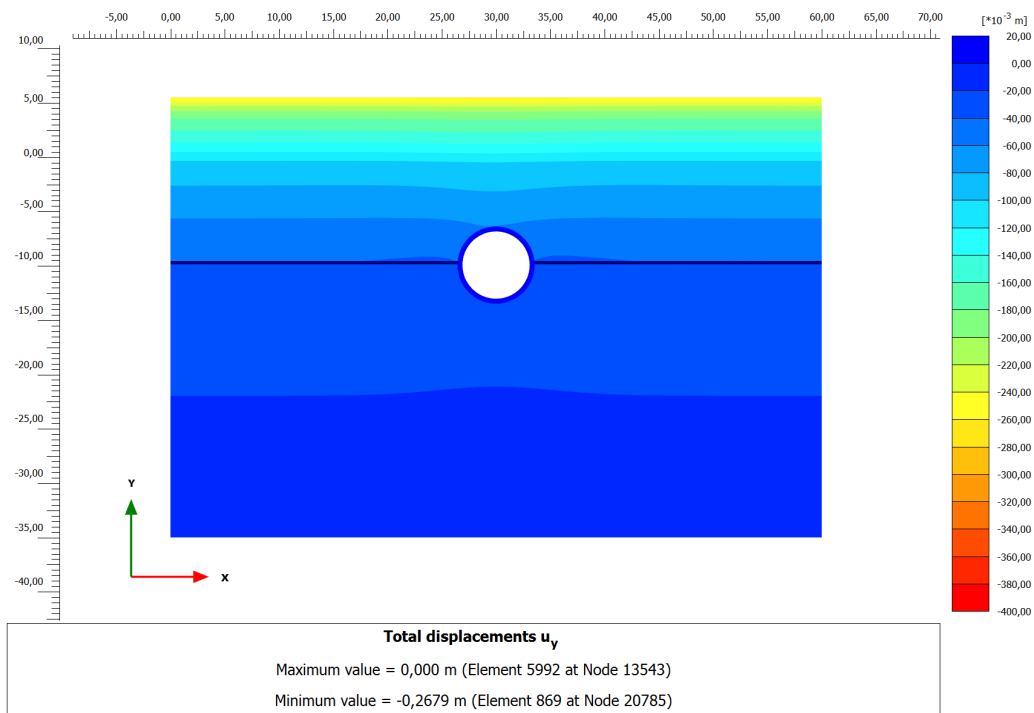


Figure B.9: Vertical displacement (u_y) of BH88 at year 2030

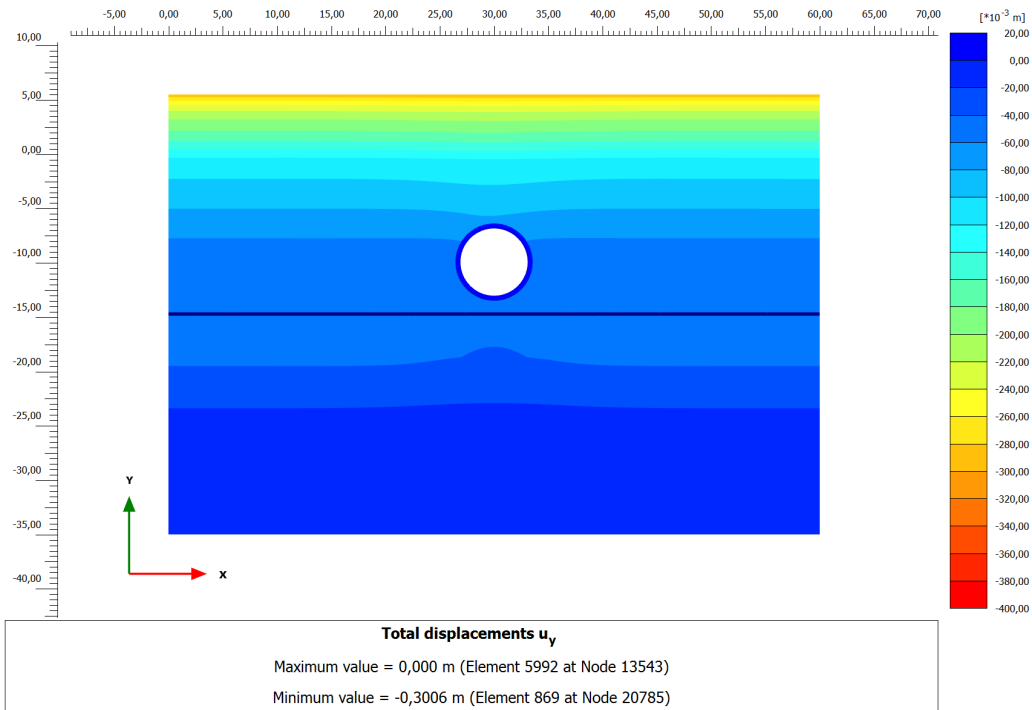


Figure B.10: Vertical displacement (u_y) of BH88 at year 2040

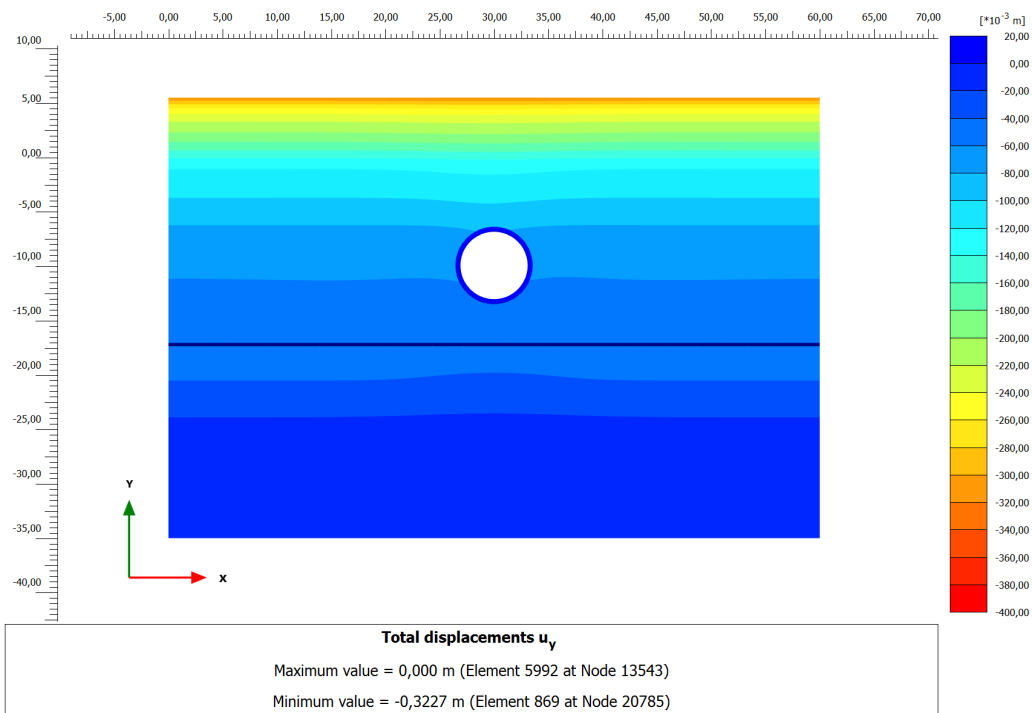


Figure B.11: Vertical displacement (u_y) of BH88 at year 2050

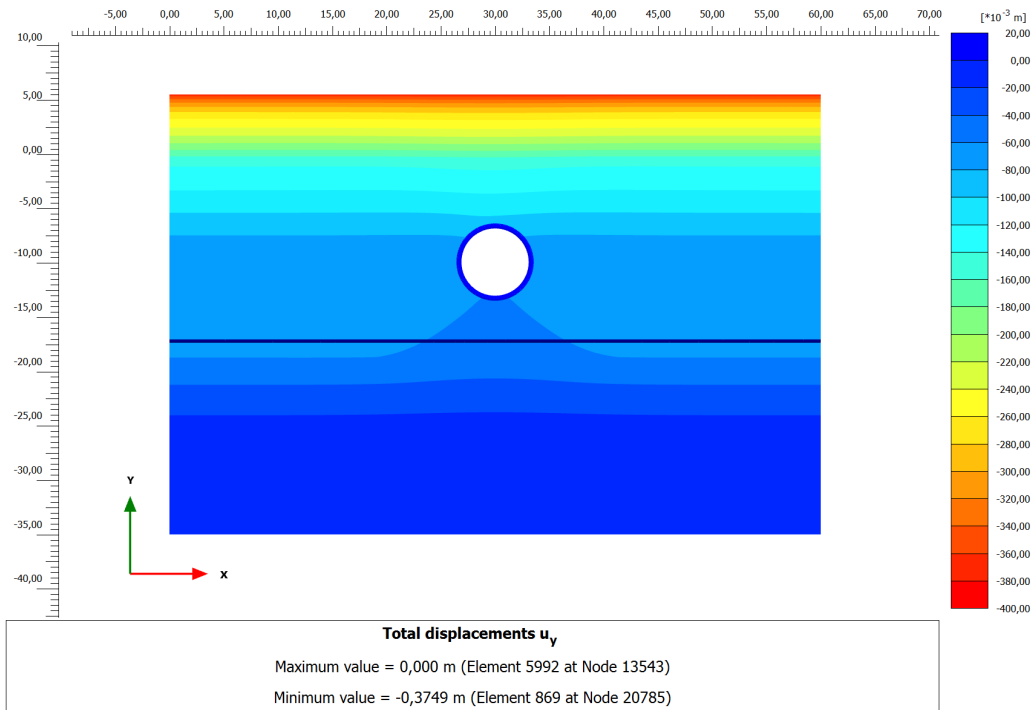


Figure B.12: Vertical displacement (u_v) of BH88 at year 2100

B.1.4 Scenario D

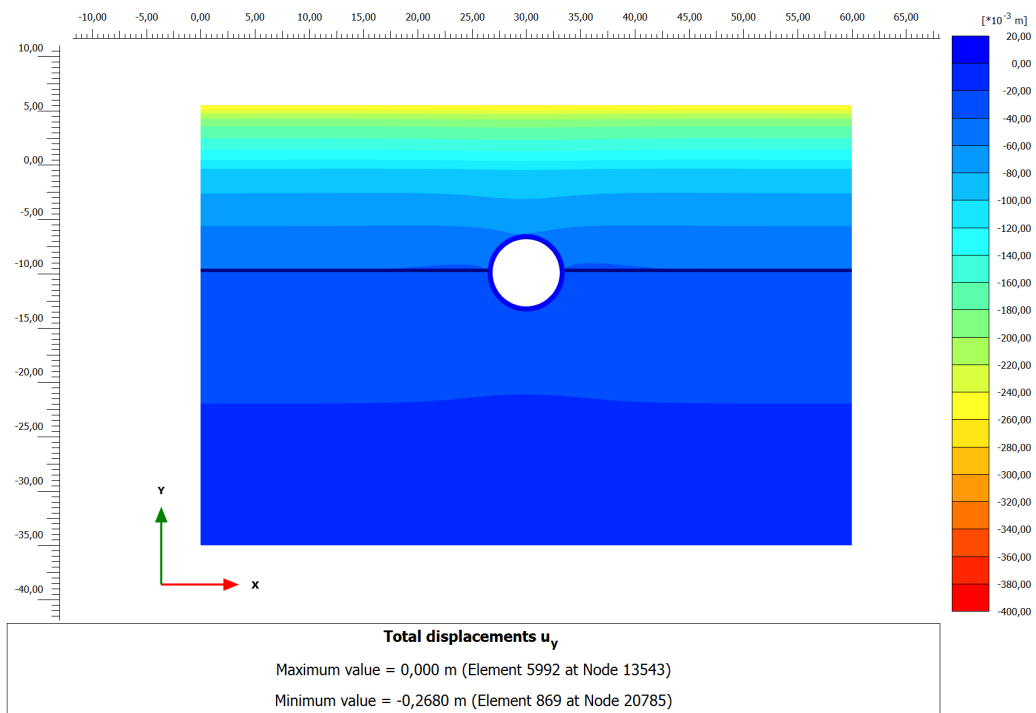


Figure B.13: Vertical displacement (u_v) of BH88 at year 2030

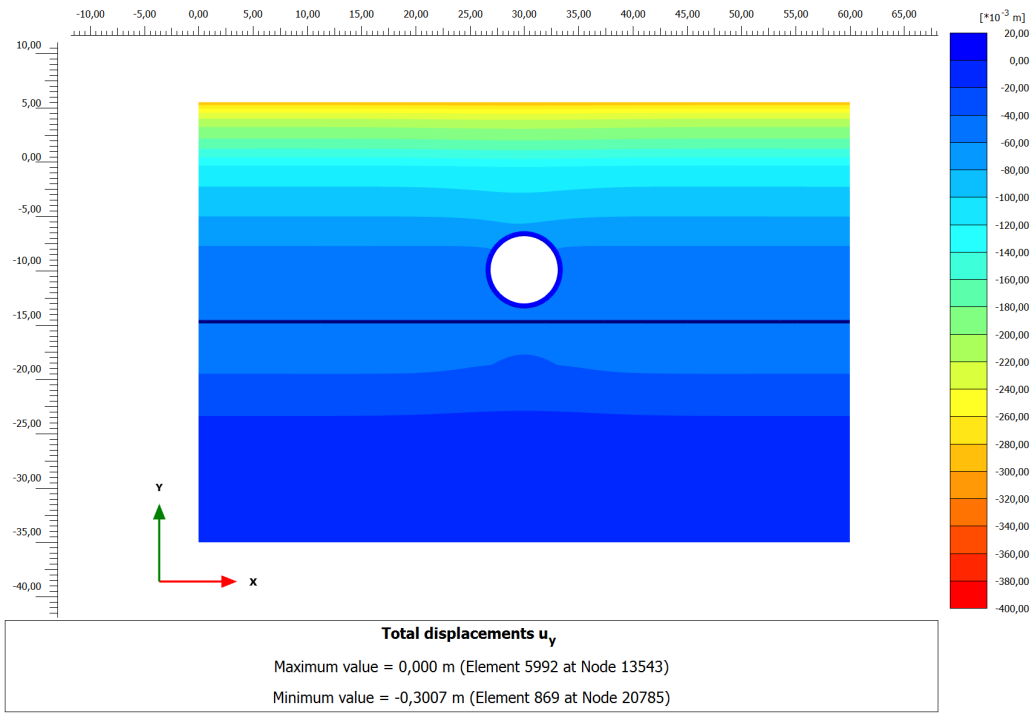


Figure B.14: Vertical displacement (u_v) of BH88 at year 2040

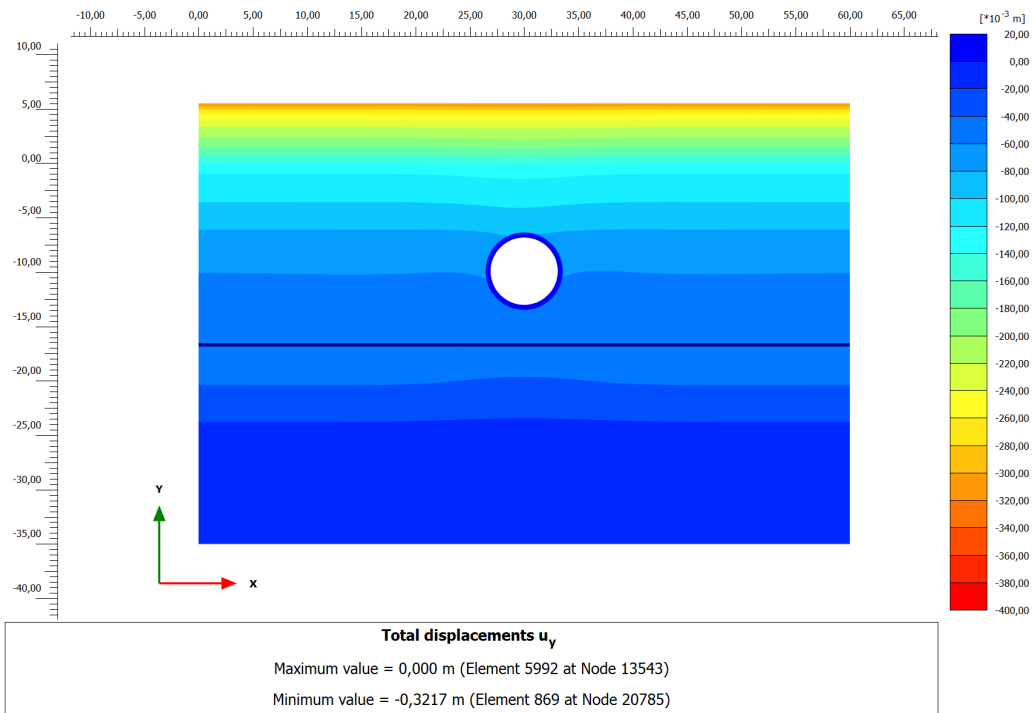


Figure B.15: Vertical displacement (u_v) of BH88 at year 2050

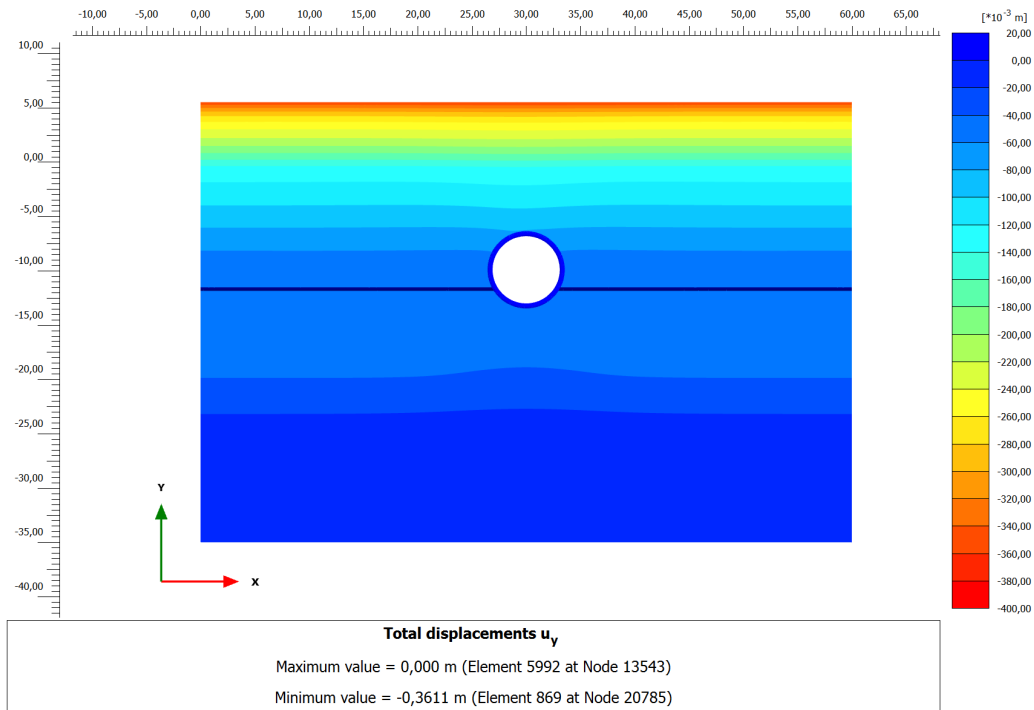


Figure B.16: Vertical displacement (u_y) of BH88 at year 2100

B.2. Horizontal Displacement

B.2.1 Scenario A

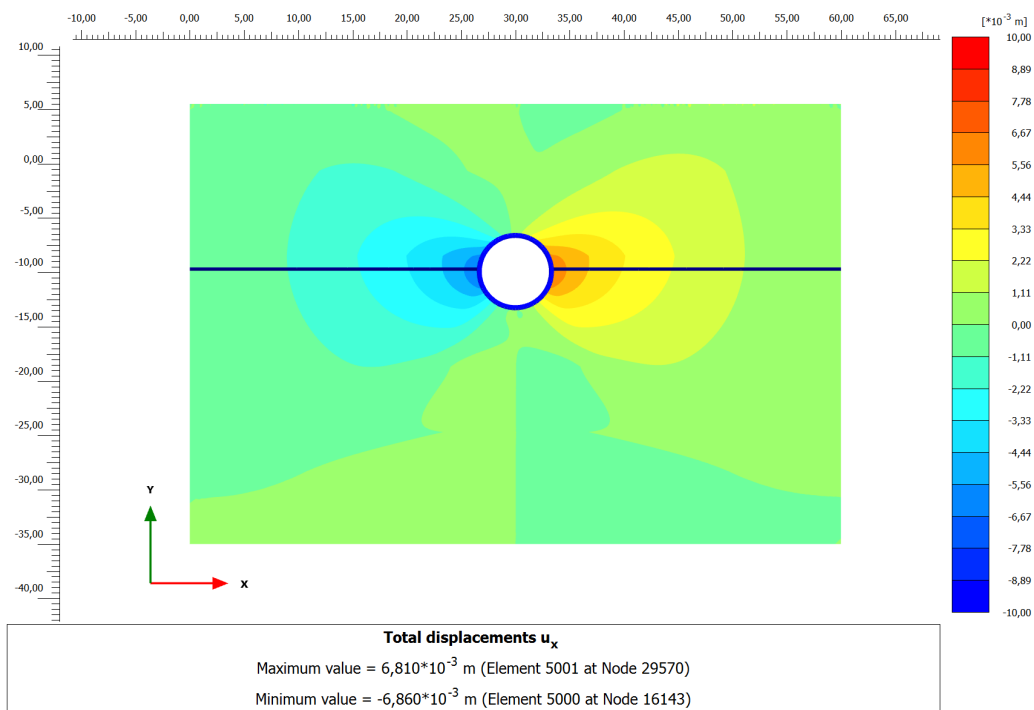


Figure B.17: Horizontal displacement (u_x) of BH88 at year 2030

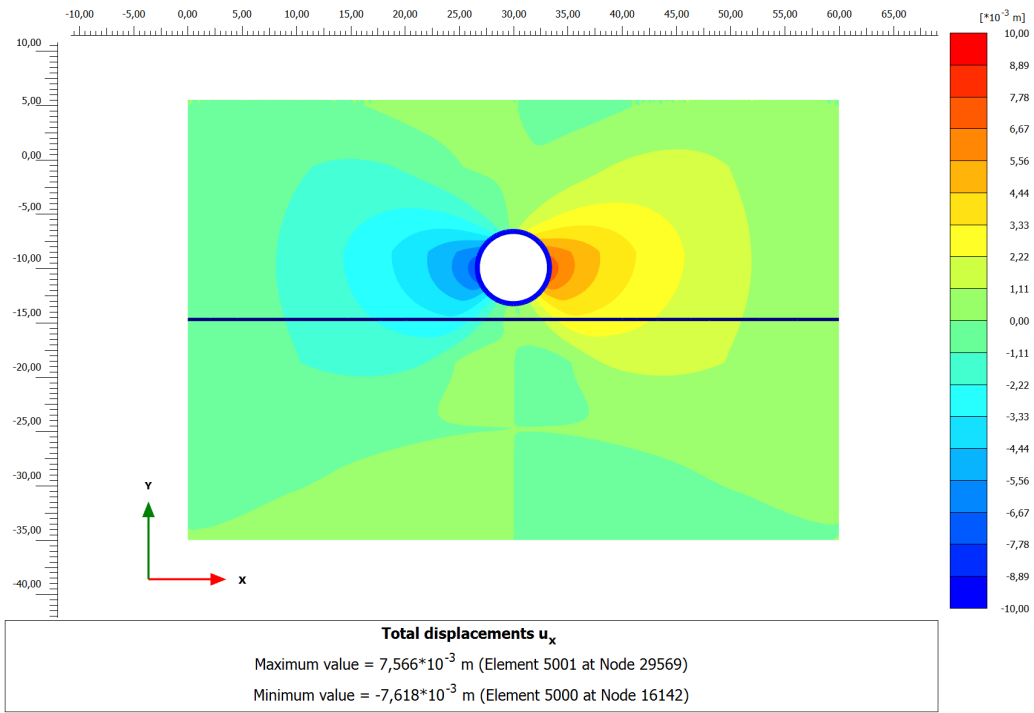


Figure B.18: Horizontal displacement (u_x) of BH88 at year 2040

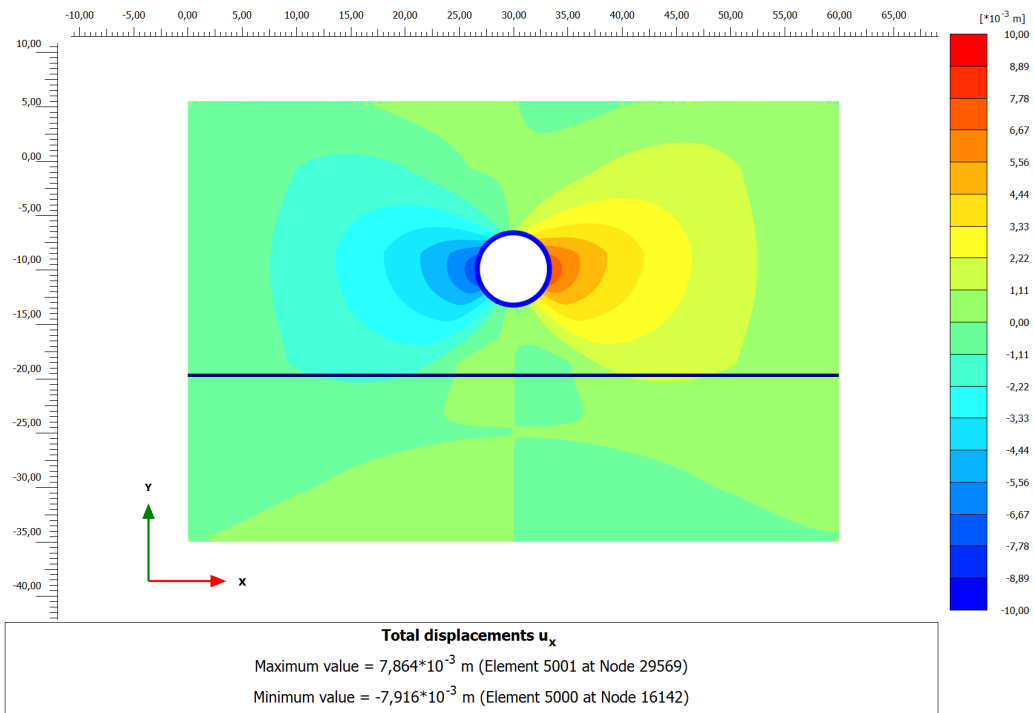


Figure B.19: Horizontal displacement (u_x) of BH88 at year 2050

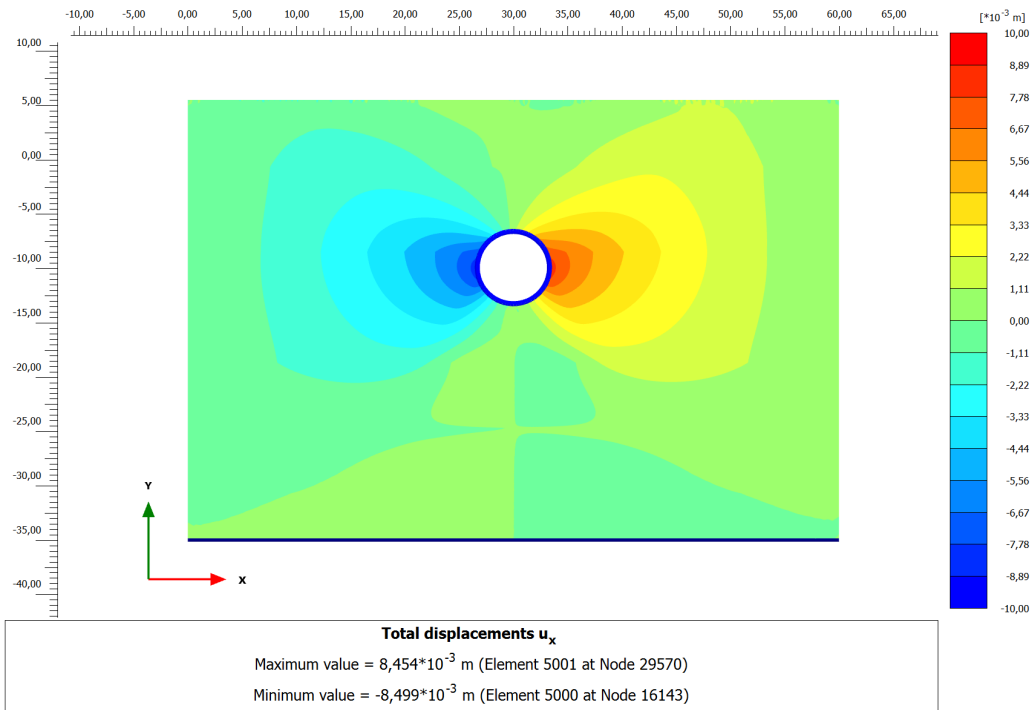


Figure B.20: Horizontal displacement (u_x) of BH88 at year 2100

B.2.2 Scenario B

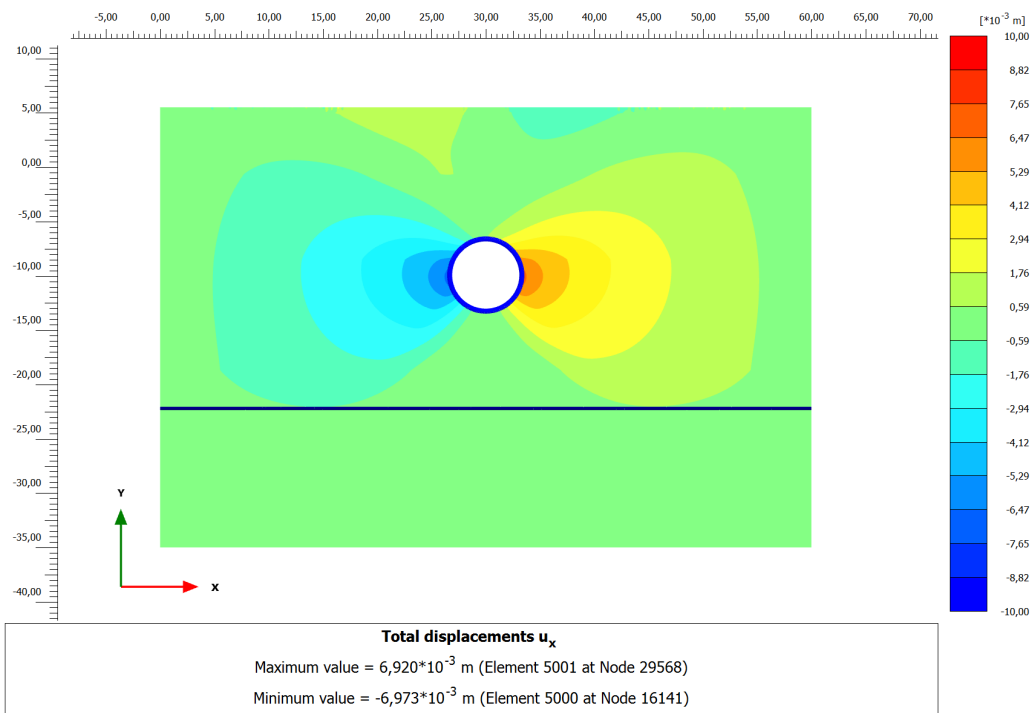


Figure B.21: Horizontal displacement (u_x) of BH88 at year 2030

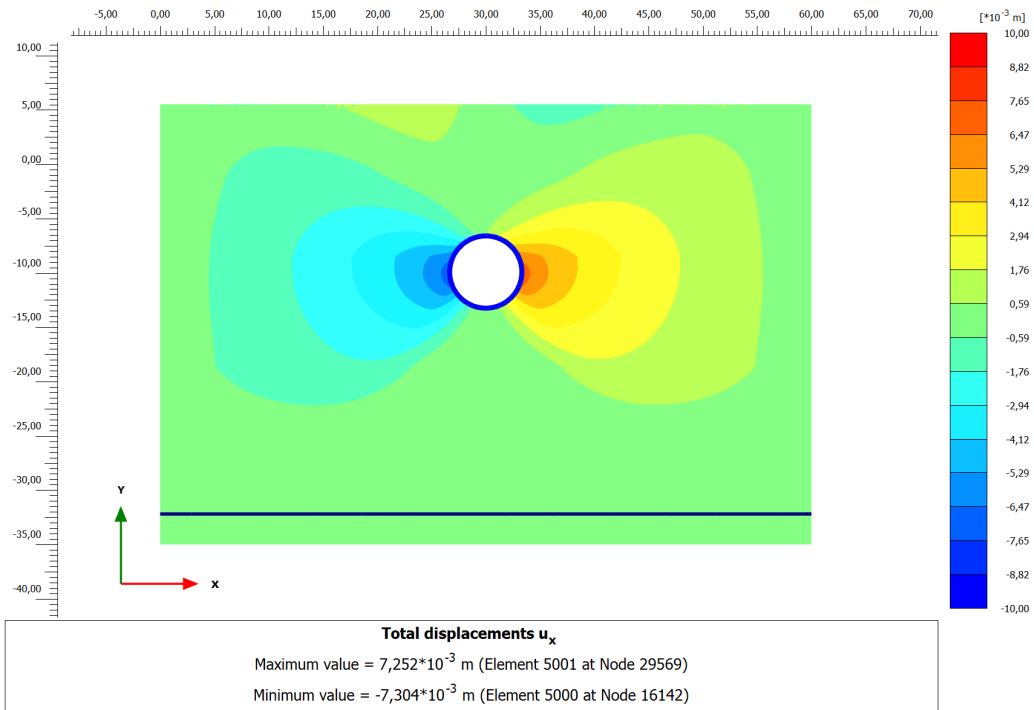


Figure B.22: Horizontal displacement (u_x) of BH88 at year 2040

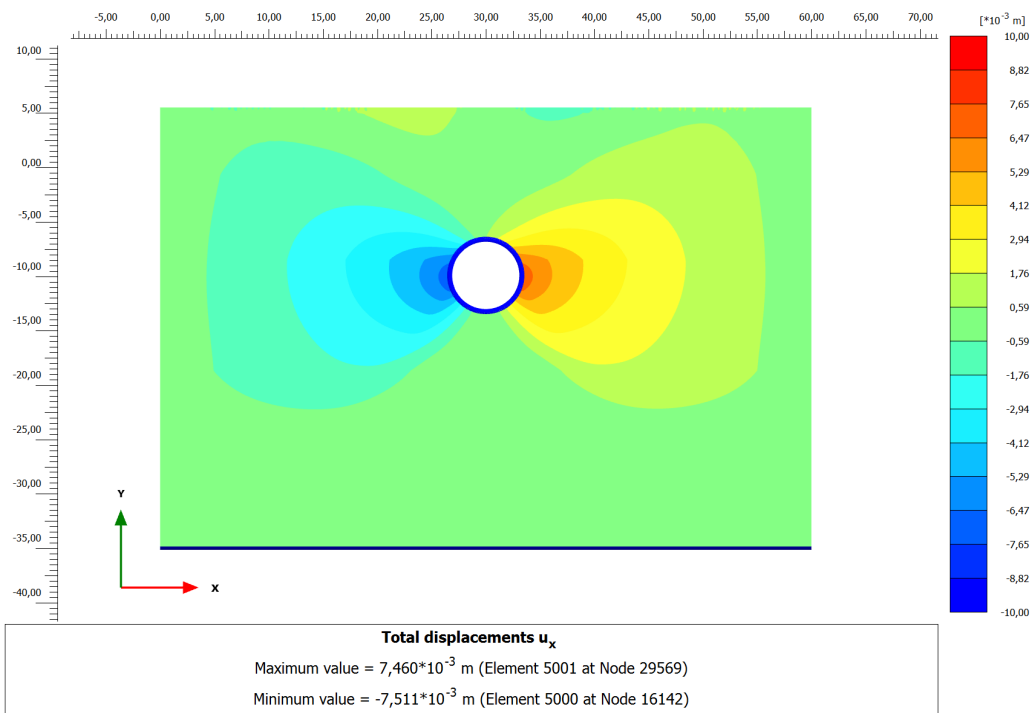


Figure B.23: Horizontal displacement (u_x) of BH88 at year 2050

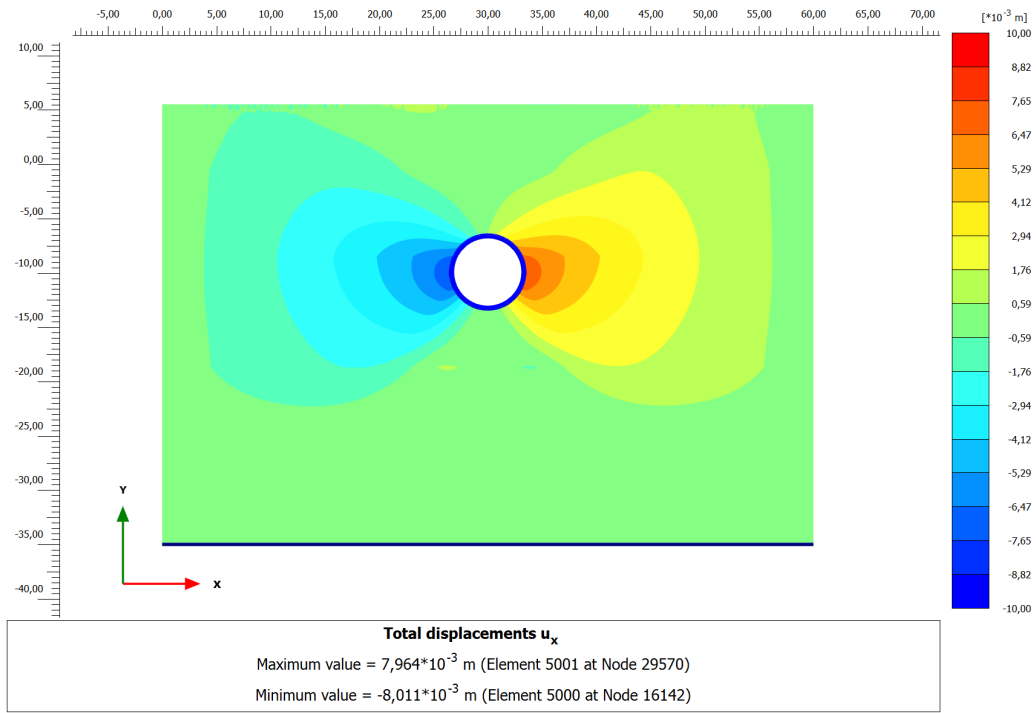


Figure B.24: Horizontal displacement (u_x) of BH88 at year 2100

B.2.3 Scenario C

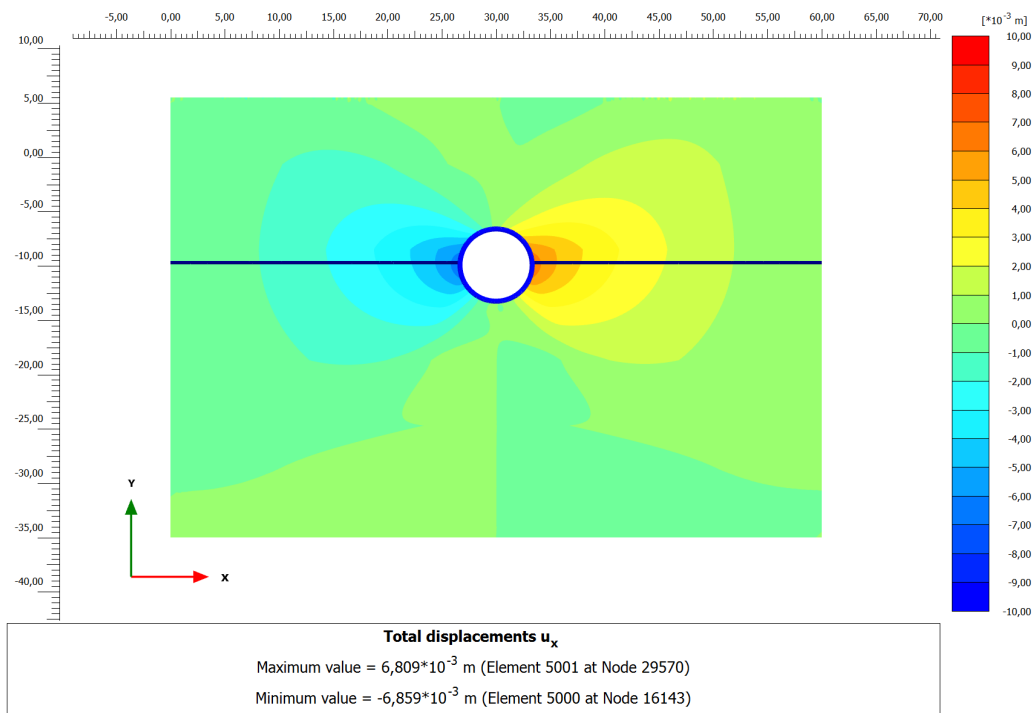


Figure B.25: Horizontal displacement (u_x) of BH88 at year 2030

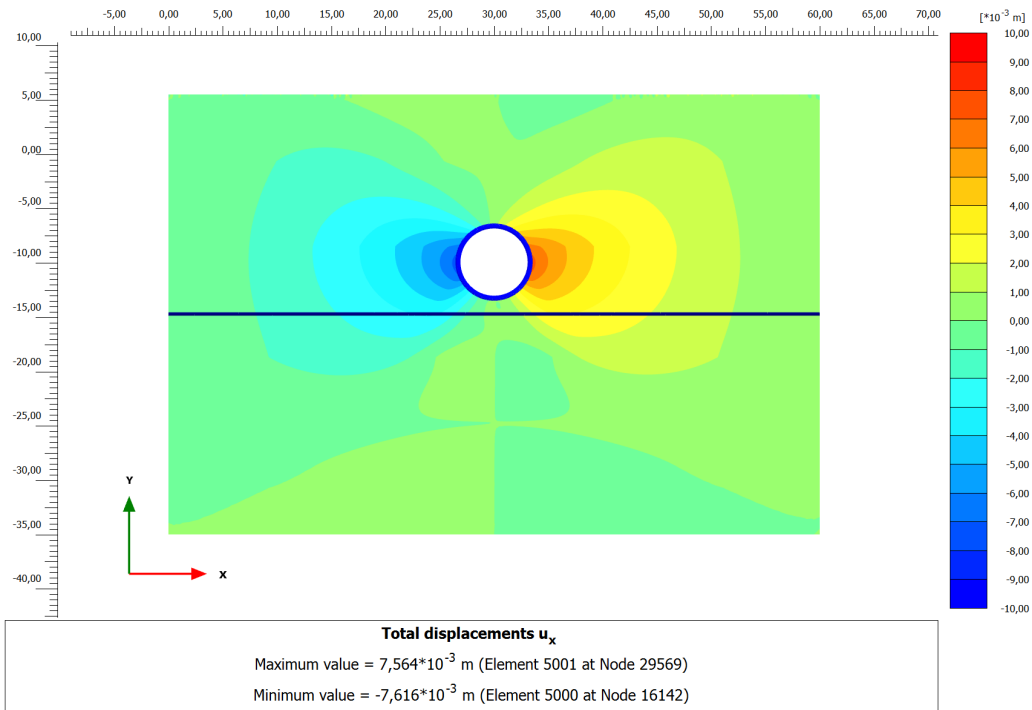


Figure B.26: Horizontal displacement (u_x) of BH88 at year 2040

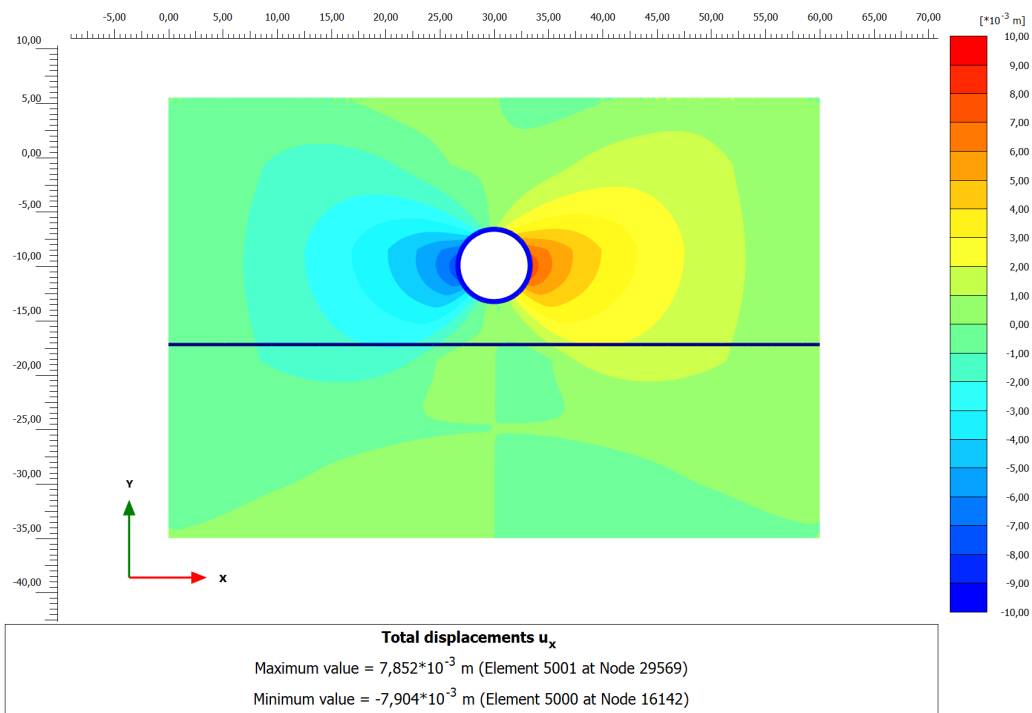


Figure B.27: Horizontal displacement (u_x) of BH88 at year 2050

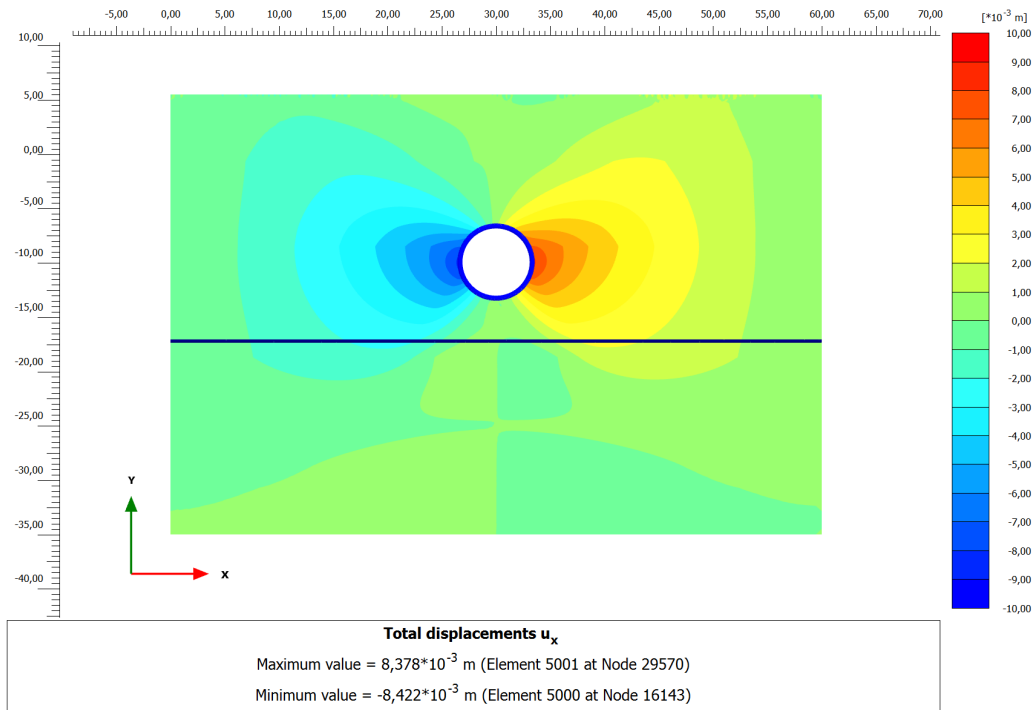


Figure B.28: Horizontal displacement (u_x) of BH88 at year 2100

B.2.4 Scenario D

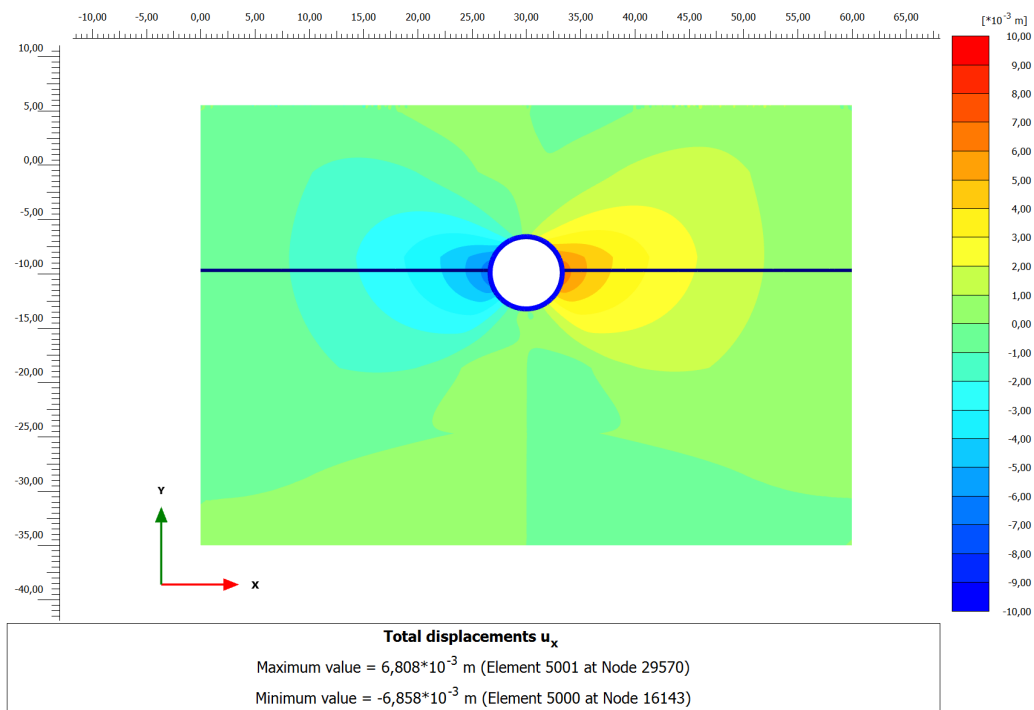


Figure B.29: Horizontal displacement (u_x) of BH88 at year 2030

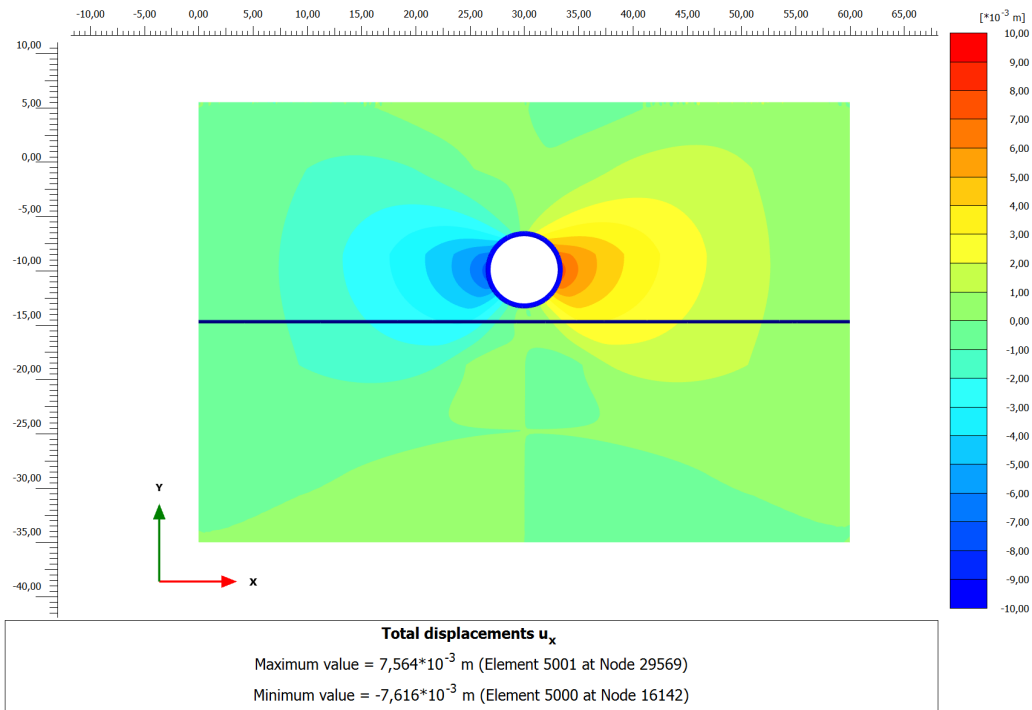


Figure B.30: Horizontal displacement (u_x) of BH88 at year 2040

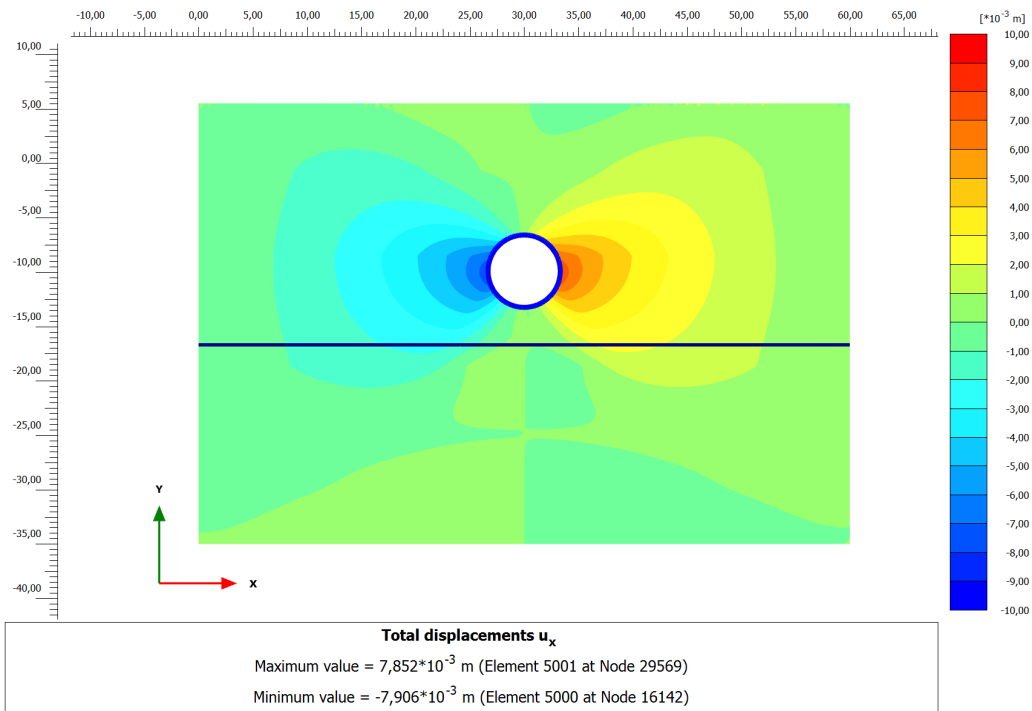


Figure B.31: Horizontal displacement (u_x) of BH88 at year 2050

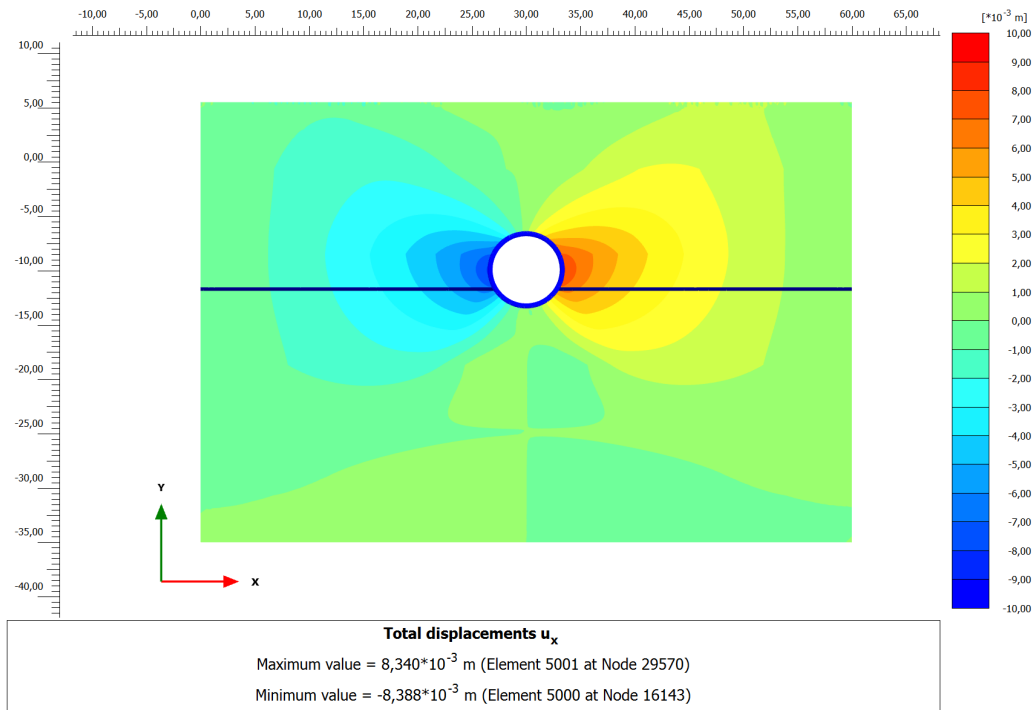


Figure B.32: Horizontal displacement (u_x) of BH88 at year 2100

B.3. Effective Vertical Soil Stress

B.3.1 Scenario A

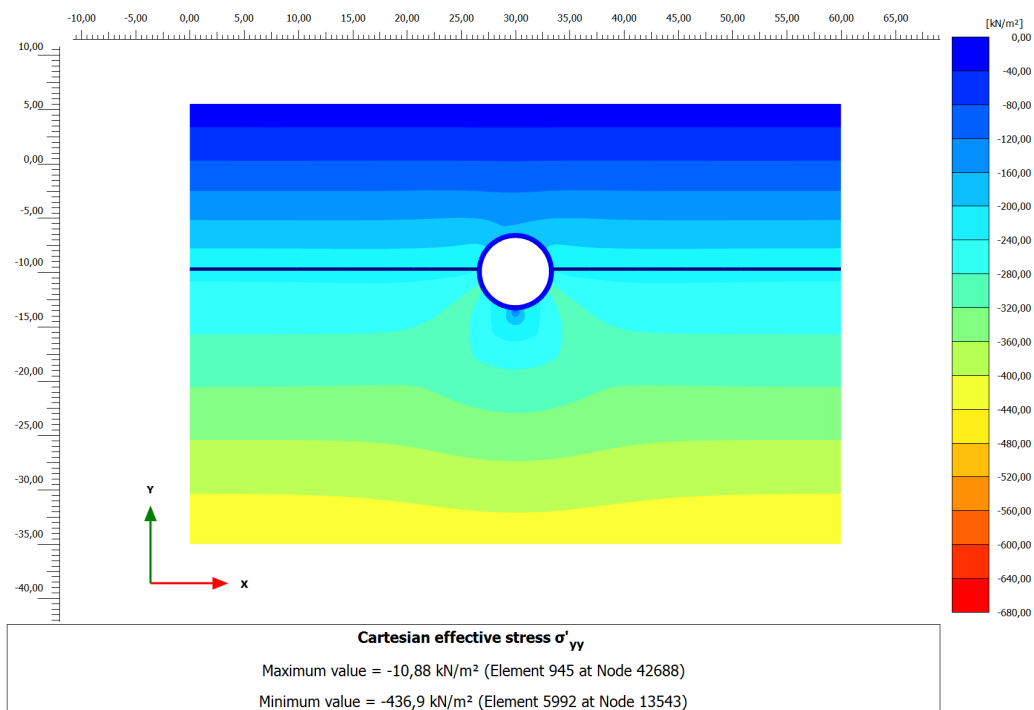


Figure B.33: Effective vertical stress (σ'_{yy}) of BH88 at year 2030

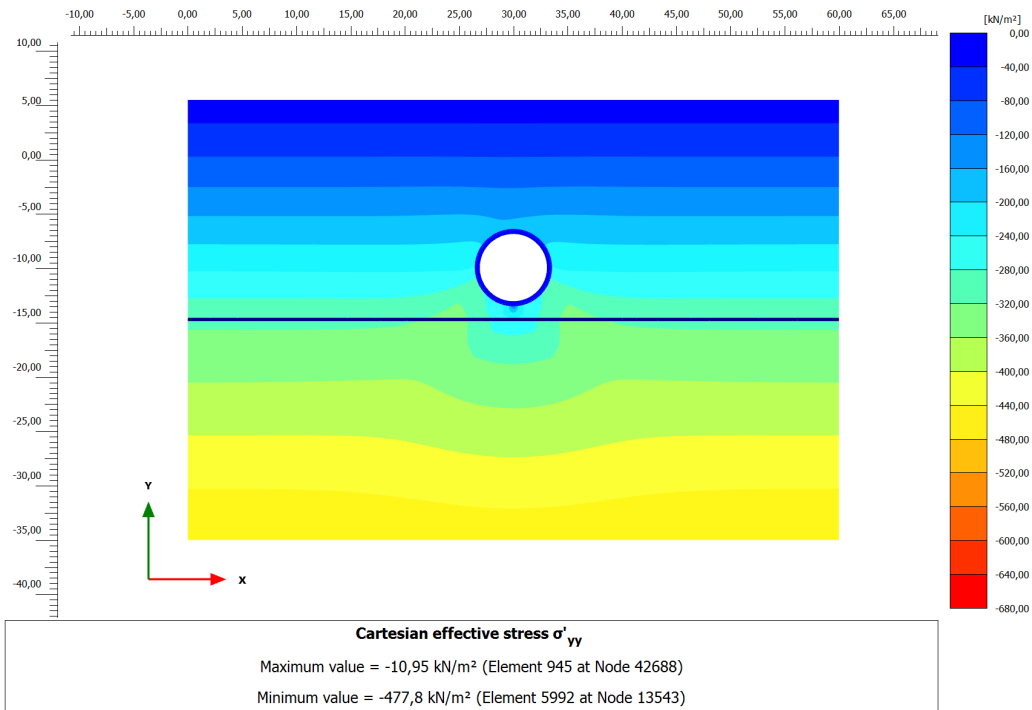


Figure B.34: Effective vertical stress (σ'_{yy}) of BH88 at year 2040

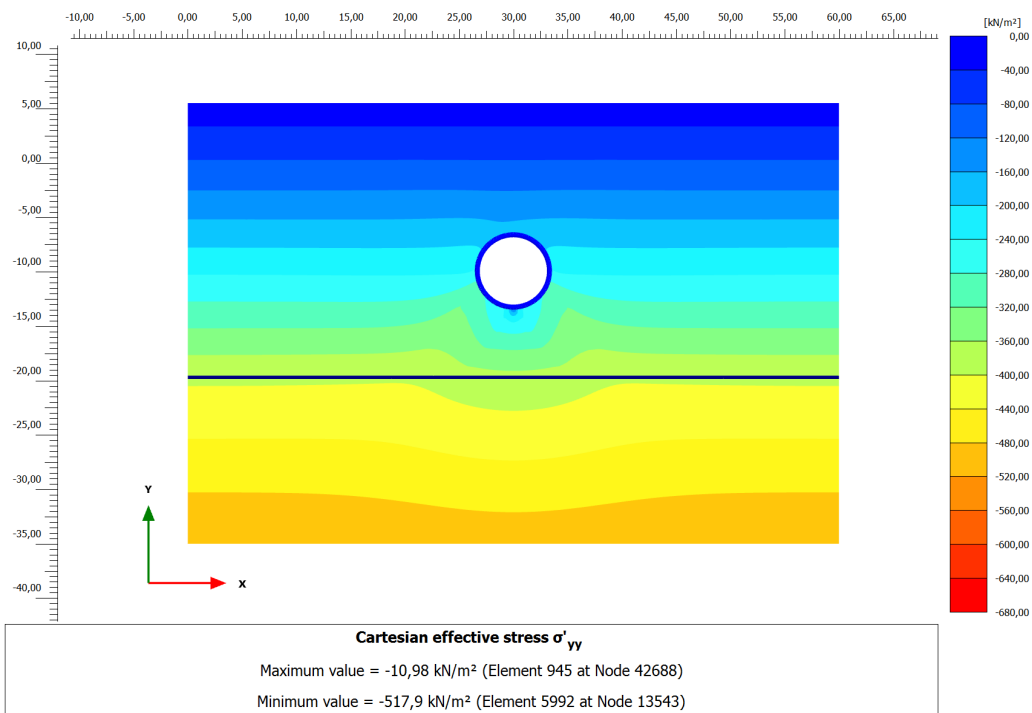


Figure B.35: Effective vertical stress (σ'_{yy}) of BH88 at year 2050

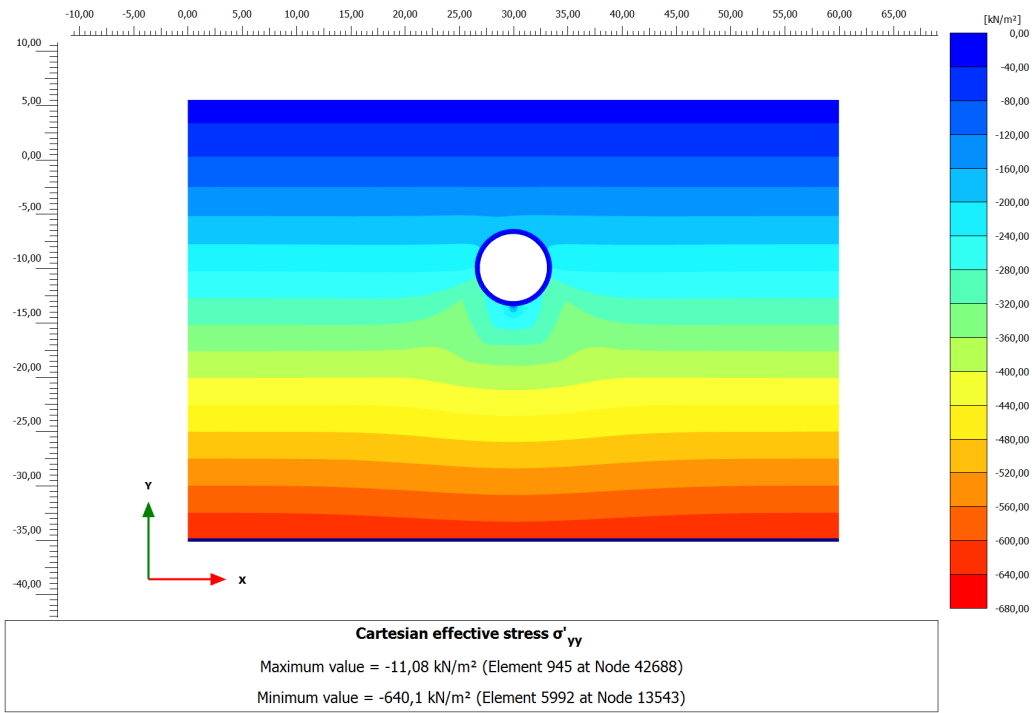


Figure B.36: Effective vertical stress (σ'_{yy}) of BH88 at year 2100

B.3.2 Scenario B

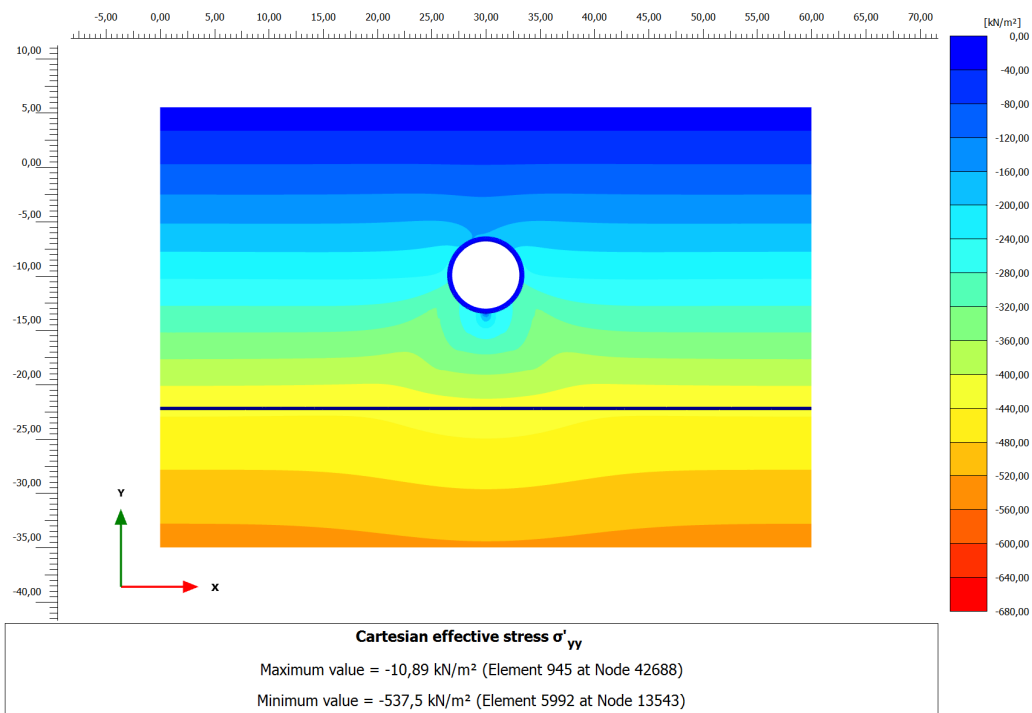


Figure B.37: Effective vertical stress (σ'_{yy}) of BH88 at year 2030

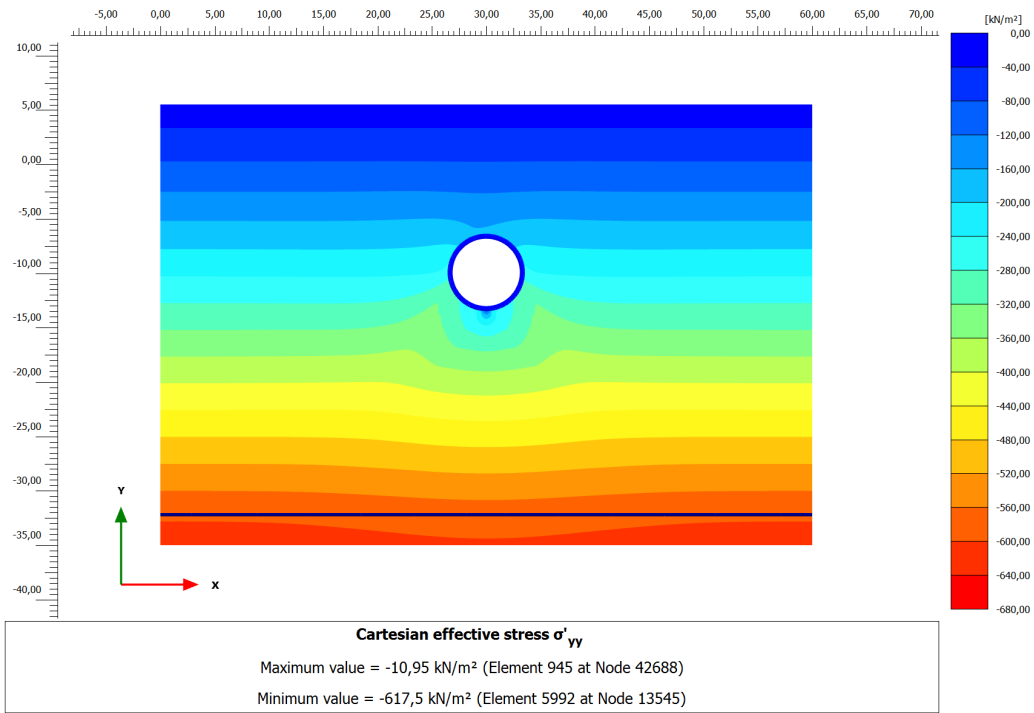


Figure B.38: Effective vertical stress (σ'_{yy}) of BH88 at year 2040

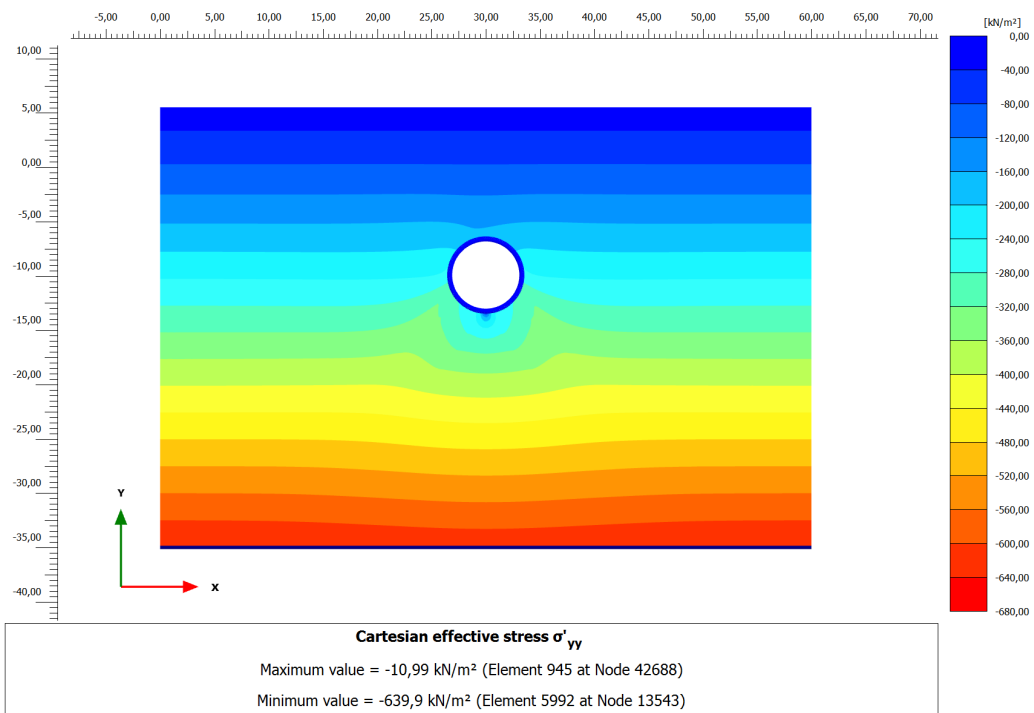


Figure B.39: Effective vertical stress (σ'_{yy}) of BH88 at year 2050

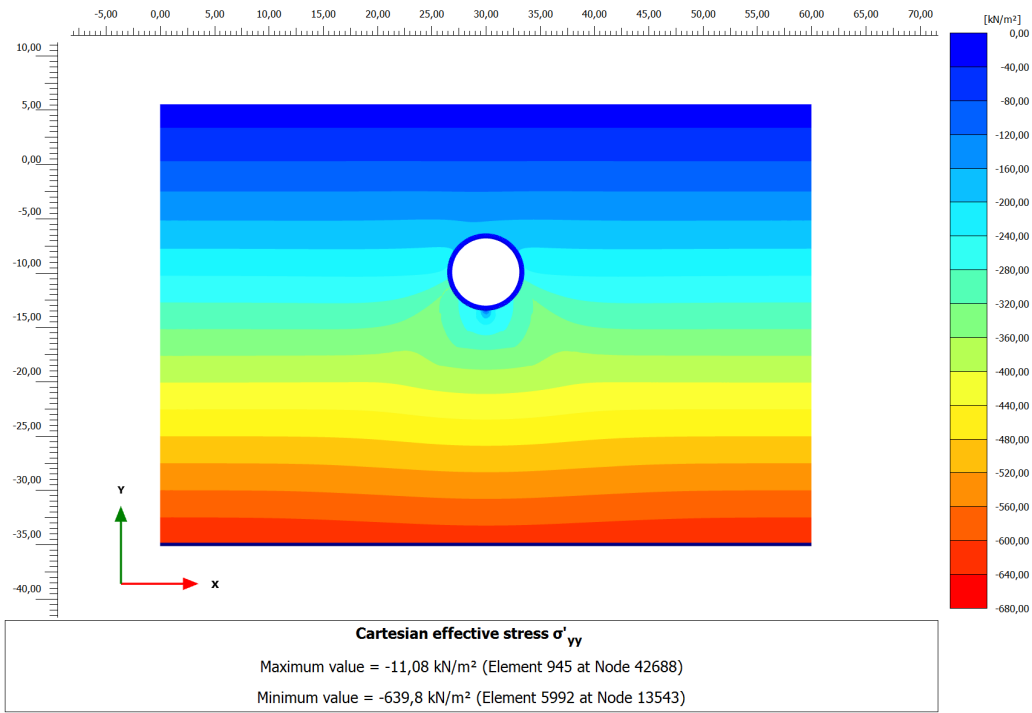


Figure B.40: Effective vertical stress (σ'_{yy}) of BH88 at year 2100

B.3.3 Scenario C

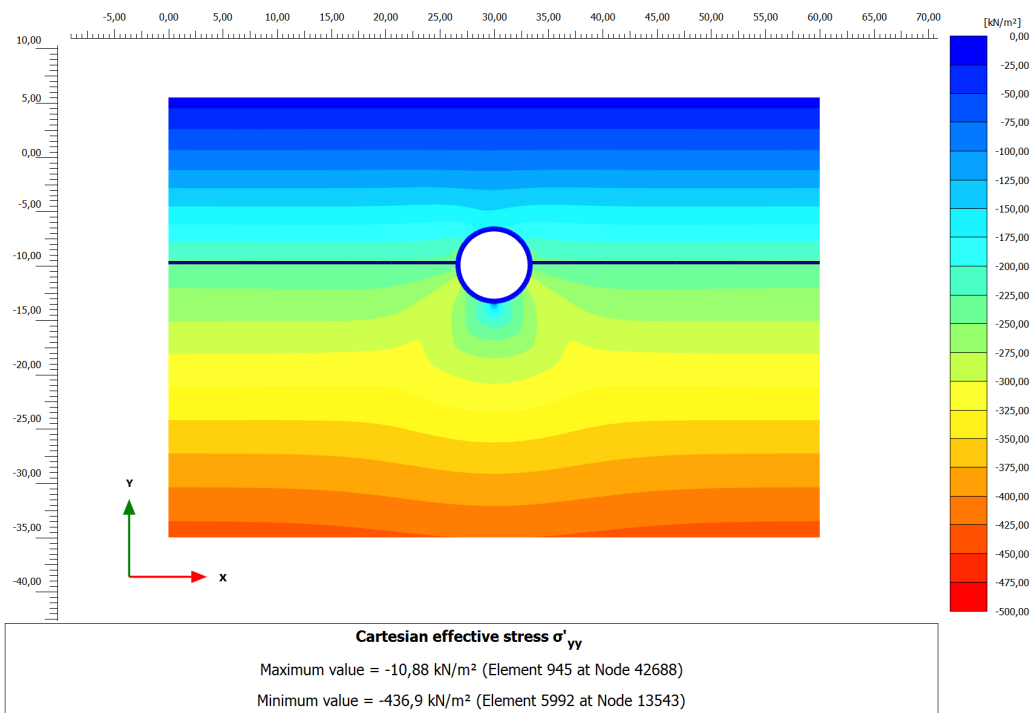


Figure B.41: Effective vertical stress (σ'_{yy}) of BH88 at year 2030

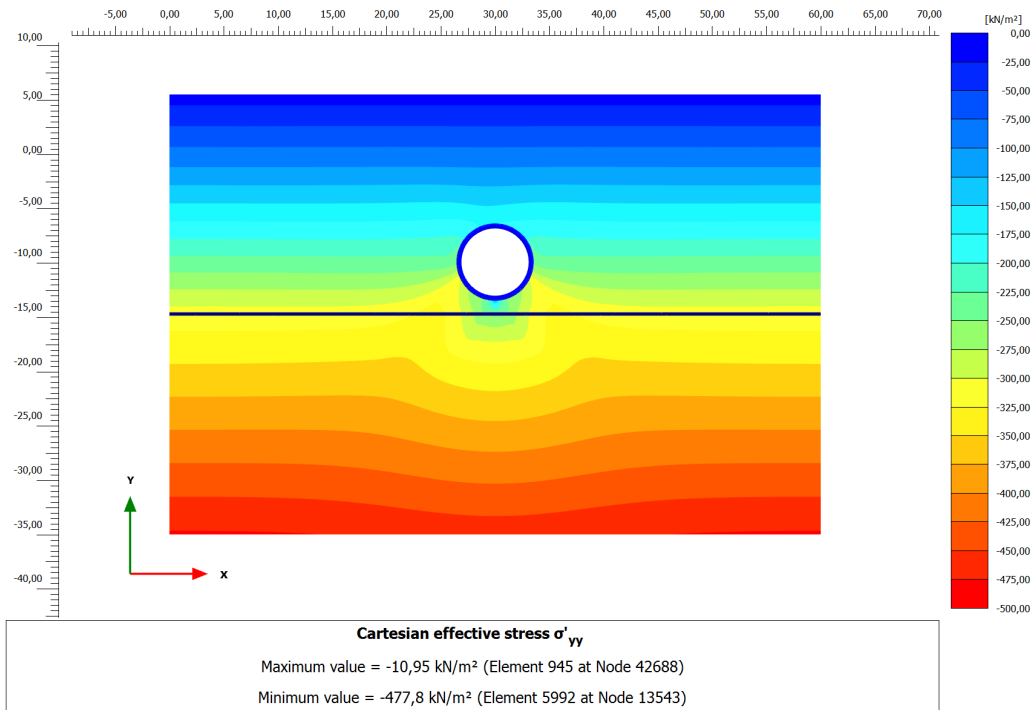


Figure B.42: Effective vertical stress (σ'_{yy}) of BH88 at year 2040

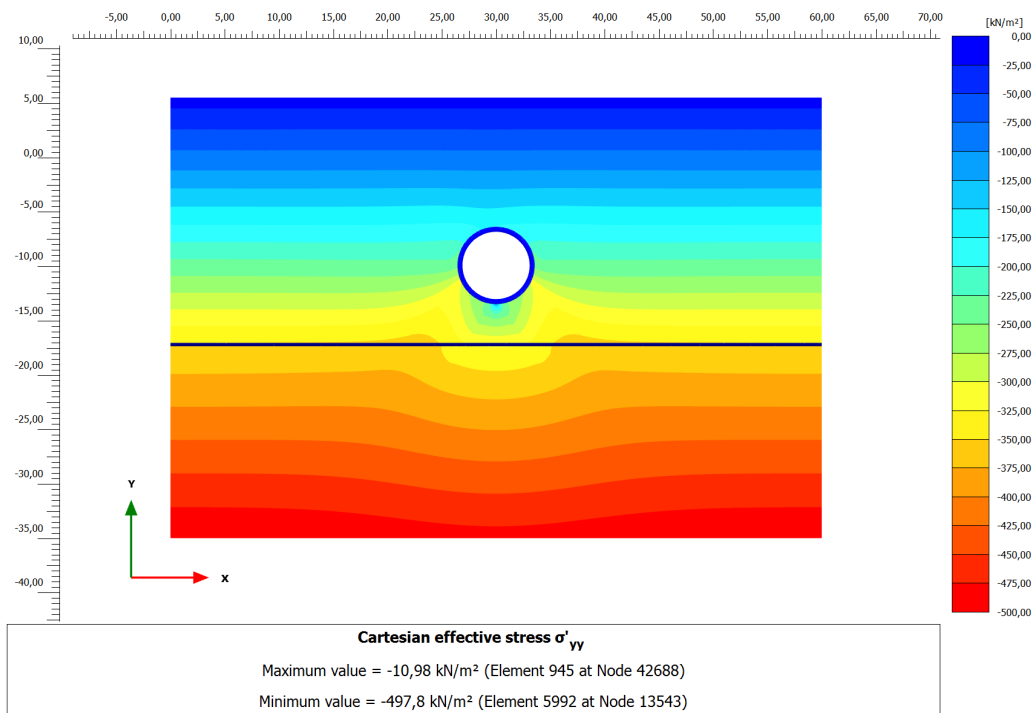


Figure B.43: Effective vertical stress (σ'_{yy}) of BH88 at year 2050

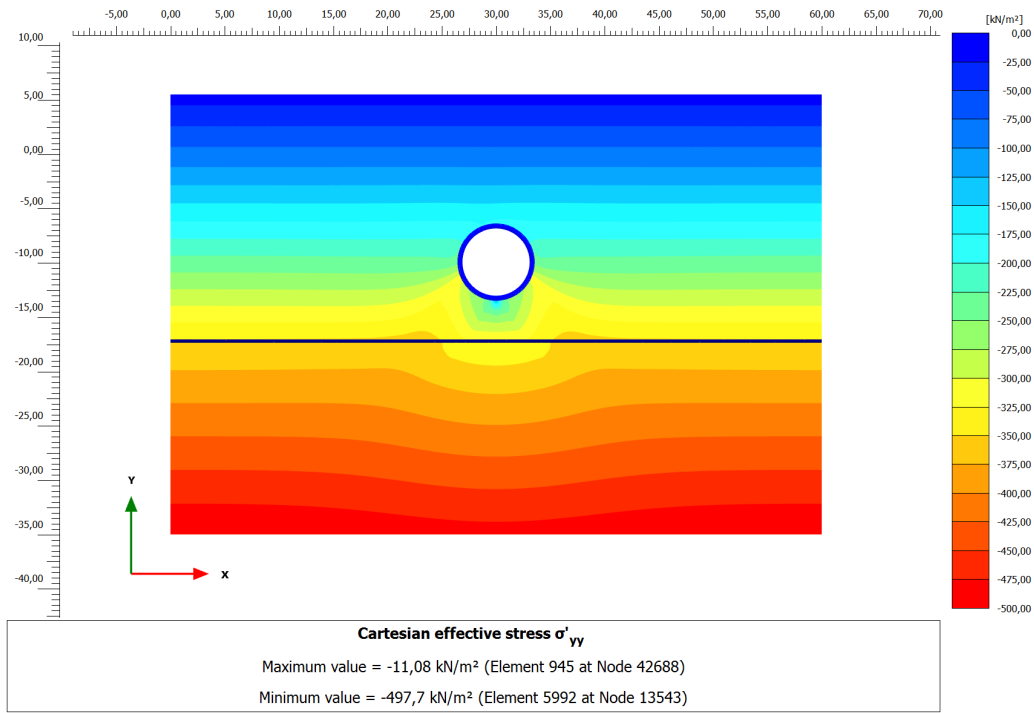


Figure B.44: Effective vertical stress (σ'_{yy}) of BH88 at year 2100

B.3.4 Scenario D

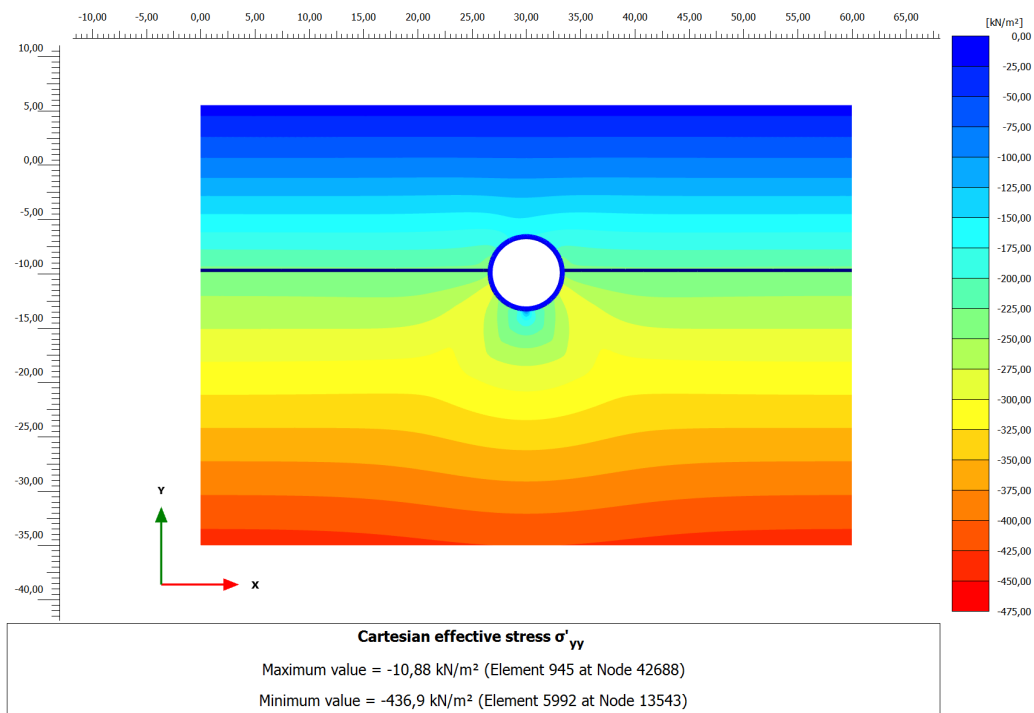


Figure B.45: Effective vertical stress (σ'_{yy}) of BH88 at year 2030

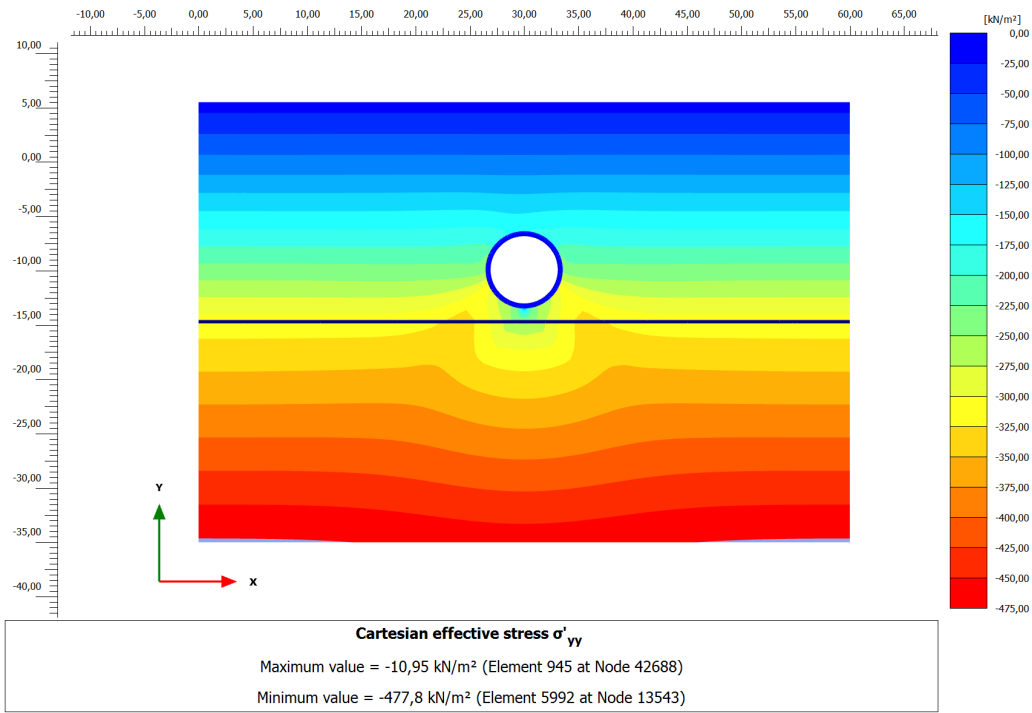


Figure B.46: Effective vertical stress (σ'_{yy}) of BH88 at year 2040

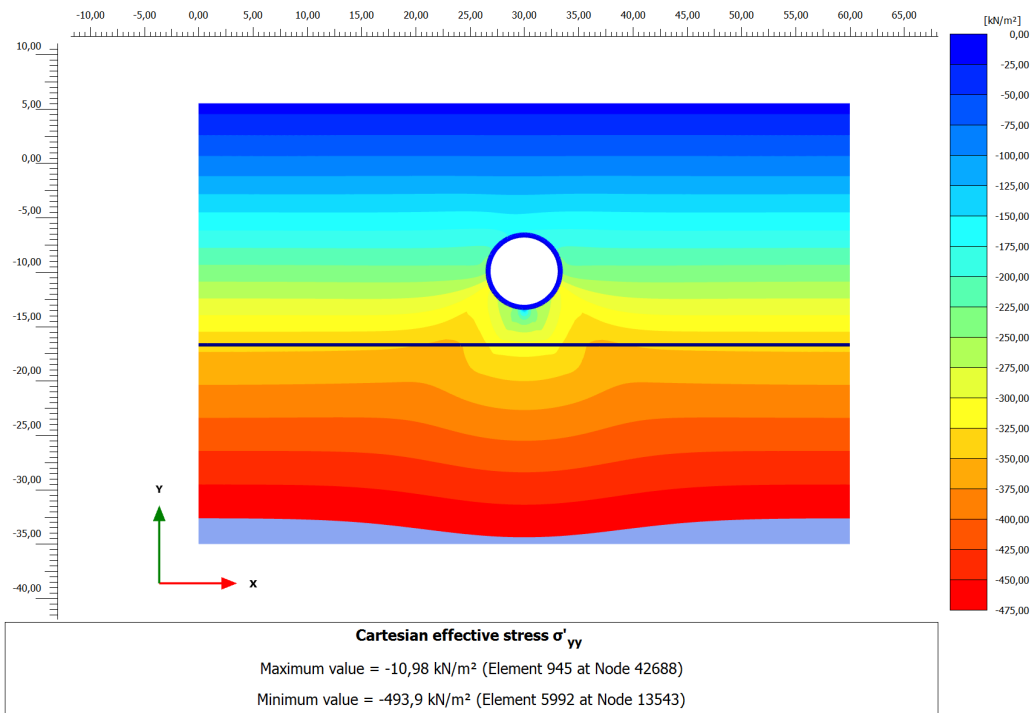


Figure B.47: Effective vertical stress (σ'_{yy}) of BH88 at year 2050

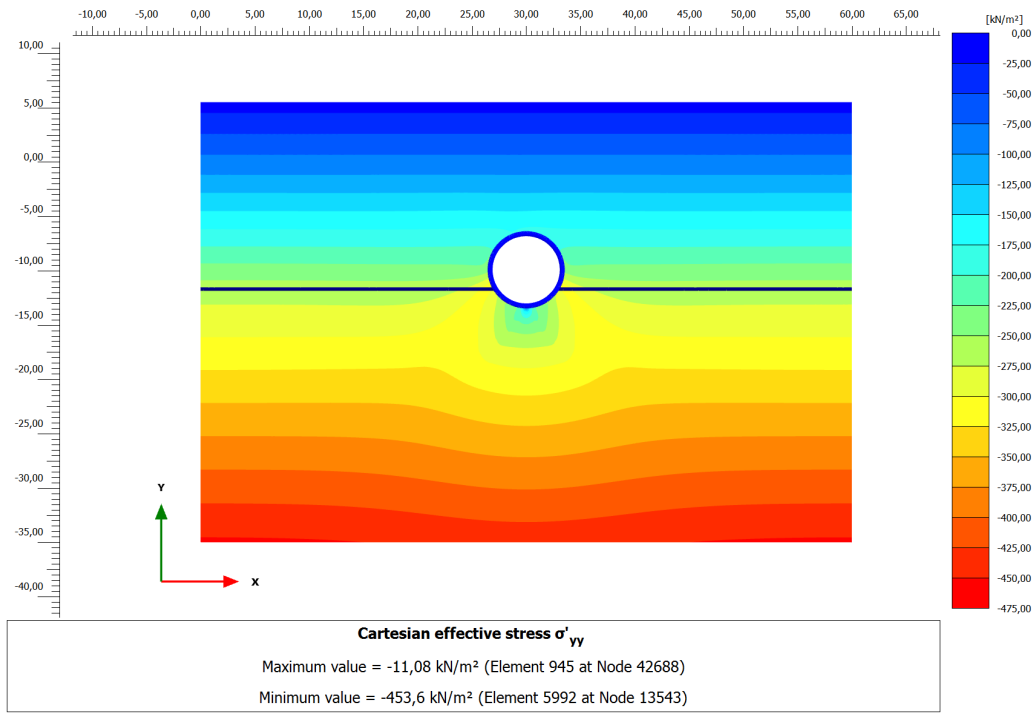


Figure B.48: Effective vertical stress (σ'_{yy}) of BH88 at year 2100

B.4. Effective Horizontal Soil Stress

B.4.1 Scenario A

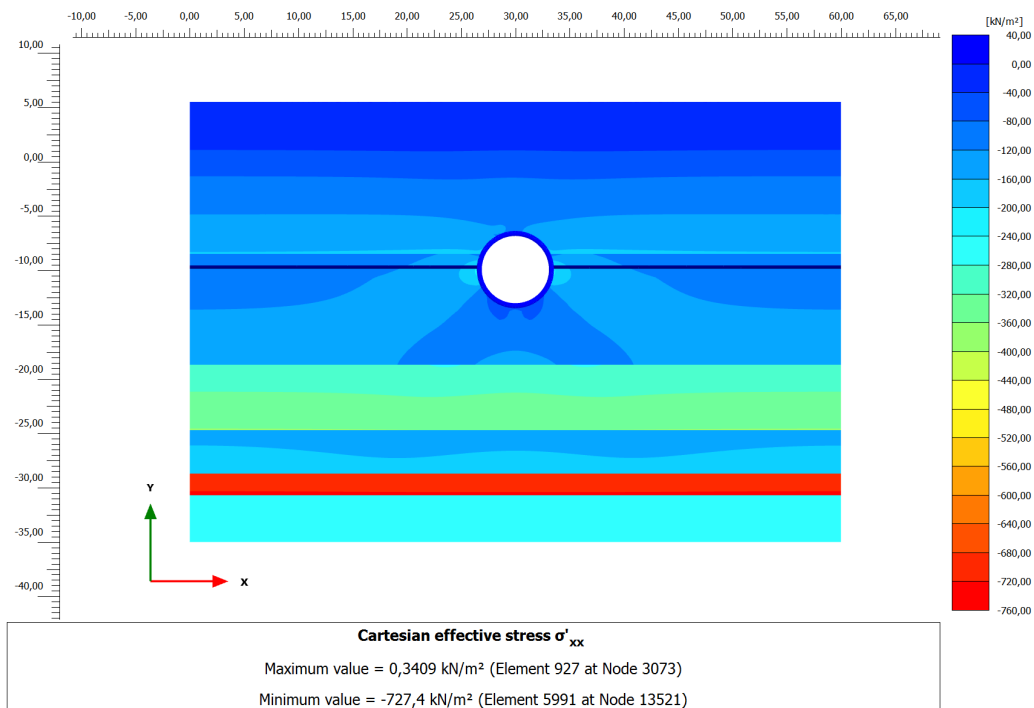


Figure B.49: Effective horizontal stress (σ'_{xx}) of BH88 at year 2030

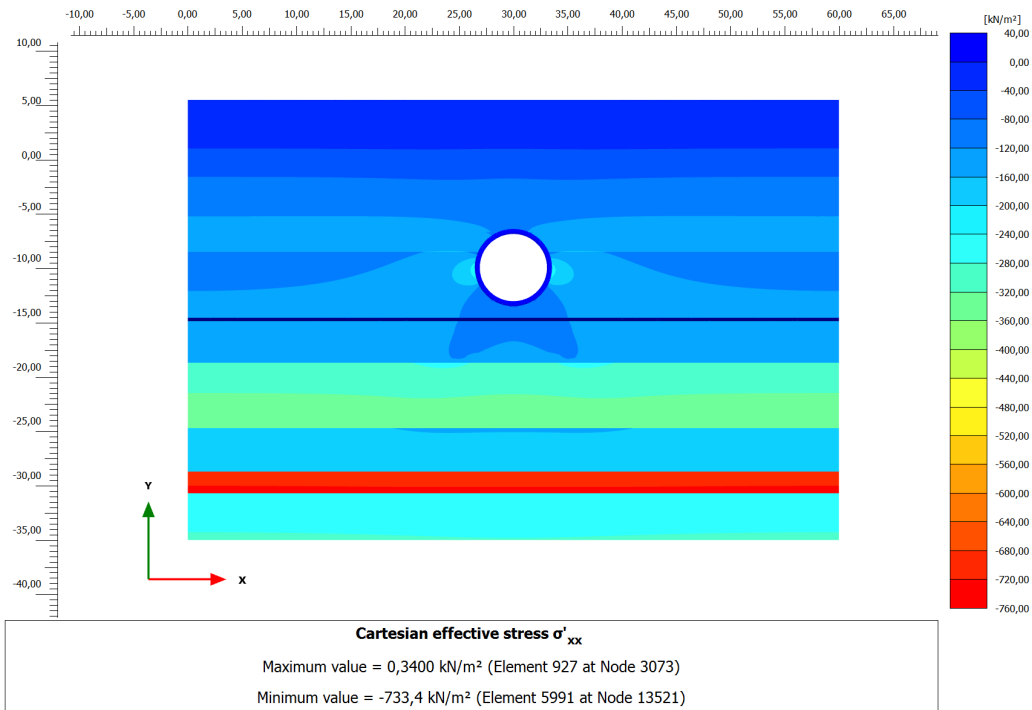


Figure B.50: Effective horizontal stress (σ'_{xx}) of BH88 at year 2040

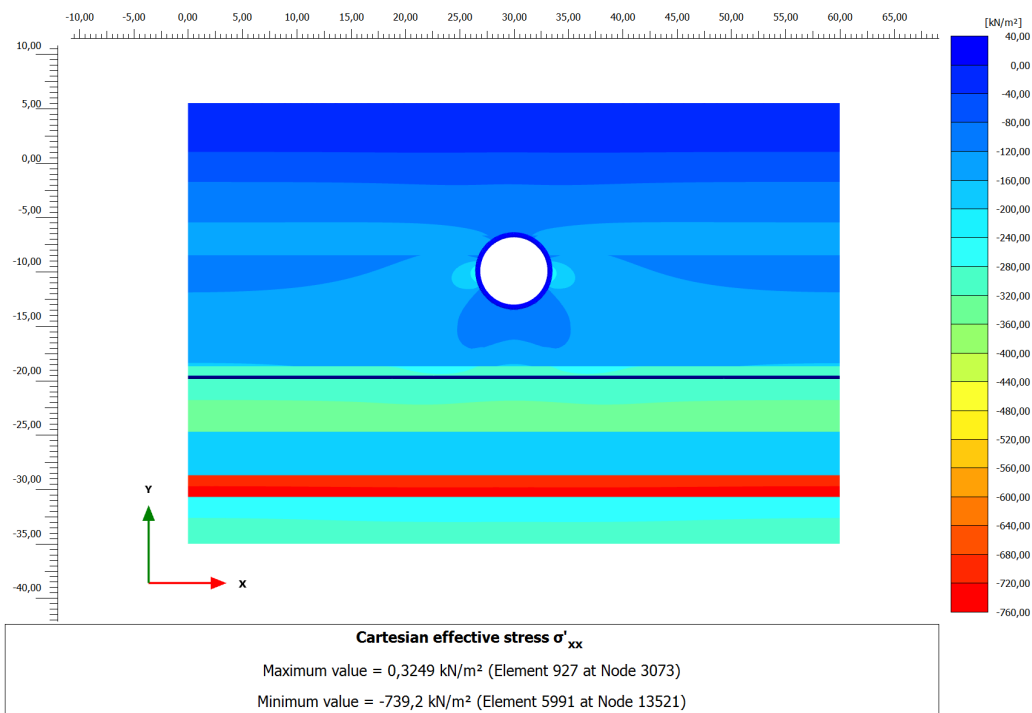


Figure B.51: Effective horizontal stress (σ'_{xx}) of BH88 at year 2050

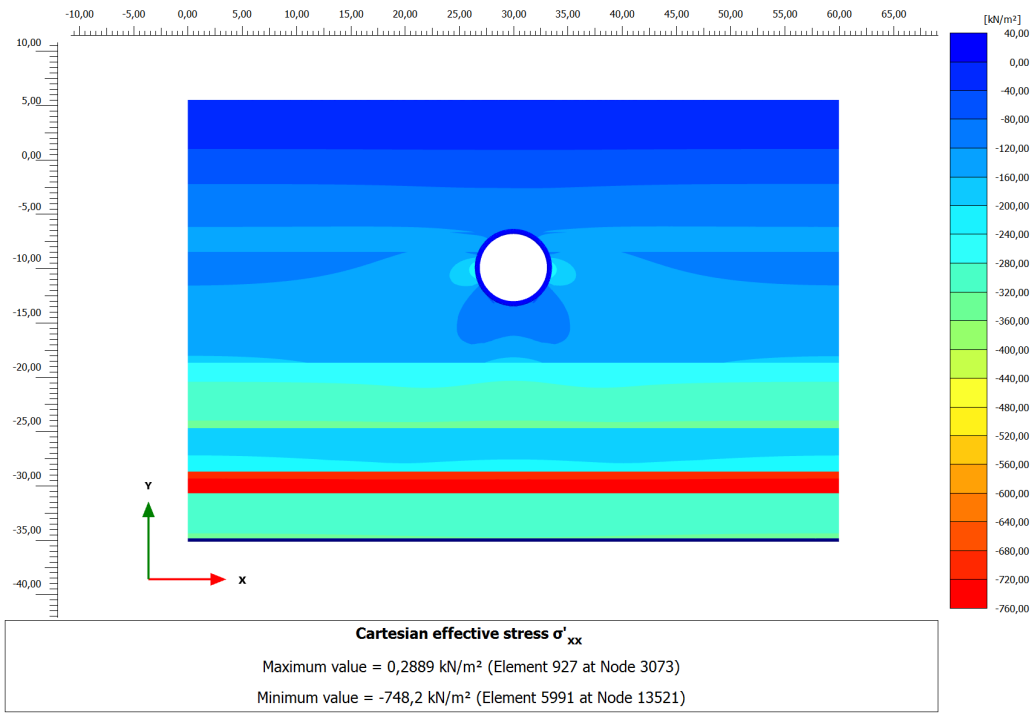


Figure B.52: Effective horizontal stress (σ'_{xx}) of BH88 at year 2100

B.4.2 Scenario B

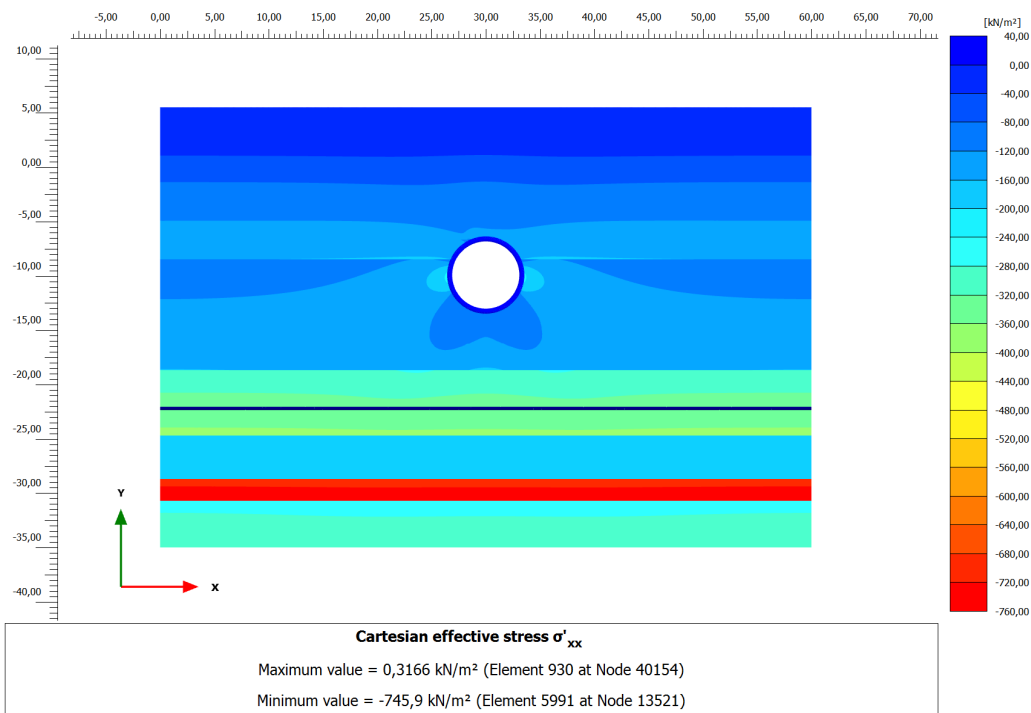


Figure B.53: Effective horizontal stress (σ'_{xx}) of BH88 at year 2030

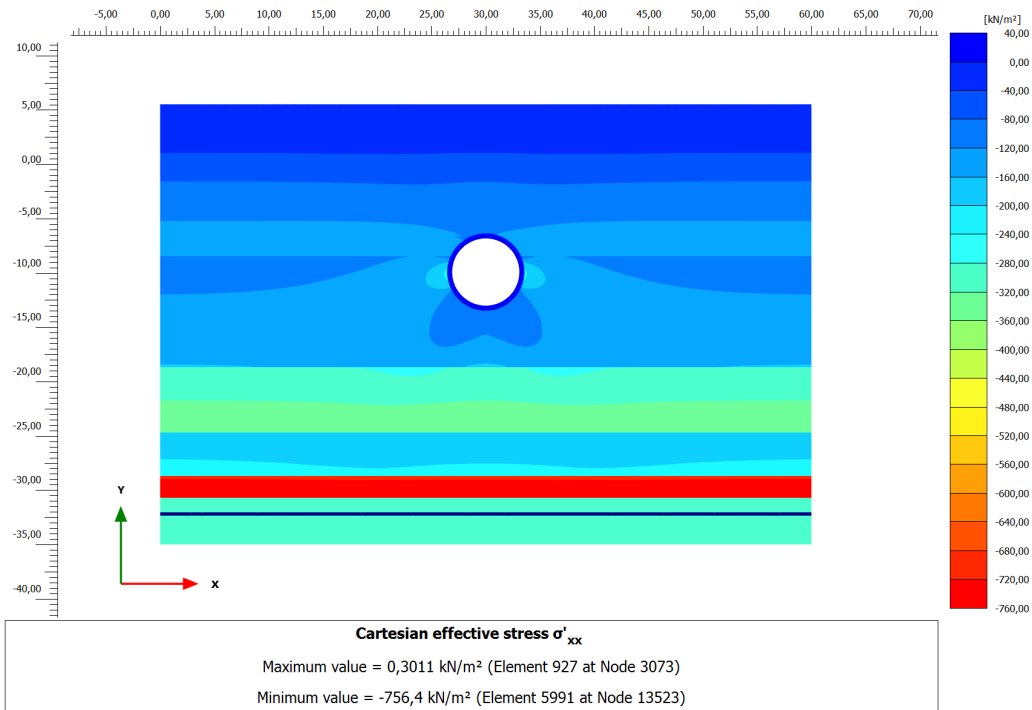


Figure B.54: Effective horizontal stress (σ'_{xx}) of BH88 at year 2040

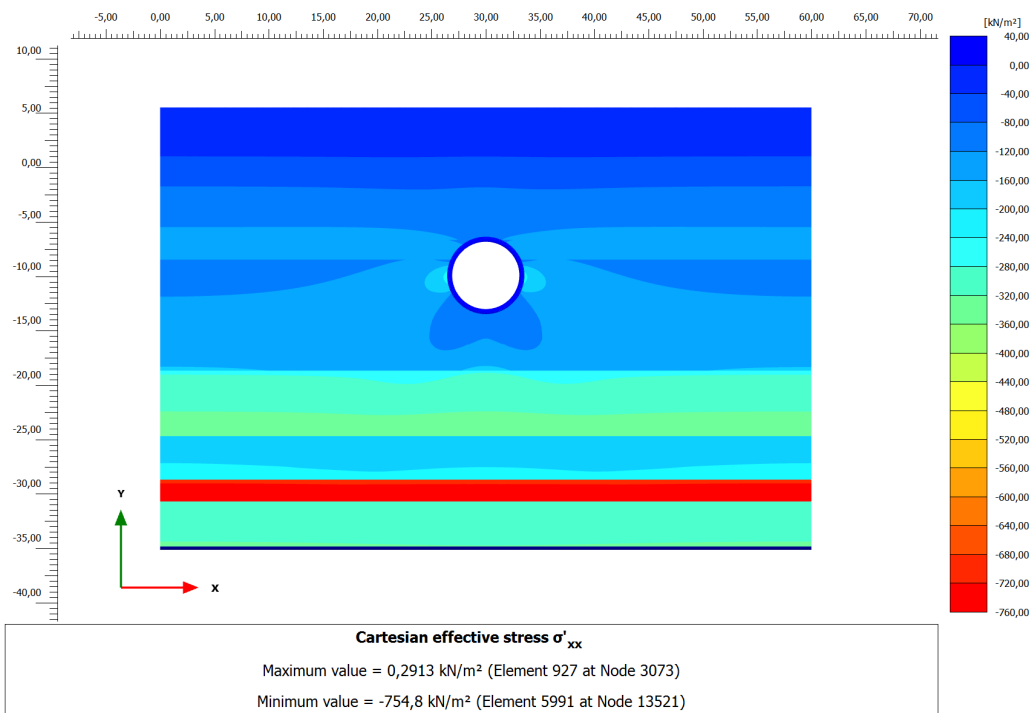


Figure B.55: Effective horizontal stress (σ'_{xx}) of BH88 at year 2050

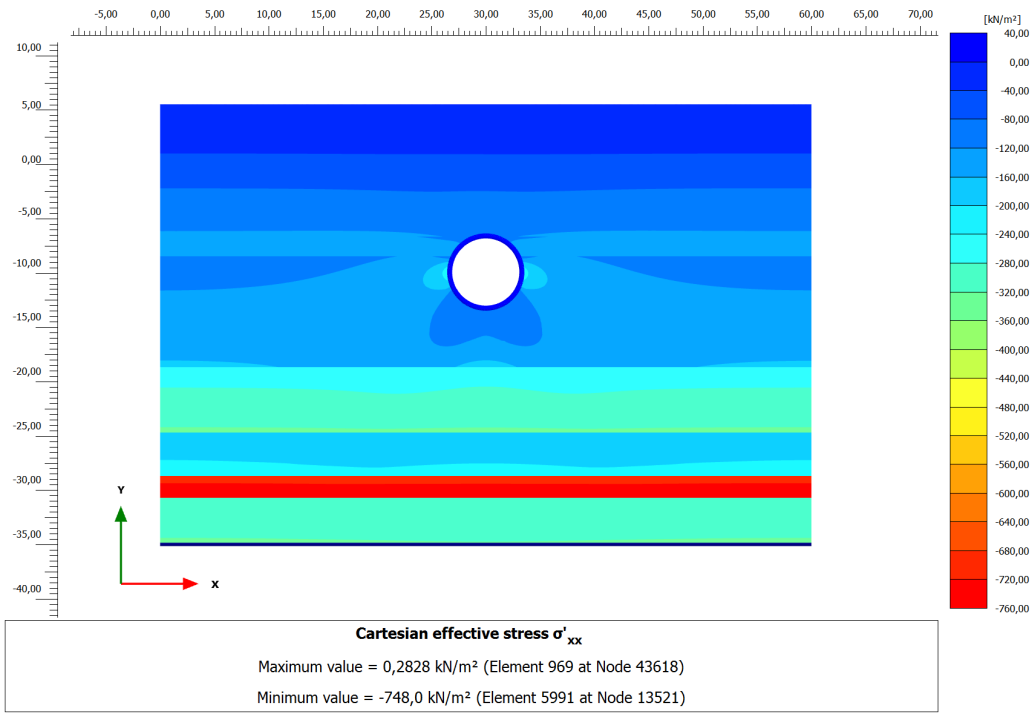


Figure B.56: Effective horizontal stress (σ'_{xx}) of BH88 at year 2100

B.4.3 Scenario C

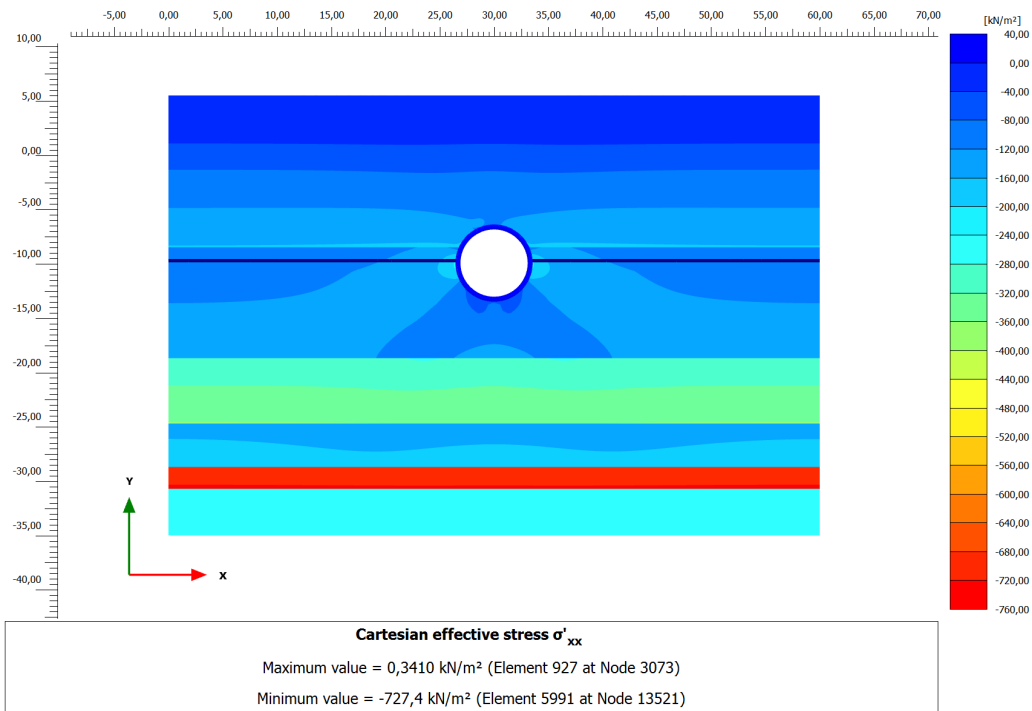


Figure B.57: Effective horizontal stress (σ'_{xx}) of BH88 at year 2030

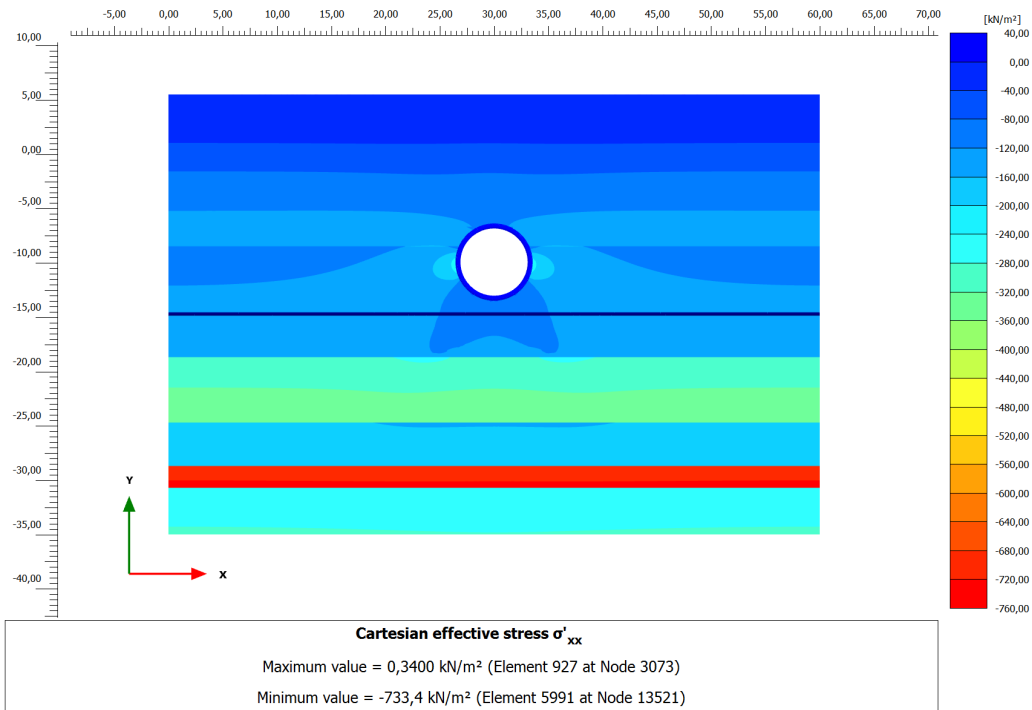


Figure B.58: Effective horizontal stress (σ'_{xx}) of BH88 at year 2040

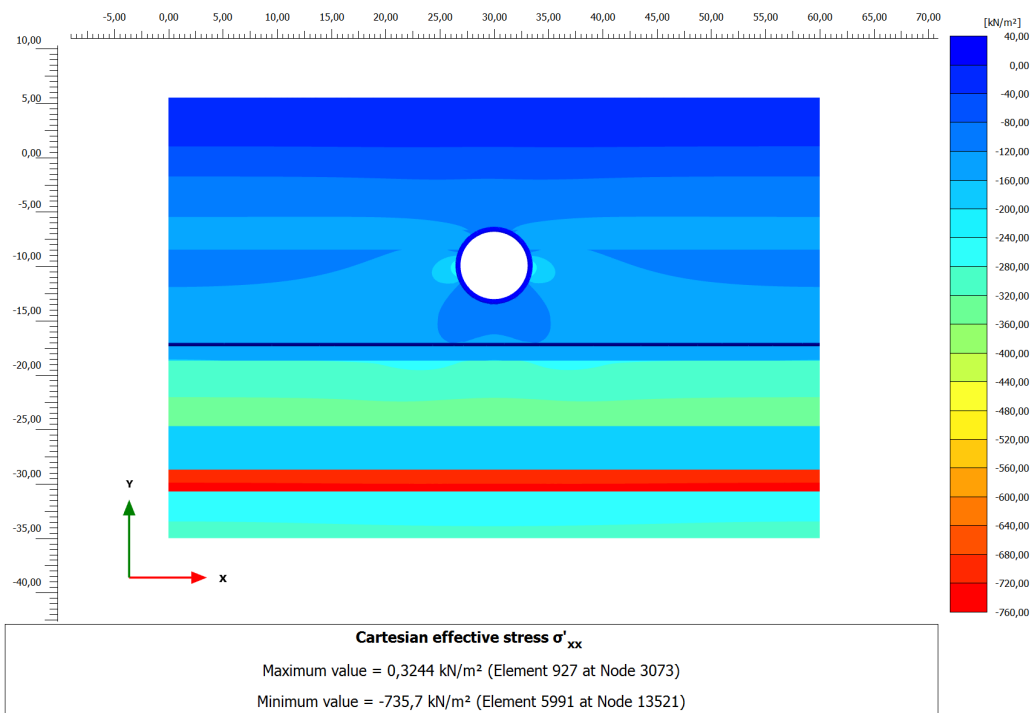


Figure B.59: Effective horizontal stress (σ'_{xx}) of BH88 at year 2050

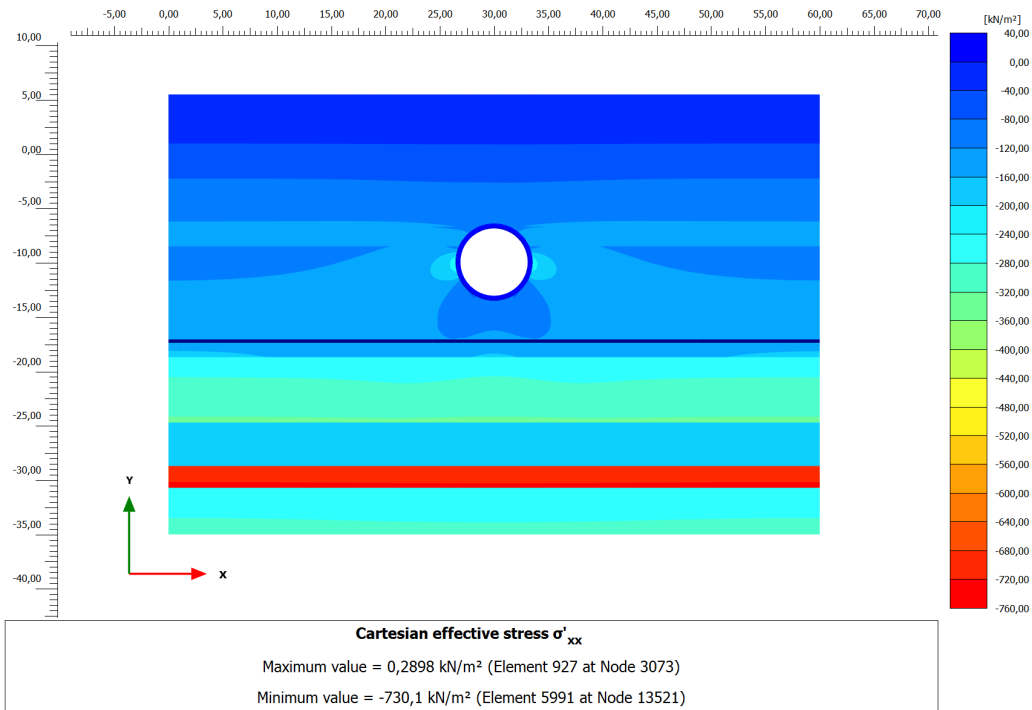


Figure B.60: Effective horizontal stress (σ'_{xx}) of BH88 at year 2100

B.4.4 Scenario D

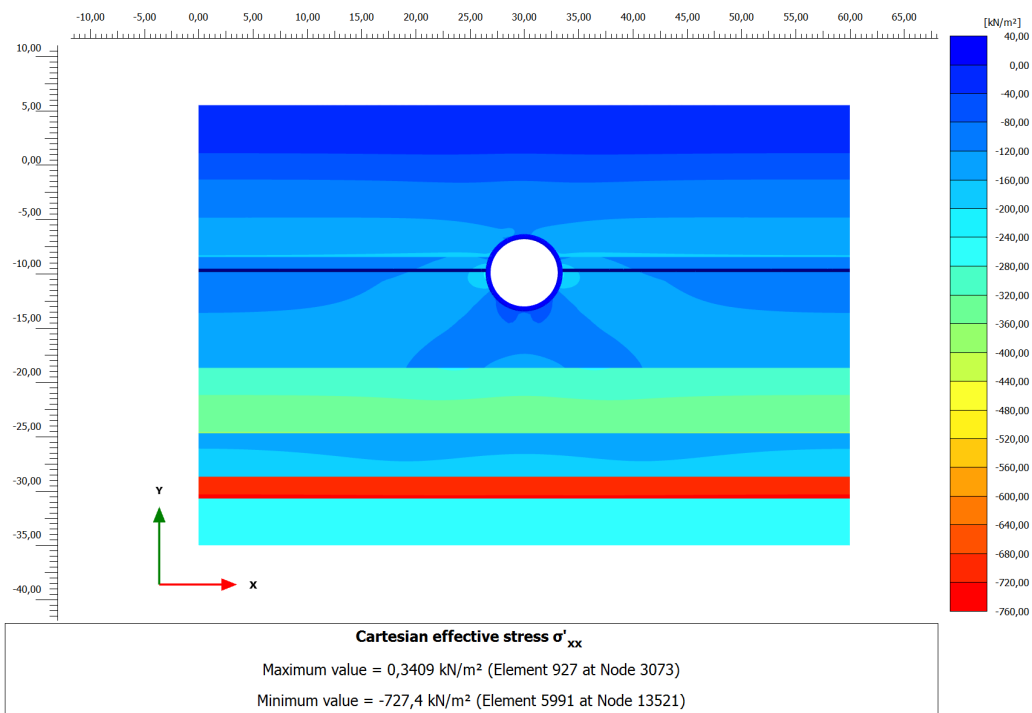


Figure B.61 Effective horizontal stress (σ'_{xx}) of BH88 at year 2030

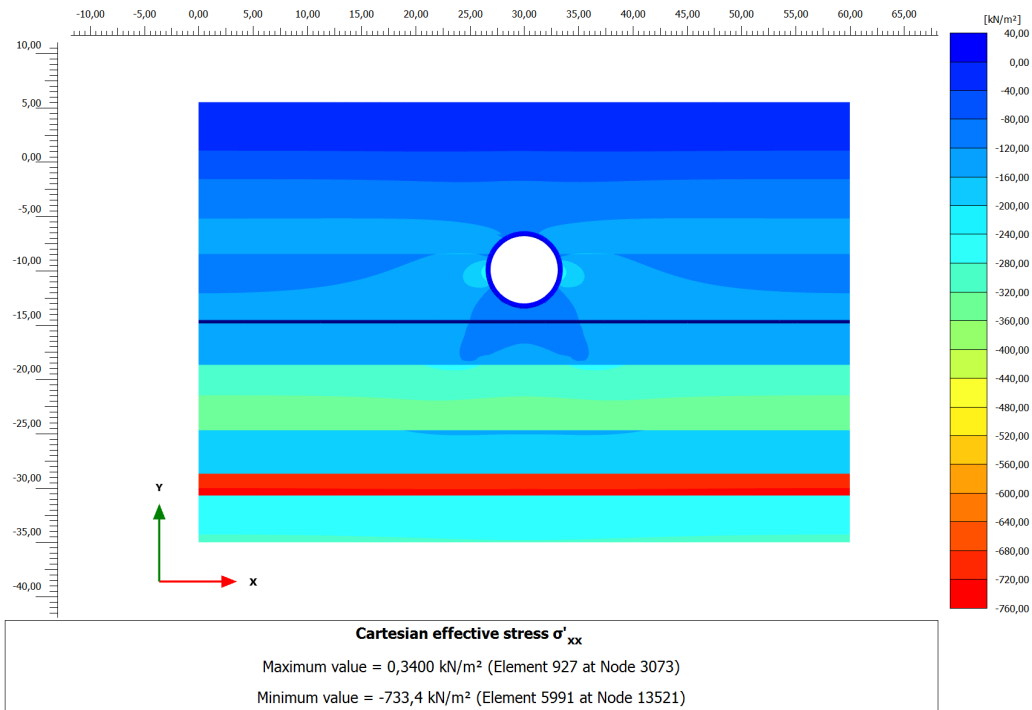


Figure B.62 Effective horizontal stress (σ'_{xx}) of BH88 at year 2040

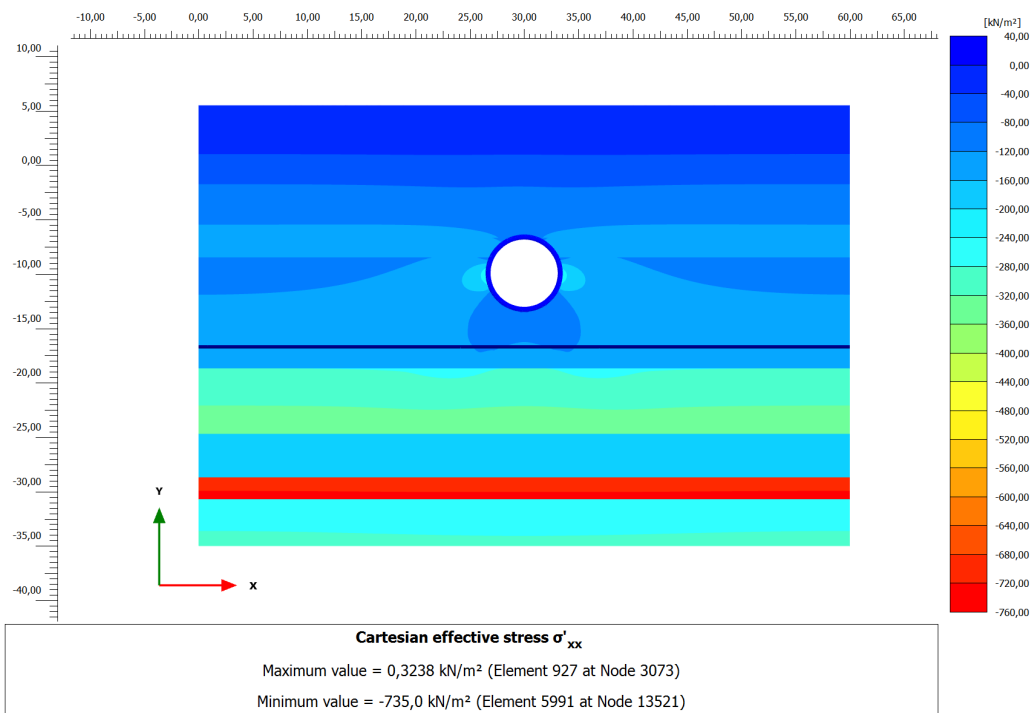


Figure B.63 Effective horizontal stress (σ'_{xx}) of BH88 at year 2050

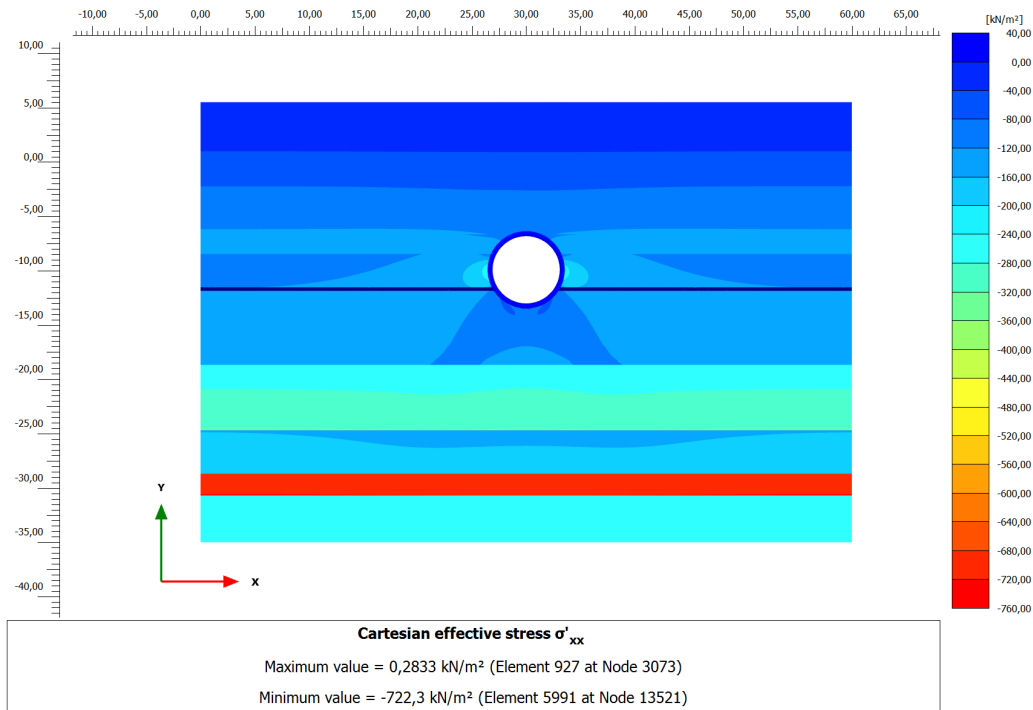


Figure B.64 Effective horizontal stress (σ'_{xx}) of BH88 at year 2100

B.5. Layer Consolidation

This segment shows the total settlement that is experienced by each layers in *BH88*. Nodes A to I is associated to the cross sectional model as shown in the Figure B.65.

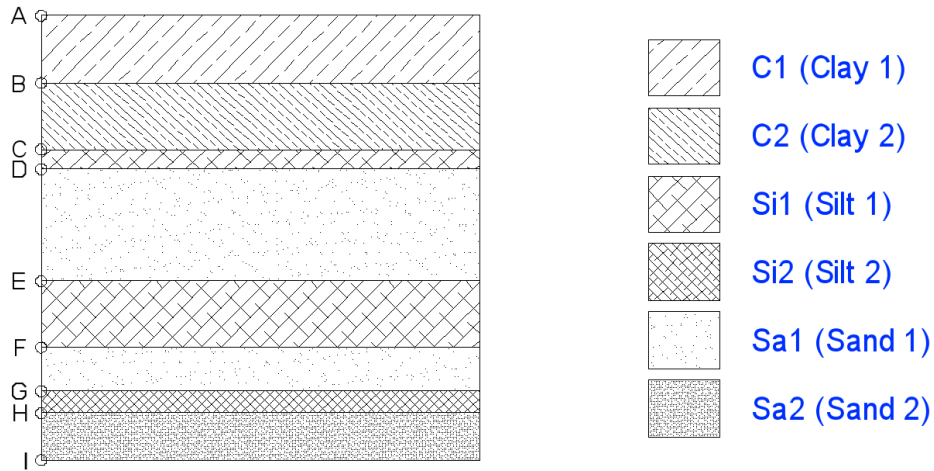


Figure B.65: Nodes assignment at BH88

Furthermore, the associated cumulative settlement is displayed in Figure B.66.

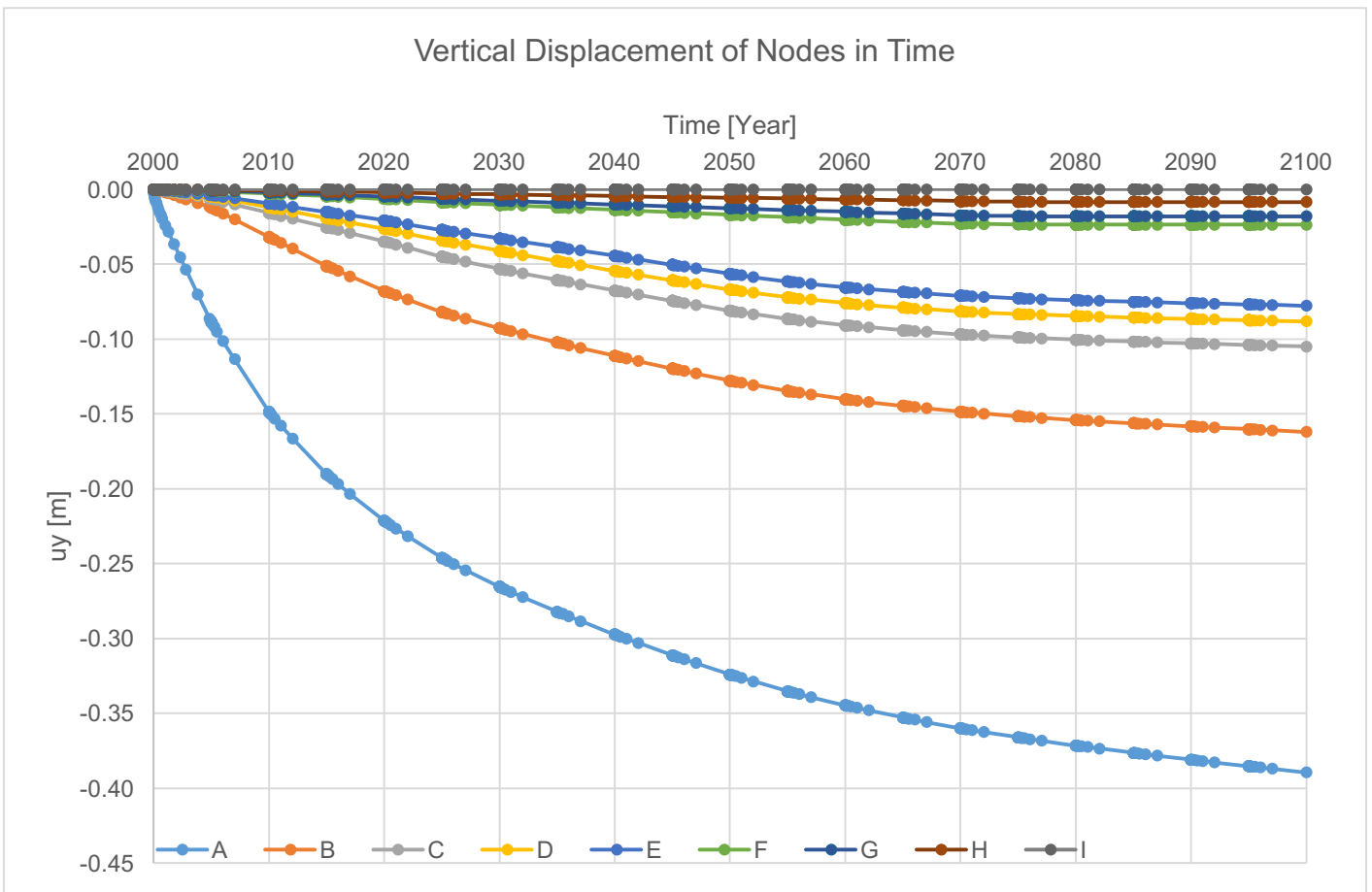


Figure B.66: Total settlement of nodes in BH88

Further interpretation of Figure B.66 was performed in tabular method. As the graph displays the total settlement, the change in layer thickness can be calculated with the equation below, where h_0 is the initial thickness, h_1 is the final thickness, d_i and d_{i+1} represent the total settlement at the top boundary and lower boundary respectively.

$$h_0 = h_1 + (d_{i+1} - d_i)$$

Departing from the change in thickness, the contribution of each layer to the total settlement can be calculated. The result of the computation is presented in the table below.

Layer	Type	Elevation [m]		Initial Thickness [m]	Node		uy [m]		Change in Thickness [m]	Contribution	Final Thickness [m]
		Top	Bot		Top	Bot	Top	Bot			
1	C1	5.51	-0.64	6.15	A	B	-0.39	-0.16	0.23	58.39%	5.92
2	C2	-0.64	-6.67	6.03	B	C	-0.16	-0.11	0.06	14.64%	5.97
3	Si1	-6.67	-8.48	1.81	C	D	-0.11	-0.09	0.02	4.29%	1.79
4	Sa1	-8.48	-18.68	10.20	D	E	-0.09	-0.08	0.01	2.70%	10.19
5	Si1	-18.68	-24.70	6.02	E	F	-0.08	-0.02	0.05	13.87%	5.97
6	Sa1	-24.70	-28.70	4.00	F	G	-0.02	-0.02	0.01	1.45%	3.99
7	Si2	-28.70	-30.70	2.00	G	H	-0.02	-0.01	0.01	2.46%	1.99
8	Sa2	-30.70	-35.00	4.30	H	I	-0.01	0.00	0.01	2.21%	4.29

B.6. 100EI Tunnel

An arbitrary case of stiffer tunnel with $EI = 100EI_{Original}$ was analyzed. Compared to other equivalent beams, this beam is one order of magnitude larger than the calculated stiffness and two orders of magnitude larger than the reported stiffness. Despite it reduces the differential settlement in the longitudinal direction, the structure is subjected to greater bending moment. The deformation and bending moment of this structure are displayed in the figures below.

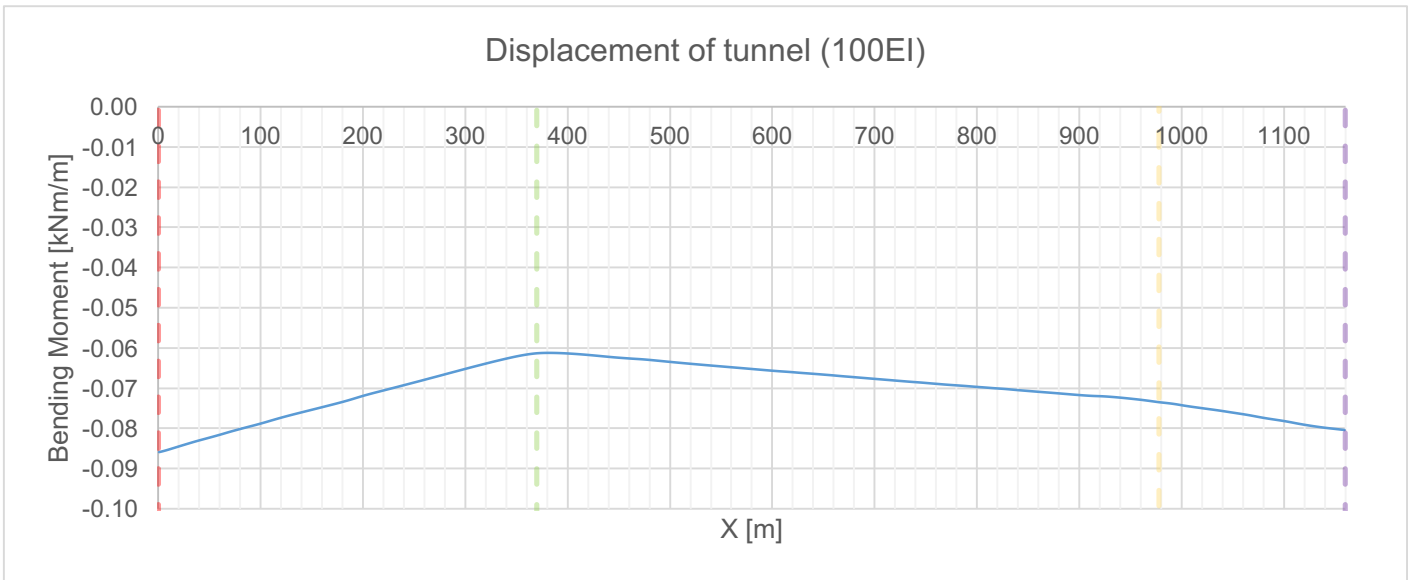


Figure B.67: Displacement profile of 100EI tunnel

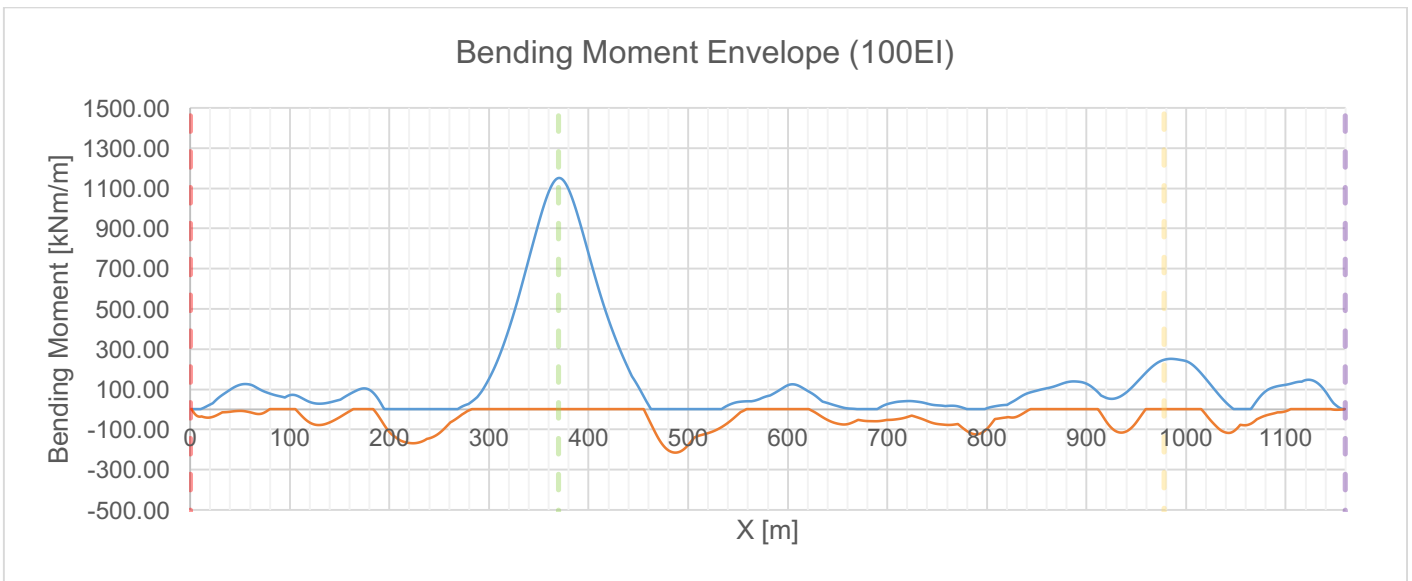


Figure B.68: Bending moment envelope of 100EI tunnel

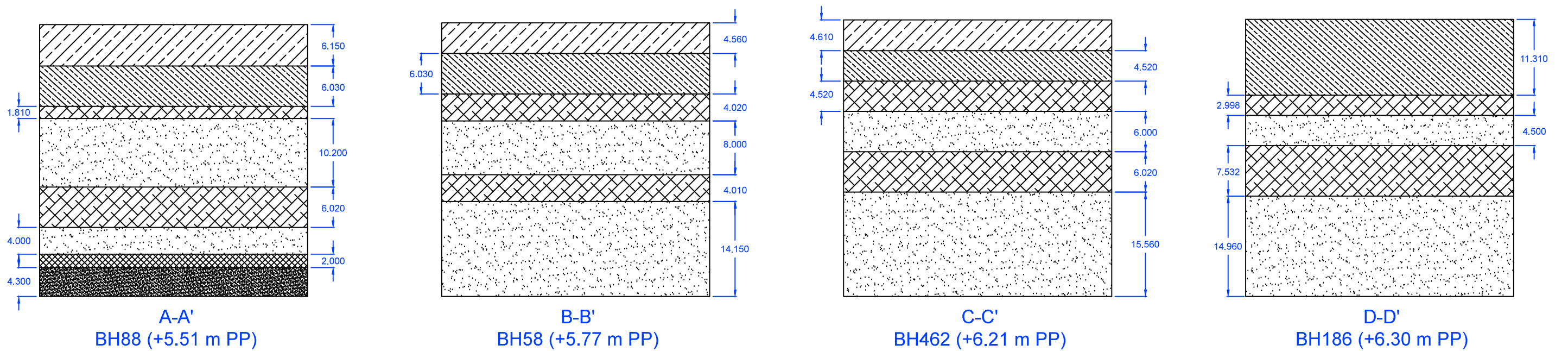
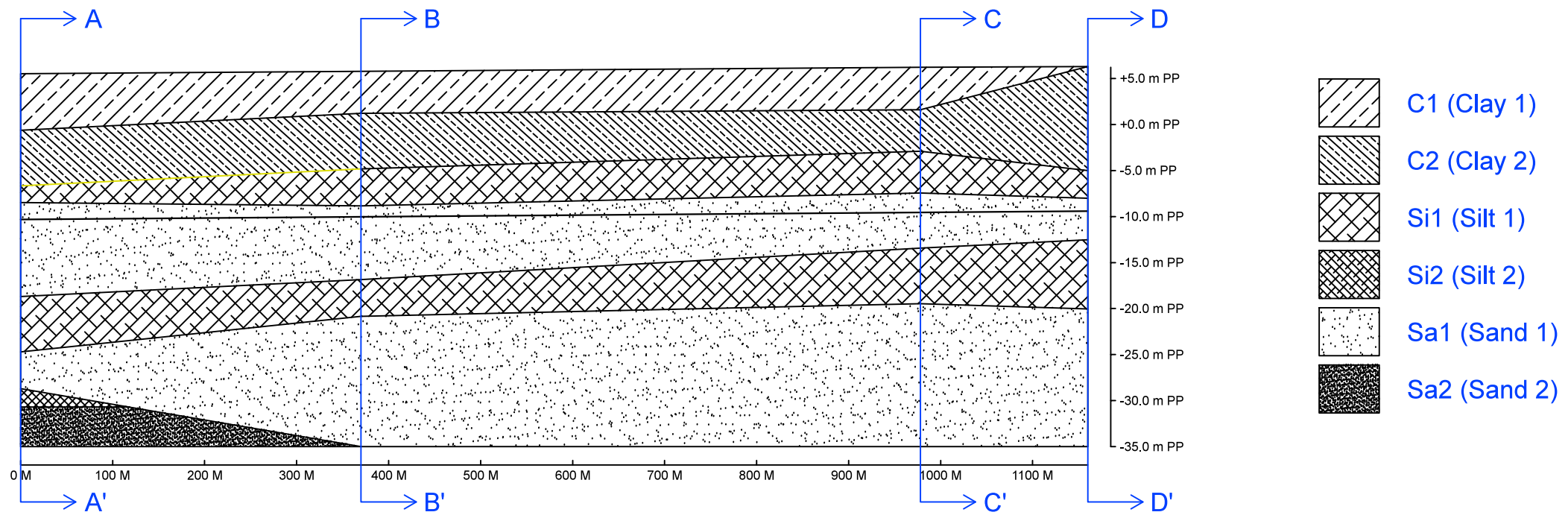
Appendix C: GEOTECHNICAL REPORT MRT JAKARTA


[Redacted]

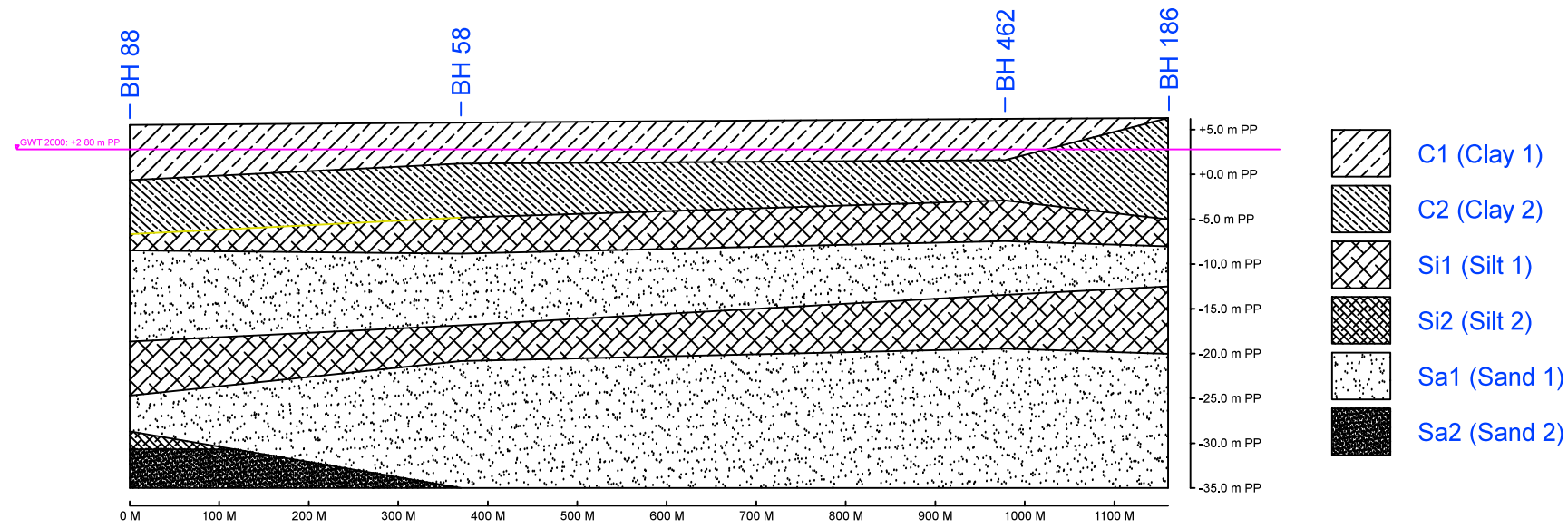
Appendix D: TECHNICAL REPORT MRT JAKARTA

[Redacted]

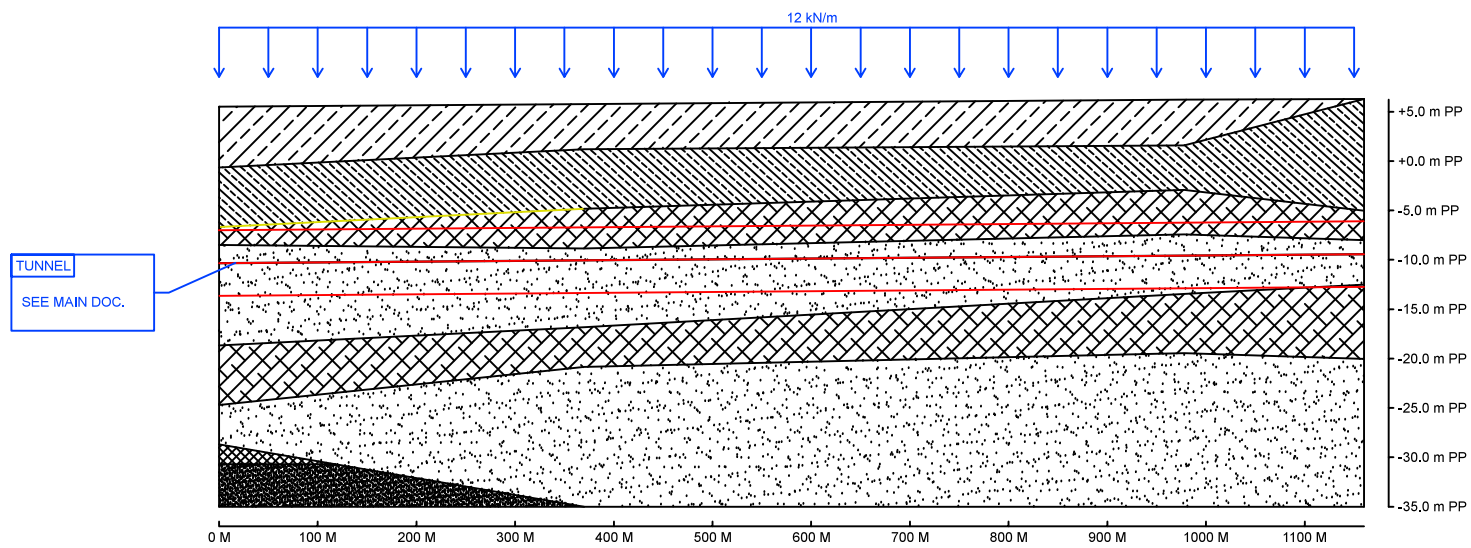
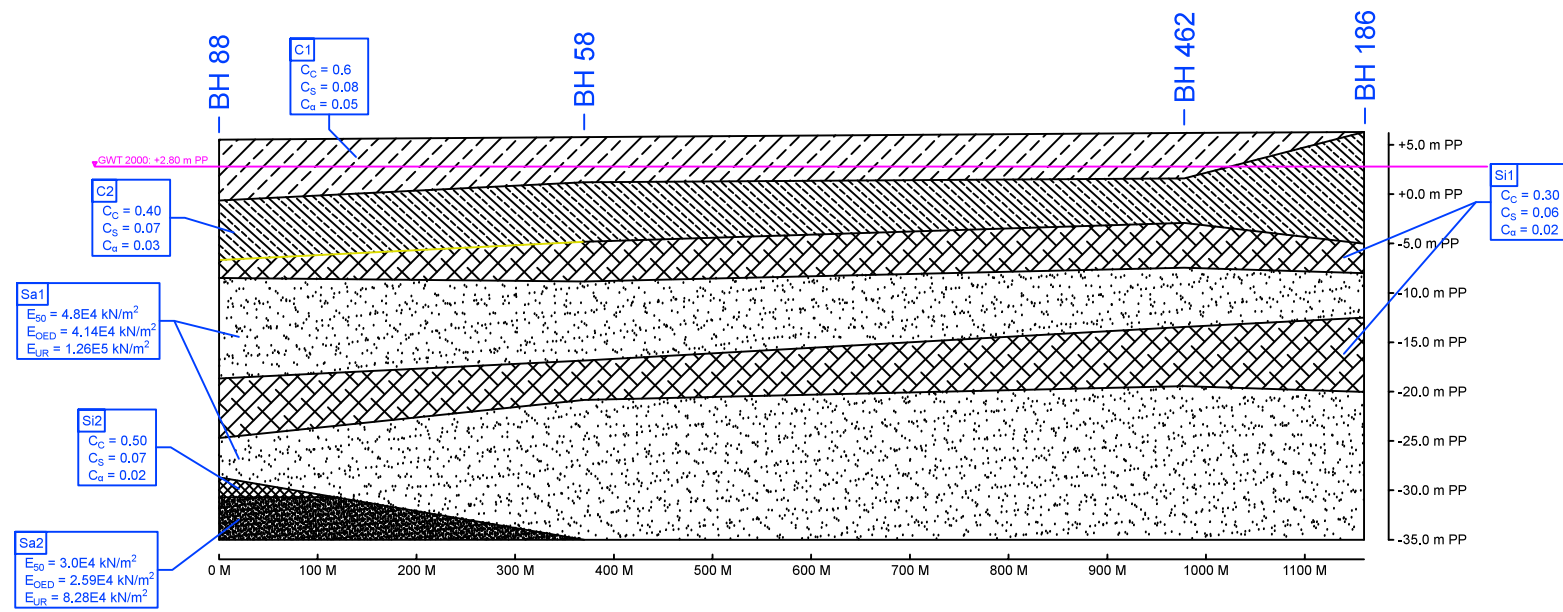
Appendix E: DRAWINGS



 TECHNISCHE UNIVERSITEIT DELFT JOHANNES SIMANJUNTAK	TITLE LONGITUDINAL AND SECTIONAL PROFILE	APPENDIX E
	REMARKS THE SOIL PROFILE WAS GENERATED FROM THE SPT RESULTS FROM DIFFERENT SOURCES. THESE SPT RESULTS WERE ORIGINALLY COLLECTED FOR SEISMIC STUDY IN JAKARTA.	DRAWING NO. 1

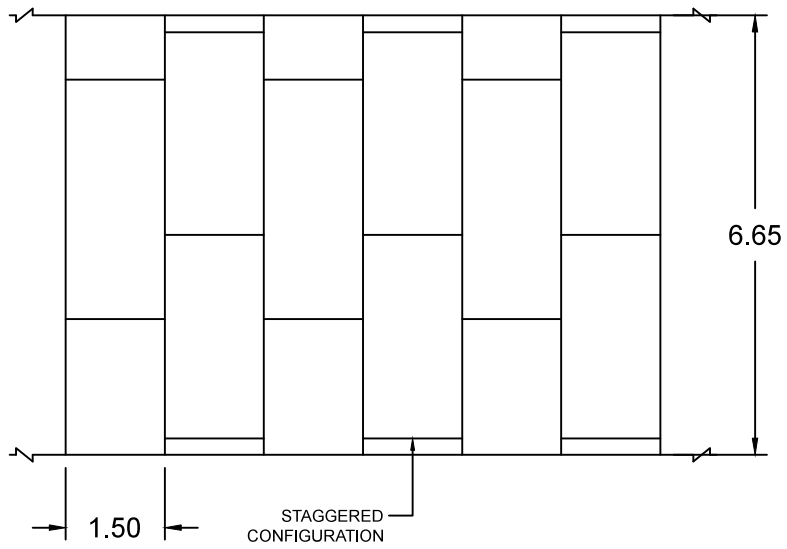
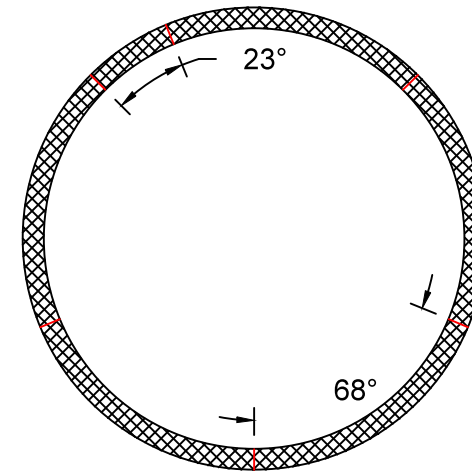
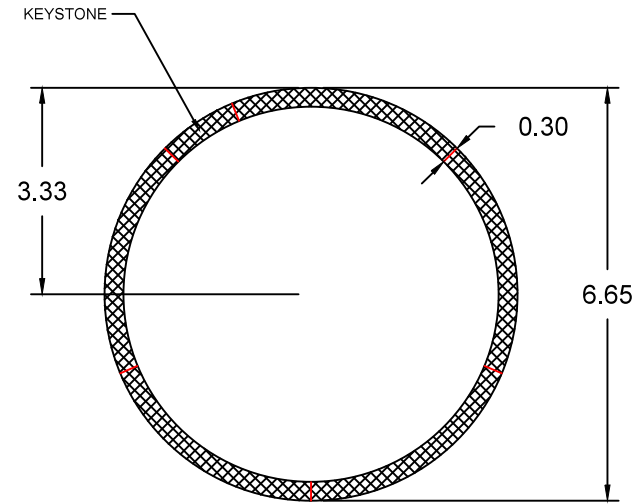
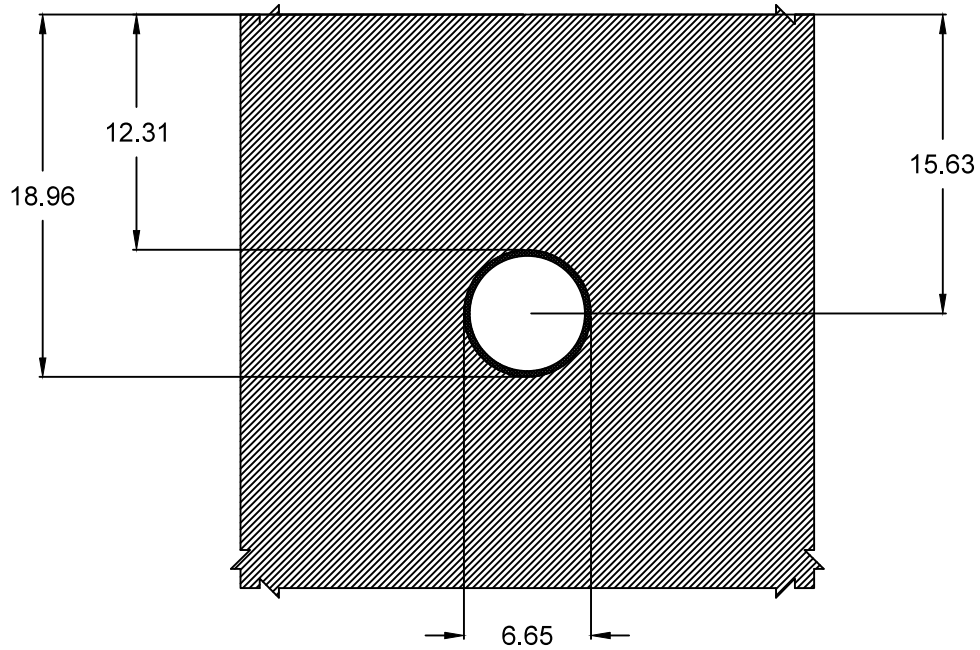



- C1 (Clay 1)
- C2 (Clay 2)
- Si1 (Silt 1)
- Si2 (Silt 2)
- Sa1 (Sand 1)
- Sa2 (Sand 2)



NOTES:
 THE UNIFORMLY DISTRIBUTED LOAD OF 12 KN/M
 WAS ASSIGNED BASED ON THE DESIGN LANE
 LOAD, PROVIDED BY INTERNATIONAL CODE
 COUNCIL FOR STRUCTURAL ENGINEERING.

 TECHNISCHE UNIVERSITEIT DELFT JOHANNES SIMANJUNTAK	TITLE SOIL PROFILE WITH PROPERTIES	APPENDIX E
	REMARKS SELECTION OF PARAMETERS ARE BASED ON PAST STUDIES AS WELL AS THE ESTABLISHED RANGES. CALIBRATION OF MODEL WAS REQUIRED TO OBTAIN THE FINAL PARAMETERS.	DRAWING NO. 2



 TECHNISCHE UNIVERSITEIT DELFT JOHANNES SIMANJUNTAK	TITLE TUNNEL GEOMETRY AND DEPTH	APPENDIX E
	REMARKS THE GEOMETRY OF THE TUNNEL IS BASED ON NSL-P1 TUNNEL AS THE DESIGN OF NSL-P2 IS NOT READY AT THE POINT OF WRITING.	DRAWING NO. 3